SANDIA REPORT

SAND2018-3116
Unlimited Release
Printed March 2018

Development and Evaluation of a Drone-Deployed Wind Turbine Blade Nondestructive Inspection System

G. Ray Ely
Dennis P. Roach
Tom M. Rice
Garrett D. Nelson
Josh Paquette

Prepared by
Sandia National Laboratories
Albuquerque, New Mexico 87185 and Livermore, California 94550

Sandia National Laboratories is a multimission laboratory managed and operated by National Technology and Engineering Solutions of Sandia, LLC, a wholly owned subsidiary of Honeywell International, Inc., for the U.S. Department of Energy's National Nuclear Security Administration under contract DE-NA0003525.

Issued by Sandia National Laboratories, operated for the United States Department of Energy by National Technology and Engineering Solutions of Sandia, LLC.

Available to DOE and DOE contractors from

U.S. Department of Energy
Office of Scientific and Technical Information
P.O. Box 62
Oak Ridge, TN 37831

Telephone: (865) 576-8401
Facsimile: (865) 576-5728
E-Mail: reports@osti.gov
Online ordering: http://www.osti.gov/scitech

Available to the public from

U.S. Department of Commerce
National Technical Information Service
5301 Shawnee Rd
Alexandria, VA 22312

Telephone: (800) 553-6847
Facsimile: (703) 605-6900
E-Mail: orders@ntis.gov
Online order: http://www.ntis.gov/search

SAND2018-3116
Printed March 2018
Unlimited Release

Development and Evaluation of a Drone-Deployed Wind Turbine Blade Nondestructive Inspection System

G. Ray Ely
Dennis P. Roach
Tom M. Rice
Transportation Safeguards and Surety Organization

Garrett Nelson
Experimental Mechanics and Dynamics

Josh Paquette
Wind Energy Technologies

Sandia National Laboratories
P. O. Box 5800
Albuquerque, New Mexico 87185-MS0781

Abstract

Wind energy is quickly becoming a significant contributor to the United States' overall energy portfolio. Wind turbine blades pose a unique set of inspection challenges that span from very thick and attenuative spar cap structures to porous bond lines, varying core material and a multitude of manufacturing defects of interest. The need for viable, accurate nondestructive inspection (NDI) technology becomes more important as the cost per blade, and lost revenue from downtime, grows. To address this growing need, Sandia and SkySpecs collaborated to evaluate NDI methods that are suitable for integration on an autonomous drone inspection platform. A trade study of these NDI methods was performed, and thermography was selected as the primary technique for further evaluation. Based on the capabilities of SkySpecs' custom inspection drone, a miniature microbolometer IR camera was successfully selected and tested in a benchtop setting. After identifying key operating parameters for inspecting wind blade materials, hardware and software integration of the IR camera was performed, and Sandia and SkySpecs conducted initial field testing. Finally, recommendations for a path forward for drone-deployed thermography inspections were provided.

ACKNOWLEDGMENTS

This program is sponsored by the U.S. Department of Energy (DOE) Small Business Voucher (SBV) program. This work was performed in conjunction with the DOE's Energy Efficiency & Renewable Energy department under the sponsorship and direction of Jose Zayas, Mike Derby, Jim Ahlgrimm, Cash Fitzpatrick and program managers Megan McCluer and Nick Johnson.

The NDI development work was formulated with the Sandia National Laboratories Wind Energy Technologies department and conducted in concert with the Sandia-organized Blade Reliability Collaborative (BRC) team. The authors would like to gratefully acknowledge the SkySpecs team for their contributions and time on this project. The authors would like to thank Dave Calkins and Ernie Gonzales for their assistance in extracting the wind blade visual inspection specimens. The authors would also like to thank Carl Jacques for his help designing X-Ray drone integration concepts. The authors would also like to thank Genaro Montoya and Jason Yoo for their help performing the thermography benchtop tests.

Special thanks goes to Steve Shepard and Thermal Wave Imaging for their thoughts on drone deployed thermography and permission to use their Thermographic Signal Reconstruction algorithm for research purposes.

TABLE OF CONTENTS

FIGURES

TABLES

THIS PAGE INTENTIONALLY LEFT BLANK

1. INTRODUCTION TO WIND BLADE INSPECTION MARKET AND CURRENT STATE OF THE ART

Wind energy is quickly becoming a significant contributor to the United States' overall energy portfolio. As wind energy's levelized cost of energy (LCOE) decreases, additional utility scale turbines are being built. In fact, the U.S. Department of Energy predicts that wind energy will achieve 35% of U.S. electrical demand by 2050 (see Figure 1-1). At year-end 2013, 39 states had utility-scale wind projects. The goal by 2050 is to have wind capacity in all 50 states, with 40 states having more than 1 GW of installed wind capacity [1.4]. This points to a growing need for operations and maintenance, including inspections and repairs.

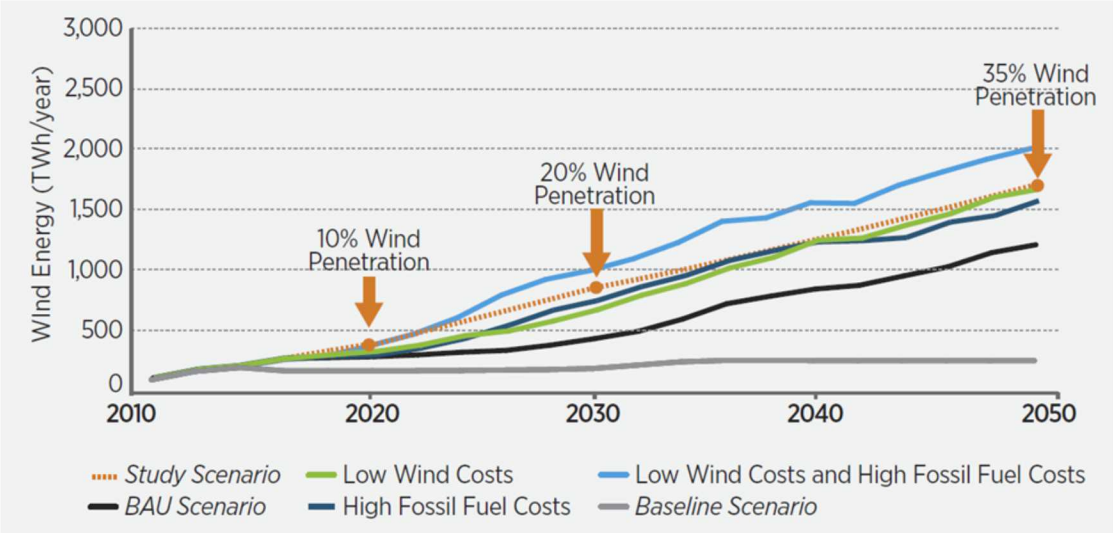

Figure 1-1: Projected Growth of Wind Energy Market Share [1.4]

Meanwhile, there is large uncertainty in the lifetime cost of maintaining and operating wind turbine rotor blades. The wind turbines that were early to the market are reaching the end of their designed 20-year lifetime and will eventually need to be repaired or replaced. Blade replacements currently affect approximately 2-3% of the fleet per year [1.2] and typically cost $200,000 to $300,000 per replacement (see Figure 1-2). The cost of these replacements is spread out over OEMs, owner-operators, and insurance companies, affecting all major components of LCOE. Moving forward, increased investments in blade inspections and repairs will be required to address the industry's growing needs. Specifically, wind farm operators will need data and tools to make informed decisions about maintenance, repairs, and ultimately, retirement/replacement.

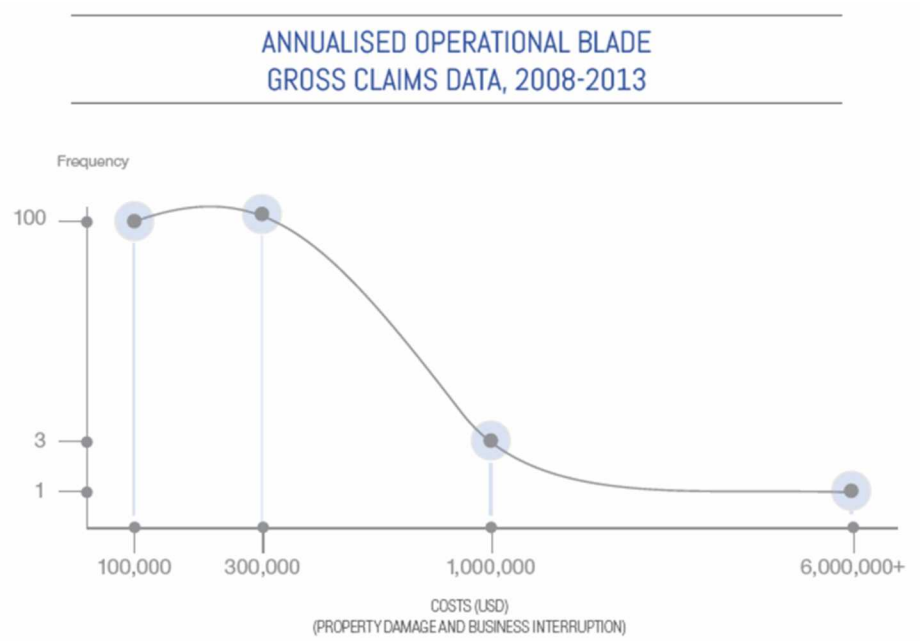

Figure 1-2: Wind Blade Replacement Costs [1.1]

At the same time, higher-energy capture wind turbine rotors with longer blades are contributing to a reduced LCOE. Figures 1-3 to 1-5 show examples of these increasing rotor sizes. As these blades grow longer, and a greater number of turbines are built offshore, they become more expensive to repair or replace. These designs have also placed added emphasis on the use of advanced materials, sophisticated manufacturing processes, and the deployment of routine inspection and health monitoring efforts to reduce the costs of turbine downtime and blade replacement.

Additional complexity arises when considering that the causes of wind blade damage are varied and range from design and manufacturing errors, to transportation and installation damage, to operational damage. The cost of these failures can be only be alleviated by prevention or repair. However, current industry practices in diagnosing and repairing defects and damage are non-standardized and in many cases inadequate. Current inspection practices are extremely limited, consisting primarily of ground-based visual inspections. These inspections are limited to visible surface damage, and there is a growing need for nondestructive inspection techniques that are capable of detecting subsurface damage. As the market grows and the environmental challenges increase (e.g., offshore turbines), the industry needs faster, more effective, and more versatile inspection solutions. Moving forward, autonomous drones inspections present an excellent opportunity for fulfilling this need by implemented both visual and nondestructive inspections. While drone-based inspections have become common in other fields, drone-deployed wind blade inspections are still an emerging market. According to Navigant Research, cumulative global revenue for wind turbine drone sales and inspection services is expected to reach nearly $6 billion by 2024 [1.3].

Figure 1-3: Increasing Size of Wind Turbines

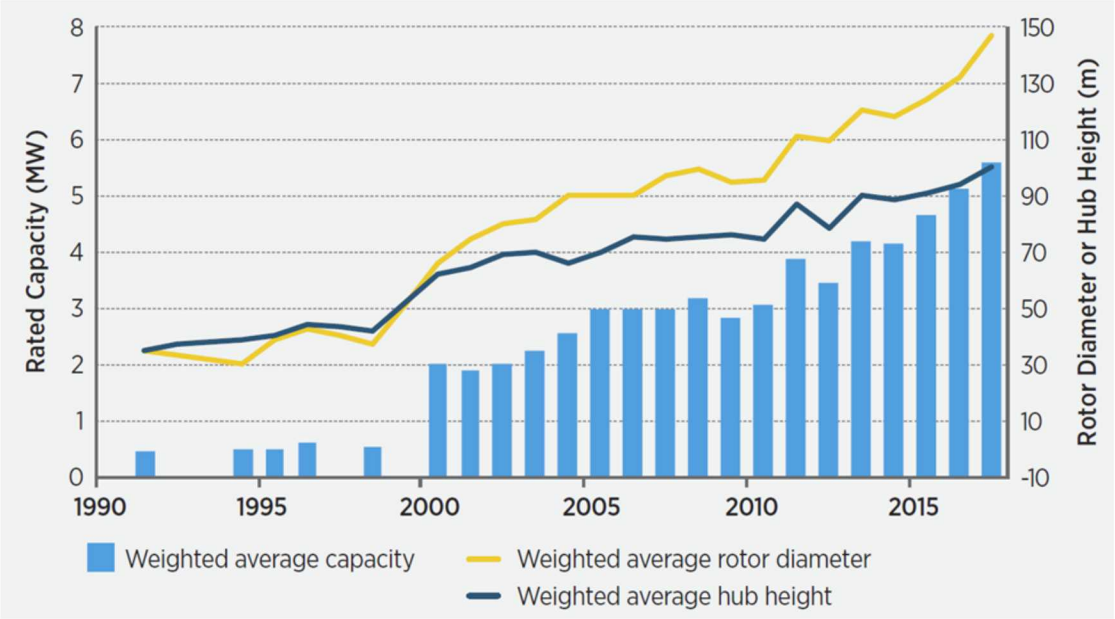

Figure 1-4: Average Turbine Size, Rotor Size, and Hub Size for Commercial Offshore Wind Plants [1.4]

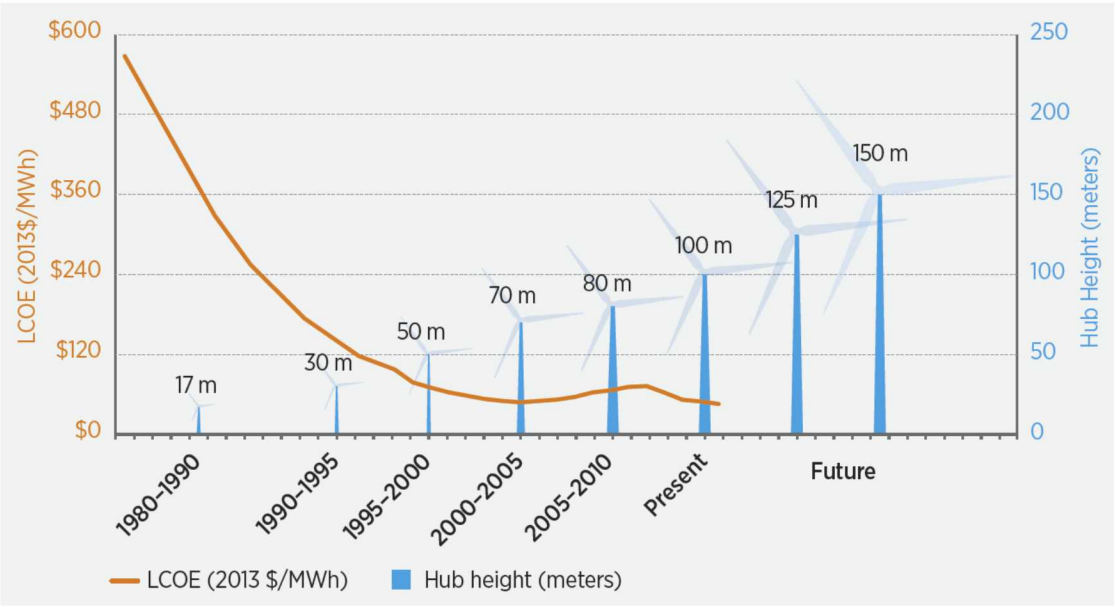

Figure 1-5: Wind Technology Scale-Up Trends and the Levelized Cost of Electricity [1.4]

The above scenarios indicate an important need for routine inspections and damage classification that enables wind farm operators to monitor damage and make informed decisions on repairs. The DOE's Wind Vision report specifically highlights this as an action area:

- "Increase reliability by reducing unplanned maintenance through better design and testing of components, and through broader adoption of condition monitoring systems and maintenance. [1.4]"

In order to achieve this goal, increased inspection capabilities, beyond just surface-level visual inspection, are required. Nondestructive inspection (NDI) of subsurface defects is crucial to understanding the full extent of underlying damage. However, NDI of wind blades is typically limited to minimal inspections (e.g., spar cap to shear web bond line) at the OEMs during Quality Assurance, and there is virtually no in-service NDI being performed, in part due to the accessibility issues. Most blade access is currently performed by humans rappelling down blades or performing work on raised platforms, which is expensive and involves inherent risks. These repair personnel typically respond to severe damage that has propagated to the surface and subsequently identified by visual inspections. Nevertheless, these inspections are often not good indicators of flaw size. Therefore, while up-tower, personnel typically use a combination of tap testing and material removal to size the repairs. They relay this information to the ground team who help pass materials up-tower to perform the repair. Using NDI data to identify the type and severity/size of damage before deploying up-tower workers could greatly optimize this process by allowing the people to plan the repair ahead of time on the ground. Additionally, identifying damage before it propagates to the surface also allows proper planning of scheduled maintenance rather than lengthier and more expensive unplanned maintenance and catastrophic failure.

As the wind industry market share grows and the need for advanced maintenance capabilities increases, rapid and effective inspections of both surface and subsurface damage will be required. The combination of the effectiveness of advanced NDI and flexibility of drone-deployed inspection systems have an opportunity to fulfill this market need. By combining these technologies, drone-deployed NDI can help wind blades reach their design life and efficiently provide the necessary life management tasks that maximizes wind farm operations.

1.1. Introduction to Sandia's Blade Reliability Collaborative NDI Initiatives

As the application of wind turbines continues to expand, there is an increased emphasis on ensuring the quality, and thus the reliability, of wind turbine blades. Blade reliability is rapidly becoming one of the highest cost elements of plant operations because blade failure can cause extensive down time and lead to expensive repairs. In addition, blades are being delivered to the site in a condition that occasionally requires additional treatment of quality issues before they can be installed. Blade repair contractors for US wind plant developers and operators report that a significant percentage of the blades they repair have never been operated. Blade reliability issues need early attention because of the lost production and cost of significant failures. A reliability effort, centered around nondestructive inspection (NDI), was initiated at Sandia Labs to address these important reliability issues as they impact development and operations costs. This effort recognizes and is addressing the need to improve the quality of blades as they are delivered to the field through enhanced inspection capabilities and associated quality metrics.

Nondestructive inspection requirements, methods and practices vary widely within the wind industry and different blade manufacturers utilize different levels of rigor and different inspection methods on their product before it leaves the factory. As the length of blades increase and more advanced materials are being used to manufacture blades, it has become increasingly important to detect fabrication defects during blade production. In addition, small defects can propagate to levels of concern during blade use while fatigue loading, impact, lightning strike and other in-service conditions can lead to new damage in the blades. Operational environments produce high stress levels in the blades, it has become increasingly important to detect the onset of damage or the propagation of fabrication defects during blade operation. The need for in-service NDI of blades at wind farms is growing. One aspect of this program is to determine how advanced NDI methods can be gracefully integrated into wind farm operations. These include both up-tower NDI deployment and equipment for inspecting blades that have been removed from the wind turbine. The first task is to determine the inspection requirements as they exist now, as well as those that are expected to exist in the near-future.

The goals of this study are to determine what Nondestructive Inspection (NDI) is being performed on blades during and after the manufacturing process, determine the level of inspection requirements and standardization within the industry, develop new and customized NDI methods to meet the inspection needs of the industry and work with blade inspectors to test and apply state of the art inspection techniques in manufacturing environments. This includes the possible introduction of automated inspections, a comprehensive assessment of various conventional and advanced NDI techniques in manufacturing environments, close interface with blade original equipment manufacturers (OEMs) to determine inspection requirements, and the completion of NDI technology transfer activities with the wind turbine blade industry.

The purpose of the "Non-Destructive Inspection for Wind Turbine Blades" effort within the *Blade Reliability Collaborative* (BRC) is to develop, evaluate and validate the potential nondestructive inspection methods that could be deployed to effectively detect flaws in composite wind turbine blades. This effort has also allowed Sandia Labs to establish a national capability – including a physical presence and methodology - to comprehensively evaluate blade inspection techniques. The primary benefit to the wind industry is the optimum deployment of automated or semi-automated NDI to detect undesirable flaws in blades before the blades enter service while minimizing the time and cost required to complete the inspections.

Figure 1-6 shows various operating wind turbines along with a blade in production. Figure 1-7 shows the main components of a wind turbine blade and Figure 1-8 shows several different cross sections of blades highlighting some variations in blade design. Such variations give rise to unique inspection needs and challenges. Typical flaws encountered during production include: disbonds, interply delaminations, dry or resin-starved regions, porosity, voids, wrinkles, ply waviness, and snowflaking. In addition to these flaws, wind turbine blades operating in the field may also sustain damage stemming from transportation, installation, stress, erosion, impact, lightning strike, and fluid ingress.

A completed SAND report has already presented the details of the BRC NDI program and the infrastructure that was established to conduct the development and evaluation of advanced NDI methods for wind turbine blades reference [1.5]. It also describes the development of a highly-sensitive NDI method that is capable of inspecting through the thick composite sections and attenuative bond lines in blades to meet the inspection requirements of blade manufacturers. Preliminary testing was completed in this first phase of the BRC program to assess some NDI methods on actual wind blade test specimens. This first SAND report was intended to describe the promising NDI methods but not to assign any quantitative performance metric with respect to the inspection of wind turbine blades.

The report contained in this SAND document takes the next step of providing quantitative NDI validation through the implementation of a Probability of Flaw Detection (POD) experiment. This report describes the design and implementation of the Wind Blade Flaw Detection Experiment (WBFDE). WBFDE was deployed to quantitatively assess the performance of the best and most viable NDI methods as determined in the preliminary testing described in reference [1.5]. This report describes the top nondestructive inspection (NDI) techniques that might possibly be applied to address the fabrication quality assurance and in-service inspection of wind turbine blades. It provides an overview description of the various methods while introducing specific instruments that are available to implement each method. A series of Probability of Detection (POD) curves are presented to clearly show the ability of both conventional inspection methods – as deployed by current wind blade inspectors – and advanced inspections methods. Such comparisons are used to provide insights into the advantages, limitations, optimized deployment and training needs associated with each technology along with results from the application of these NDI methods to the set of WBFDE POD test specimens. Insights gained during the WBFDE testing are being used to develop both NDI reference standards, formal inspection procedures and an inspector training regimen to further improve the inspection performance on wind blades.

Figure 1-6: Sample Wind Turbine Blades in Production and Operation

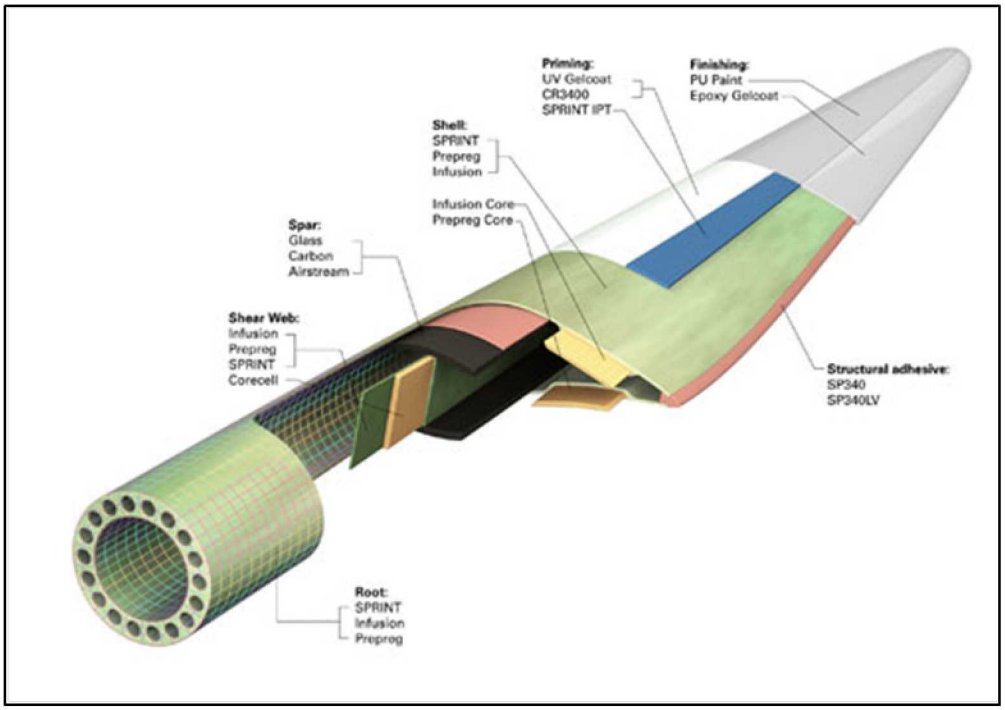

Figure 1-7: Components of a Wind Turbine Blade Construction

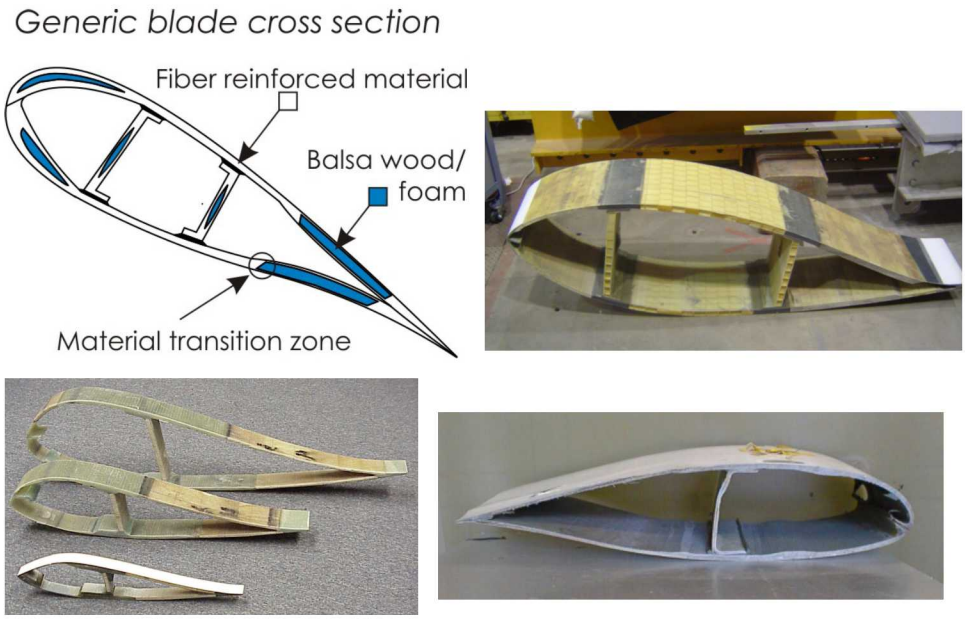

Figure 1-8: Sample Wind Turbine Blade Cross Sections Showing Different Design and Construction Scenarios

1.1.1. Objectives

The overall objectives of this NDI activity are:

- Plan and implement a national capability – including a physical presence and methodology - to comprehensively evaluate blade inspection techniques.
- Develop, evaluate and validate the array of potential nondestructive inspection methods for the detection of flaws in composite wind turbine blades. Transfer this NDI technology to wind blade production facilities.
- Produce optimum deployment of automated or semi-automated NDI to reliably detect undesirable flaws in blades (major criteria are time, cost and sensitivity).
- Create the ability for manufacturers to determine the quality of their product before it leaves the factory. Develop an array of inspection tools to comprehensively assess blade integrity (determine needs, challenges, and NDI limitations).
- Possibly use successful NDI to extend blade operational life.

Inspections must address all field deployment issues:

- Vertical and horizontal inspection surfaces
- Hand scan vs. attachable scanner

- Signal coupling into part
- Wide range of thicknesses
- Quantitative information
- Ease and rate of inspection

Inspections must overcome all inspection impediments

- Some methods may need access to both sides of blade
- Wide area inspection method needed (scanners)
- Porosity/attenuation levels of blades are high
- Depth of penetration and sensitivity at depth is needed
- Inspections must accommodate surface curvature and complex geometries

The BRC NDI initiative is addressing multiple methods to improve performance:

- Evolve existing NDI
- Introduce advanced NDI
- Assess NDI performance – conventional baseline and advanced NDI improvements
- Improve and/or add training
- Develop NDI standards
- Training – including feedback on experiment
- Process optimization
- Inspector certification

Figure 1-9 depicts the approach used to arrive at the desired NDI performance levels. Structural analysis and testing, which include a damage tolerance assessment, are used to determine the level of damage that can be sustained by the blade such that it can still achieve its desired function and lifetime. Inspection methods must then be developed and validated to ensure that all flaws can be detected prior to reaching a critical size. Damage tolerance assessments (DTA) are difficult to complete in composite materials, especially those produced with the VARTM process, and are exceptionally challenging in structures as large as wind turbine blades. Wide variations in operational environments and sources of damage onset also exacerbate a damage tolerance assessment. As a result, this NDI effort uses a conservative approach and includes flaw sizes that are expected to be below the DTA levels. This ensures that the results from the NDI evolution work will produce NDI methods that perform at or above the desired performance levels. DTA analysis and testing

conducted to date has confirmed that the flaw sizes used in the NDI test specimens are conservative.

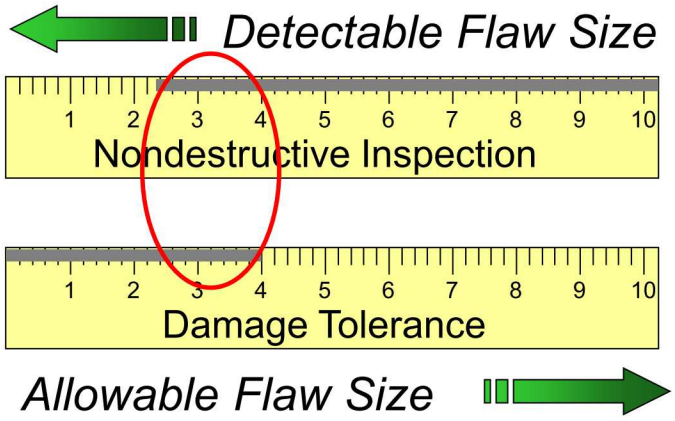

Figure 1-9: Required Relationship Between Structural Integrity and Inspection Sensitivity

Figure 1-10 shows the five key pieces of an NDI system that include the method, the equipment, inspection procedures and training needed to produce the optimum results in a repeatable manner. They include:

- Use of NDI reference standards to form a sound basis of comparison and ensure proper equipment set-up.
- Use of material property and calibration curves (e.g. attenuation, velocity) to guide NDI deployment and signal interpretation and to set proper accept-reject thresholds.
- Human factors – use of extensive NDI deployment testing to adjust procedures and minimize human factors concerns.
- Improved flaw detection via:
  - Advanced NDI
  - Hybrid inspection approach - stack multiple methods which address array of flaw types (data fusion)

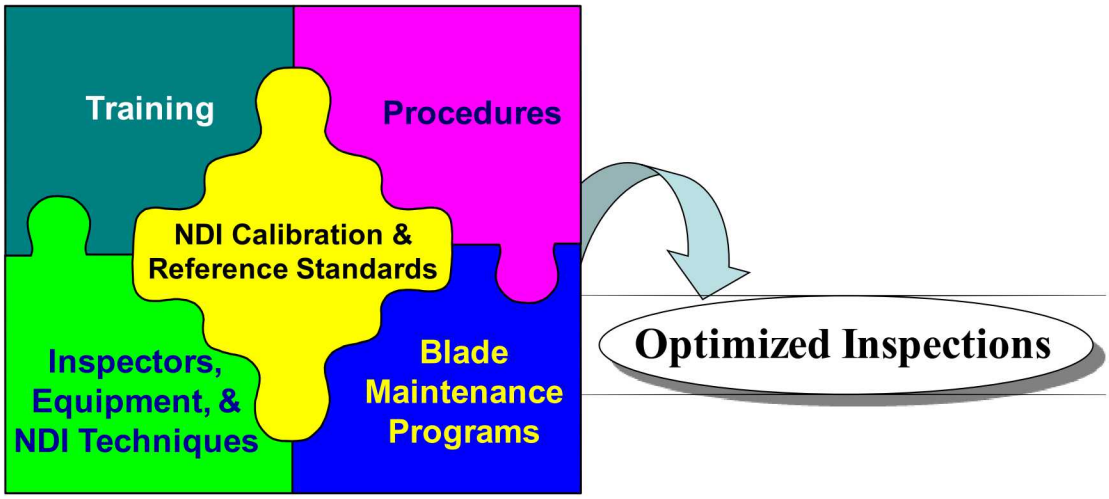

Figure 1-10: Depiction of the Critical Elements Contained in an

1.1.2. Blade Reliability Collaborative Task Descriptions

One of the primary, early, activities conducted by Sandia Labs was the development and evaluation of ultrasonic (UT) inspection methods to improve the current state of blade inspection capabilities. These methods, categorized into single-element pulse-echo UT and phased array UT, were then used to accurately characterize the wind blade test specimens that were fabricated with engineered flaws and to propose an advanced NDI method for improving wind turbine blade inspections. The flaws include an array of interply delaminations, spar-to-shear web disbonds, contamination/FOD, laminate waves, porosity and dry regions. The Sandia-evolved ultrasonic NDI methods were demonstrated to produce some of the best sensitivity (highest contrast C-scan images) on wind turbine blades to date. A series of tasks developed deployment devices to: 1) allow the UT techniques to be conducted on rough surfaces at any orientation, and 2) produce reliable and optimized signal coupling to produce the strongest and most sensitive signal possible. The use of multiple gates, along with customized time-corrected gain, was explored in order to detect the full set of flaws through the assembly thickness. The combined use of A-scan (raw UT signal), B-scan (section view), C-scan (2-D planform view) data was also evaluated to enhance flaw detection and characterization. In order to better explain the subsequent NDI performance evaluations that were completed as part of the WBFDE, some of the NDI developments – primarily hardware and data acquisition improvements – are also briefly described in this report.

Activities from the completed portion of the BRC NDI initiative produced an initial screening of NDI methods; to identify the methods that show the greatest promise for flaw detection and potential deployment on wind turbine blade geometry reference [1.5]. A series of NDI Reference Standards and NDI Feedback Specimens were designed and fabricated to facilitate initial assessments of candidate NDI methods. Blade design and fabrication information from multiple manufacturers was digested into general construction scenarios so that this NDI effort could address the wind industry as a whole. The specimen designs, and associated fabrication processes, were

reviewed by several wind energy experts to insure specimen realism. The NDI specimens were applied in a "feedback" mode where the inspector was aware of the flaw profile in each specimen (i.e. not blind mode inspections). Inspection systems at NDI vendors, research labs including Sandia Labs, and universities were evaluated using the representative test standards. The results were compiled in a structured manner to arrive at preliminary rankings of performance. The candidate array of flaws that were studied include: snowflaking, porosity, resin-starved regions, adhesive voids, interply delaminations, spar and shear web disbonds, and wrinkles. Discussions with blade manufacturers coupled with operational history were used to identify the most representative flaw types to be used in this study. The flaw sizes deemed necessary to be detected were determined by a complimentary BRC "Effects of Defects" study. Custom test panels with engineered flaws were supplemented by full-scale blades and blade sections that contain natural flaws found in the field along with engineered flaws. Candidate NDI methods are presented in Chapter 6.

Major tasks included:

- Acquire retired blade sections and add engineered flaws
- Understand blade designs and define blade NDI issues (design, inspection requirements, NDI impediments, desired deployment)
- Inspect retired blades using various NDI methods to understand challenges and characterize flaws
- Choose flaw types to include and the optimum methods to produce these flaws
- Perform trials to consistently reproduce realistic flaws
- Complete final design of NDI Reference Standards and NDI Feedback Specimens
- Complete fabrication of NDI Feedback Specimen set
- Identify NDI methods to be included in the WINDIE screening effort
- Develop WINDIE experiment protocols and invite participants
- Complete flaw characterization of NDI Feedback specimens
- Implement WINDIE - conduct round-robin testing on NDI Feedback specimens with "advanced" NDI methods
- Complete analysis of inspection results with NDI comparisons (sensitivity, repeatability, coverage, adaptability, deployment, cost, etc.)
- Assess NDI in the field - deploy NDI methods to allow for routine use of validated NDI method(s) in blade production environments (technology transfer)
    1. Develop, then evaluate technology in full-scale factory testing environment and obtain inspector feedback

2. Conduct training and develop inspection procedures aimed at manufacturer needs using advanced NDI
3. Carry out technology transfer to industry

1.2. References

1.1 GCube Renewable Energy Insurance. “Breaking Blades: Global Trends in Wind Turbine Downtime Events,” September 2014 Report.

1.2 Sheng, S., Lantz, E., “Experiences with Two Reliability Data Collection Efforts,” NREL/PR-5000-60255, August 2013.

1.3 Navigant Research. “Unmmanned Aerial Vehicles and Inspection Services for Wind Turbines: Global Market Assessment and Forecasts,” 2015.

1.4 U.S. Department of Energy. “Wind Vision: A New Era for Wind Power in the United States,” DOE/GO-102015-4557, April 2015.

1.5 Roach, D., Neidigk, S., Rice, T., Duvall, R., Paquette, J., “Blade Reliability Collaborative: Development and Evaluation of Nondestructive Inspection Methods for Wind Turbine Blades,” Sandia DOE Report, SAND2014-16965, September 2014.

2. WIND BLADE FLAW DETECTION NEEDS

2.1. Post-Production Inspection of New Blades

While there are a wide array of blade designs and customized production processes, there are common flaws that can be produced in composite wind blade structures. Typical flaws encountered during production include: disbonds, interply delaminations, dry or resin-starved regions, porosity, adhesive voids, wrinkles, ply waviness, and snowflaking. In addition to these flaws, wind turbine blades operating in the field may also sustain damage stemming from stress, erosion, impact, lightning strike, fluid ingress and other stress risers that may occur during shipping and installation. Figure 2-1 shows a cross section of a blade highlighting some primary inspection regions. Blade design variations give rise to unique inspection needs and challenges. Sample flaws found in the thick, fiberglass and carbon blades are shown in Figure 2-2 through Figure 2-5.

The most general list of flaws, damage and non-standard production items that the industry would like to detect are:

- Thickness variations
- Disbonds, including kissing (intimate contact) disbonds
- Presence of adhesive (ensuring proper bond line width)
- Missing adhesive (voids)
- Width and placement of adhesive
- Interply delaminations
- Dry regions (incomplete resin transfer)
- Gelcoat disbands
- Snowflaking
- Porosity
- In-plane and out-of-plane waves
- Composite fiber fracture (cracks)
- In-service damage such as erosion, overstress, impact, lightning strike and fluid ingress.

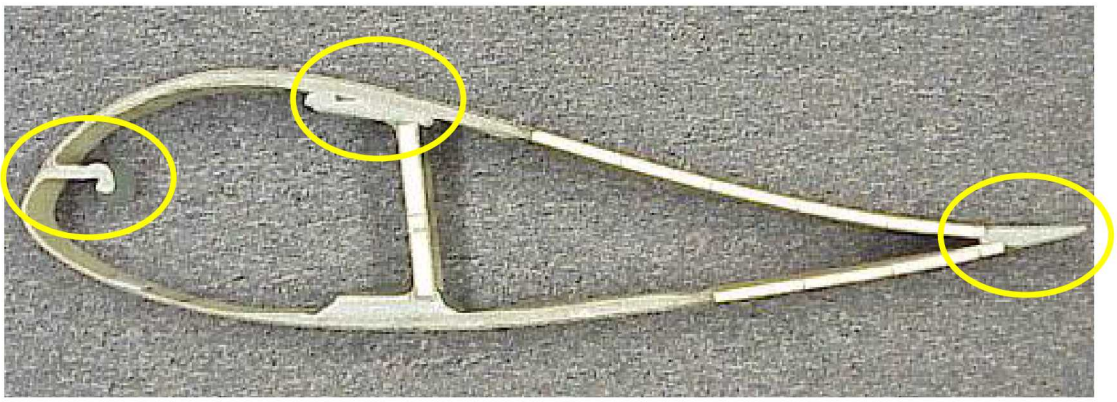

Figure 2-1: Inspection Areas of Interest – 1) Leading Edge Bond, 2) Spar Cap, 3) Spar Cap-to-Shear Web Flange Bond Line and 4) Trailing Edge

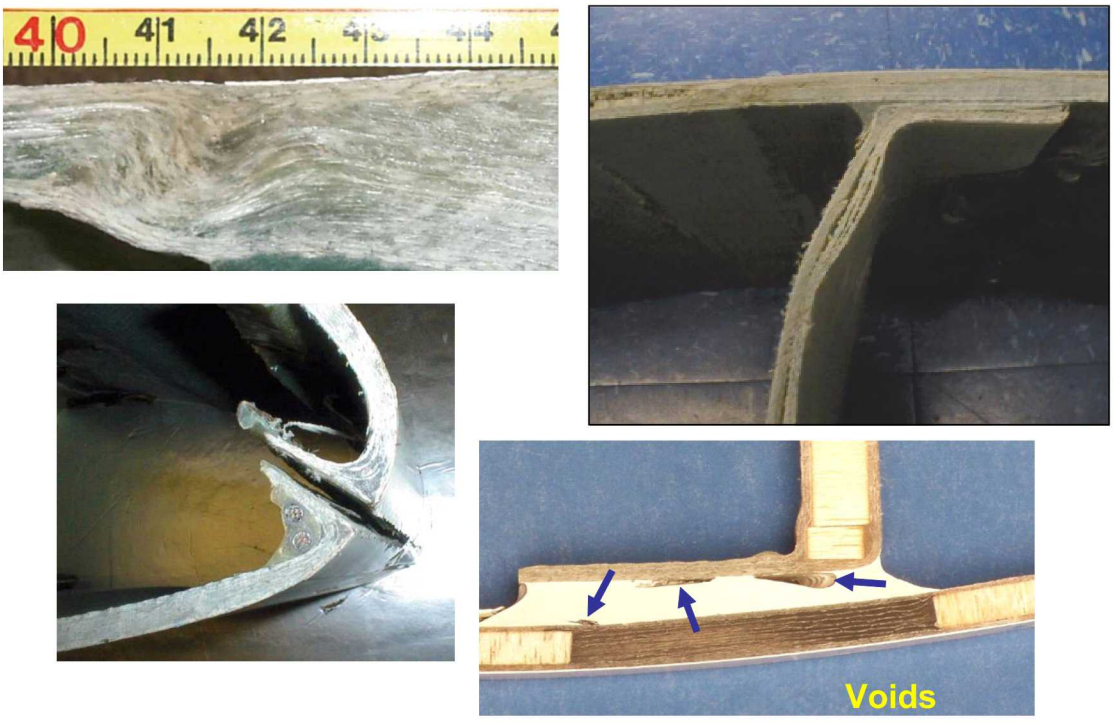

Figure 2-2: Flaw Types That Are Desirable to Detect with NDI Including Ply Wrinkles and Delaminations, Adhesive Voids and Joint Disbonds

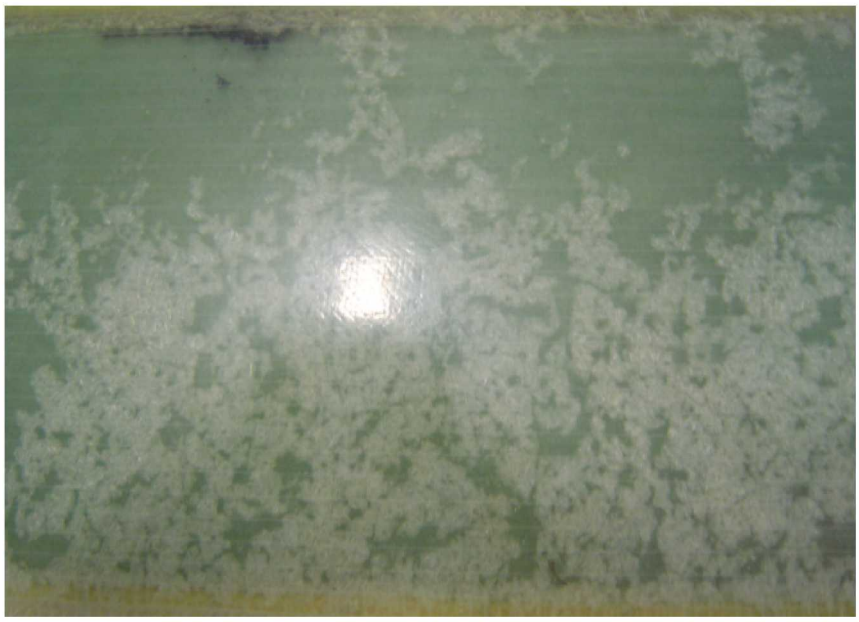

Figure 2-3: "Snowflaking" Flaws in Spar Cap Created by Entrapped Air During Cure

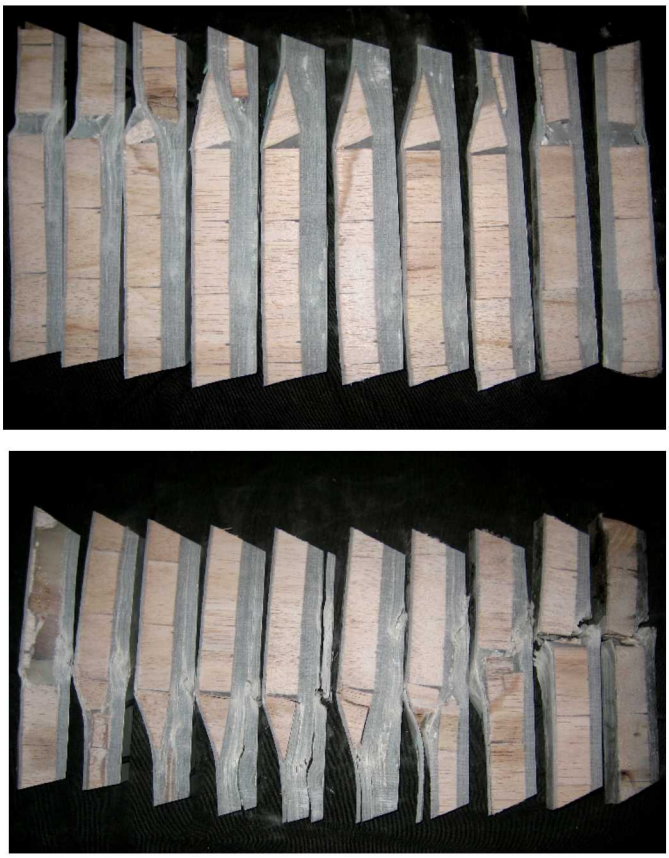

Figure 2-4: Figure Comparing Pristine Blades with Cracks, Delaminations and Other Laminate Fractures that Can Occur in Wind Blades

The inspections must address all deployment issues including: a) vertical and horizontal inspection surfaces, b) hand scan vs. attachable scanner, c) signal coupling via water flow or other signal couplant, d) wide range of thicknesses which may require equipment adjustments such as transducer selection and gate adjustments in ultrasonic inspections, e) need for quantitative information, f) ease of equipment use to minimize human factors concerns and performance variations, and g) rate of inspection to produce necessary coverage.

Some inspection considerations and impediments that must be overcome in order to produce the desired NDI performance include: a) some methods may need access to both sides of blade, b) wide area inspection methods may be needed (scanners), c) porosity/attenuation levels of blades are high, d) depth of penetration and sensitivity at depth is needed, and e) inspections must accommodate surface curvature and complex geometries.

Figure 2-5: In-Plane (top) and Out-of-Plane (bottom) Wave Flaws in Wind Blade Composite Laminate

2.2. In-Service Inspection of Operating Blades

2.2.1. Background on In-Service NDI Needs

Small defects can propagate to levels of concern during blade use while fatigue loading, impact, lightning strike and other in-service conditions can lead to new damage in the blades. As the length of blades increase and operational environments produce high stress levels in the blades, it has become increasingly important to detect the onset of damage or the propagation of fabrication defects during blade operation. The need for in-service NDI of blades at wind farms is growing. Additional NDI fidelity beyond what can be provided by visual methods is required to identify and repair defects before they reach a critical size. In addition, the use of larger and more expensive blades means that it will be necessary to install more invasive repairs and repairs to primary blade structure in order to avoid the cost of blade removal and replacement. These more extensive repairs will require close scrutiny from NDI methods to ensure the long-term viability of the repair.

One aspect of this program is to determine how advanced NDI methods can be gracefully integrated into wind farm operations. These include both up-tower NDI deployment and equipment for inspecting blades that have been removed from the wind turbine. The first task is to determine the inspection requirements as they exist now, as well as those that are expected to exist in the near-future. This includes the identification of current inspection practices at wind farms, the level of standardization across the industry and the ability of operators to deploy NDI methods in the field. This information will allow us to focus our activities on developing new and customized NDI methods to meet these inspection needs while ensuring the ability of wind farm operators to avail themselves of such inspections. The latter item could involve the use of wind service companies to provide skilled inspectors with proven equipment and procedures.

Thus, this project includes close interactions with wind farm operators to test and apply state of the art inspection techniques in in-service environments. This project also includes NDI technology transfer activities with both wind service companies and wind farm operators. The benefit will be optimum deployment of automated or semi-automated NDI to detect undesirable flaws and damage in blades in order to help the blades reach their design lifetime or beyond.

Application of NDI technology in the field, and specifically up-tower has the same challenges associated with deployment as factory inspections, with the addition of many more. Wind farms are typically located in rural, rugged areas of the country with high winds, elevated work areas, and dangerous conditions. Nondestructive inspection technology being proposed for field use needs to be portable, battery powered and durable so that inspectors can bring the equipment to different locations on the blade including areas that may only accommodate rope access. The most common use of NDI applied up-tower has been to inspect specific, critical regions of a blade that have been identified as having a high probability of containing a serial manufacturing defect that was not detected at the plant on a large number of blades. These have been very specialized and confined to a particular set of blades. The

operator typically identifies the issue over time because the defect manifests itself as early damage onset and eventually failure in more than one blade. Often when an issue like this is identified the first question is: "How many of the blades are affected and can the blades be repaired before the defect grows?" In-service NDI is critical to assess and detect defects, even those that were not seeded by manufacturing problems.

2.2.2. *In-Service Blade Damage*

The most common operational damage is from surface impact and rain/dust erosion. Other damage stems from bird strikes, lightning strikes, other object strikes, the propagation of manufacturing anomalies and the origination of new damage stemming from normal fatigue stress loads, off-design overloads or other environmental conditions. Figure 2-6 to Figure 2-8 show various types of wind blade damage. Note that all photos feature damage that is extreme or that has propagated to the point of blade failure. The goal of this effort to conduct nondestructive inspections before minor damage can grow to levels of concern. Figure 2-9 shows several images of subsurface damage that can be detected via NDI methods.

Lightning Strike Damage

Impact Damage

Figure 2-6: Types of Damage to Wind Blades Experienced During Operation (1)

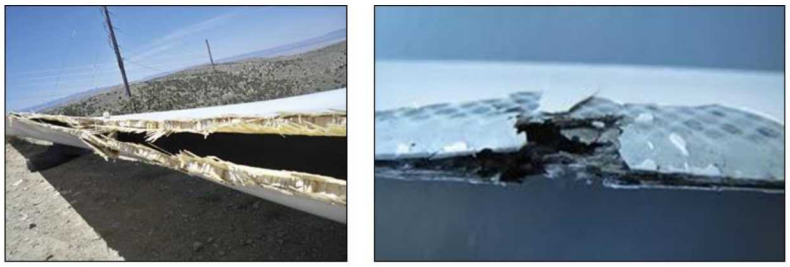

Trailing Edge Disbond and Fracture Damage

Erosion and Impact Damage

Damage from Shipping and Installation Handling

Figure 2-7: Types of Damage to Wind Blades Experienced During Operation (2)

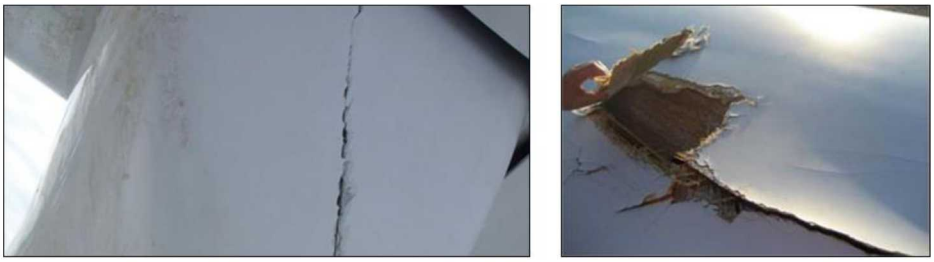

Severe Growth of Fiber Fracture

Delamination and Subsequent Laminate Fracture

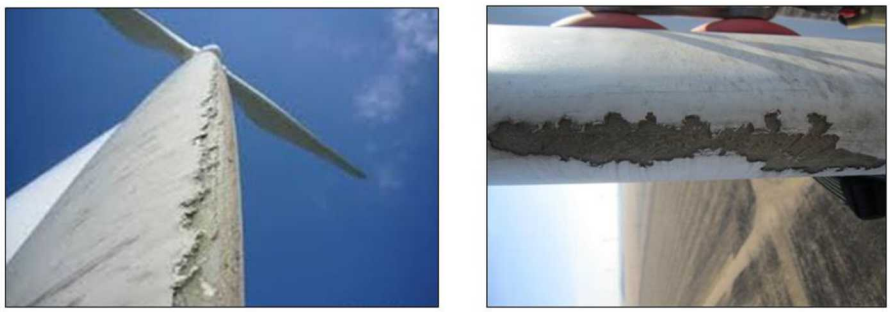

Erosion Damage

Figure 2-8: Types of Damage to Wind Blades Experienced During Operation (3)

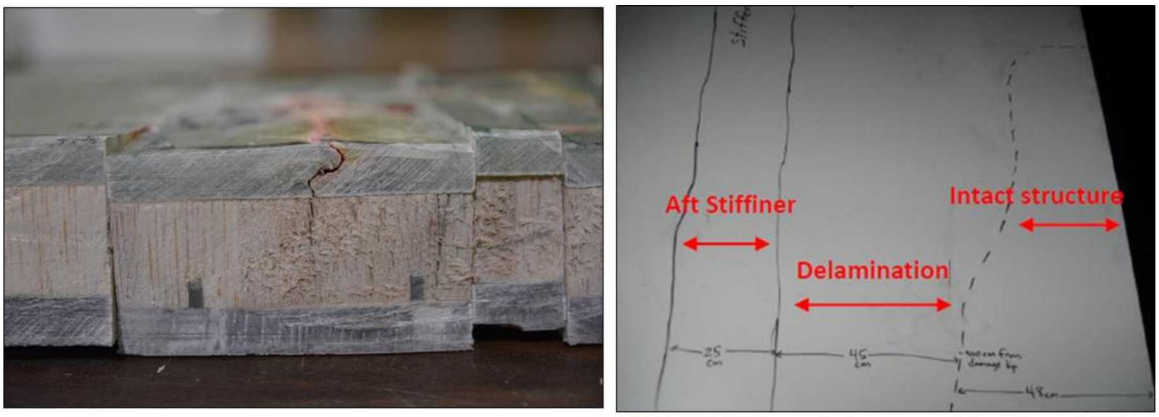

Skin Laminate Fracture

Interply Delamination in Skin and Spar Cap

Figure 2-9: Subsurface Wind Blade Damage Detectable Using NDI Methods in the Field

2.2.3. In-Service Blade Repairs

The same techniques used to detect damage may also be used to determine the integrity of a structural repair to a blade. Enhanced NDI techniques could open up new opportunities for more invasive and complete spar cap and root repairs. The integrity of the structural repair could be verified through inspection, giving repair designers and engineers added confidence that the blade can be recertified for use, which would lead to significant cost savings. In order to assess these challenges, collaborative relationships with blade maintenance and inspection companies has been pursued by Sandia Labs. Increased damage detection sensitivity in the field will improve blade reliability and minimize blade downtime.

Most turbine blade damage from erosion or impact is repaired with primary near-surface type of repairs using epoxy or polyurethane filler material or with the addition of a ply or two of material using an ambient bond adhesive. Repairs to core structure are common and can extend to double-sided repairs of through-thickness damage. While core structure is not considered primary structure, extensive damage to the core region can affect the overall stability and structural integrity of the blade. As the wind blades have become larger and more expensive, there is a corresponding desire to install more extensive repairs that reach many layers in depth and are placed on and around primary structure such as spar caps and root sections. The criticality of these repairs will then require the use of through-thickness depth inspection methods to ensure the quality of the repair. Periodic up-tower inspections may also be required, depending on the repair analysis conducted by the wind farm operator in concert with the original blade manufacturer. The repair, the post-repair inspection and subsequent in-service inspection could be carried out in a centralized fashion by a third-party wind service company. This allows for a centralized location of expertise, repeatable inspection methods and reliable results. Blade repairs require consideration of both aerodynamic and aeroelastic loads to the structure. The repair design is adjusted to meet the zone requirements as shown in Figure 2-10. Repairs conducted in Zones (1)

and (4) involve primary structure (blade root or spar cap) and must be designed and installed for structural purposes.

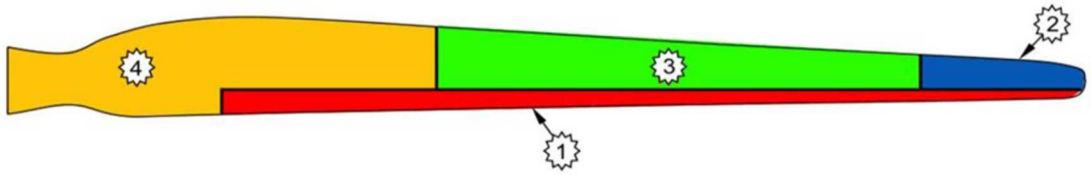

Figure 2-10: Repair Zones on Wind Blades that Identify Criticality and Limits on Level of Repair Allowed

A typical repair process is shown in Figure 2-11 where a tapered sanding process is used to remove the damaged region. Then, replacement plies of similar material and orientation are placed into the repair region and cured using in-situ vacuum and heating equipment (if elevated cure temperatures are needed). An example of a blade tip repair is shown in Figure 2-12. The success of a repair can be affected by numerous factors including: surface preparation, the ambient temperature and humidity conditions during curing, proper mixing and uniform application of the resin, improper curing profiles and improper placement/orientation of the plies. Most of the problems associated with improper repairs will result in damage within the repair that can be detected by NDI methods. Normally, the damage could be detectable during a post-installation inspection or within 6-12 months of operation.

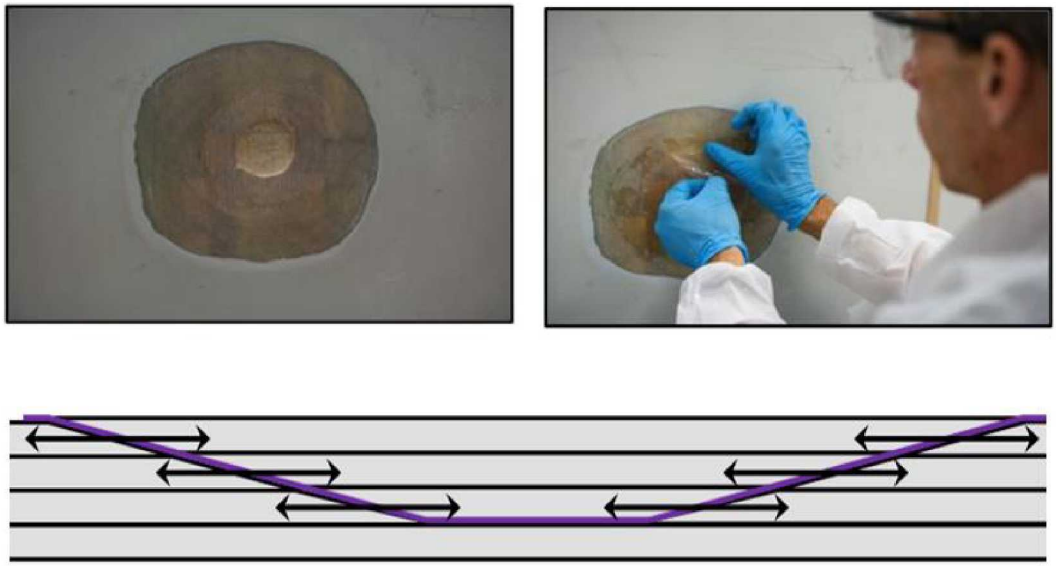

Figure 2-11: Tapered Scarf Angle, Replacement of Plies and Resulting Shear Stress Distribution in the Scarfed Repair Joint

Manual tap testing is the most common method of NDI used to evaluate damaged areas of a blade in the field. This method involves the use of a coin or other small, hard item such as hammer/tool to tap on the structure while the inspector or repairman listens to audible changes in the sound of the tapping. This is a fairly effective method to size damage in core materials (moisture ingress and skin delamination), but not effective in the critical, thicker structures such as solid laminate spar caps and thick bond lines in the trailing edge.

Figure 2-12: Picture of a Lightning Strike Tip Repair

Repairmen also use a method of visual inspection and evaluation of wind blade structure during the repair process. Once a repairable damage is identified and the mechanic begins to remove damaged material, they visually determine how much material needs to be removed and replaced. In this case, in-field NDI to assess damage in sandwich structure, leading and trailing edges, and other aero shell components may be needed to identify the initial damage and subsequently ensure the success of the repair.

2.2.3.1. In-Service Repair Inspections

Manufacturers perform repairs on blades quite often in the manufacturing plant. Repairs can range from the simple addition of adhesive to a joint that was insufficiently wide, to multi-ply depth scarfed repairs on spar caps and root laminates. The type of repairs a company will perform depends on the original construction process (e.g. shear web to spar or box beam configurations) and their tolerance for invasive repairs on primary structure. Repairs in the manufacturing plant are not

typically inspected with NDI after they are performed, but they are visually inspected by quality personnel.

Repairs performed in the manufacturing plant can be much larger than repairs made up-tower. This is because manufacturers have much better access to resources - such as engineering support, materials, and larger work spaces – and can maintain the proper control over the repair process. Wind blades that have been significantly damaged in the field are typically taken down and replaced with a new blade. Typical service repair companies will not repair spar cap-to-shear web adhesive bond lines due to warranty issues, structural criticality of the area, and the extensive amount of work it requires up-tower. Although this scenario is rare, if the damage is extensive and non-repairable up-tower, then the blade can be taken down, repaired in the field, and put back on the tower.

Enhanced NDI techniques could open up new opportunities for spar cap and root repairs in the field. The integrity of the structural repair could be verified through inspection, giving repair designers and engineers added confidence that the blade can be recertified for use. This would lead to significant cost savings.

2.2.4. Up-Tower Blade Access

With a growing number of blades now in service - many well outside their warranty periods - rotor blade maintenance is becoming a major issue. One of the most challenging aspects of wind farm operations is the means to conduct periodic maintenance of the blades while they are still installed on the rotor hub (i.e. up-tower maintenance). Access to the blades and deployment of equipment severely hinders both the ability of workers to conduct their tasks but also limits the amount and type of work that can be carried out up-tower. Up until recently, the excellent reputation of composite materials for high durability has induced wind farm operators to defer general blade maintenance and oversight tasks. The increasing knowledge of wind blade aging issues has produced an increase in demand for blade inspection, maintenance and repair. In response, several wind service companies have been formed to supply a new breed of worker called skyworkers. These workers combine skills in the inspection and repair of wind blades with climbing skills. The technicians themselves are normally suspended from the rotor hub, working on the subject blade – which is stopped in the down position as shown in Figure 2-13. Anchor lines may be deployed to the tower or around the blade.

Almost all of the inspections are confined to visual assessments. Erosion, surface fracture and, to a lesser extent, impact damage can be identified with visual inspections. However, many of the more aggressive and destructive types of damage that can severely reduce blade life do not manifest themselves as surface demarcations. Such subsurface damage must be detected via high-penetration, inspections methods such as ultrasonics.

Currently most repairs are of the ‘cut out and fill’ type or, in the case of laminate repairs, wet lay-up. However, a smaller number of technicians can also handle infusion and prepreg repairs, along with restitution of gel-coats and surface finishes. Vacuum bagging and heat curing up-tower is a challenge and workers must execute

everything from small surface repairs to medium structural repairs, dealing with a wide range of materials including polyester, vinyl ester and epoxy resins, along with glass, carbon, aramid and biocomposite fibers. A technician's visit can encompass anything from a close visual inspection with report, through blade cleaning, to a modest structural repair – a damaged tip or edge for example. Because a skyworker has either to take everything required for a job with him (or her), or have it hoisted up or lowered down to the working position, repair procedures have to be carefully pre-planned and managed, with adequate back-up from other team members.

Figure 2-13: Use of Skyworkers to Access Blades Via Climbing Ropes

A variation on this theme involves the use of adaptive platforms to provide an enhanced work area with the ability to provide more controlled use of extensive equipment in an up-tower environment. Figure 2-14 shows several different types of work platforms that can accommodate more extensive blade maintenance activities.

2.2.5. Deployment of NDI Methods

The platforms highlighted in Figure 2-14 allow for the direct application of proven NDI methods [2.1]. These could be deployed manually or in a scan mode. However, the use of these platforms is very rare at this time and quite expensive. Thus, there is a need for more frequent, rapid inspections means that other NDI deployment options should be pursued for use in the absence of such expensive work platform deployments.

2.2.5.1. Remote Visual Inspections

The use of Unmanned Aerial Systems (UAS) or ground-based telescopic devices to inspect wind blades has received a lot of attention in the last 2-3 years. Such devices, such as the ones shown in Figure 2-15, utilize high resolution optics to produce excellent visual inspections of the surface of the blade. While these are quite useful for identifying surface-based damage such as erosion, these inspections are not useful for detecting the more extensive subsurface damage that can be present in wind blades. This damage, such as delaminations, disbonds and fracture in the composite fibers, represent damage that can reduce blade life and even result in catastrophic failure in-service. This critical damage must be detected using NDI methods that can interrogate the entire thickness of the blade (e.g. spar cap and shear web bond line, thick laminate root and transition sections).

Figure 2-14: Use of Adaptive Platforms to Provide Larger Work Space for Blade Maintenance Activities

2.2.5.2. Remote and Semi-Automated Access to Blades

In order to obtain a more accurate picture of the overall health of wind turbine blades in operation, it is important to consider independent deployment of up-tower inspection devices without the aid of work platforms or other personnel present along the blade. Several different scanning systems have been developed to accommodate

automated inspections and even more are in the concept stage. The scanners shown in Figure 2-16 can produce C-scan images which Sandia has shown to be very beneficial in improving flaw detection accuracy. Such scanning systems, that utilize X-Y motion carriages to move a transducer across a wide area of the blade, do require some level of access to the area of interest. Sandia's scanning system (Figure 2-16, right side) was successfully deployed in a factory setting and could be adapted for up-tower inspections. A true, remotely controlled inspection could be performed using a robotic crawler device that can scale a wind tower (see Figure 2-17 for concept crawlers and those used in other industries).

Figure 2-15: Unmanned Aerial Systems and Ground-Based Devices Used to Conduct Visual Inspection of Wind Blades

Figure 2-16: X-Y Scanning Systems Can Temporarily Adhere to the Surface of Interest to Produce High-Quality, Through-Thickness Flaw Detection Images Over Wide Areas

Figure 2-17: Remotely Controlled Auto Crawler Devices for Possible Deployment of NDI Equipment

These are concept devices that could be adapted to allow for ground-based, easy access to remote portions of the blade. This would allow wind farm operators to quickly inspect their blades if they need to respond to unanticipated overload conditions. Such inspections are necessary to make GO – NO GO decisions and to determine the need for any immediate repairs. This will minimize the risk of failure or forced down-time of the turbine. Power and data connection requirements may require a tether to be added to the concept crawler. Another option for remote inspections might be accomplished by adapting NDI methods onto UAS vehicles. Experienced gained from expanding visual assessments via UAS vehicles could be leveraged to provide more detailed inspection data. Integration of minimal NDI

hardware (i.e. weight) would be stressed as would on-board power and data logging capabilities. Problem spots, such as high stress regions or areas thought to contain systemic manufacturing flaws, could be routinely and quickly inspected with such an NDI vehicle.

2.3. References

2.1. Roach, D., Neidigk, S., Rice, T., Duvall, R., Paquette, J., "Blade Reliability Collaborative: Development and Evaluation of Nondestructive Inspection Methods for Wind Turbine Blades," Sandia DOT Report, SAND2014-16965, September 2014.

3. VISUAL INSPECTION OF WIND BLADE FLAWS

3.1. Current State-of-the-Art

The current state-of-the-art for wind blade inspections is primarily ground based visual inspections. These inspections are performed using a high resolution camera on a tripod to inspect the blades on stopped turbines. Typically, the turbine needs to be repositioned (i.e., rotor rotated, blades pitched) multiple times to complete the full set of inspections. SkySpecs is disrupting this industry by performing much faster and more repeatable autonomous drone-deployed visual inspections. Moving forward, there is increased value to the customer in adding nondestructive inspection techniques to monitor blades for subsurface damage.

3.1.1. Overview of Existing SkySpecs Drone Platform

The SkySpecs drone platform is designed to perform autonomous inspections of wind turbine blades. The novel attribute of the drone is the sophisticated sensor rig. The sensor rig and its accompanying software enable the drone to autonomously position itself at predetermined waypoints with a high level of accuracy. This positioning is critical for relating the position of flaw indications to a specific location on the blade with accuracy and repeatability.

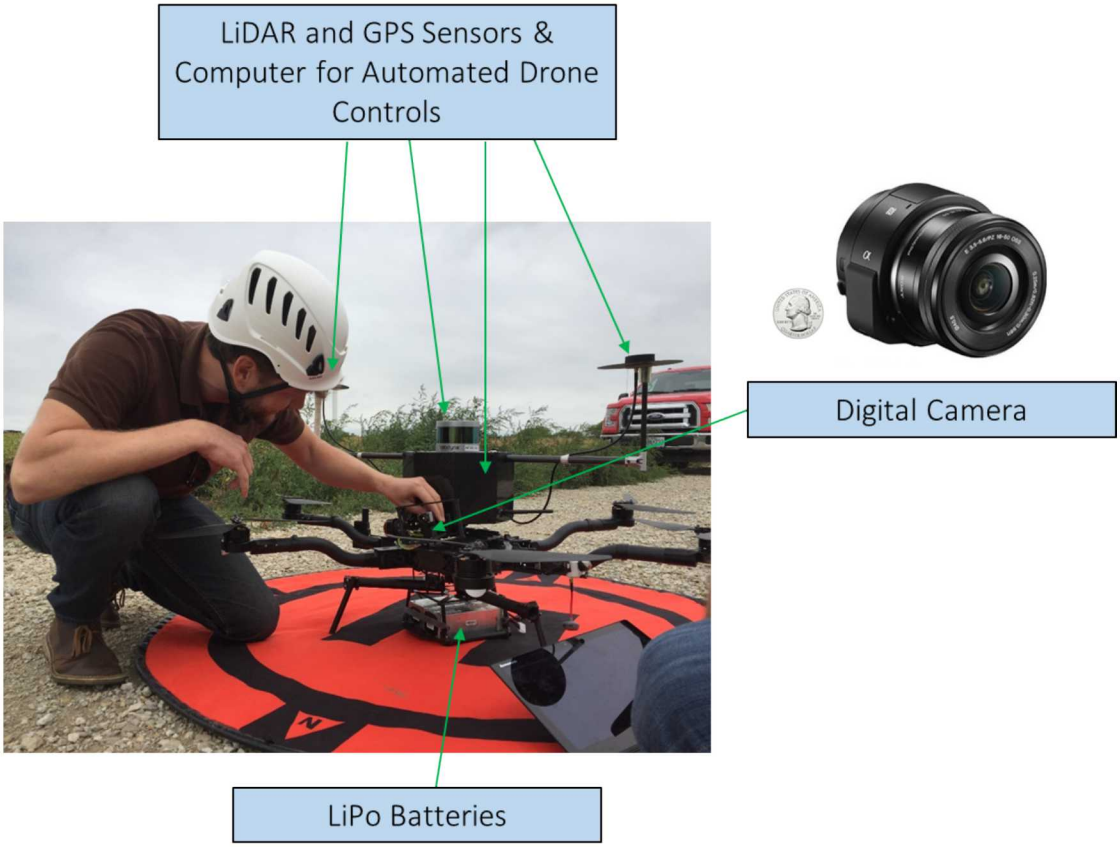

Figure 3-1: Overview of SkySpecs Drone Platform

Figure 3-1 shows an overview of the key features of the drone platform. The SkySpecs inspection platform employs two primary systems: (1) a commercial-off-the-shelf (COTS) Freefly Alta 6 drone (Figure 3-2) and (2) a custom-built rig with a variety of integrated sensors, software, and systems that is mounted to the top of the airframe (Figure 3-3). The sensor rig's computer, outfitted with SkySpecs' proprietary automation software, interfaces with the drone's embedded flight control system to achieve autonomous aerial inspections of wind turbine blades. The Alta 6 drone is largely unmodified from its COTS configuration, whereas the sensor rig is custom-fabricated from a combination of carbon fiber plates and tubes, aluminum standoffs, custom hardware mounts and interface parts, and other COTS sensors. The advanced positioning capabilities of the sensor rig are performed using a combination of these COTS sensors, including an inertial measurement unit (IMU), global navigation satellite system (GNSS) receivers, Velodyne VLP-16 light detection and ranging (LiDAR) puck, and data transmitting radio, combined with a CPU and motherboard.

Figure 3-2: Alta Freefly 6 in COTS Configuration

The current visual inspection equipment consists of a Sony UMC-R10C 20 megapixel lens-style camera (Figure 3-4) mounted on a HD AirStudio Infinity MR-S Very Lite two-axis gimbal (Figure 3-5). This setup allows the drone to orient the camera, as needed, to take high resolution photos of the wind blade surface. The most efficient way to add subsurface damage detection capabilities to the drone is to integrate a sensor or inspection transducer with similar form factor, power, and weight specifications as the Sony UMC-R10C onto this existing gimbal, either alongside the camera or adding the ability to swap out the camera. Additionally, SkySpecs' engineering personnel should be able to rapidly model and 3D print any interface mounts required to fit a new sensor onto the integrated, 2-axis gimbal.

Figure 3-3: SkySpecs Custom-Built Sensor Rig

Figure 3-4: Sony UMC-R10C 20 Megapixel Camera

Figure 3-5: HD AirStudio Infinity MR-S Very Lite Gimbal

For the purposes of this project and the associated sensor down-select and integration process discussed in Section 5, the guidelines noted below were used when evaluating potential sensor options. In some cases, it is possible to exceed a particular constraint if a trade study deems one sensor far superior to other options.

- Weight: < 450g
- Power: 5-12 VDC, 120 W max, preferably <20 W max (N/A for internal battery-powered sensors)
- Max Dimensions: 4” width, 2.75” height, 2.5” depth
- Drone Positional (Relative Displacement) Accuracy: < 1 cm
- Drone Distance from Blade: 4-8 m
- Drone Speed: Approx. 1-2 m/s
- Battery Life: Currently approx. 20 minutes but under continuous improvement
- Data Storage: Multi-terabyte (TB) solid state hard drive

Once a list of sensor down-selects was made using these specification guidelines, SkySpecs and Sandia collaborated to evaluate each option.

3.1.1.1. Current SkySpecs Inspection and Damage Detection Strategy

The current SkySpecs inspection strategy consists of the following approach:

- Stop the wind turbine in any orientation.
- Position the drone near the base of the tower.
- Direct the drone to begin autonomous flight.
- The drone autonomously inspects all four sides of each blade, stopping briefly to take a photo at each waypoint, and then moving on to the next waypoint.
- The drone autonomously lands.
- The drone reports to the pilot whether the flight successfully captured 100% of the required images.
- If no additional inspections are required, the turbine is restarted.

This flight strategy is extremely efficient and enables the SkySpecs team to inspect a tower in approximately 15 minutes. Figure 3-6 shows an image of this process in action. Ideally, an additional NDI method would be integrated directly into this approach or only require minor modifications.

Once the inspections are completed, the images are downloaded from the onboard solid state hard drive. Currently, these images are then manually reviewed offsite to identify damage based on type, location, and severity. A summary of this approach to damage classification in provided in the following sections. These images are also tied to the blade location using the position locating features of the custom-built rig.

Figure 3-6: SkySpecs Drone Inspecting a Wind Blade

3.2. Damage Classification

An important part of the inspection value that SkySpecs provides to their wind farm operator customers is damage classification. Identifying the type, severity, and location of damage in summary reports is important to enable the customer to make informed decisions about their turbines. The following sections provide information on how this classification is currently performed.

3.2.1. Manual Damage Classification of Severity

Because wind farms typically consist of dozens of turbines and each wind blade contains a large surface area, it's important to summarize the inspection results in a format that limits the data to the subset of critical information. SkySpecs satisfies this requirement by reviewing the inspection data and condensing the data to highlight visual inspection flaw indications. These flaw indications are characterized by flaw type and severity.

A proactive approach to wind blade inspections is recommended to minimize total lifecycle costs. Wind farm operators should monitor for damage at an early stage

before such damage can propagate from a lower cost repair situation to a full replacement requirement. The goal is to inspect a subset of the turbine population each inspection cycle so that the full fleet is covered by the N^{th} inspection cycle. Ultimately, the goal is to catch damage while it is still cost-effectively repairable, and to compile a list of turbines that need to be monitored and revisited to ensure that damage has not progressed. Additionally, while leading edge erosion does not typically cause wind blade failures, moderate levels of erosion can negatively affect Annual Energy Production (AEP) and should be monitored for potential repair. Figure 3-6 shows the results of a Sandia survey of wind farm operators and 3rd party inspection companies on the frequency of damage types. Note that currently, no subsurface nondestructive inspection is conducted in-service, so the subsurface damage statistics shown here may be less than actual occurrence.

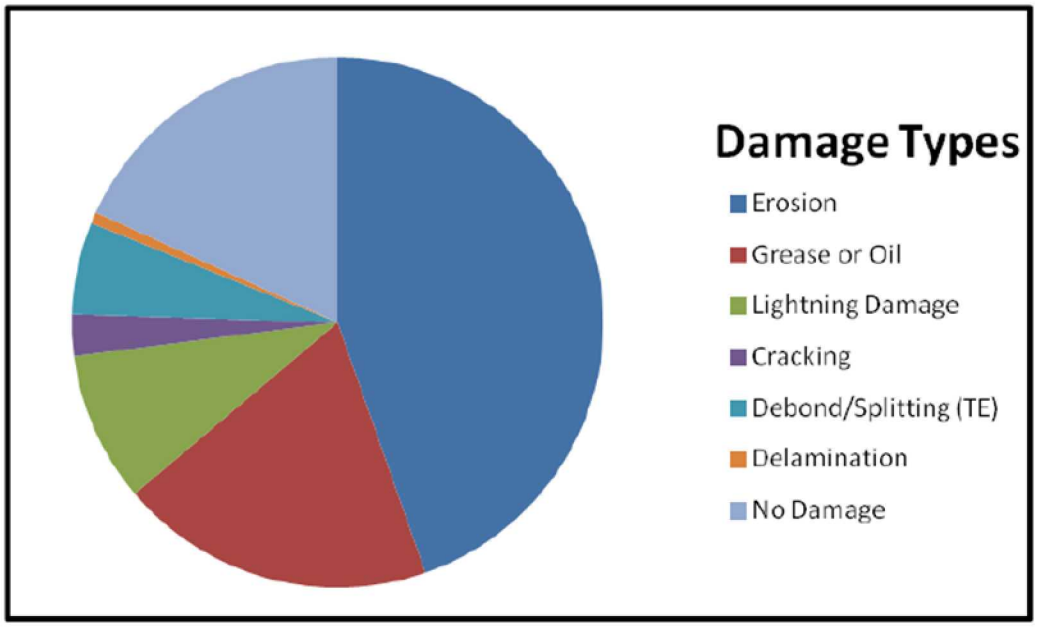

Figure 3-7: Results of Sandia Survey on the Frequency of Various Damage Types

With large turbine populations, full site inspections may be impractical, so a combination of targeted proactive and sampling periodic inspections is useful in capturing damage and avoiding larger repair/replacement costs. Based on these considerations and experience, visually detectable flaw types can be classified by the following groups:

- Erosion
- Shell Contamination
- Cracks
- Gelcoat/Top Coat Damage
- Chips

- Waves/Discontinuity in Base Laminate
- Laminate Damage
- Lightning Damage
- Leading Edge Damage
- Trailing Edge Damage
- Other

To date, these inspection considerations have been focusing on damage that can be identified with visual inspection. Based on the addition of additional nondestructive inspection sensors, as described in subsequent sections, these flaw types should updated in the future to include subsurface flaws such as disbonds, delaminations, ply waves, and fiber fracture.

In addition to classifying the damage type, damage categorization is important in standardizing and executing reinspection and repair work scheduling. Figure 3-8 shows an example of how these damage categories can affect the maintenance interval on a set of turbines. Figure 3-9 summarizes the criteria for each of the categories on a scale of 1 – 5, with 5 being the most severe. These categories provide the wind farm operators with the necessary quasi-quantitative information to make informed decisions on repairs and inspection intervals. The following sections provide examples of the damage categories for a sample of damage types.

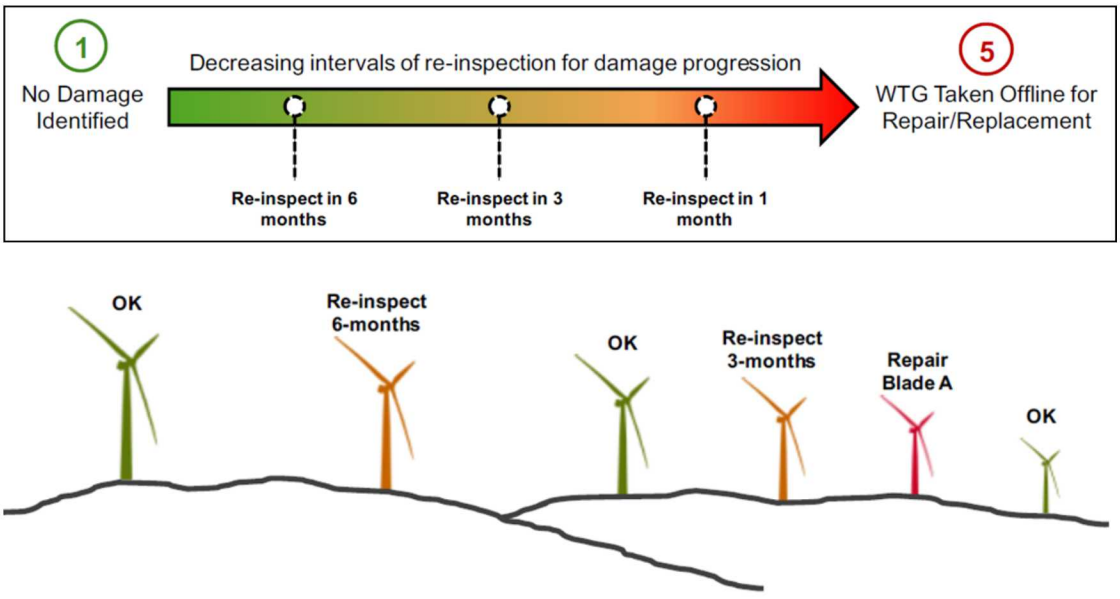

Figure 3-8: Damage Severity Affects Maintenance Interval

Category	Repair Priority	Description	Action
1	None	Light wear & minor cosmetic irregularities on blade.	No action required. Annual inspections recommended.
2	None	Early signs of wear or damage.	No immediate action required. Inspect within 12 months.
3	Low	Minor structural defects. Noticeable wear or damage.	Inspect & re-categorize in 6 months.
4	Medium	Moderate structural damage. Major signs of wear to blade.	Repair work recommended.
5	High	Major structural damage. Blade failure.	Repair immediately.

Figure 3-9: Overview of Damage Severity Categories

3.2.1.1. Erosion

Erosion is predominantly found on the leading edge and is typically a result of environmental conditions, such as dust/sand, rain, and ice. Due to the high speed of the wind blade tips, these environmental conditions can cause significant erosion over time. As shown in Figure 3-10, the downward velocity of rain also causes a non-negligible change in rain drop impact velocity with respect to blade position [3.2]. Based on Sandia aerodynamics models, Figure 3-11 shows that the surface roughness caused by erosion can decrease the AEP by approximately 2.5% at a moderate wind speed site and 5% at a low wind speed site [3.2].

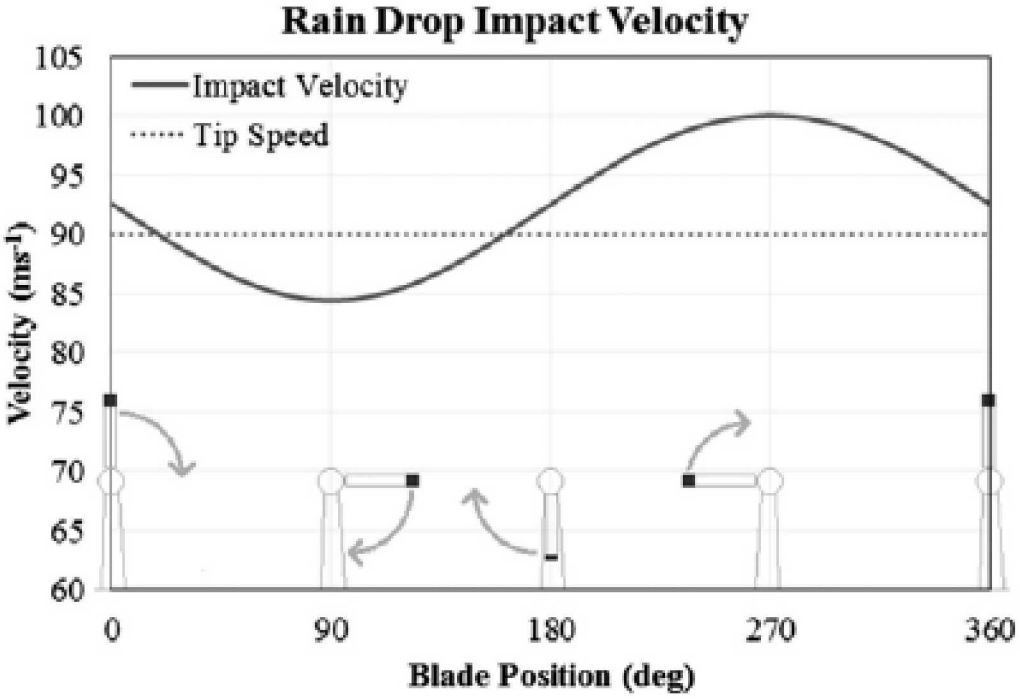

Figure 3-10: Rain Drop Impact Velocity vs. Blade Position

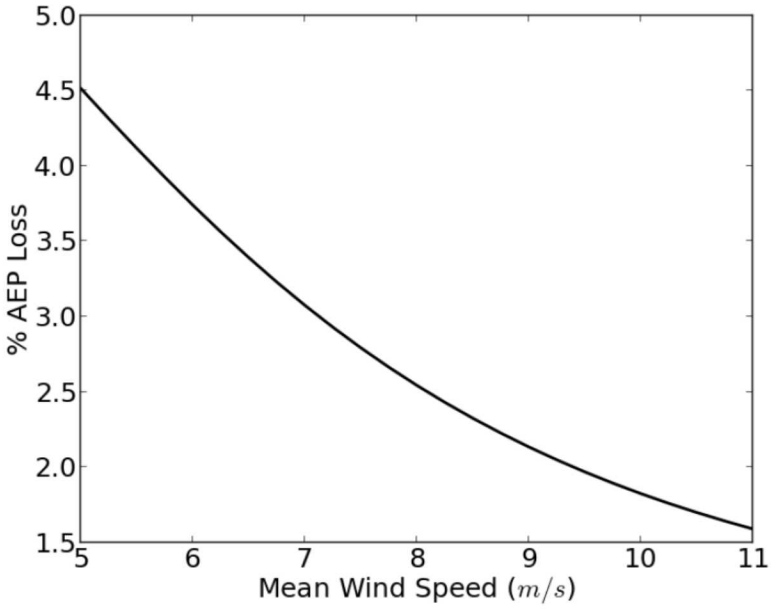

Figure 3-11: Decrease in Annual Energy Production vs. Mean Wind Speed

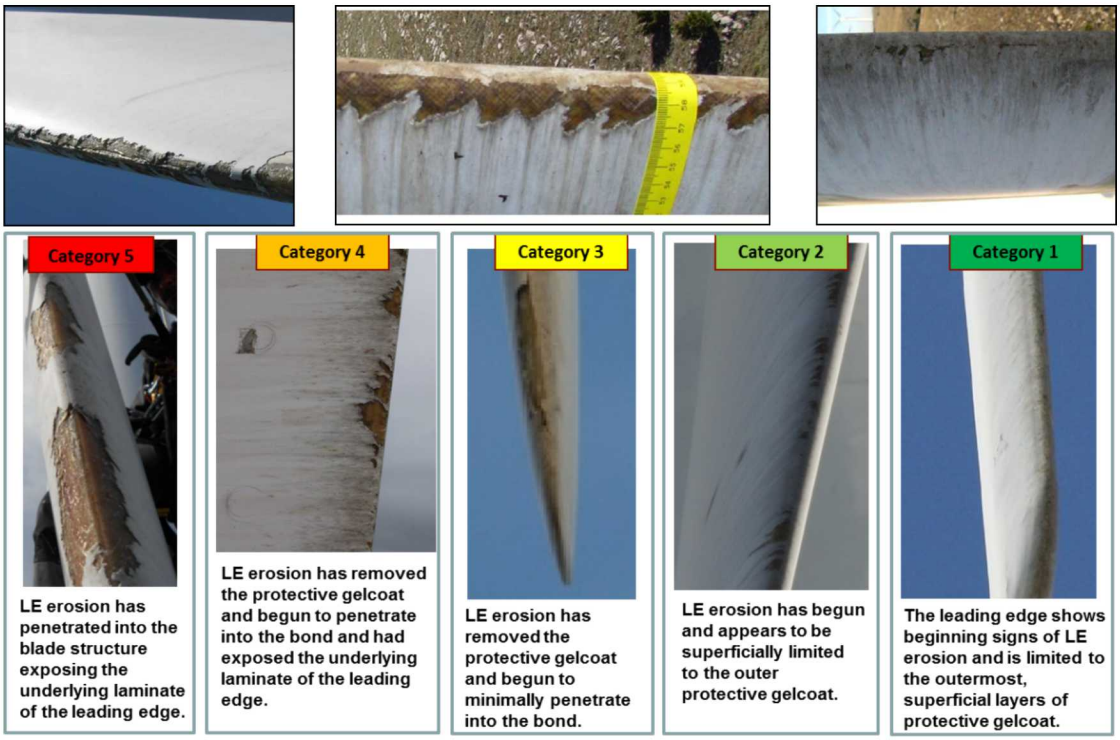

Figure 3-12: Leading Edge Erosion – Damage Severity Examples

Leading edge erosion can range from Category 1-5. Examples of these categories are provided in Figure 3-12. Category 2 might be erosion limited to the coating, whereas Category 3-4 might be contained within the bond paste securing both sides of the blade shell along the leading edge. Finally, Category 5 would penetrate the structure almost into the inner cavity of the blade.

3.2.1.2. Shell Contamination

Shell Contamination includes contaminants such as bugs, dirt, hydraulic oil or blade bearing grease that may negatively impact blade structure and/or turbine performance. Figure 3-13 provides examples of Category 1-3 damage. Note, a Category 4 or 5 rating for contamination is not likely to occur since there will generally be more severe issues that lead to taking a turbine offline ahead of contamination (e.g., hydraulic pump burst).

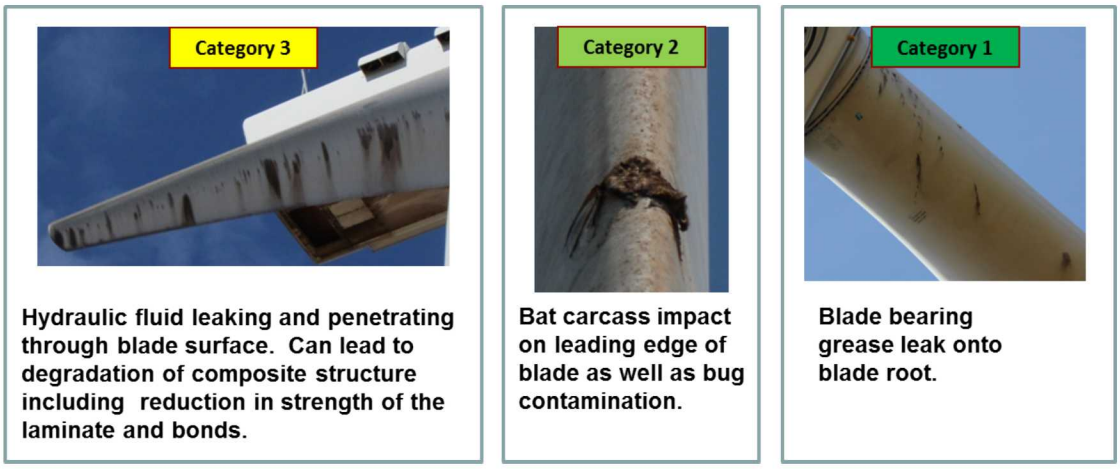

Figure 3-13: Shell Contamination – Damage Severity Examples

3.2.1.3. Cracks

Cracks may penetrate through the blade gel coat or even the primary blade structure. Cracks can possibly occur during manufacturing, object impact, or blade loads that exceed the design intent and cause the blade to bend and shell to crack. A coating crack is typically narrow and does not appear to have much depth. Whereas, a crack penetrating the coating into the structure may appear wider with greater depth. Figure 3-14 shows examples of cracks with varying severity.

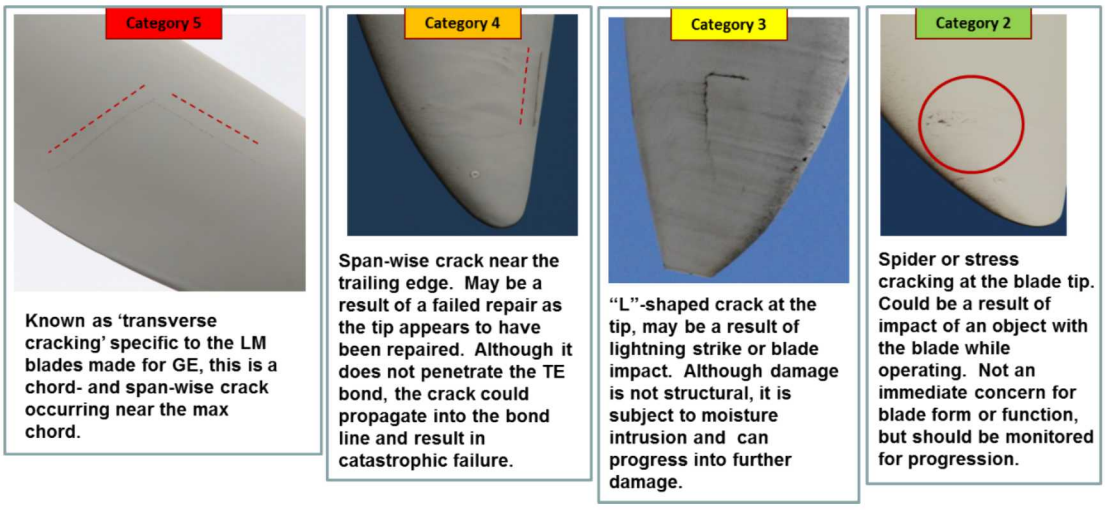

Figure 3-14: Cracks – Damage Severity Examples

3.2.1.4. Gel Coat/Top Coat Damage

Gel coat/top coat damage contains a chipped, dented, and/or irregular surface compared to new blade condition. Fiberglass is possibly exposed and can lead to moisture intrusion, progressed damage, and affect turbine performance. The gel coat is the protective skin of the blade and damage is typically due to object impact, ice shedding, poor prior repairs, or blade loads which exceed design intent and cause the

blade to bend and shell to buckle. Figure 3-15 illustrates varying severity levels of gel coat/top coat damage.

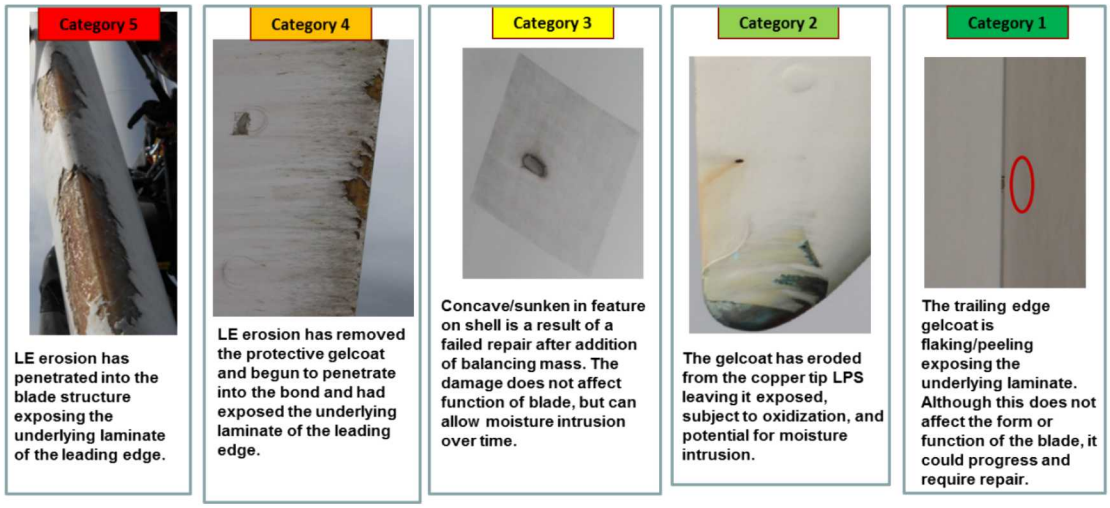

Figure 3-15: Gel Coat/Top Coat – Damage Severity Examples

3.2.1.5. Laminate Damage

Fiberglass delamination is the separation of fiberglass ply layers of the blade laminate that can greatly lower blade strength depending on location and severity. Possible causes can be poor manufacturing, structural impact, blade loads which exceed design intent and cause the blade to bend and shell to buckle, temperature fluctuations, or water/fluid intrusion which expands either when struck by lightning or as it freezes causing ply delamination. Examples of laminate damage are shown in Figure 3-16.

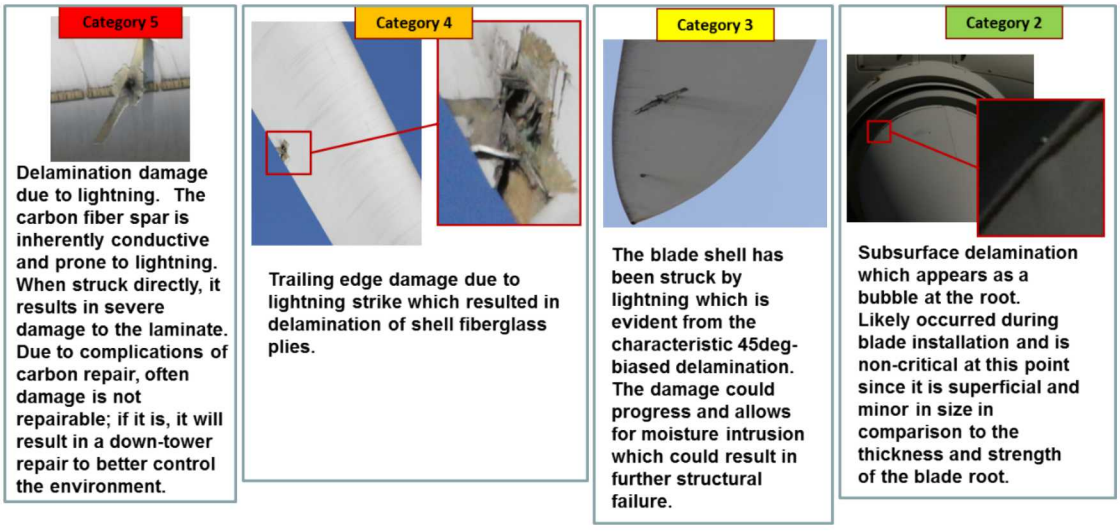

Figure 3-16: Laminate Damage – Damage Severity Examples

3.2.1.6. Lightning Damage

Because the LPS provides no remote indication of a strike occurring and the manufacturer has little incentive to monitor for damage that is outside the scope of the

warranty, the owner is placed in the position of monitoring for damage at an early stage before it moves from a lower cost repair situation, to a full replacement requirement. Damage types include, but are not limited to, gel coat damage, cracks, delamination, disbonding, and trailing edge separation. For example, a lightning strike to the lightning cable through the blade shell can result in trailing edge delamination due to high pressure inside the blade. Typical locations of lightning damage are at the tip of the blade near the lightning receptor. Scorching is also likely and may include holes or delaminations where lightning entered or exited the blade at a location other than receptor. Figure 3-17 and Figure 3-18 show various categories of lightning damage.

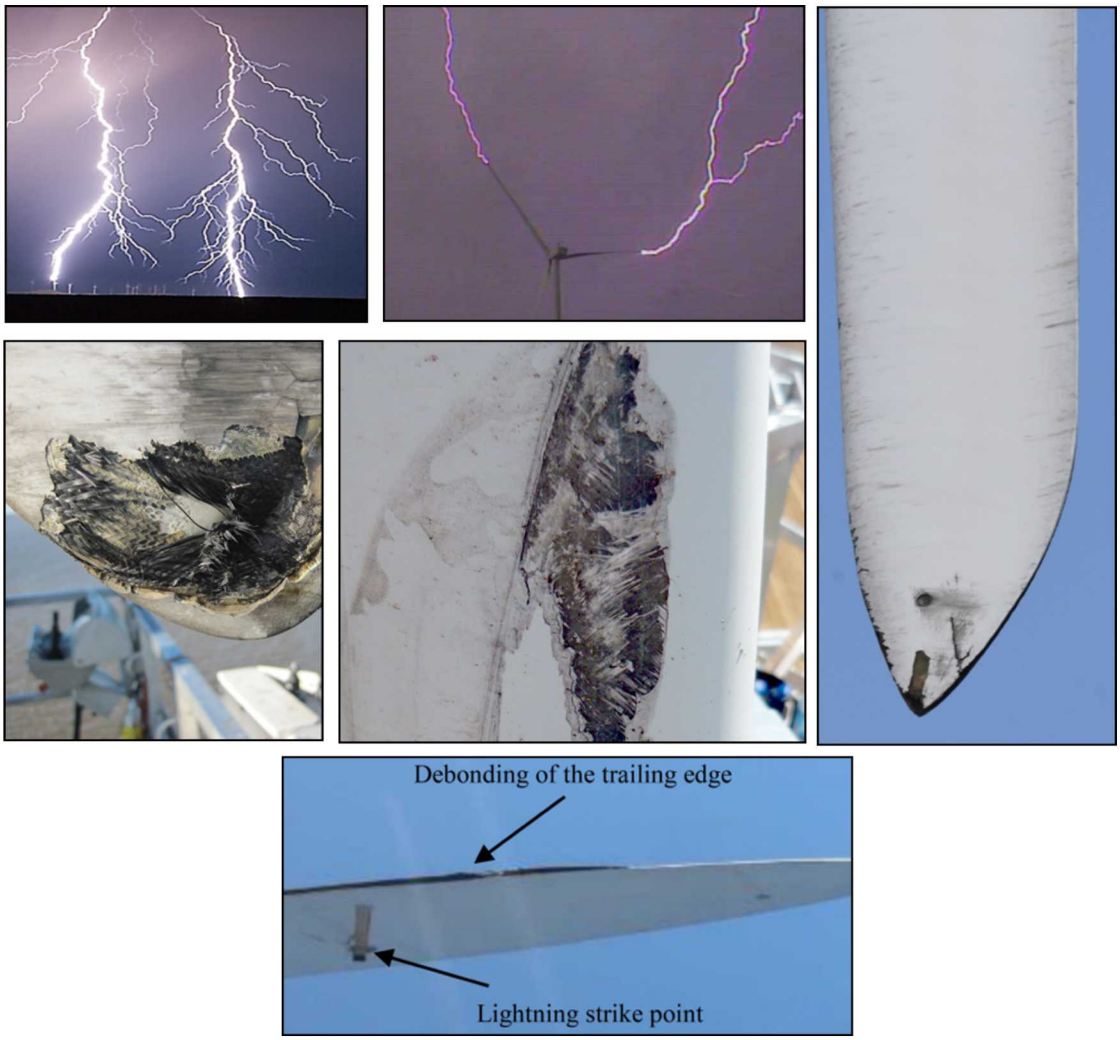

Figure 3-17: Lightning – Damage Severity Examples

Figure 3-18: Lightning – Damage Severity Examples

3.2.1.7. Leading Edge Damage

Leading edge damage includes but is not limited to erosion, cracks, and de-bonding of the leading edge bonded joint. Damage on the leading edge can progress quickly due to the high speed wind inflow experienced and because it is most susceptible to impact (e.g., rain, dirt, bugs). Figure 3-19 summarizes different types of leading edge damage.

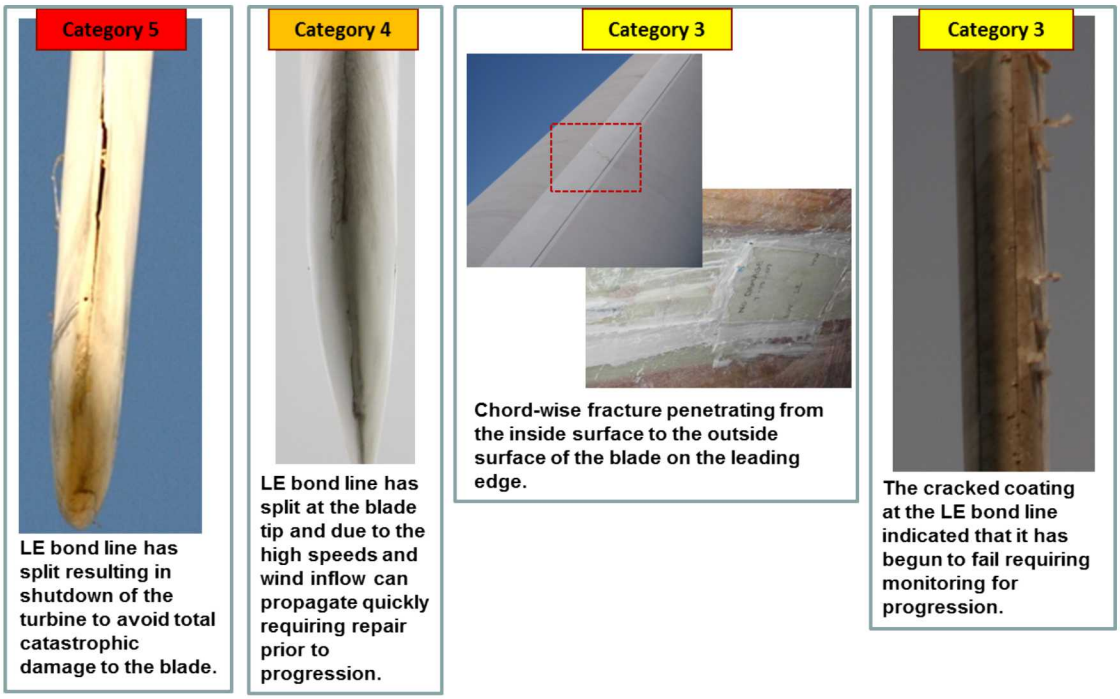

Figure 3-19: Leading Edge – Damage Severity Examples

3.2.1.8. Trailing Edge Damage

Trailing edge disbonding and fracture/splitting includes but is not limited to trailing edge structural damage and adhesive joint de-bonding (i.e., trailing edge split). The damage typically occurs near the tip where higher velocity is experienced. Due to the narrow profile of the trailing edge near the tip, damage occurring there can easily progress depending on location and severity. Trailing edge splitting can occur due to water/fluid ingress which expands either when struck by lightning or as it freezes causing failure at the trailing edge bond. Examples of trailing edge damage are given in Figure 3-20.

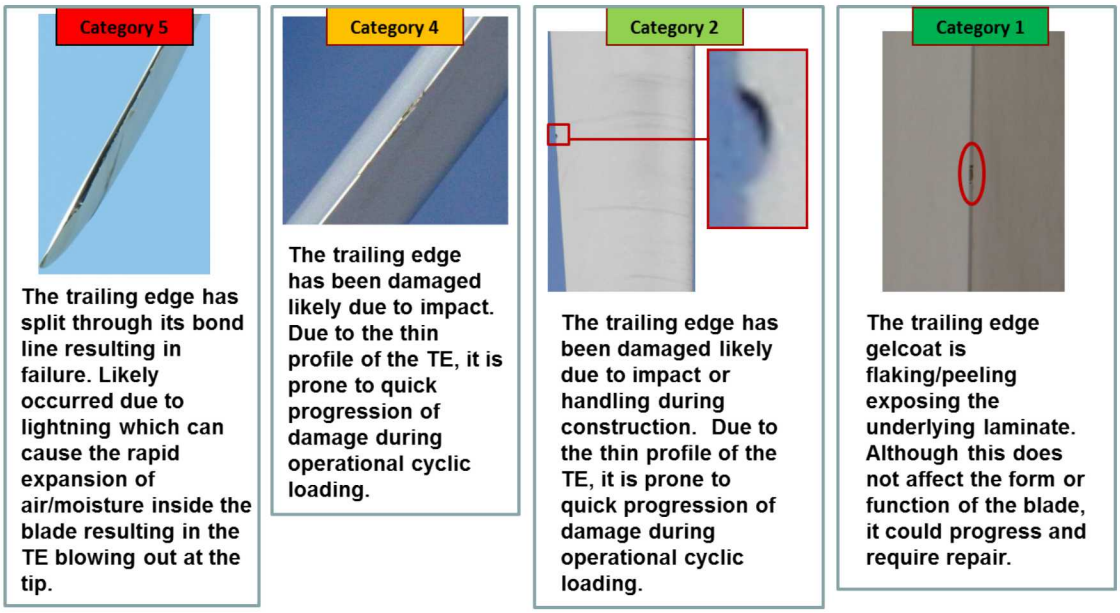

Figure 3-20: Trailing Edge Disbond and Fracture – Damage Severity Examples

3.2.2. Considerations for Automated Damage Classification

An automated damage classification process would ideally include data fusion of flaw indications from multiple inspection techniques. Figure 3-21 displays a notional example of the data fusion of two inspection techniques – visual inspection and thermography; however, this approach could be extended to additional inspection techniques. In this example, the user is able to switch between multiple views that show the unaltered visual inspection data as well as the flaw indications from the data classification engine. These flaw indications are projected onto a 3D model of the blade, based on drone position and gimbal orientation data. This location data is critical for correlating the test results from multiple inspection techniques and recurring inspections of the same turbine.

The data fusion example also provides information on the type of damage and severity. The user is able to compare and contrast the results of the different techniques. In this case, the thermography data compliments the visual inspection data by corroborating the existence of the lightning damage and providing supplemental information on the slightly larger extent of the subsurface damage. This information would allow the wind farm operator to make an informed decision on the size of the damage and whether it should be repaired. Additionally, the thermography results identified a small impact that wasn't detectable with only visual inspection.

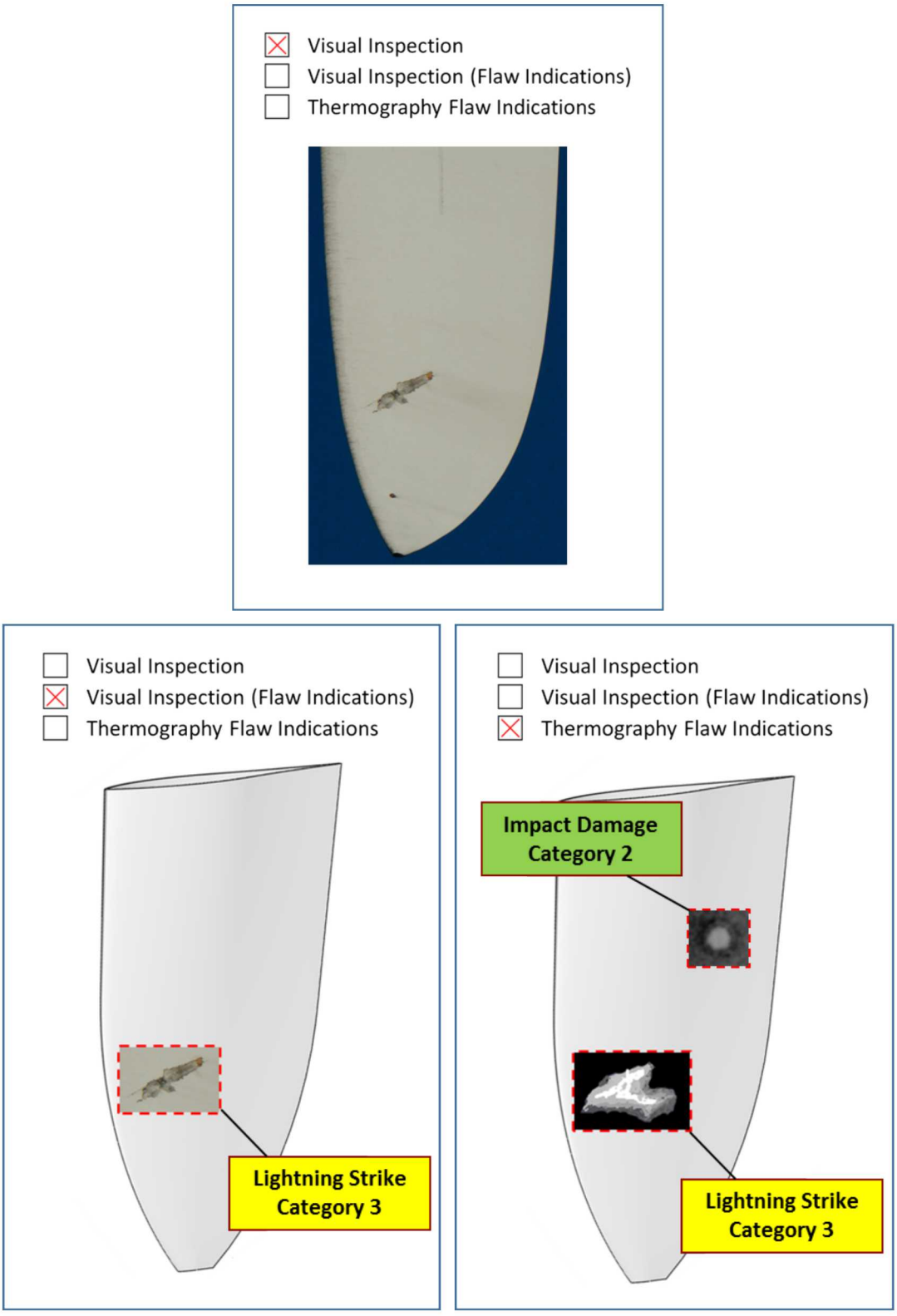

Figure 3-21: Example Automated Data Classification of a Lightning Strike

While the benefits of this type of analysis are obvious, the implementation comes with multiple challenges. Building a robust solution will require complex, multi-disciplinary work to develop the model, pair it with SkySpecs inspection data, and train the model to make accurate damage classification.

3.2.3. Development of Wind Blade Visual Test Specimens

In order to aid the transition to automated damage detection, visual inspection specimens were built to increase the number of training and validation images. These specimens focused on the types of damage and severity categories previously described.

The first specimen, CB-V1, is a 30 inch section of blade that was cut from a 9 meter carbon-fiberglass hybrid TX-100 Blade. The TX-100 blade was designed by Sandia and manufactured by TPI to demonstrate the use of bend-twist coupled behavior for fatigue loads alleviation in a wind turbine blade [3.1]. Table 3-1 provides a description of all the representative flaws that were engineered into this blade section. Figures 3-22 to 3-29 provide images of each of the defects.

Table 3-1: Wind Blade Visual Test Specimen: CB-V1 (Carbon Fiber Skin – Balsa Core) Flaw Descriptions

Flaw ID	Blade Location	Flaw Description
HP1	High Pressure Side	Pitting/Chipping (-)
HP2	High Pressure Side	Contamination (+), Simulates Insect Accumulation
HP3	High Pressure Side	Slight Lightning Burn
HP4	High Pressure Side	Shell Impact Depression & Gelcoat cracks (Scuff Mark)
HP5	High Pressure Side	Trailing Edge Impact Gelcoat (Scuff Mark)
HP6	High Pressure Side	Lightning Burn & Shell Damage
HP7	High Pressure Side	Shell Impact Depression & Gelcoat cracks (No Scuff Mark)
HP8		Delaminations Under Skin - See Below:
HP8-A	High Pressure Side	Delamination Under Skin (IR Flaw), ~0.50" Wide
HP8-B	High Pressure Side	Delamination Under Skin (IR Flaw), ~0.75" Wide
HP8-C	High Pressure Side	Delamination Under Skin (IR Flaw), ~1.00" Wide
LP1	Low Pressure Side	Lightning Burn
LP2	Low Pressure Side	Gelcoat cracking
LP3	Low Pressure Side	Lightning Burn & Shell Damage
LP4		Flat Bottomed Holes (FBH) - See Below:
LP4-1	Low Pressure Side	FBH, Diameter = 0.365", Average Depth = 0.0239"

LP4-2	Low Pressure Side	FBH, Diameter = 0.365", Average Depth = 0.0640"
LP4-3	Low Pressure Side	FBH, Diameter = 0.365", Average Depth = 0.1095"
LP4-4	Low Pressure Side	FBH, Diameter = 0.365", Average Depth = 0.1440"
LP4-5	Low Pressure Side	FBH, Diameter = 0.125", Average Depth = 0.0379"
LP4-6	Low Pressure Side	FBH, Diameter = 0.125", Average Depth = 0.0946"
LP4-7	Low Pressure Side	FBH, Diameter = 0.125", Average Depth = 0.1438"
LP4-8	Low Pressure Side	FBH, Diameter = 0.125", Average Depth = 0.1795"
LP4-9	Low Pressure Side	FBH, Diameter = 0.250", Average Depth = 0.0368"
LP4-10	Low Pressure Side	FBH, Diameter = 0.250", Average Depth = 0.0800"
LP4-11	Low Pressure Side	FBH, Diameter = 0.250", Average Depth = 0.1250"
LP4-12	Low Pressure Side	FBH, Diameter = 0.250", Average Depth = 0.1636"
LP5	Low Pressure Side	Transverse Cracking
LP6	Low Pressure Side	Sharpie Marks (Surface Only)
LP7	Low Pressure Side	Deep Scratch Marks (Through Gelcoat)
LE1	Leading Edge	Extreme Leading Edge Erosion
LE2	Leading Edge	Mild Leading Edge Erosion
TE1	Trailing Edge	Trailing Edge Split, ~11.5" Long
TE2	Trailing Edge	Trailing Sharpie Mark (No Depth), ~3.0" Long
TE3		Trailing Edge Chipping (Impacts) - See Below:
TE3-A	Trailing Edge	Trailing Edge Chipping
TE3-B	Trailing Edge	Trailing Edge Chipping
TE3-C	Trailing Edge	Trailing Edge Chipping

High Pressure Side

Low Pressure Side

Figure 3-22: Wind Blade Visual Test Specimen CB-V1 (Carbon Skin – Balsa Core)

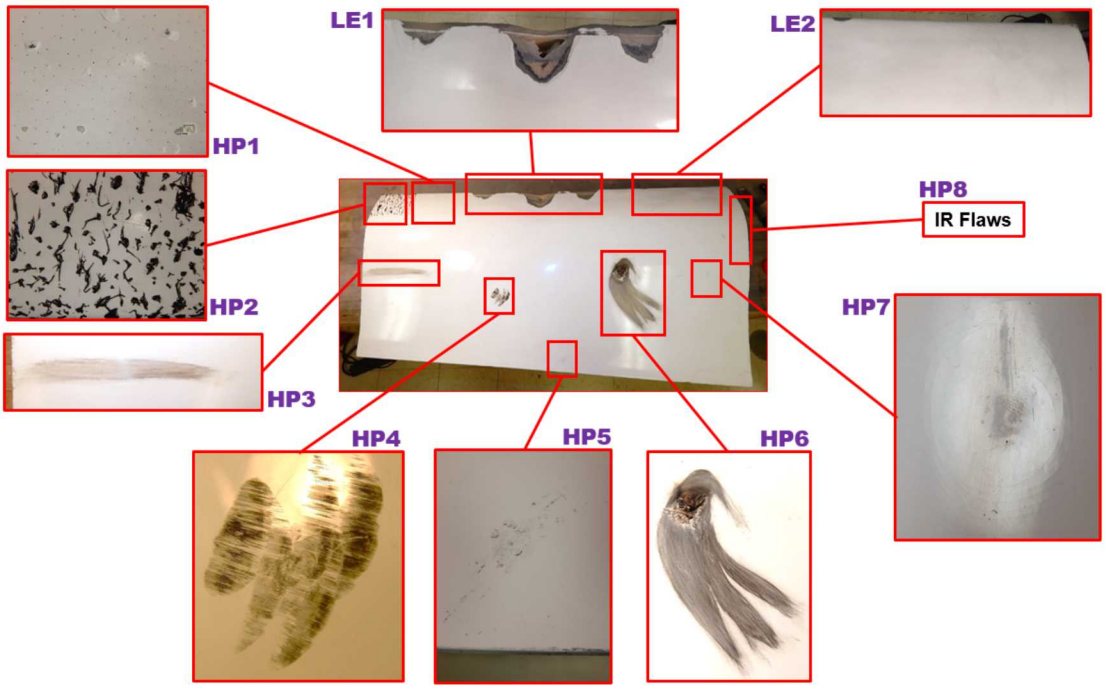

Figure 3-23: Wind Blade Visual Test Specimen CB-V1
High Pressure Side Flaws

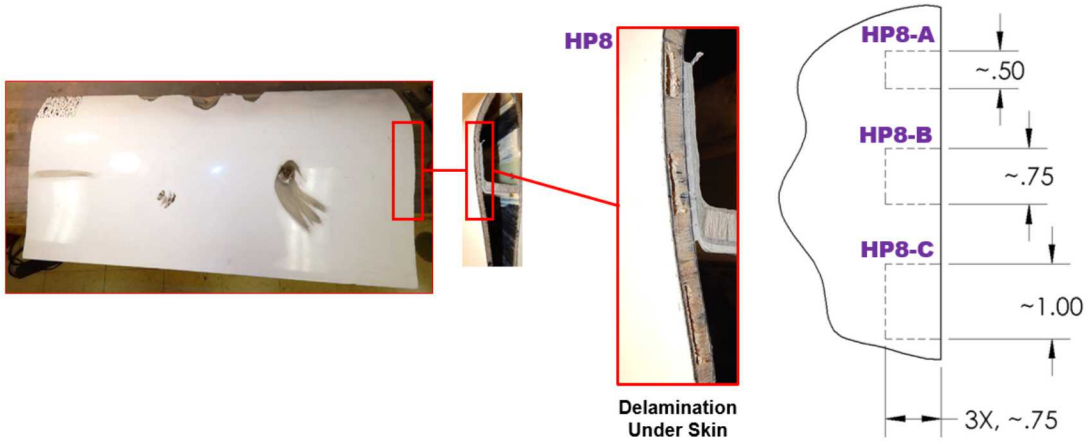

Figure 3-24: Wind Blade Visual Test Specimen CB-V1
HP8 Flaws Used to Assess the Subsurface Damage Detection of IR Inspections

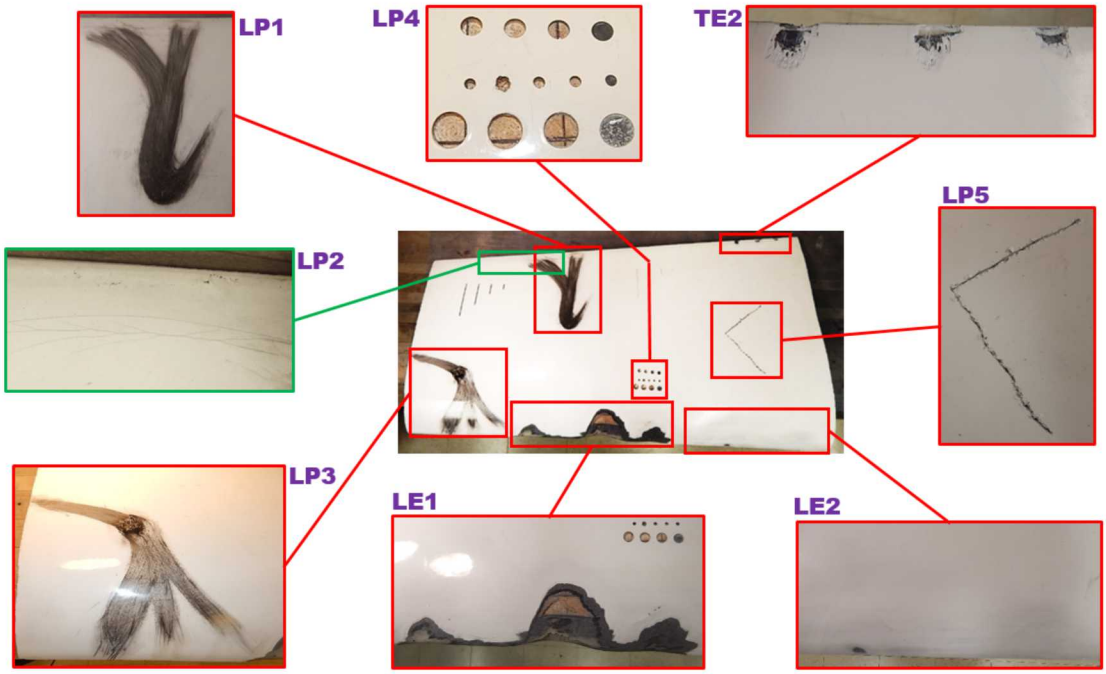

Figure 3-25: Wind Blade Visual Test Specimen CB-V1 Low Pressure Side Flaws

Figure 3-26: Wind Blade Visual Test Specimen CB-V1 LP4 Detailed Image

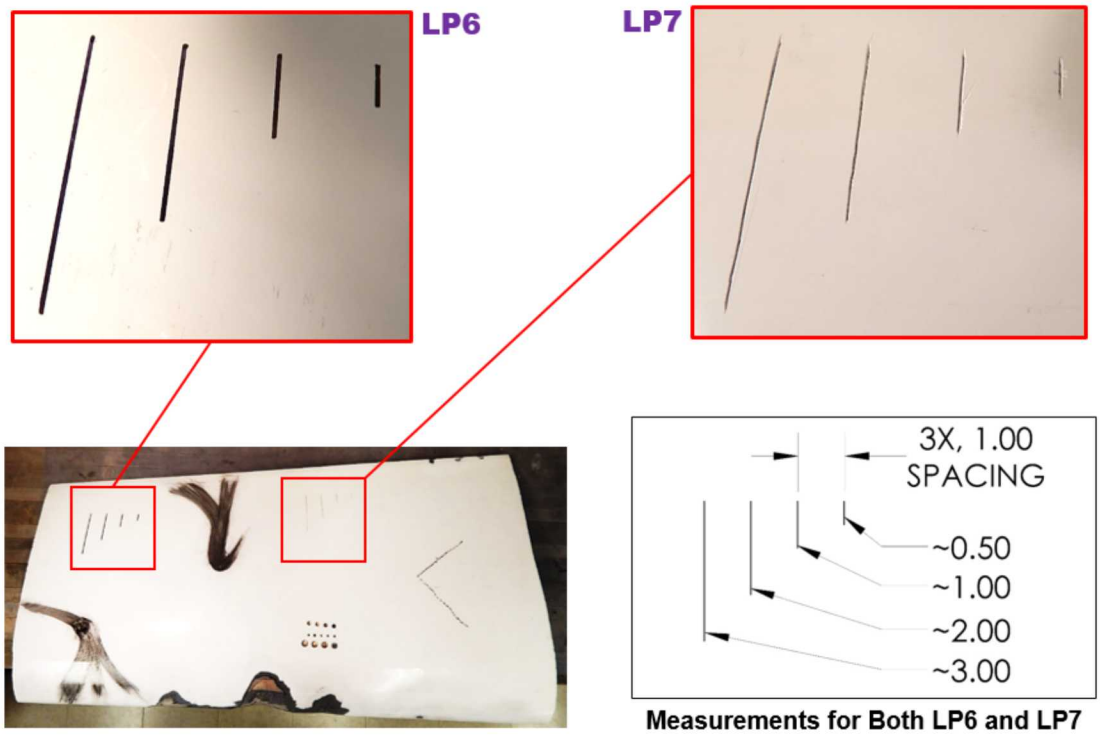

Figure 3-27: Wind Blade Visual Test Specimen CB-V1
Other Low Pressure Side Flaws

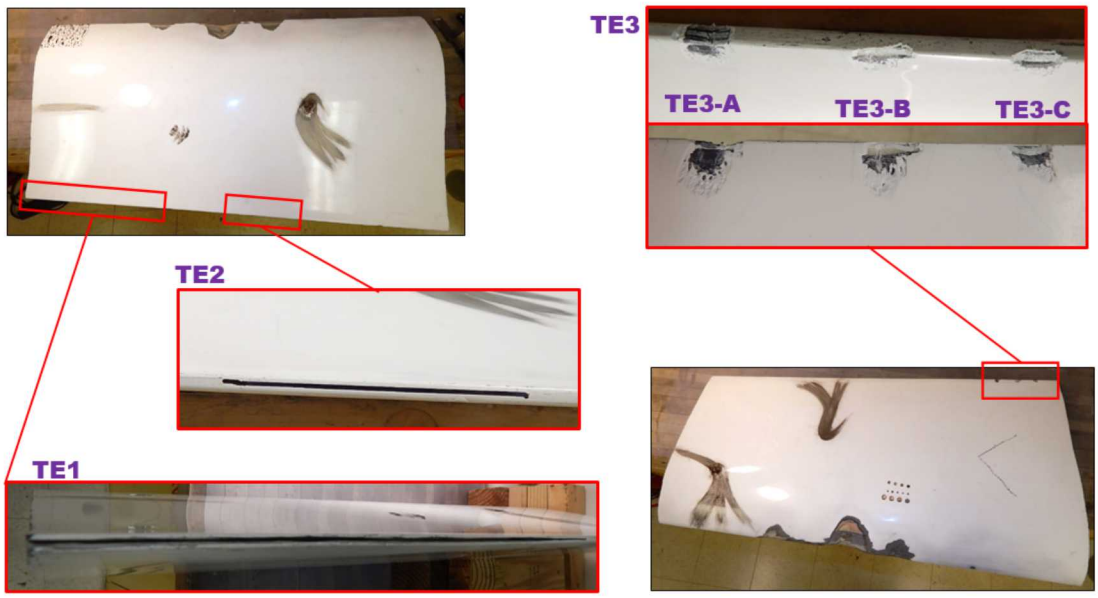

Figure 3-28: Wind Blade Visual Test Specimen CB-V1
Trailing Edge Flaws

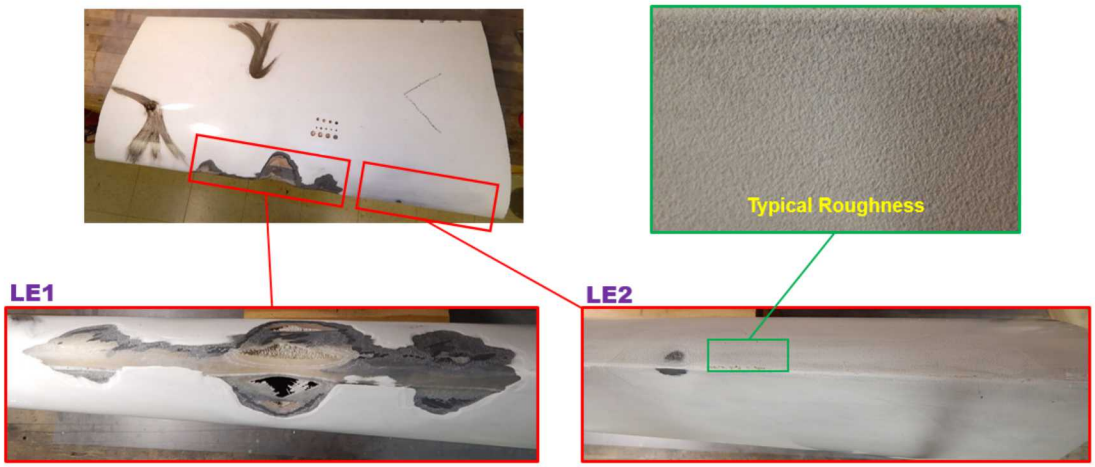

Figure 3-29: Wind Blade Visual Test Specimen CB-V1 Leading Edge Flaws

The second specimen, FF-V2, is a 30 inch section of blade that was cut from a 39 meter fiberglass foam core GE blade, manufactured by Tecsis. The cut was performed approximately 15 feet from the tip of the blade by the Sandia Composites Department (see Figure 3-30).

Table 3-2 summarizes all of the representative flaws that were engineered into this blade section. Images of each of the flaws are shown in Figures 3-31 to 3-37.

The inspection of these specimens were outside the scope of this project. Plans for the future use of these specimens is provided in Section 0.

Figure 3-30: Wind Blade Visual Test Specimen FF-V2
Cut From 39m GE Blade, Manufactured by Tecsis

Table 3-2: Wind Blade Visual Test Specimen FF-V2 (Fiberglass Skin – Balsa Core) Flaw Descriptions

Wind Blade Visual Test Specimen: FF-V2 (Fiberglass Skin – Foam Core)		
Flaw ID	**Blade Location**	**Flaw Description**
HP1	High Pressure Side	Major Delamination (Foam Split)
HP2	High Pressure Side	Ultrasonic/IR Flaws: Foam-Spar Cap, ~1.50" Wide
HP3	High Pressure Side	Ultrasonic/IR Flaws: Bond Line-Spar Cap Interface, ~1.50" Wide
HP4	High Pressure Side	Ultrasonic/IR Flaws: Bond Line-Web Flange Interface, ~1.50" Wide
LP1	Low Pressure Side	Lightning Burn & Shell Damage
LP2	Low Pressure Side	Gouge (1.25” X 0.1”) ~0.03” Deep
LP3	Low Pressure Side	Pitting/Chipping
LP4	Low Pressure Side	Shell Impact Depression (Scuff Mark)
LP5	Low Pressure Side	Scuff, No Damage
LP6	Low Pressure Side	Shell Impact, Slight Marks & Depression
LP7	Low Pressure Side	Shell Impact, Slight Marks & Depression
LP8	Low Pressure Side	Shell Impact & Depression (No Scuff Mark)
LP9	Low Pressure Side	Transverse Cracking
LP10	Low Pressure Side	Shell Impact, Slight Marks & Depression
LP11	Low Pressure Side	Impact & Depression (Scuff Mark)
LP12	Low Pressure Side	Impact & Depression (Slight Scuff Mark)
LP13	Low Pressure Side	Delamination Under Skin (IR Flaw), ~0.85" Wide, ~1.00" Deep
LP14	Low Pressure Side	Delamination Under Skin (IR Flaw), ~1.25" Wide, ~1.00" Deep
LP15	Low Pressure Side	Delamination Under Skin (IR Flaw), ~1.85" Wide, ~1.00" Deep
LE1	Leading Edge	Mild Leading Edge Erosion
LE2	Leading Edge	Medium Leading Edge Erosion
TE1	Trailing Edge	Trailing Edge Split, ~4.0” Long
TE2	Trailing Edge	Trailing Edge Split, ~2.0” Long
TE3	Trailing Edge	Trailing Edge Split, ~1.0” Long

TE4	Trailing Edge	Ultrasonic/IR Flaws: Bond Line-Skin Interface, ~1.00" Wide, ~1.70" Deep
TE5	Trailing Edge	Ultrasonic/IR Flaws: Bond Line, ~1.50" Wide, ~1.25" Deep
Bond1	Low Pressure Side	Ultrasonic/IR Flaws: Bond Line-Spar Cap Interface, ~Ø 0.25", ~1.50" Deep
Bond2	Low Pressure Side	Ultrasonic/IR Flaws: Bond Line-Spar Cap Interface, ~Ø 0.25", ~1.50" Deep
Spar1	Low Pressure Side	Ultrasonic/IR Flaws: Skin-Spar Cap Interface, ~Ø 0.40", ~1.50" Deep
Spar2	Low Pressure Side	Ultrasonic/IR Flaws: Spar Cap, ~Ø 0.40", ~0.20 From Skin, ~1.50" Deep
Spar3	Low Pressure Side	Ultrasonic/IR Flaws: Spar Cap, ~Ø 0.40", ~0.40 From Skin, ~1.50" Deep

High Pressure Side **Low Pressure Side**

Figure 3-31: Wind Blade Visual Test Specimen FF-V2 (Fiberglass Skin – Foam Core)

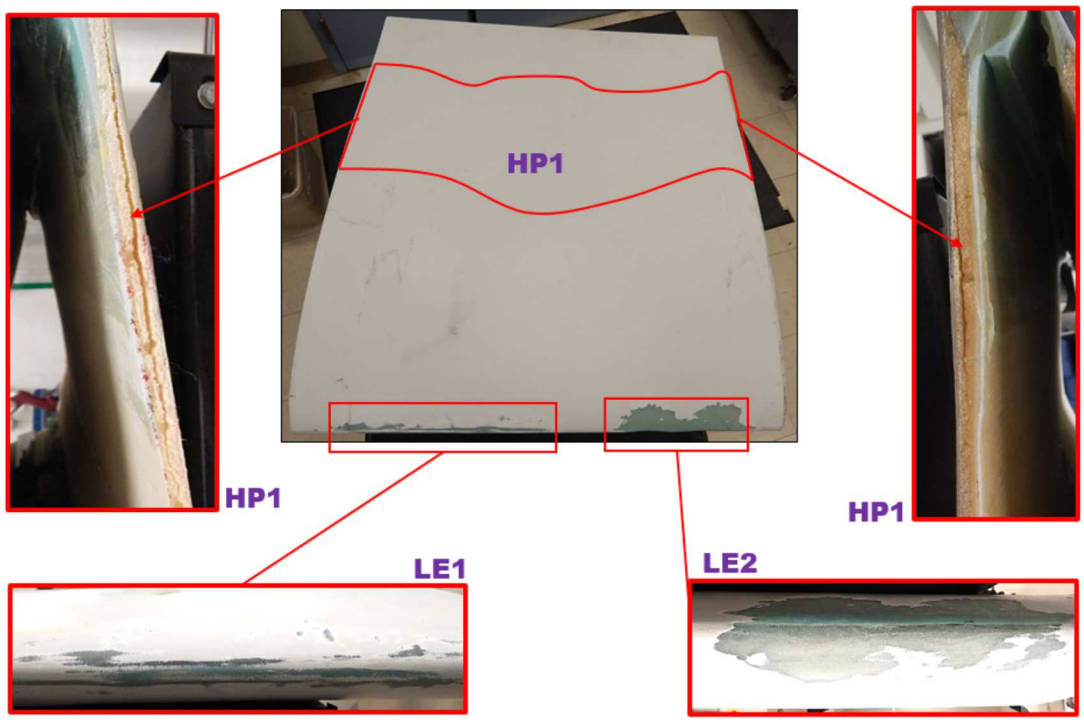

Figure 3-32: Wind Blade Visual Test Specimen FF-V2
High Pressure Side & Leading Edge Flaws

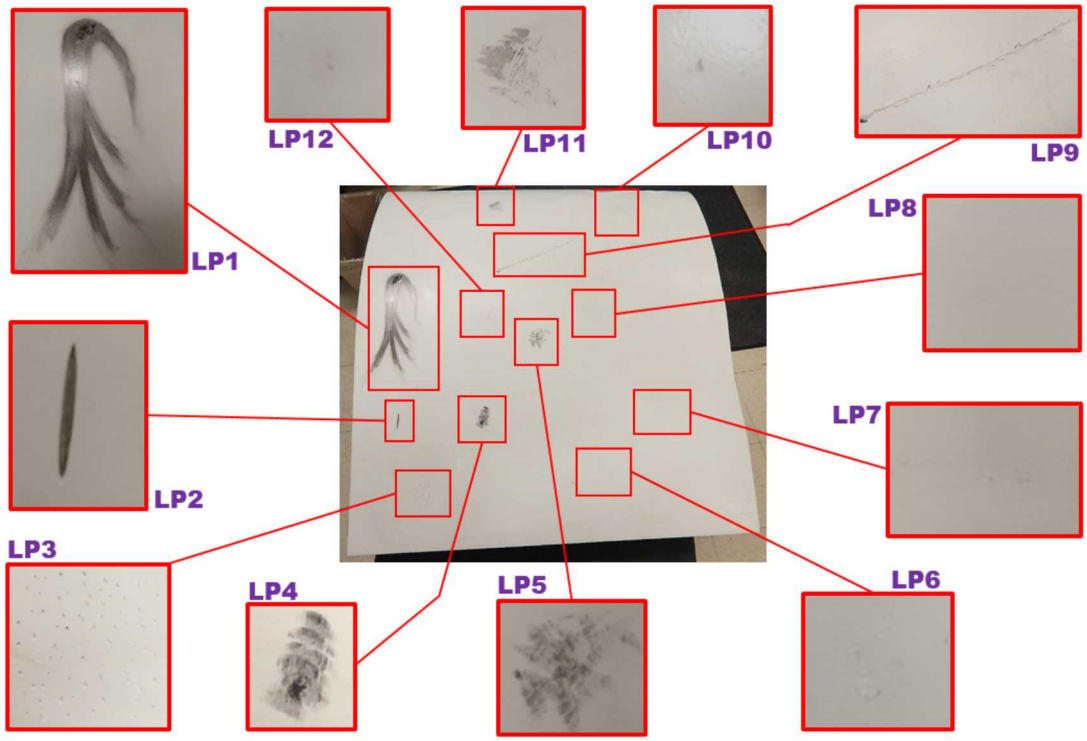

Figure 3-33: Wind Blade Visual Test Specimen FF-V2
Low Pressure Side Flaws

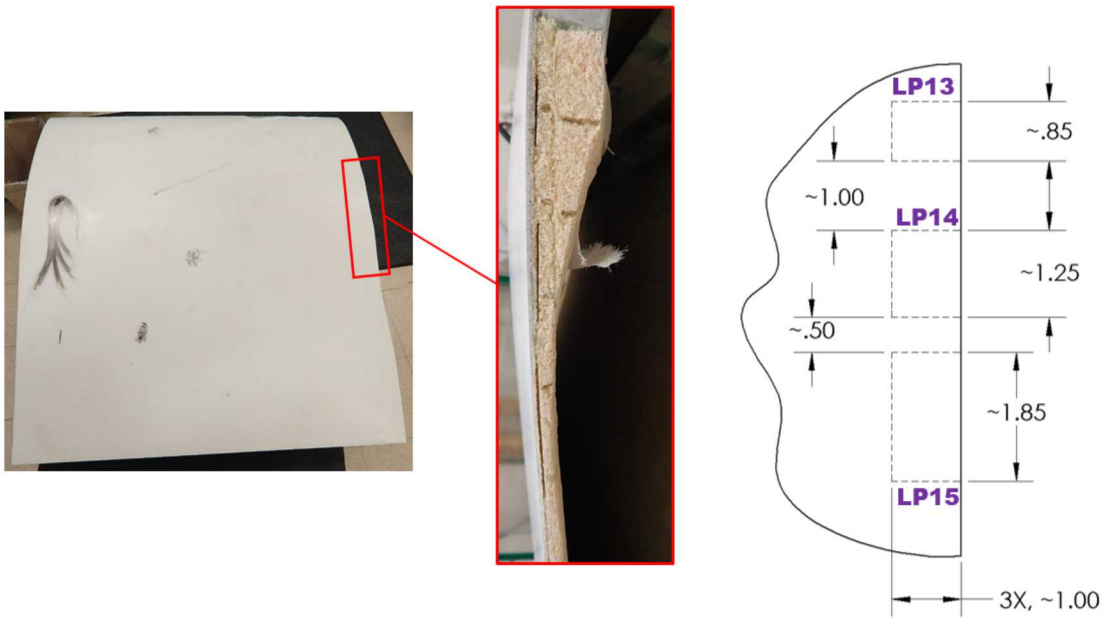

Figure 3-34: Wind Blade Visual Test Specimen FF-V2
Low Pressure Side Flaws Used to Assess the Subsurface Damage Detection of IR Inspections

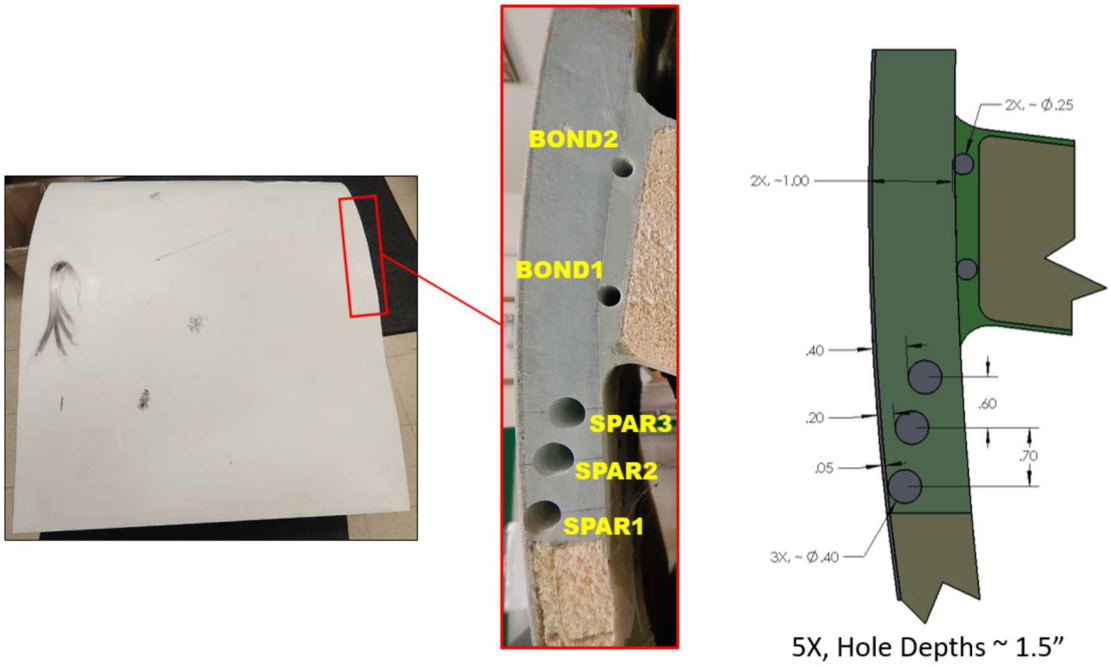

Figure 3-35: Wind Blade Visual Test Specimen FF-V2
Low Pressure Side UT & IR Flaws

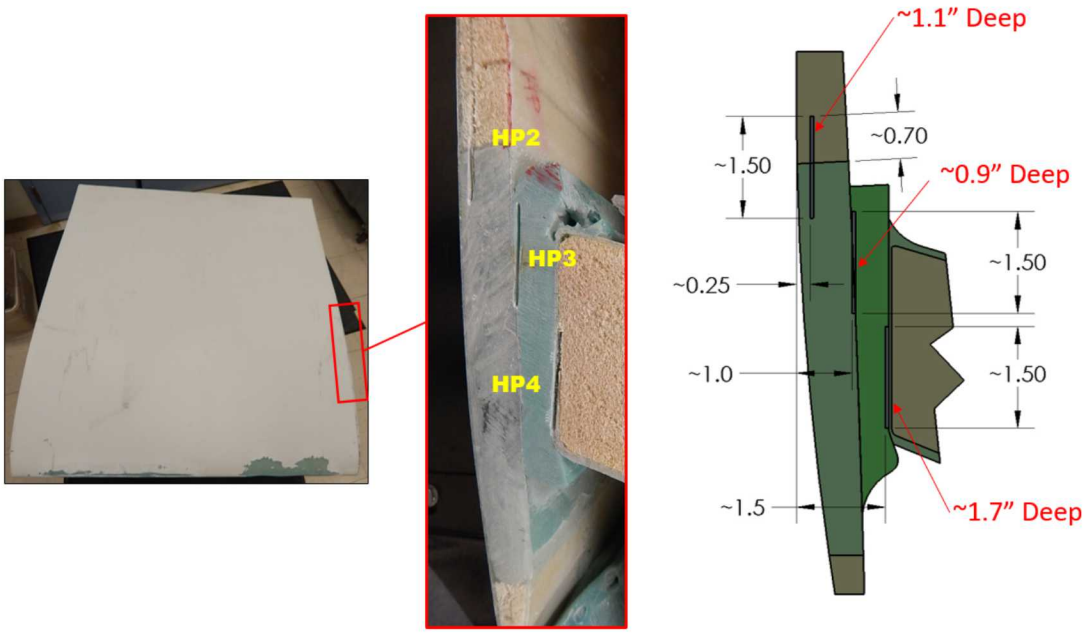

Figure 3-36: Wind Blade Visual Test Specimen FF-V2
High Pressure Side UT & IR Flaws

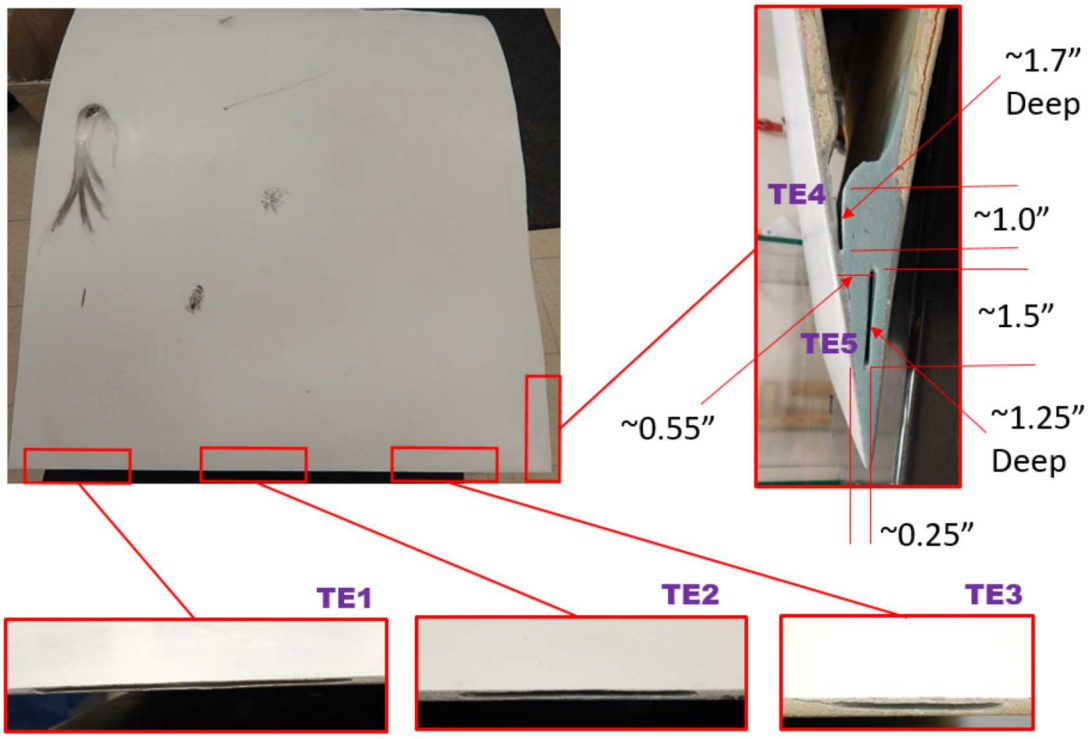

Figure 3-37: Wind Blade Visual Test Specimen FF-V2
Trailing Edge Flaws

3.3. References

3.1 Berry, D., Ashwill, T. "Design of 9-Meter Carbon-Fiberglass Prototype Blades: CX-100 and TX-100," SAND07-0201.

3.2 Maniaci, D., “Leading Edge Erosion: Measurement and Modeling Campaigns,” Sandia Report, SAND2016-8898, August 2016.

THIS PAGE INTENTIONALLY LEFT BLANK

4. DESCRIPTION OF THE NONDESTRUCTIVE INSPECTION METHODS EVALUATED FOR DRONE-DEPLOYED INSPECTIONS

As part of Sandia's Blade Reliability Collaborative work for the DOE, Sandia determined which NDI methods are currently best suited for wind blade inspections [4.1]. The following sections provide a brief technical overview of each of these inspection techniques. In addition to the NDI methods that were previously assessed by Sandia, acoustic beamforming was reviewed based on promising work performed by UMASS Lowell [4.19]. The overviews of these NDI methods provide a background for the trade study conducted in Section 5.

Additionally, a number of up-and-coming NDI techniques were identified in Sandia's previous work (i.e., Lock-In Thermography, Millimeter Wave Inspection, Oblique Incident Ultrasonics, and Terahertz Imaging). Due to the time constraints of this project and the need to select a NDI method with a high level of technology readiness, these methods are not included in this report. However, SkySpecs should continue to monitor these NDI methods for potential future applications.

4.1. Ultrasonics

4.1.1. Pulse-Echo Single-Element and Phased/Linear Array Ultrasonics

Conventional ultrasonic transducers for NDI commonly consists of either a single active element that both generates and receives high frequency sound waves, or two paired elements, one for transmitting and one for receiving. Phased array probes, on the other hand, typically consist of a transducer assembly with 16 to as many as 256 small individual elements that can each be pulsed separately. A phased array system will also include a sophisticated computer-based instrument that is capable of driving the multi-element probe, receiving and digitizing the returning echoes, and plotting that echo information in various standard formats. Unlike conventional flaw detectors, phased array systems can sweep a sound beam through a range of refracted angles or along a linear path, or dynamically focus at a number of different depths, thus increasing both flexibility and capability in inspection setups.

In Pulse-Echo Ultrasonic (PE UT) inspections, short bursts of high frequency sound waves are introduced into materials for the detection of surface and subsurface flaws in the material. Ultrasonic test equipment usually operates in the range of 200KHz to 25 MHz. The speed with which the sound waves travel through a material is dependent on the composition and density of the material. The sound waves travel through the material with some attendant loss of energy (attenuation) and are reflected at interfaces. The reflected beam is displayed and then analyzed to define the presence and location of flaws. Ultrasonic inspection methods currently provide the best option for inspecting wind blades due to its exceptional depth of penetration, signal resolution and wide variation in deployment options. This section describes the customized UT inspection methods and hardware that were developed and deployed by Sandia Labs to optimize wind blade NDI.

A-Scan Mode - Ultrasonic testing involves one or more of the following measurements: time of wave transit (or delay), path length, frequency, phase angle,

amplitude, impedance, and angle of wave deflection (reflection and refraction). In conventional Pulse-Echo Ultrasonics (PE UT), pulses of high frequency sound waves are introduced into a structure being inspected. A-Scan signals represent the response of the stress waves, in amplitude and time, as they travel through the material. As the waves interact with defects or flaw interfaces within the solid and portions of the pulse's energy are reflected back to the transducer, the flaws are detected, amplified and displayed. The interaction of the ultrasonic waves with defects and the resulting time vs. amplitude signal produced depends on the wave mode, its frequency and the material properties of the structure. Flaw size can be estimated by comparing the amplitude of a discontinuity signal with that of a signal from a discontinuity of known size and shape. Flaw location (depth) is determined from the position of the flaw echo along a calibrated time base. In the pitch-catch UT method, one transducer introduces a pressure wave into the specimen and a second transducer detects the transmitted wave. A complex wave front is generated internally in the material as a result of velocity characteristics, acoustical impedance, and thickness. The time and amount of energy is affected by the changes in material properties, such as thickness, disbonds, and discontinuities. The mechanical vibration (ultrasound) is introduced into the specimen through a couplant and travels by wave motion through the specimen at the velocity of sound. If the pulses encounter a reflecting surface, some or all of the energy is reflected and monitored by the transducer. The reflected beam, or echo, can be created by any normal or abnormal (flaw) interface. Complete reflection, partial reflection, scattering, or other detectable effects on the ultrasonic waves can be used as the basis of flaw detection.

In most pulse-echo systems, a single transducer acts alternately as the sending and receiving transducer. If the pulses encounter a reflecting surface, some or all of the energy is reflected and monitored by the transducer. Figure 4-1 shows a schematic of the pulse-echo technique. It shows the interaction of UT waves with various interfaces within a structure and the corresponding A-scan waveforms that are displayed on an ultrasonic inspection instrument. Complete reflection, partial reflection, scattering, or other detectable effect on the ultrasonic waves can be used as the basis of flaw detection. In addition to wave reflection, other variations in the wave that can be monitored include: time of transit through the test piece, attenuation, and features of the spectral response [4.7, 4.8]. The degree of reflection depends largely on the physical state of the materials forming the interface. Cracks, delaminations, shrinkage cavities, pores, disbonds, and other discontinuities that produce reflective interfaces can be detected.

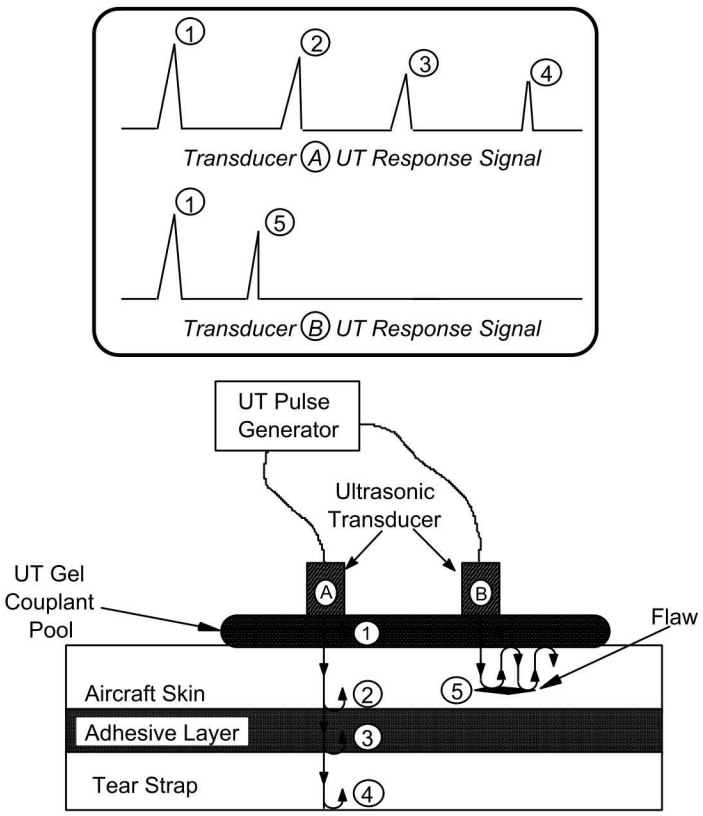

Figure 4-1: Schematic of Pulse-Echo Ultrasonic Inspection and A-Scan Signal Showing Reflection of UT Waves at Assorted Interfaces

C-Scan Mode: Use of UT Scanning Technology - It is sometimes difficult to clearly identify flaws using ultrasonic A-Scan signals alone. Small porosity pockets commonly found in composites, coupled with signal fluctuations caused by material nonuniformities can create signal interpretation difficulties. Significant improvements in disbond and delamination detection can be achieved by taking the A-scan signals and transforming them into a single C-scan image of the part being inspected. C-scans are two-dimensional images (area maps) produced by digitizing the point-by-point signal variations of an interrogating sensor while it is scanned over a surface. A computer converts the point-by-point data into a color representation and displays it at the appropriate point in an image. Specific "gates" can be set within the data acquisition software to focus on response signals from particular regions within the structure. C-scan area views provide the inspector with easier-to-use and more reliable data with which to recognize flaw patterns. This format provides a quantitative display of signal amplitudes or time-of-flight data obtained over an area. The X-Y position of flaws can be mapped and time-of-flight data can be converted and displayed by image processing-equipment to provide an indication of flaw depth. A variety of PC-based manual and automated scanning devices can provide position information with digitized ultrasonic signals [4.9].

In the basic C-scan system, shown schematically in Figure 4-2, the scanning unit containing the transducer is moved over the surface of the test piece using a search pattern of closely spaced parallel lines. A mechanical linkage connects the scanning unit to X-axis and Y-axis position indicators which feed position data to the computer. The echo signal is recorded, versus its X-Y position on the test piece, and a color coded image is produced from the relative characteristics of the sum total of signals received. A photograph of an automated (motorized) scanner, the Boeing MAUS system, inspecting an aircraft fuselage section is shown in Figure 4-3. The entire ultrasonic C-Scan device is attached to the structure using suction cups connected to a vacuum pump. The unit is tethered to a remotely located computer for control and data acquisition. Figure 4-4 shows a comparison of A-scan signals, from damaged and undamaged portions of a composite structure that were produced by the pulse-echo ultrasonic inspection method. Note the clear reflection peak produced by uninterrupted signal travel to the back wall in the "undamaged" A-scan signal. Compare this to the A-scan signal from the "damaged" region where the amplitude of the back wall signal is decreased and a new intermediate peak (reflection) is observed. Both of these A-scan changes indicate the presence of damage or other anomaly.

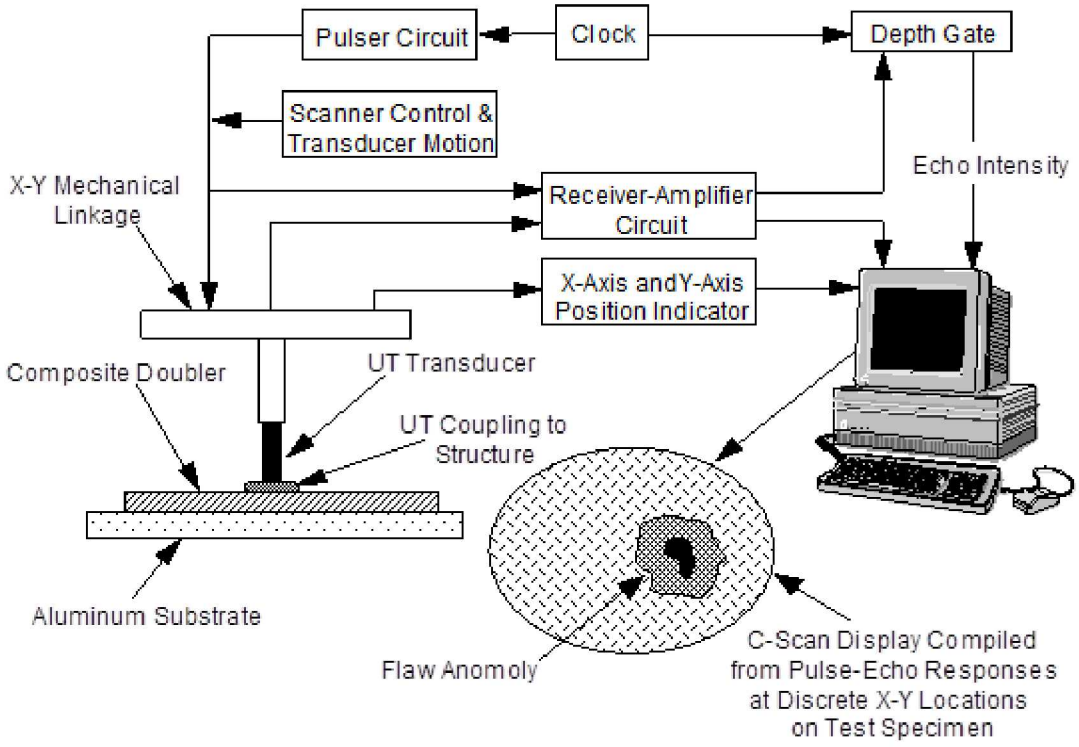

Figure 4-2: Schematic of C-Scan Setup for Pulse-Echo Ultrasonic Inspection

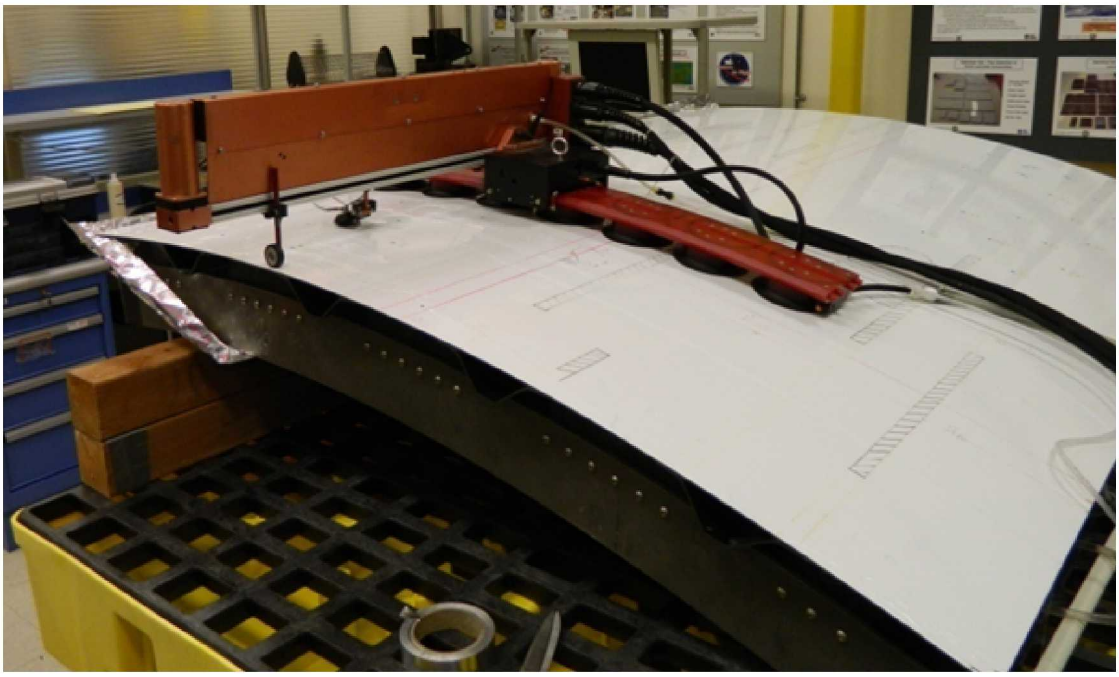

Figure 4-3: MAUS Automated Ultrasonic Scanning System

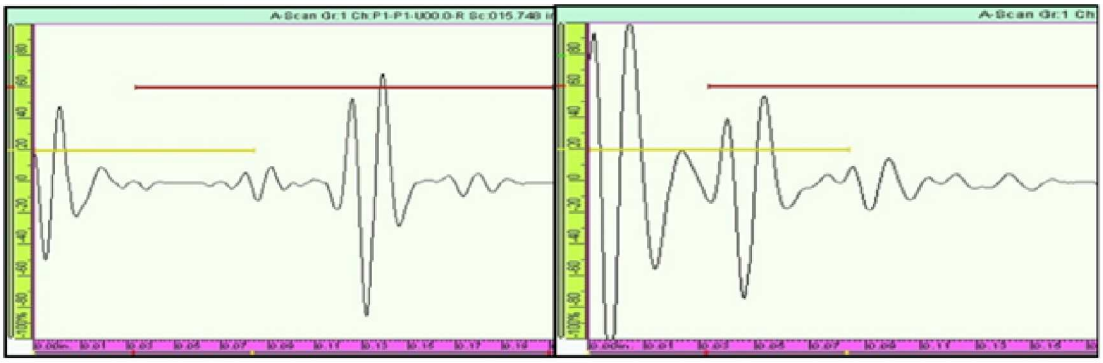

a) b)

Figure 4-4: Sample Ultrasonic Signals Generated from: a) Structure Without Damage and b) Structure With Damage

Figure 4-5 shows a sample C-scan image (based on amplitude) from a pulse-echo UT inspection of a composite fuselage structure containing stringers and frame shear ties. Dark spots and irregularly-shaped regions of nonuniform color indicate the presence of impact damage in this panel. The value of using two-dimensional color coding, stemming from the sum total of the A-scan signals, to identify and size composite flaws is evident in this C-scan image. The discussion below describes the use of both A-scan and C-scan data to inspect wind turbine blades.

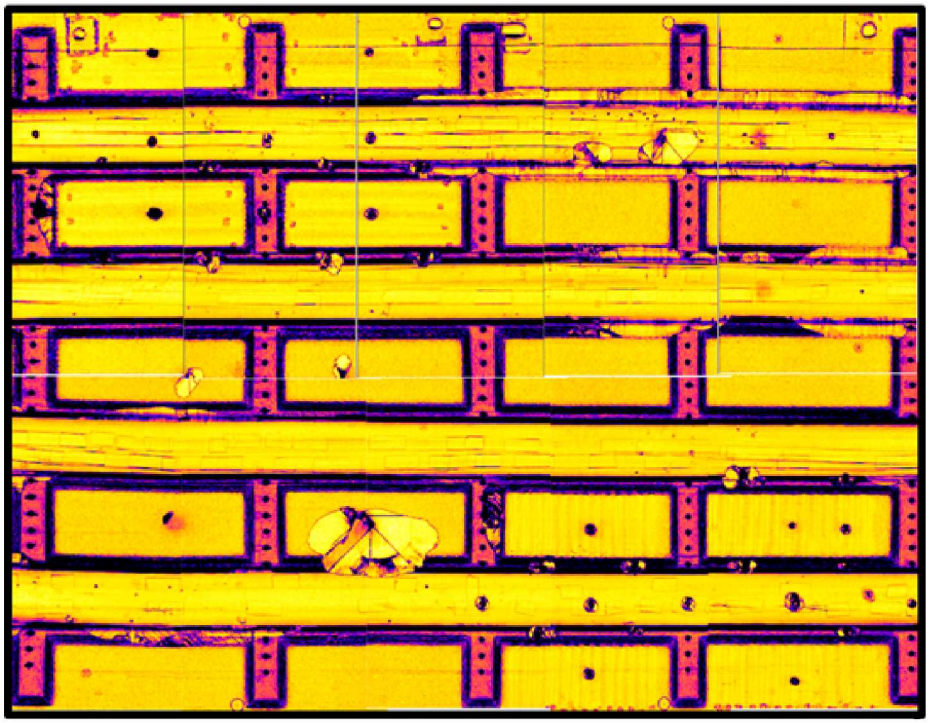

Figure 4-5: Sample C-Scan produced by an Automated Ultrasonic Scanning Device

Phased Array Ultrasonics (PA-UT) involves the use of multiple signals from a contained series of transducers (phased arrays) to produce diagnostic images in the form of ultrasonic C-scans. Conventional ultrasonic transducers for NDI commonly consist of either a single active element that both generates and receives high frequency sound waves, or two paired elements, one for transmitting and one for receiving. Phased array probes, on the other hand, typically consist of a transducer assembly with 16 to as many as 256 small individual elements that can each be pulsed separately. A phased array system will also include a sophisticated computer-based instrument that is capable of driving the multi-element probe, receiving and digitizing the returning echoes, and plotting that echo information in various formats. Unlike conventional flaw detectors, phased array systems can sweep a sound beam through a range of refracted angles or along a linear path, or dynamically focus at a number of different depths, thus increasing both flexibility and capability in inspection setups.

PA-UT operation is similar to single-element UT transducers, however, the simultaneous use of multiple sensors allows for rapid coverage and two-dimensional images from which to assess structural integrity. A linear array of ultrasonic sensors is placed within a single, scanning probe. The width of the linear probe array determines the swath of the inspection "scan" as the probe is moved along the surface. A compression wave beam is electronically scanned along the array at pulse repetition frequencies in excess of 10 KHz. The response of each individual sensor is monitored and assessed using the ultrasonic wave analysis approaches described above. High speed pulsing combined with rapid data capture permits the array to be quickly moved

over the structure. The individual responses from each UT sensor are integrated to produce a real-time, C-scan image of the covered area. An example of a linear array UT inspection device deployed by Sonatest in a rolling wheel arrangement is shown in Figure 4-6. The physics of how the ultrasonic array works is depicted in Figure 4-7. By carefully controlling the generation of UT signals and data acquisition from select elements in a phased array, it is possible to produce customized focusing of the array to improve the sensitivity of the inspection. Electronic focusing permits optimizing the beam shape and size at the expected defect location, thus further optimizing probability of flaw detection. The ability to focus at multiple depths also improves flaw sizing of critical defects in volumetric inspections. Focusing can significantly improve signal-to-noise ratio in challenging applications, and electronic scanning across many groups of elements allows for C-Scan images to be produced very rapidly. The main difference between a phased array and a linear array is that linear arrays aren't capable of steering the sound beam at different angles or focusing the beam. Thus, the sound waves stay parallel to each other regardless of the depth.

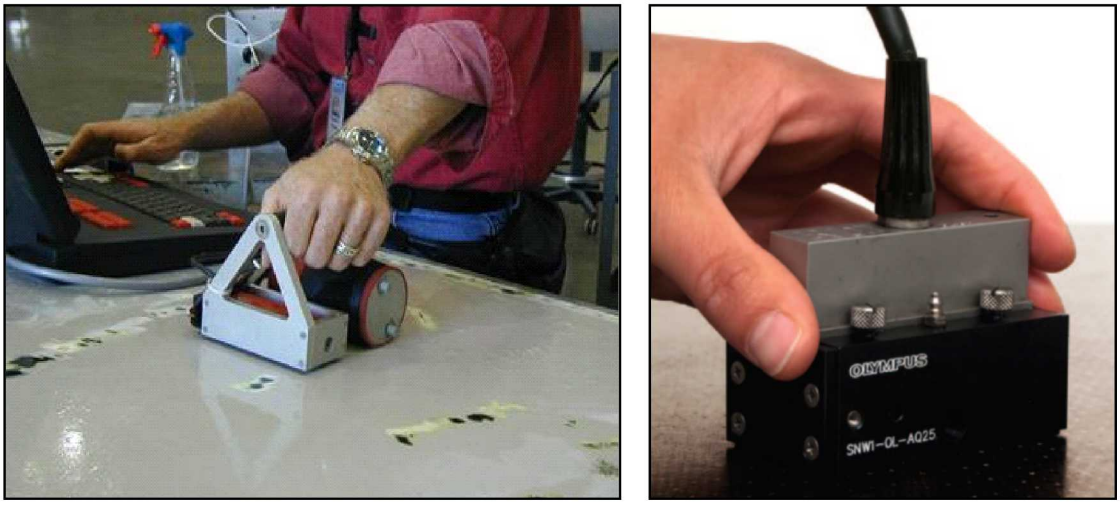

Figure 4-6: Phased Array UT Deployed in Rolling Wheel Mechanism (left) and Contained in a Single Probe Housing (right)

Associated with this effort, a series of new and unique phased array probe housings were designed and fabricated to improve field deployment. The custom probe housing facilitates phased array inspections through a wide range of material thicknesses, adjusts for slight contours, maximizes UT signal strength and makes deploying a phased array probe on blades more effective than conventional housings. Various probe offset designs (water column heights) were studied in order to eliminate the confounding effects of signal harmonics which are prevalent in thick composite structures.

To provide a baseline understanding of the current ultrasonic inspection method used in wind blades, Figure 4-8 and Figure 4-9 present some of the basic, building-block UT signals that are used to conduct the wind blade inspections. Figure 4-8 is a

schematic of a bonded joint between a spar cap and a shear web flange. This particular bonded joint has some adhesive squeeze-out. Figure 4-8 also shows an ultrasonic transducer moving over four different construction regions in a typical blade which includes: 1) the spar cap laminate alone, 2) the adhesive squeeze out adjacent to the near side of the bonded shear web joint, 3) the adhesive thickness at the spar cap-to-shear web joint, and 4) the adhesive squeeze out adjacent to the far side of the bonded shear web joint.

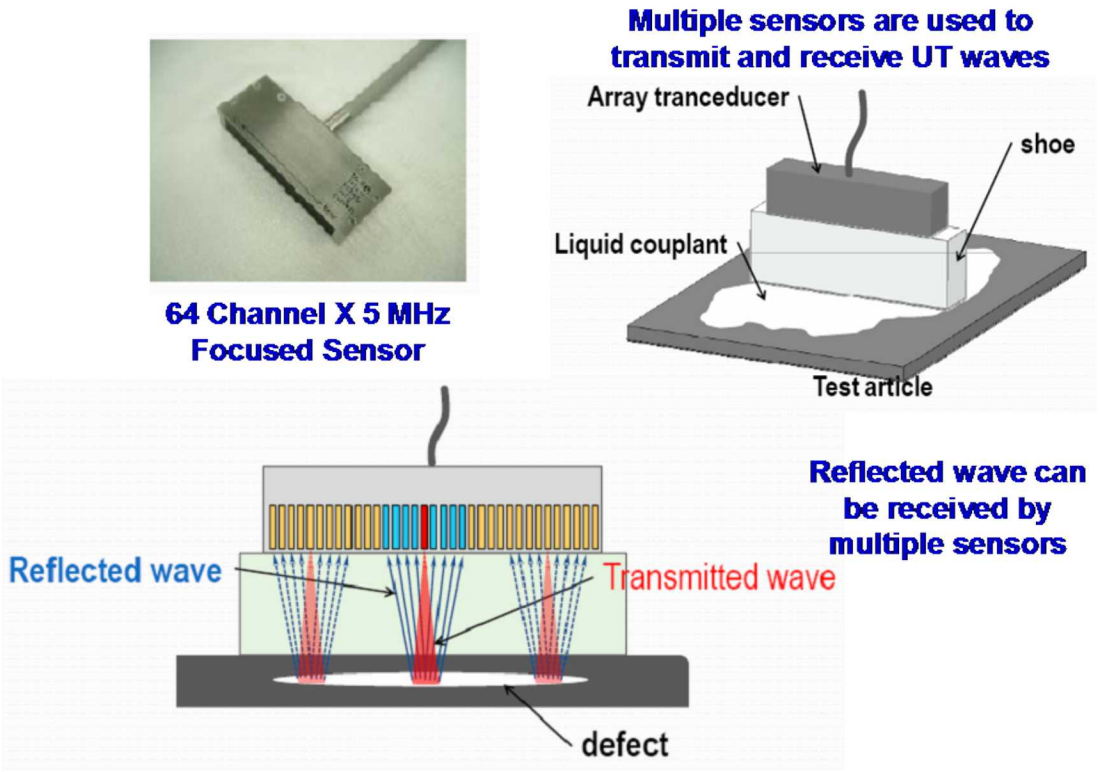

Figure 4-7: Schematic Showing the Operation of an Ultrasonic Array – Contains Multiple UT Elements in a Single Transducer Which Allows for the Generation and Acquisition of Multiple UT Signals

Figure 4-8 also depicts a scenario where the adhesive paste bulges out and can be detected using ultrasonics. It also shows the UT A-scan signals that are produced when a transducer is placed over various regions of the bond line. These distinct signals can be used to detect the presence of the desired adhesive bond width. The resulting, expected A-scan signals that are generated at each of these points are also shown to demonstrate critical signal interpretation needs. In addition, gate settings can be selected based on these desired signals such that deviations from the norm can be detected and imaged in UT C-scans. Many of the existing, routine inspections tend to focus on the upper and lower portions of the bond line and use the presence of adhesive squeeze-out to infer a successful bonded joint. Figure 4-9 provides another example of UT signals generated from different depths of penetration in the blade

structure. Several different phased array UT devices will now be described in order to introduce some different deployment approaches which may lend themselves quite well to wind blade inspections.

Olympus OmniScan Phased Array UT System - The OmniScan device, shown in Figure 4-10, is manufactured by Olympus. The one-line scan capability of the OmniScan allows inspectors to collect data in one axis and visualize it using the top view. This feature is easy to set up and allows the data to be played back after the acquisition for offline analysis and reporting. Data can be encoder- or time-based and phased array images can be displayed in real time. Transducers are available with up to 128 elements. The OmniScan device can be operated in manual mode or can be connected to an X-Y scanner to automate the inspection of large areas. The hardware and equipment set-up used for the OmniScan phased array UT inspections were:

- 1.5 MHz, 42 and 64 element phased array probes
- Custom ABWX1935 water fed housing (multiple housing used for full experiment)
- OmniScan MX2 unit (module 16/128)
- Software MXU 3.0R2
- Mini-wheel encoder and X-Y glider (manual X-Y scanner)
- CFU-05 water pump
- Probes/Wedges: Three probe and wedge combinations were used with the majority of the tests performed with the two large aperture combinations. The 25 mm water column (WC) shoe used a contained water column to provide the UT coupling between the probe and the part. The contact wedge used a solid block of an impedance-matching plastic material with a thin film of base water to provide the offset and coupling to the part. The Aqualene wedge used a delay line block made from Aqualene along with a wetted surface to provide the offset and coupling to the part. The details of these shoe designs are discussed in Chapter 4.

Figure 4-11 and Figure 4-12 show the OmniScan equipment set-up and deployment for phased array UT inspections of wind blade specimens while Figure 4-12 and Figure 4-13 highlight the various features of the UT transducers and the shoes or wedges used to optimize the NDI signals. Ultrasonic phased array technology, along with the widely adaptable range of probe housings and deployment options were shown to have strong flaw detection capabilities in multiple wind turbine blade structures. These include both thin and thick fiberglass spar cap laminates and bond line interfaces. Figure 4-14 and Figure 4-15 show sample results produced by the OmniScan from the inspection of carbon laminate test specimens that contain engineered flaws. Damage in the parts are shown in the photos and schematics while the accompanying C-scan images show the ability of the inspection method and equipment to detect the flaws.

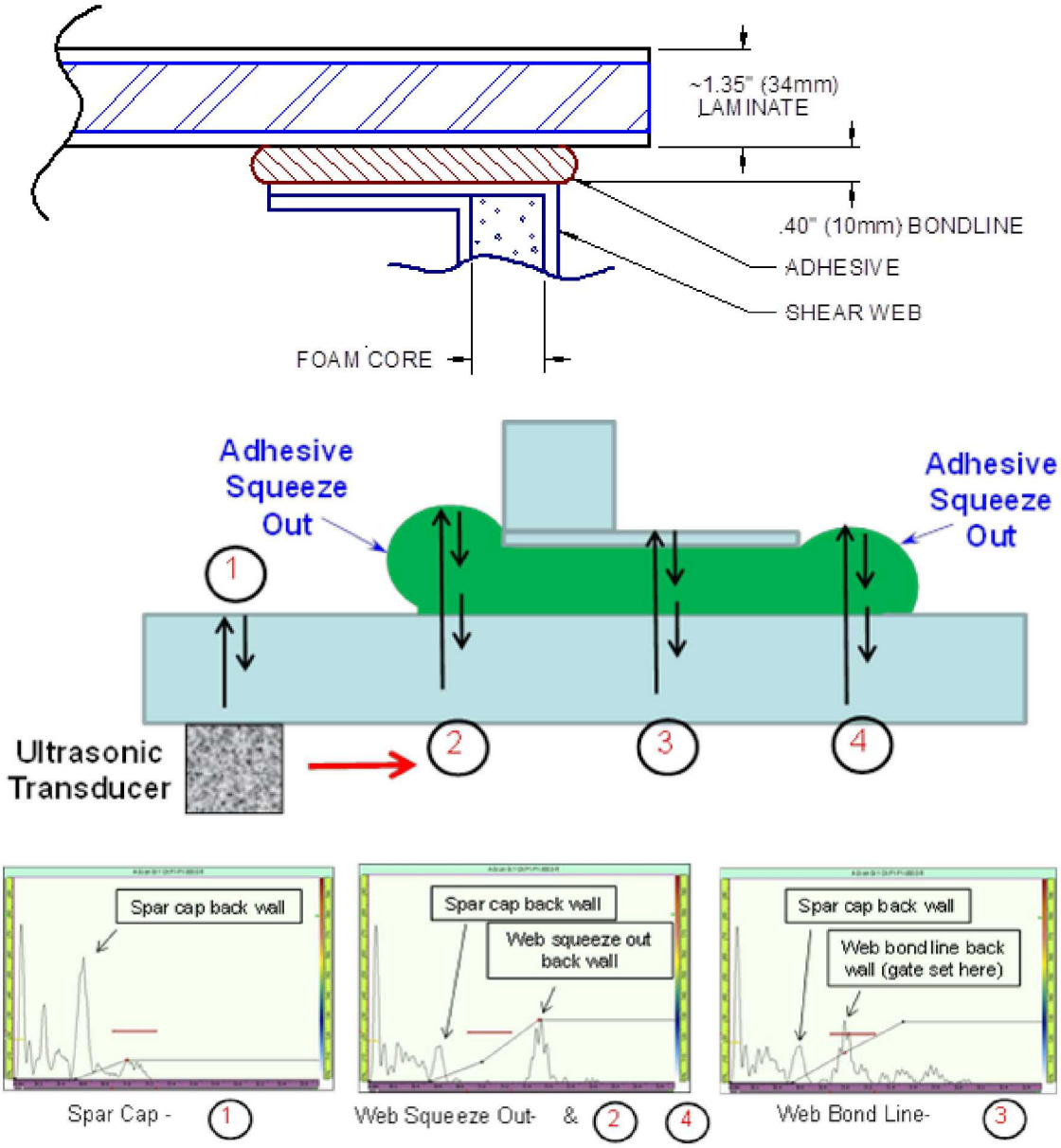

Figure 4-8: Typical Bond Joint Configuration Used in NDI Feedback and NDI Reference Standard Specimens

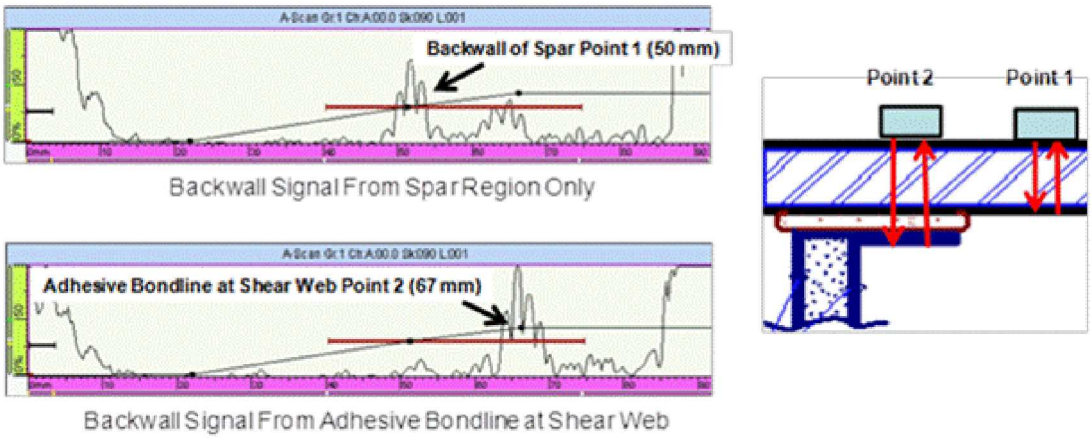

Figure 4-9: Schematic of Two Different Depth of Penetration Regions in a Blade and the Resulting A-scan Signals Generated for Each Thickness

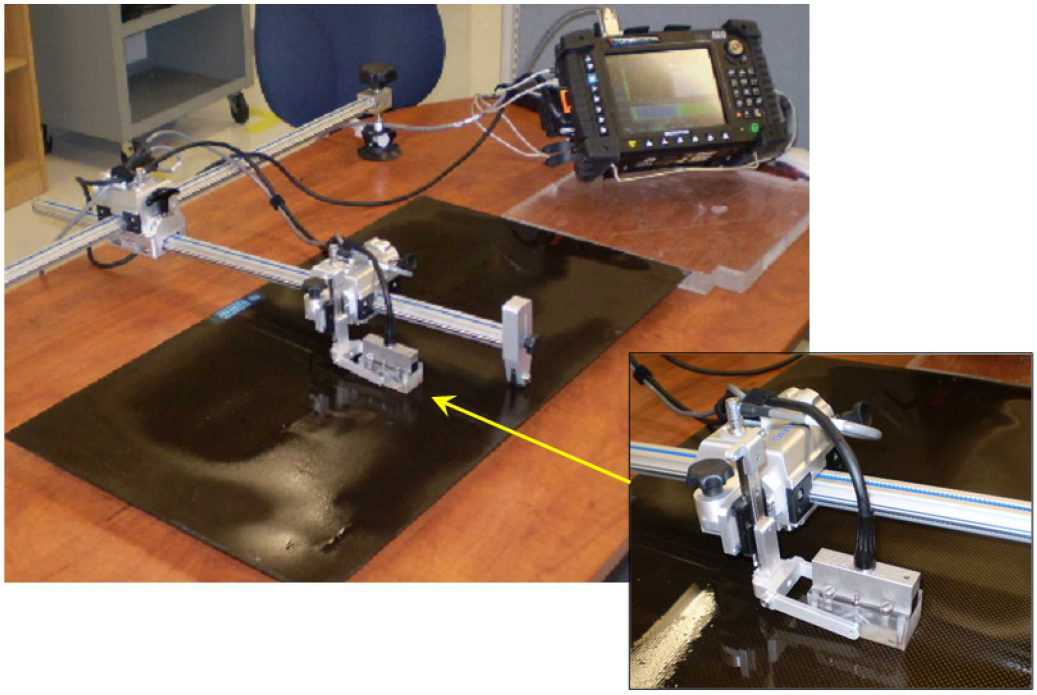

Figure 4-10: Olympus OmniScan Device with a 16:128 Phased Array Module

Figure 4-11: Phased Array Ultrasonics Inspection with OmniScan System

Figure 4-12: Phased Array Probes and OmniScan Deployment on Wind Blade NDI Specimens

	Configuration 1 Large aperture	Configuration 2 Large Aperture	Configuration 3 Small Aperture
Probe	1.5L42 (XAAB-10011)	1.5L42 (XAAB-10118)	1.5L64-I4
Wedge	25mm water column (ABWX1875)	Contact wedge (ABWX1935)	Aqualene wedge (SNW1-0L-AQ25)

	Configuration 1	Configuration 2	Configuration 3
Probe Name	1.5L42	1.5L42	1.5L64-I4
Part #	XAAB-10118	XAAB-10011	1.5L64-I4
Housing	Custom	Custom	I4
Frequency	1.5MHz	1.5MHz	1.5MHz
Number of elements	42	42	64
Pitch	2.8mm	2.8mm	1mm
Elevation	26mm	26mm	7mm
		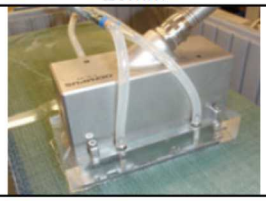	

Figure 4-13: Summary of Prototype Phased Array Probes and Wedges Used with the OmniScan Device to Conduct the Phased Array UT Inspections

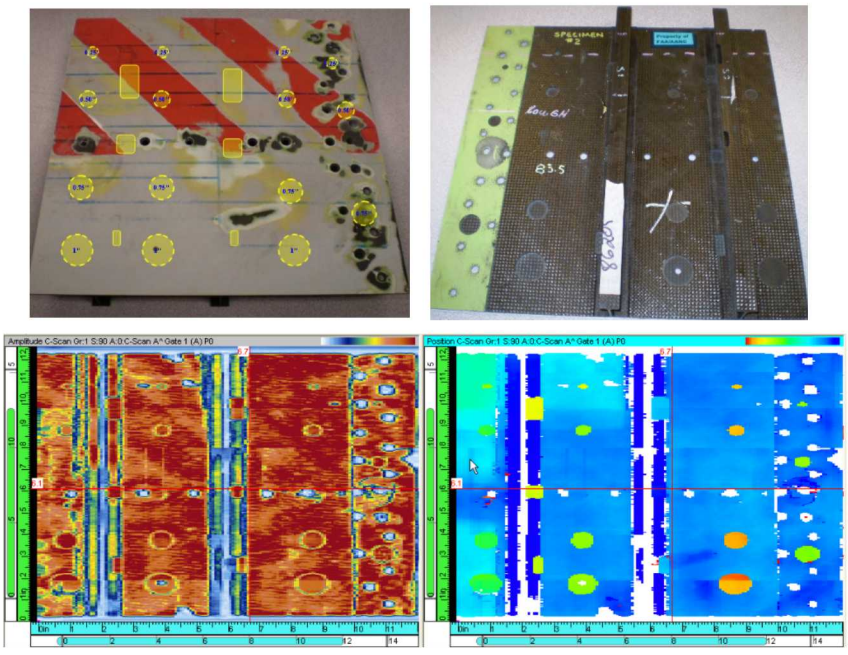

Figure 4-14: Amplitude (right) and Time of Flight (left) Data Produced by OmniScan Inspection of Composite Laminate Aircraft Panel with Flaw Profile as Shown

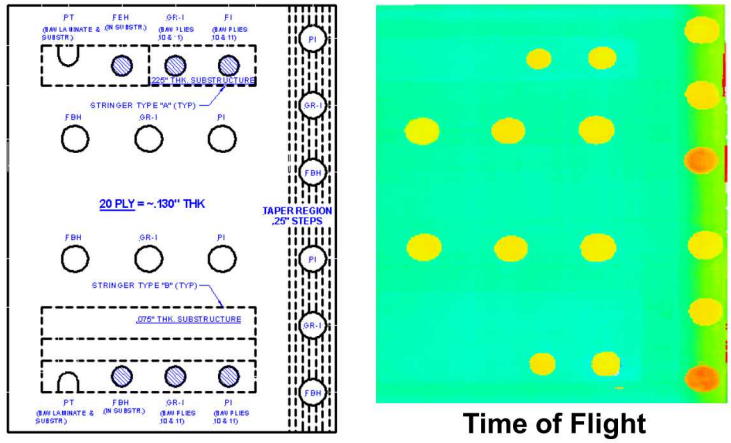

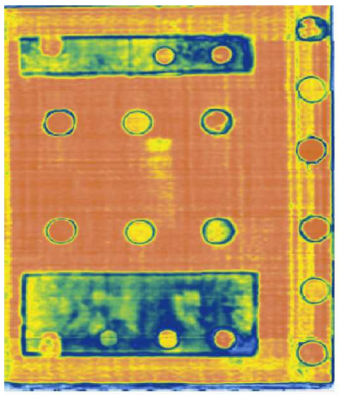
Amplitude

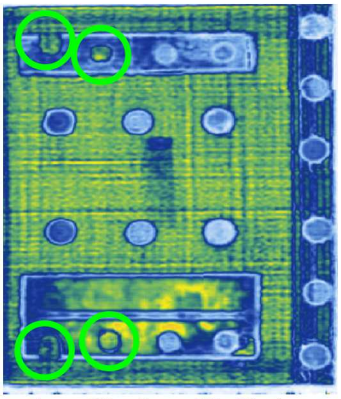
Amplitude with Gate
in Substructure
(deeper flaw detection)

Figure 4-15: C-Scan Images Produced by OmniScan Phased Array UT Inspection of 20 Ply Composite Laminate Feedback Panel with the Flaw Profile as Shown

Sample Inspection Results Demonstrating Capabilities of Phased Array UT – This section presents results from OmniScan PA-UT inspections conducted on several Sandia specimens from the Wind Blade Test Specimen Library. Figure 4-16 and Figure 4-17 show the details of an adhesive step wedge that includes a section with adhesive of different thicknesses and a section where the stepped adhesive is bonded to a composite laminate (spar cap). This is an example of a specimen produced to study specific capabilities of NDI methods. Inspections of this specimen allow for the assessment of the ability of NDI to quantify adhesive thickness which would allow it to determine if an adhesive layer is outside of a required thickness range (i.e. too thick or too thin). Figure 4-18 shows two different characterizations of this NDI test specimen. The upper graph plots the UT velocity of the material. It is fairly consistent across the various thicknesses which ensures that the adhesive properties are consistent. The lower graph plots the signal attenuation through the various thicknesses. As expected, the relationship between the bond line thickness and the associated attenuation level is linear.

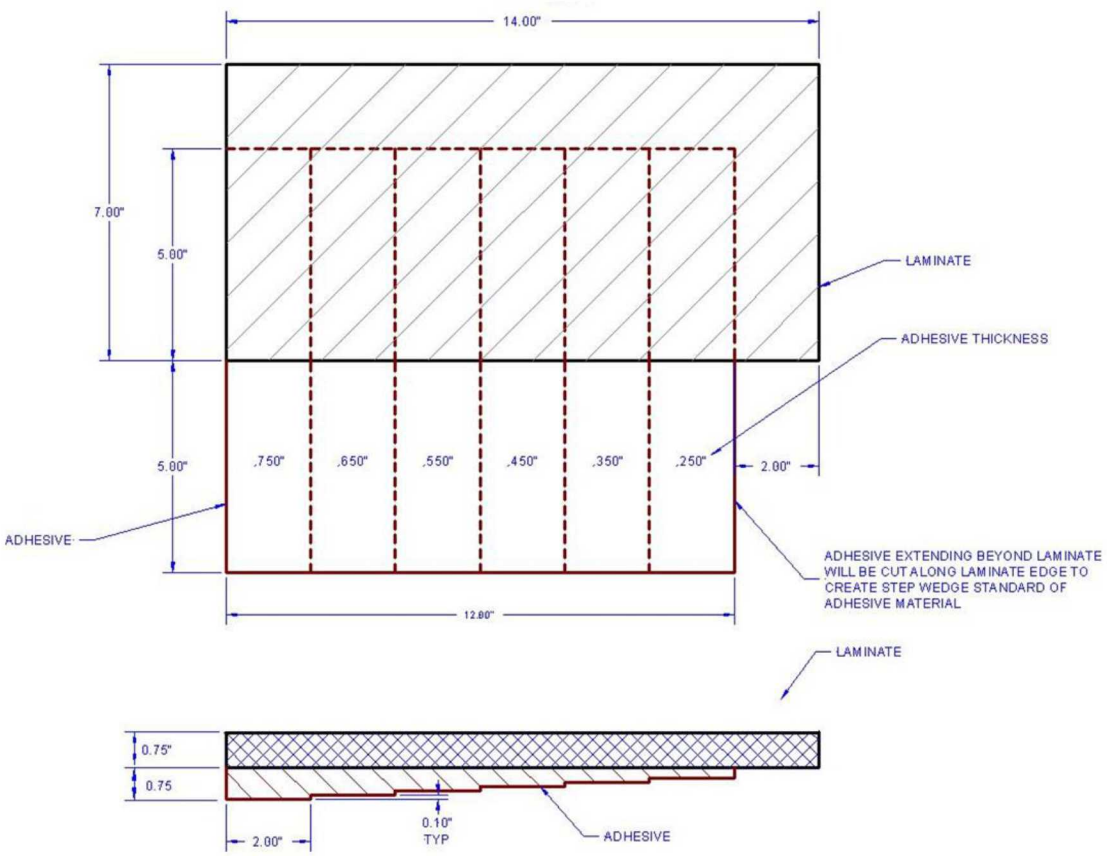

Figure 4-16: Adhesive Step Wedge NDI Reference Standard - Schematic

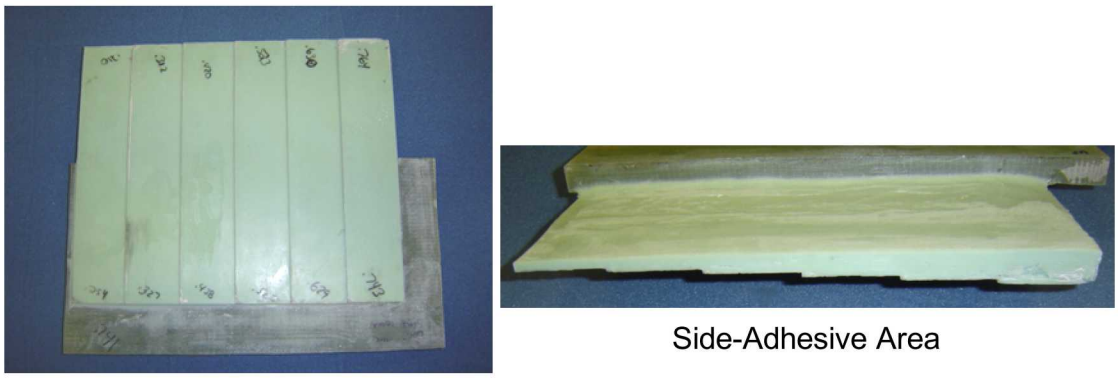

Bottom View

Side-Adhesive Area

Figure 4-17: Adhesive Step Wedge NDI Reference Standard

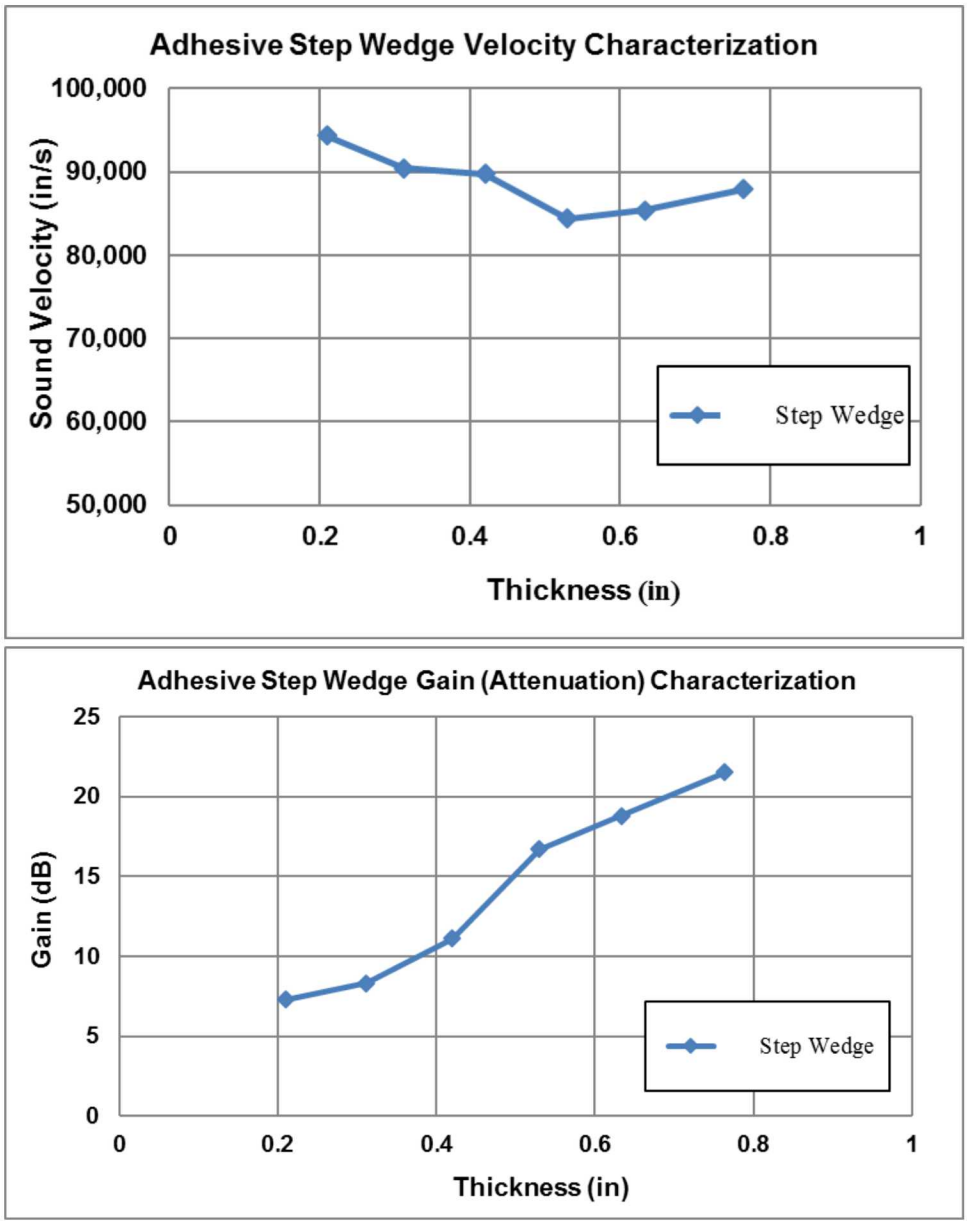

Figure 4-18: Pulse-Echo Ultrasonic Wave Velocity and Attenuation Results Showing Consistency of Adhesive Step Wedge and Linear Relationship Between Bond Line Thickness and Attenuation

Figure 4-19 and Figure 4-20 show a phased array UT inspection deployment and the resulting C-scan image of the various specimen thicknesses. The results show that this inspection method is able to differentiate the various adhesive thicknesses even when inspecting through a thick spar cap laminate. Each bond line thickness is assigned a color code that can then be calibrated to a specific thickness or tight thickness range. Figure 4-21 shows the results from a single element UT inspection of this same specimen. Again, it was possible to differentiate the various adhesive thicknesses and each bond line thickness is assigned a color code in the C-scan that is related to an

adhesive tight thickness range. Figure 4-22 shows the set of A-scan signals generated at each thickness step and the associated shift in the back wall peaks which allow the thickness to be determined.

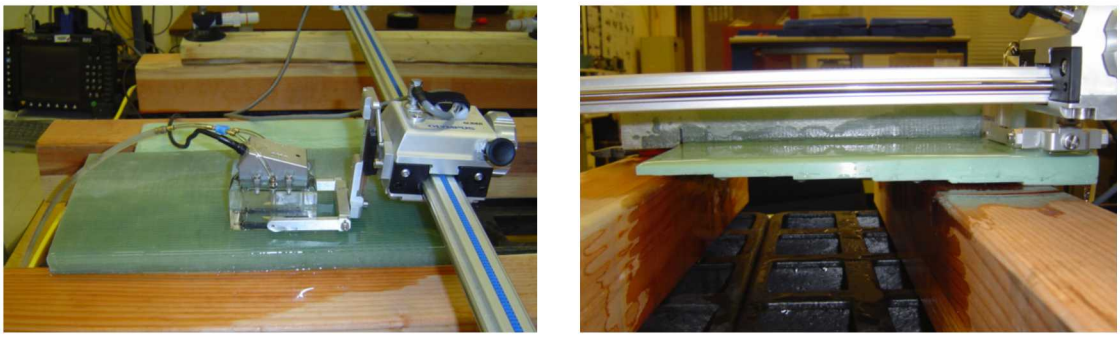

Figure 4-19: Phased Array PE-UT Inspection of Fiberglass Step Wedge Bond Line Specimen Using 1.5 MHz, 16 Element Array and a 40 mm Thick Open Water Box Shoe

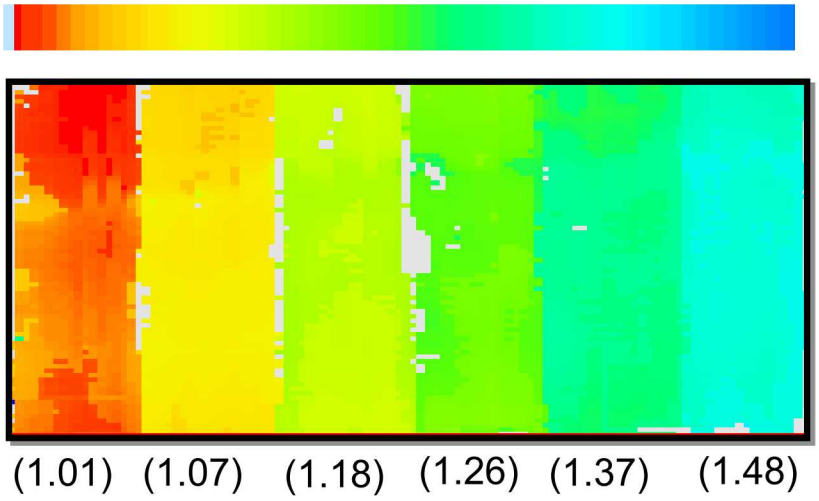

Figure 4-20: Color Coded Time-of Flight C-scan Generated by Phased Array PE-UT Inspection of Fiberglass Step Wedge Bond (OmniScan system with 1.5 MHz phased array probe and 40 mm thick shoe) – Shows Ability of UT to Differentiate the Various Bond Line Thicknesses Beneath the Laminate (labelled below each color segment)

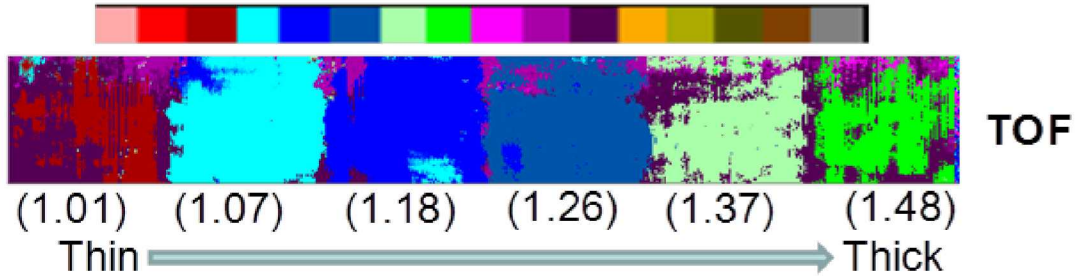

Figure 4-21: Color Coded Time-of Flight C-scan Generated by Pulse Echo UT (MAUS V system with 1 MHz contact probe) – Shows Ability of UT to Differentiate the Various Bond Line Thicknesses Beneath the Laminate (labelled below each color segment)

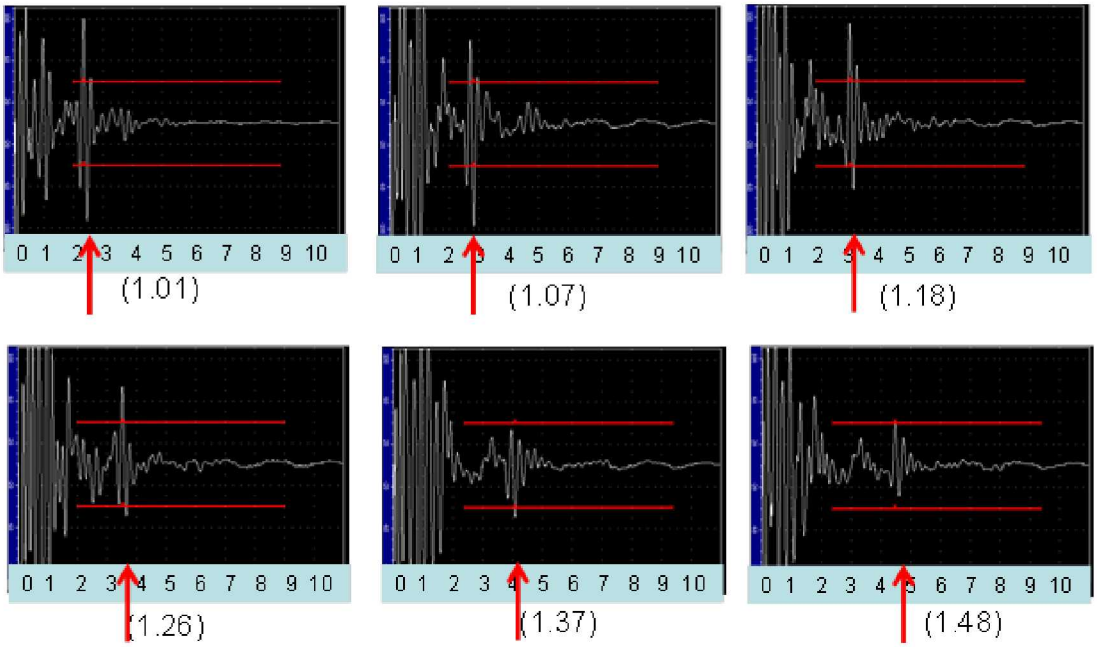

Figure 4-22: A-scan Amplitude Plots Generated by Pulse-Echo UT (MAUS V system with 1 MHz contact probe) – Shows Amplitude Decrease and Time to Back Wall Increase (indicated by red arrow) as Bond Line Thickness Increases

As part of the WBFDE, the OmniScan completed inspections on the NDI Feedback Specimens. Figure 4-23 through Figure 4-25 show the PA-UT results for wind specimen REF-STD-2-127-173-SNL-1 (see [4.19] Figure 3-43 for design drawing). The 25 mm water column on the OmniScan PA-UT device (1.5L42 probe) provided good coupling to the specimen and the needed offset (delay line) to avoid the interference of the harmonic signals. Thus, the 25 mm water column allows for inspecting the adhesive joint on this specimen (between the spar and adhesive and

between adhesive and shear web). Flat bottom holes in spar cap laminate were detected at the various depths and the flat bottom holes in the bonded shear web joint were also detected. It appears that all sizes of the flat bottom holes were detected (difficult to see 75% FBH – 1.0" diameter in bonded shear web joint). Pull tab flaws in laminate at 25% depth and at 75% depth were detected. The pull tabs in the shear web bonded joint, both at the upper and lower adhesive interface, were detected. Figure 4-23 shows the amplitude and B-scan (flaw depth) images produced by a back wall gate ranging from 0.4" to 1.6" in depth. Figure 4-25 shows how the various gate settings can focus the inspections to detect flaws at various depths. The back wall gating worked well for inspecting the laminate for delamination flaws. Alternative gating can be used to specifically look at the adhesive joint. Most indications within the laminate showed up relatively well including the 0.50" diameter FBHs and pillow inserts, especially when gating the off of the back wall of the laminate.

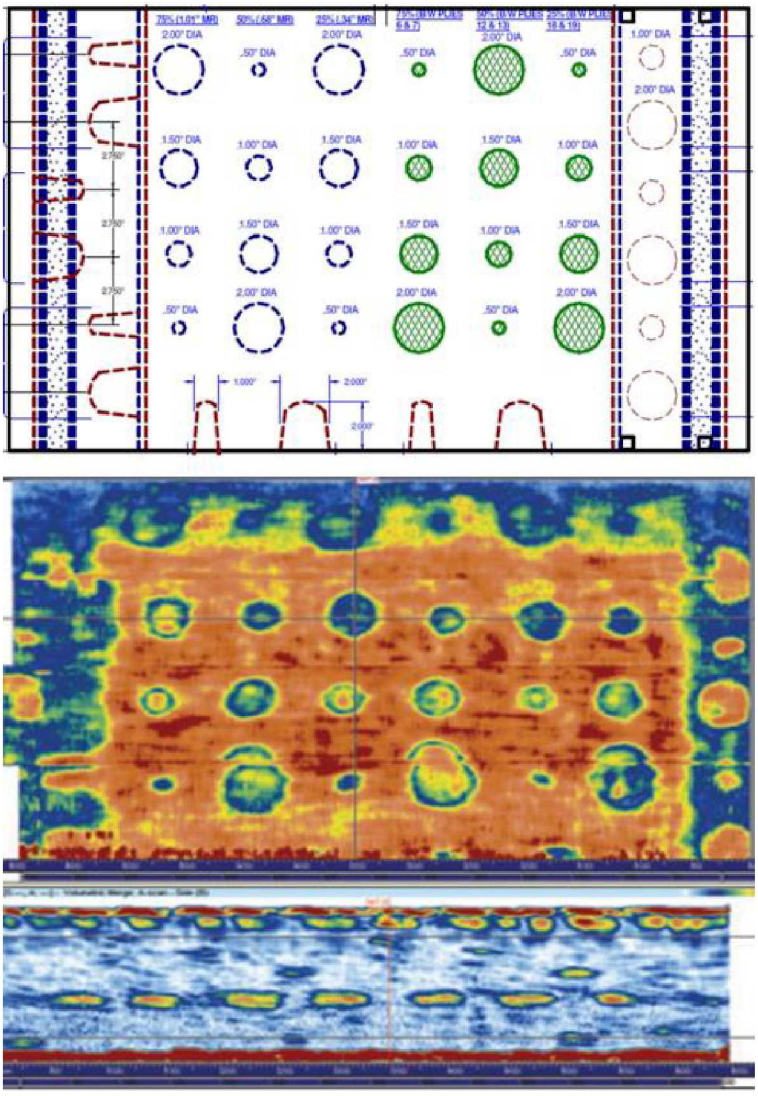

Figure 4-23: OmniScan PA-UT C-Scan of REF-STD-2-127-173-SNL-1 Produced by the 25 mm Water Column Shoe

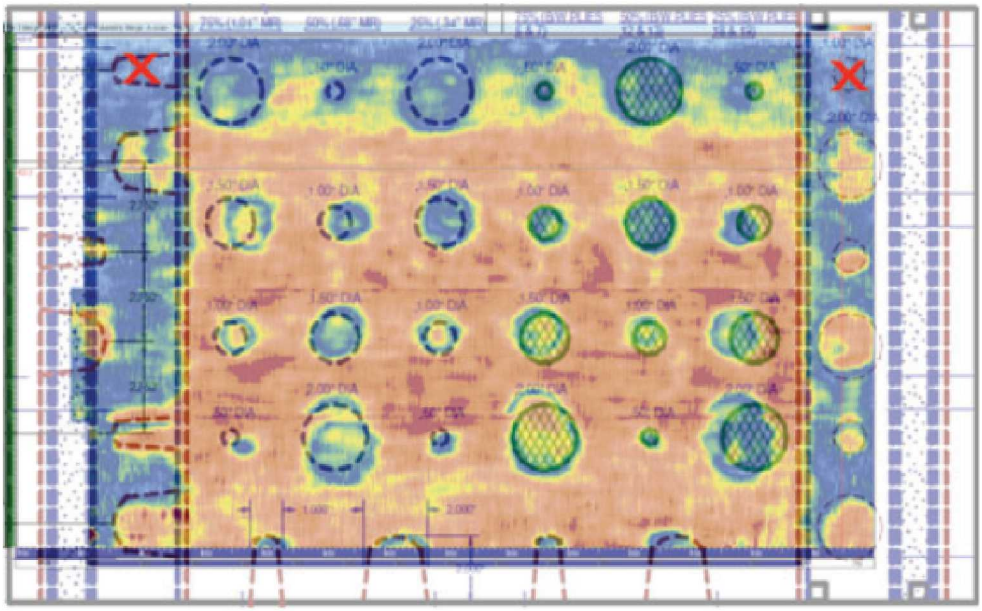

Figure 4-24: Overlay of Flaw profile with PA-UT Image Showing the Two Small Flaws Not Detected by the OmniScan Inspection (Water Column Shoe)

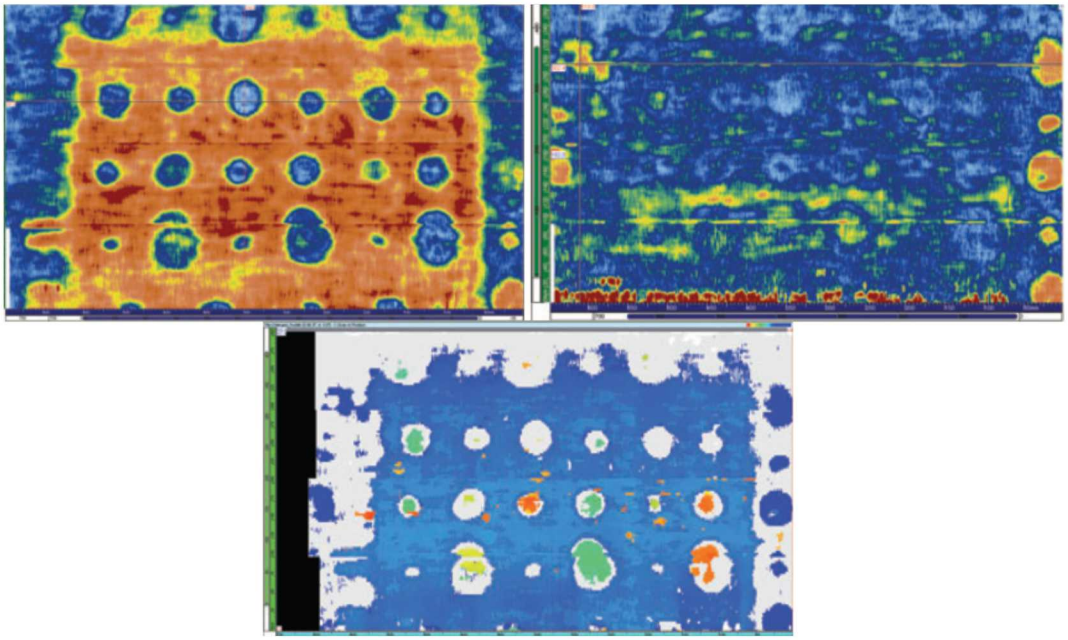

Figure 4-25: OmniScan PA-UT C-Scans of REF-STD-2-127-173-SNL-1 – Gate Set on Back Wall Only (top left), Gate Set Between Back Wall (1.3")

and Wedge Reflection Echo (1.7" depth) (top right) and Time-of-Flight Image (bottom)

The OmniScan PA-UT system was also applied to wind specimen REF-STD-5-154-SNL-1. Specimen REF-STD-5-154-SNL-1 is a sample dedicated to inspecting the adhesive joint between the spar cap and the adhesive. All of the flaws are located at this junction. Figure 7-58 shows the PA-UT inspection results. All flaw types – Pillow Inserts, microballoons and Pull Tabs – were detected. Only the smallest flaws of each type (0.5" or smaller) along the left hand side were not adequately detected. It is assumed that this is due to the very large probe elevation that is not optimal for these flaws.

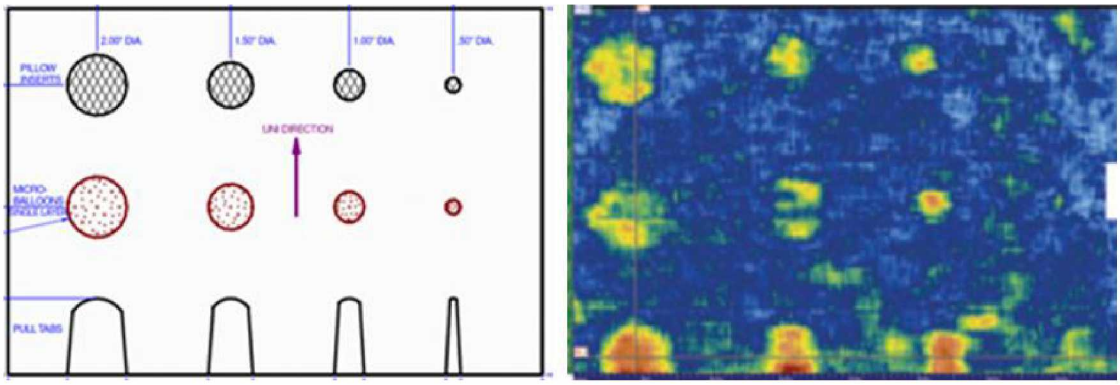

Figure 4-26: OmniScan PA-UT C-Scan of REF-STD-5-154-SNL-1 Produced by the 25 mm Water Column Shoe

Sonatest RapidScan 2 - The RapidScan rolling array WheelProbe was developed by Sonatest and provides a capability for A, B and C-scan inspections. It uses a novel, rubber-coupled sensor array that provides rapid, wide area C-scan data in the field. Powerful gating and evaluation tools are used to ensure proper analysis of the ultrasonic signals. RapidScan 2, shown in Figure 4-27, operates in a pulse-echo mode suitable for inspecting medium to large areas. A water film coupling that can be sprayed onto the inspection surface is used to transmit the UT pulse and return signals from the rolling wheel and back to the linear array transducer housed within the wheel. Multiple scan strips can be assembled to produce images of entire structures such as the horizontal stabilizer image shown in Figure 4-28. The high resolution C-scans, such as those in the examples of Figure 4-29 through Figure 4-31, show time of flight and amplitude data. Both A and B-scans can be simultaneously displayed. The system includes a 128-channel multiplexing pulser/receiver module; data capture electronics and a standard PC laptop, housed in a low-profile plastic enclosure for easy portability. Array WheelProbes incorporate a 64 element linear array (50mm) or 128 element linear array (100mm) with 0.8mm resolution, and a high resolution position encoder. The array WheelProbe provides high quality, high resolution data. Current array probes are available in 1, 2, 5, and 10 MHz to provide a range of resolutions and depth of penetration in thick and highly-attenuative structures.

Figure 4-27: RapidScan UT Rolling Wheel Array Device

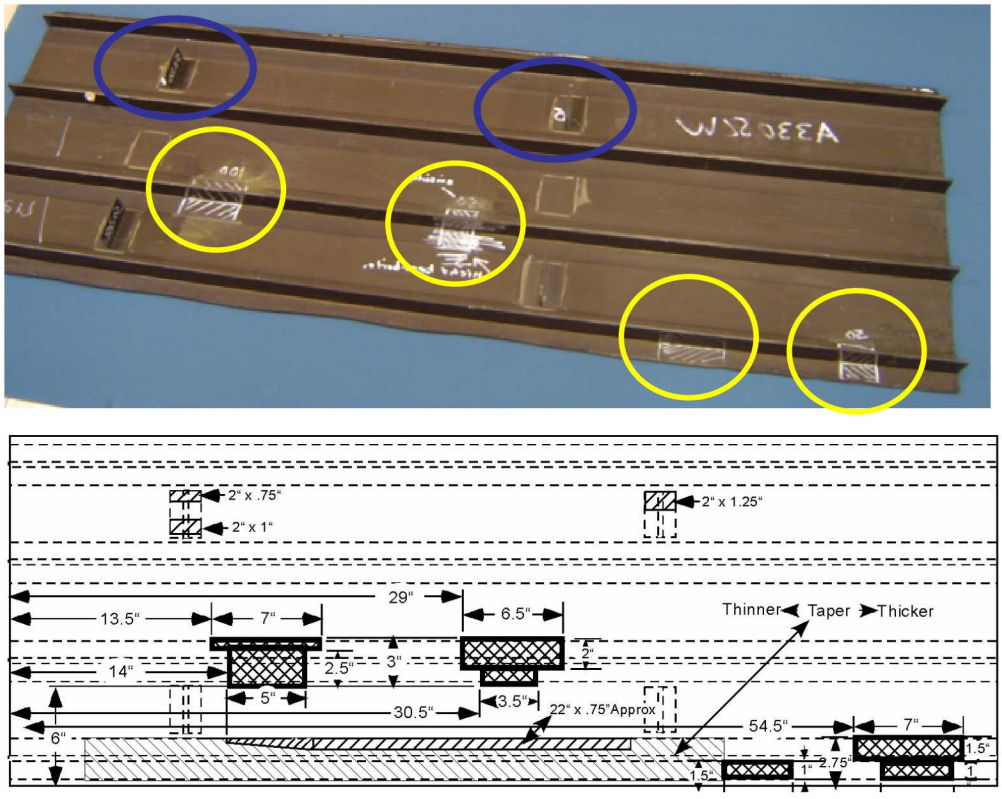

Figure 4-28: Carbon Composite Panel with Stringers, Ribs and Engineered Flaws Three Stringer-to-Skin Disbonds (yellow) Two Rib to-Skin-Partial Disbonds (blue)

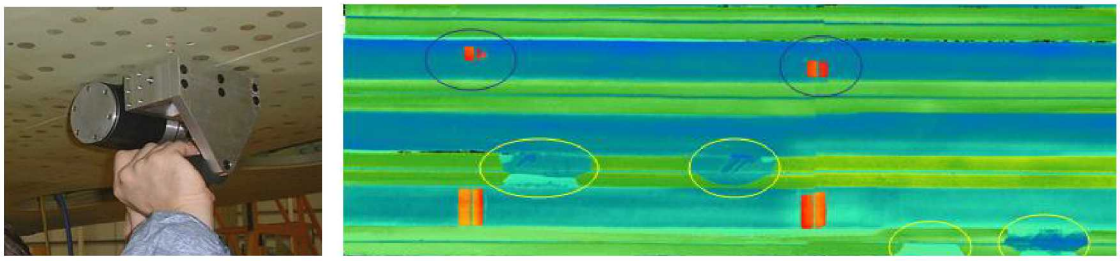

Figure 4-29: Inspection Scans of Composite Panel Produced by the RapidScan UT Array Device

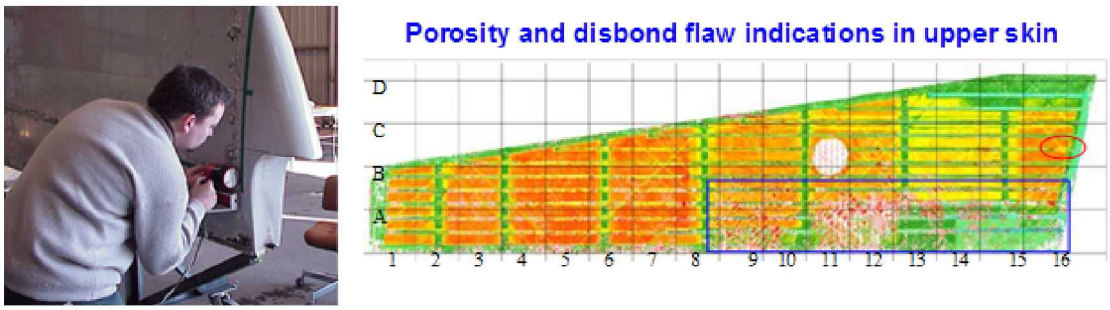

Figure 4-30: Scan of Composite Horizontal Stabilizer with Ultrasonic Rapidscan Array Probe

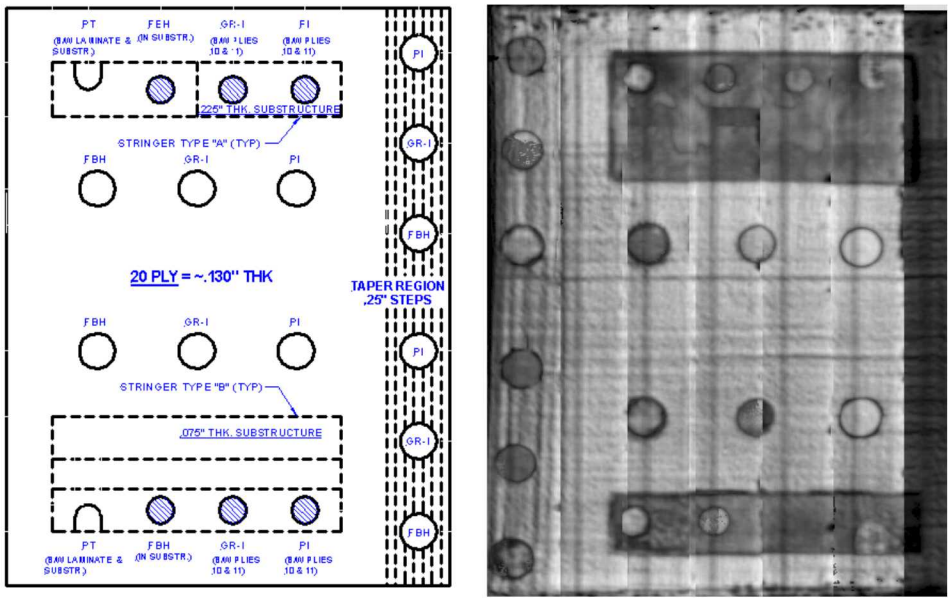

Amplitude

Figure 4-31: C-Scan Images Produced by Rapidscan Array WheelProbe on a20 Ply Composite Laminate Feedback Panel with the Flaw Profile as Shown

4.1.2. *Air Coupled Ultrasonics*

In Pulse-Echo Ultrasonic (PE-UT) inspections, short bursts of high frequency sound waves are introduced into materials for the detection of surface and subsurface flaws in the material. The sound waves travel through the material with some attendant loss of energy (attenuation) and are reflected at interfaces. The reflected beam is displayed and then analyzed to define the presence and location of flaws. Ultrasonic testing involves one or more of the following measurements: time of wave transit (or delay), path length, frequency, phase angle, amplitude, impedance, and angle of wave deflection (reflection and refraction). In most pulse-echo systems, a single transducer acts alternately as the sending and receiving transducer. If the pulses encounter a reflecting surface, some or all of the energy is reflected and monitored by the transducer. The reflected beam, or echo, can be created by any normal (e.g. in multi-layered structures) or abnormal (flaw) interface. Complete reflection, partial reflection, scattering, or other detectable effect on the ultrasonic waves can be used as the basis of flaw detection. In addition to wave reflection, other variations in the wave that can be monitored include: time of transit through the test piece, attenuation, and features of the spectral response.

Traditionally, UT inspections involve the use of a couplant material between the transducer and the inspection surface, use of a water immersion tank, or use of a water squirter system to properly transmit the ultrasonic wave from the transducer into the part being inspected. Sometimes ultrasonic inspection by immersion or squirter systems cannot be conveniently applied in the field. Although, water-coupled systems have been developed for field use, water-coupled ultrasonic inspection is sometimes not desirable due to contamination and property alteration concerns. Examples include composite structures and honeycomb sandwiches that cannot tolerate water ingress. For these practical and operational reasons, non-contact, air-coupled ultrasonic testing (ACUT) has the distinct advantage of being couplant-free. It is therefore an attractive alternative for certain applications, even if ACUT also suffers from several disadvantages, the most significant of which is the attenuation and loss of signal that accompanies air transmission of the UT signals. Air coupled ultrasonics testing is able to transmit the interrogating ultrasonic wave into the test article without the use of a liquid couplant [4.3]. Inspections can be made in through-transmission mode as shown in Figure 4-32. In this case, there are separate sending and receiving transducers. Results from ACUT applied in in through-transmission mode correspond to the capabilities of this inspection method when: a) both sides of the structure are accessible, and b) it is possible to fixture the probes such that they are in proper alignment. Cracks, delaminations, shrinkage cavities, pores, disbonds, and other discontinuities that produce reflective interfaces can be detected. The yoke system that keeps the two transducers in proper alignment is often connected to a position controller/encoding device, as shown in Figure 4-33 so that C-scan images can be produced from an ACUT scan of a component.

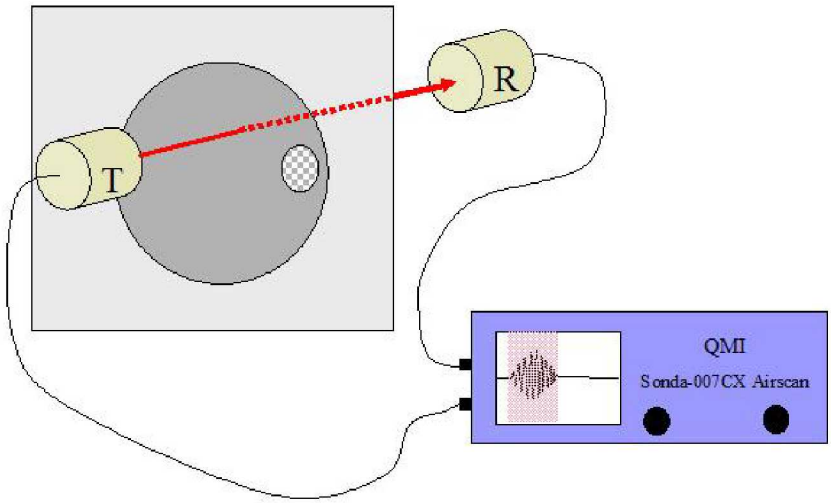

Figure 4-32: Schematic of Air Coupled Ultrasonic Inspection of Panel in Through-Transmission Mode

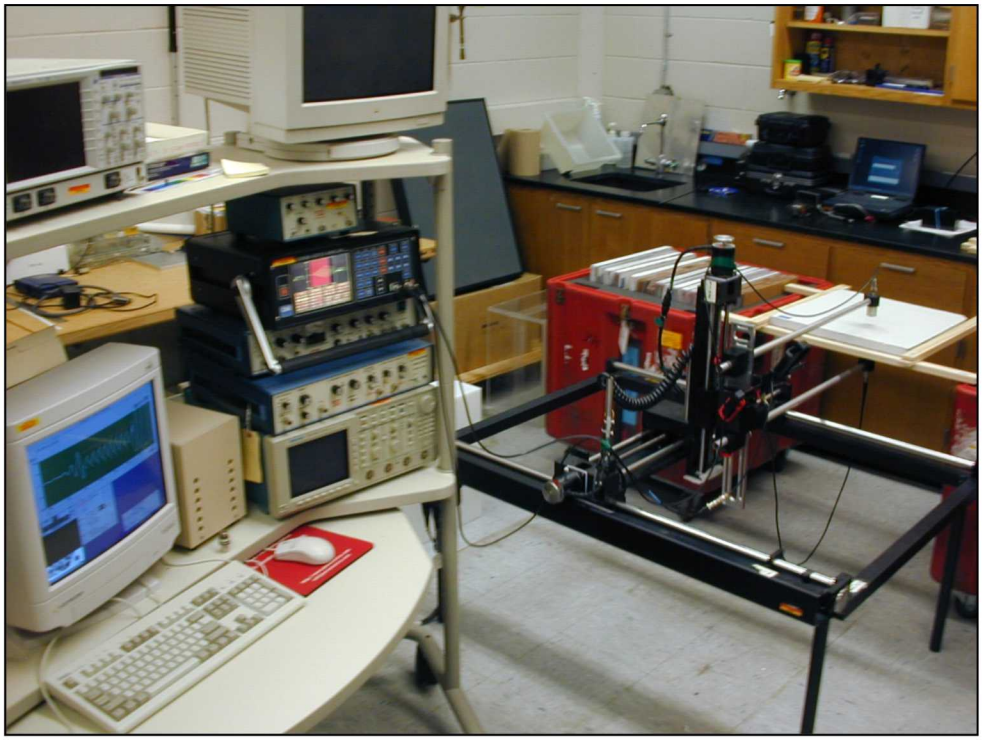

Figure 4-33: Set-Up of Transducers in Air Coupled UT Inspections and Sample Data Produced by Method on Honeycomb Test Specimen

When sound passes across an interface between two materials only a portion of the sound is transmitted, the rest of the sound is reflected. The proportion of the sound

that is transmitted depends on how close the acoustic impedance of the two materials matches. Water is a fairly good match for most commonly used materials - for example typically around half the sound energy is transmitted at the interface between water and a carbon laminate. After four solid- liquid interfaces (from the probe, to the couplant, to the test piece, and then back again) there is still a few percent of the original energy left so accurate measurement is possible. Conversely if the sound has to move between the test piece and air (which has very low acoustic impedance) only a small percentage of the sound energy is transmitted. Typically the overall path loss may be 100 dB higher using air as a couplant, than when water is used [4.4-4.5].

The main limitation of Air Coupled UT is the large reflection loss at the air-solid interface and the large attenuation of high frequency ultrasound in air. The latter consideration has limited the application of ACUT to frequencies mainly below 1MHz or so. It is therefore necessary to minimize losses at every stage in order to achieve acceptable signal-to-noise levels for ACUT for the inspection. Despite the enormous reflection loss at an air-solid interface due to their acoustic impedance difference, the advances in transducer technology and electronics are gradually making air-coupled ultrasound a viable NDI technique for composite structures in the field [4.6]. There are two types of air-coupled transducers, piezoceramic based (disk or composite) and capacitive transducers. Most of the field applications use piezoceramic type transducers. Because of the tremendous difference in transmitted and received signal amplitudes, and the inherent difficulties in achieving adequate transducer/amplifier isolation and recovery, no current air-coupled NDT systems work in single probe mode. Separate transmit and receive transducers are always used. To date, air-coupled ultrasonic NDI has been implemented in the through-transmission mode, with the transducers mounted on a yoke for components that allow for two-sided access, and pitch/catch mode where the two transducers are located on the same side of the component. Figures 4-34 and 4-35 show the through-transmission and one-sided pitch/catch mode of ACUT operation, respectively.

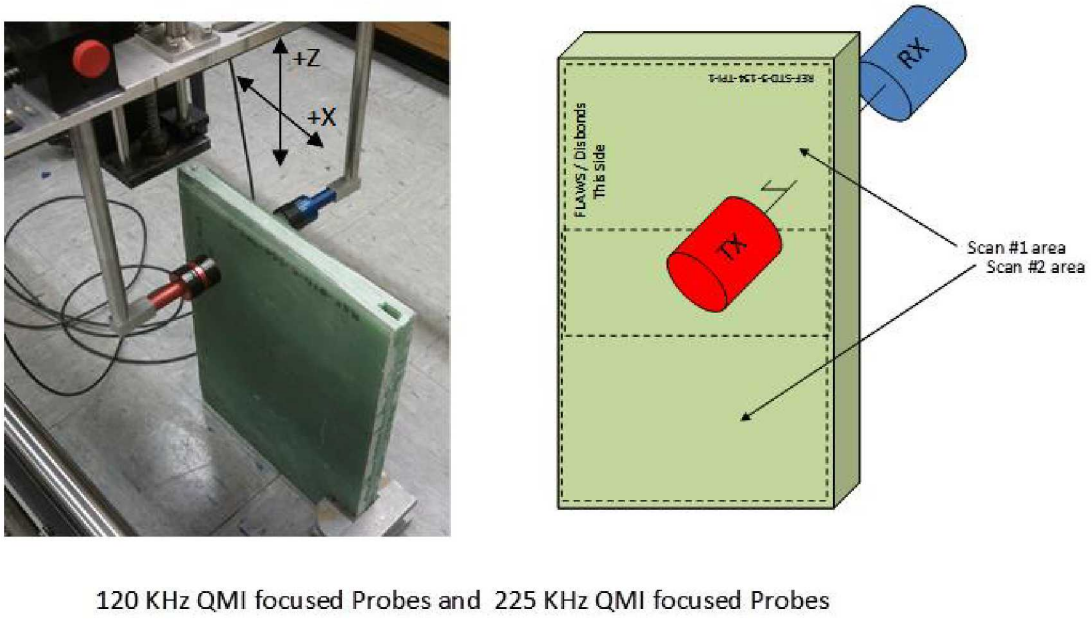

Figure 4-34: Air Coupled UT Through Transmission Setup on Wind Blade Test Specimen

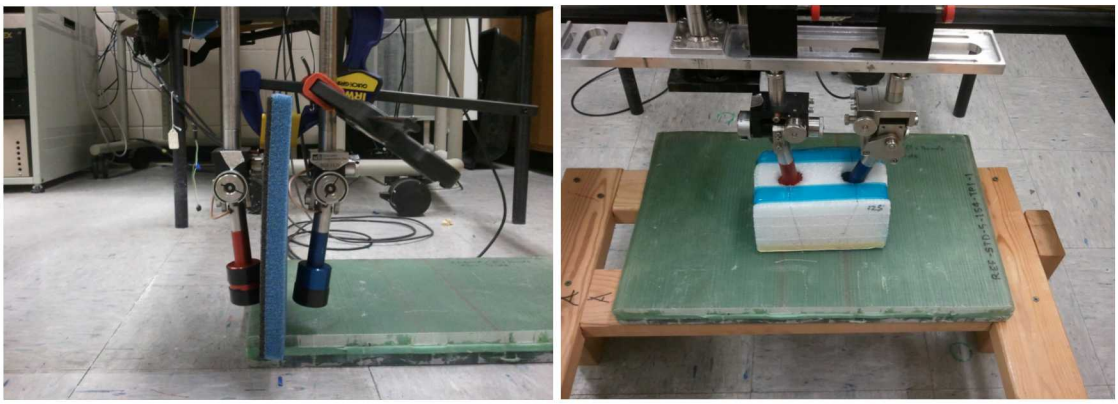

Figure 4-35: Air Coupled UT One-Sided Pitch/Catch Setup on Blade Test Specimen

4.1.3. Through-Transmission Ultrasonics

Through-transmission ultrasonic testing (TTU) is used in various applications to include verification of flaws, sizing defects on a C-Scan Display, and monitoring flaw growth rates. Through-transmission UT can be applied by contact testing, immersion, and squirter applications in a tank like system (See Figure 4-36). The approach uses two transducers in a pitch-catch type of arrangement with one ultrasonic transmitter placed on one side of the material and the receiver (detector) located on the other side of the material. The two transducers must be very closely aligned so some fashion of a yoke mechanism, as shown in Figure 4-36, is used to accurately position the transducers. Thus, access to both sides of the part is necessary to deploy the TTU

inspection method. TTU is highly utilized to inspect multi-layered materials and materials that are highly attenuated. Through-transmission UT is most widely known as a method of inspection in automated immersion testing for detection of disbonding in composite/fiberglass materials where two opposite and parallel surfaces can be used for scanning. A sample C-scan image generated by TTU is shown in Figure 4-37. It demonstrates that TTU inspections can locate defects on an X-Y plane, but cannot locate the depth of the flaw within the part.

Figure 4-36: Automated Through-Transmission Ultrasonic Immersion Tank System

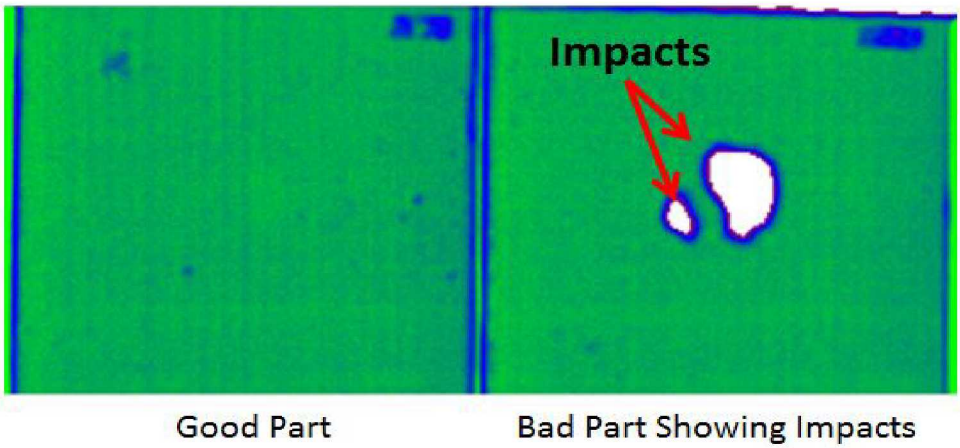

Figure 4-37: C-Scan of an 8 ply Carbon Fiber Panel in an X-Y Plane

Through-transmission testing allows sound travel from the transmitting transducer through the inspection medium (water) and into the part with the sound being received by the receiving transducer. Any void, inclusion, or disbond will act like an interface and hinder or prevent the sound from making it to the receiving transducer. With through-transmission testing, the receiving transducer diameter determines what flaw size you will be able to detect. Figure 4-38 depicts the UT wave travel through a part and shows the change in received signal created by the presence of a flaw within the part.

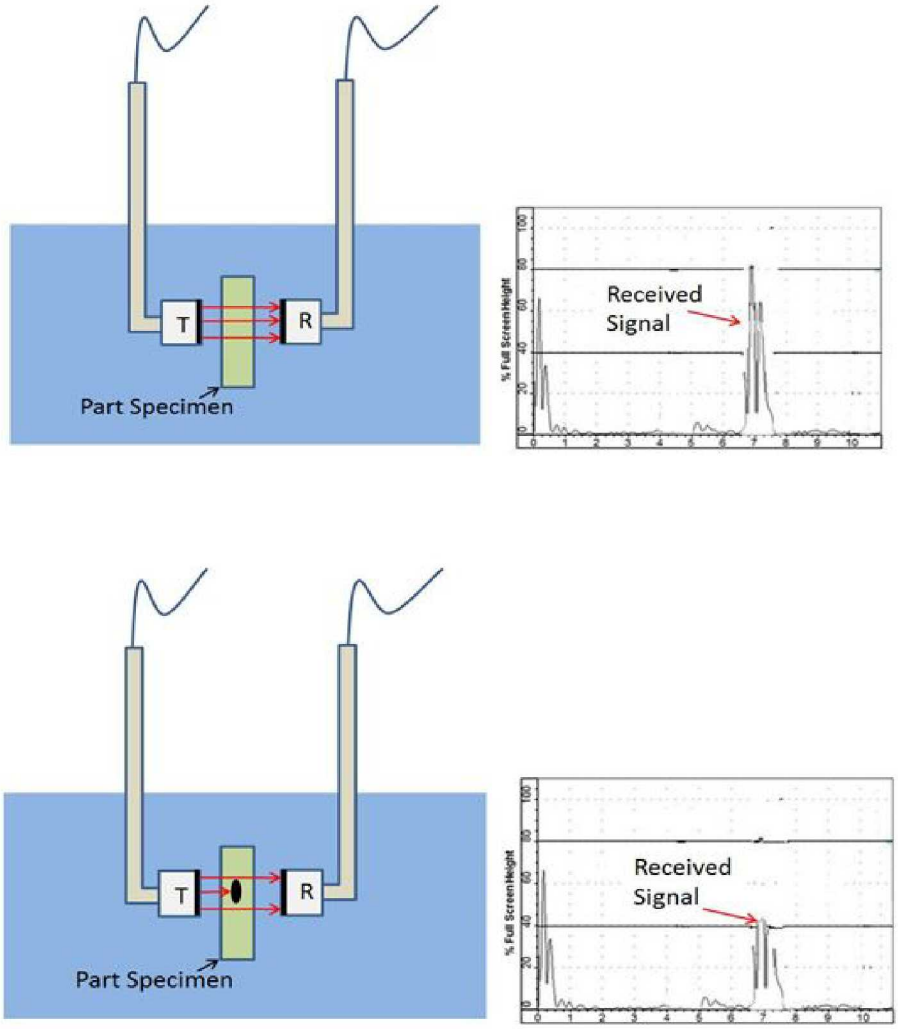

Figure 4-38: Through-Transmission UT in Immersion Tank Showing Good vs. Bad Areas – Damage Creates a 40% Reduction in Amplitude of the Received Signal

4.2. Active Thermography

Thermography is a nondestructive inspection method that uses thermal gradients to analyze the physical characteristics of a structure such as internal defects. This is done by converting a thermal gradient into a visible image by using a thermally sensitive detector such as an infrared (IR) camera [4.10 to 4.12]. Flash thermography relies on the heat absorption characteristics of the structure to indicate the presence of defects. In Thermographic NDI (TNDI), part of the IR band of the electromagnetic spectrum is used to map the surface temperature of an inspected item. The temperature distribution on a structure can be measured optically by the radiation that it produces at infrared wavelengths. Many defects affect the thermal properties of materials. Examples are corrosion, disbonds, cracks, impact damage, panel thinning, fluid

ingress or contamination, foreign objects and damaged or broken structural assemblies in composite or metallic materials. In general, a source of energy is used to create a temperature difference between the specimen and the surrounding environment. Variations in the structure or material properties result in variations in heat flow and surface temperature which are recorded by the IR camera. Figure 4-39 shows a schematic of a thermographic inspection system and highlights the physics of flaw detection.

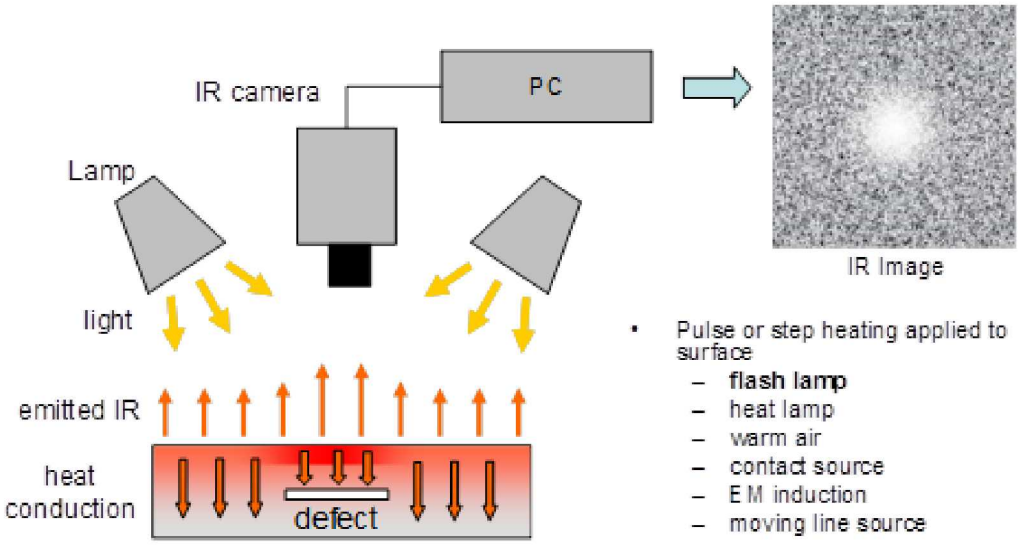

Figure 4-39: Principle of Active Pulsed Thermography

In TNDI, an IR camera is used to measure the surface temperature of a test piece as it responds to externally applied stimulation. The collected IR image sequence is processed using a PC to detect subsurface flaws such as voids, delamination or inclusions in metals, composites and ceramics. Applications range from simple qualitative inspections that require only a handheld IR camera (e.g. detection of trapped water in a composite aircraft control structure) to advanced material characterization using flash thermography excitation and dedicated analysis software (e.g. detection and measurement of low levels of porosity in composite laminates).

Thermographic inspection is accomplished using high-power flash lamps or other heat source (e.g. lamps, hot air gun or heat blanket), an infrared video camera, and image processing hardware and software, all of which are controlled by a personal computer. Modern systems typically use a computer to process data and display results to the operator. They can be configured to accommodate inspection scenarios ranging from handheld to large-area projection for in-service inspection, to fully automated operation for manufacturing quality control. Compared to many conventional inspection methods, TNDI offers several attractive benefits:

- Results are images or maps of an entire area, rather than a compilation of point results.

- Two-dimensional image of the inspected surface helps the operator visualize the location and extent of any defect.
- Fast coverage of large areas - single images can include relatively large areas (1-4 ft^2) allowing for rapid inspections of large surface areas.
- Thermography can be performed without physical contact with the surface - no couplant, immersion or contact with the test article.
- Only single-side access is required.
- Flat or curved surfaces may easily be inspected.

The primary disadvantages of thermography are: 1) it is often necessary to apply a high-emissivity coating during inspections to obtain an acceptable image; steps have been taken to minimize the labor time associated with this task, 2) damage to layers deep within a structure is more difficult to detect than damage in surface layers because the larger mass of material tends to dissipate the applied heat energy.

By the judicious application of external heat sources, common structural defects can be detected by an appropriate infrared survey. The heat source, such as flash lamps, is used to raise the surface temperature of the structure. The subsequent heat transfer into the material is affected by any defects that may be present. The resulting temperature distribution is then recorded by the IR camera and displayed on the computer monitor. As the heat diffuses through the structure the surface temperature is monitored for a period of time by an infrared camera. A subsurface feature that obstructs incident heat from the surface, e.g. a thermally insulating flaw, creates a "trap" that retards cooling of the local surface compared to surrounding areas. As the rest of the sample cools, trapped heat "leaks" radially from the sample, until the sample returns to steady state cooling. Figure 4-40 shows typical heat diffusion through a structure in a region that contains a flaw or damage. Heat deposited at the surface of the sample diffuses into the cooler bulk material (left image). Incident heat is trapped by a subsurface defect, raising the local surface temperature. The trapped heat flows laterally to escape as surrounding areas cool (center image). The transient diffusion process eventually terminates as the entire sample reaches a steady state temperature (right image). In a sample with a thermally conductive flaw (relative to the surrounding matrix), the opposite response occurs. The flaw absorbs incident heat more readily than its surroundings and acts as a heat sink, appearing colder than surrounding areas. Heat from surrounding areas is drawn into the sink, eventually causing it to return to the local temperature.

The means of excitation, the detection method and the inspection parameters can be varied depending on the material to be inspected and the flaws to be detected. The sensitivity, resolution and detectability limits of TNDI are dependent on system parameters including the IR camera performance, scale and intensity of excitation and the data processing used. However, there are fundamental limits on detectability using TNDI that exist regardless of equipment or computational considerations:

- Flaw diameter must be greater than flaw depth.

- The thermal conductivity of the flaw must differ sufficiently from that of the host matrix.

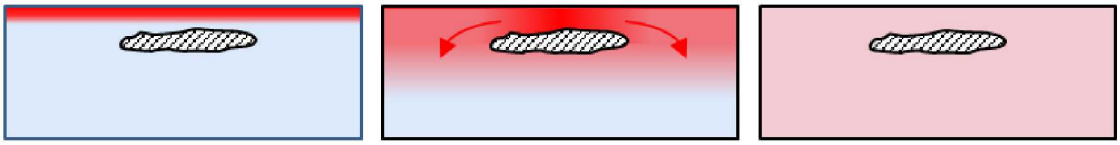

Figure 4-40: Heat Transfer in a Structure Containing a Subsurface Defect

In practice, the computer actually obtains several images at progressively later times after each flash or heat application. Areas that appear hotter than normal may indicate the presence of a delamination or disbond beneath the surface that is preventing heat diffusion into deeper layers. By using a computer to analyze and manipulate the infrared data captured over time, subtle variations can be enhanced in the image. Typical computer enhancements include analysis of the first and second derivatives of the heat versus time signatures at each point in the time sequence to produce images showing rates of change. Through the use of temperature versus time images produced by the thermography system, it is possible to determine the depths of disbonds, delaminations and other flaws in a structure. Typical gantry-based and hand-held thermographic inspection systems are shown in Figure 4-41.

Figure 4-41: Laboratory Thermal Wave Imaging System Inspecting Composite Flaw Detection Panels and Portable Field System Inspecting an Aircraft Fuselage

The infrared camera is a non-contact device that detects infrared energy (heat) and converts it into an electronic signal, which is then processed to produce a thermal image on a video monitor and perform temperature calculations. Heat sensed by an infrared camera can be very precisely quantified, or measured to monitor thermal

performance, as well as to identify and evaluate the relative severity of heat-related problems. Recent innovations have produced more cost-effective and sensitive thermal analysis solutions. These include improvements in detector technology, the incorporation of built-in visual imaging, automatic functionality, and infrared software development.

4.2.1. Flash Excitation and Thermographic Signal Reconstruction (TSR)

Optical flash excitation has proven to be one of the most precise and versatile methods for TNDI excitation [4.13]. Dedicated flash hardware in current TNDI can be scaled to accommodate application requirements, producing highly uniform surface heating over surface areas as large as 4 sq. ft. with durations that can be scaled from 800 microseconds (for inspection of coatings or high conductivity materials) to several minutes (for penetration of large, massive structures). When scaled appropriately, the excitation occurs before incident heat from the surface reaches the internal depth plane of interest, so that the IR data collected after excitation cooling can be thoroughly analyzed.

Several methods have emerged for processing and analyzing TNDI data, including lock-in, pulse phase analysis, principal component analysis and Thermographic Signal Reconstruction (TSR). These methods all exploit the considerable power of modern computing technology, and perform sophisticated mathematical operations on the time history of every pixel in the camera frame (a typical IR camera has ~ 320,000 pixels). However, the TSR approach is unique in that a single pixel time history can be interrogated to provide quantitative information about the subsurface state of the test article, while other approaches ultimately rely on comparison to a reference standard, or identification of contrast between a defect and the intact area surrounding it [4.14]. In numerous independent studies, the combination of flash excitation and TSR has demonstrated superior TNDI results in terms of flaw probability of detection, depth range, and measurements to quantify both defect size and depth [4.15-4.16].

In TSR, the logarithmic temperature response of each pixel is fit to a simple equation (e.g. a low order polynomial), using a least squares fit algorithm. The resulting equation is a replica of the original data that is free of temporal noise, enabling further processing without generation of additional noise. The method builds on the simplicity of the surface temperature response of an opaque sample to a uniform instantaneous heat pulse that is best illustrated by considering two limiting cases of transient heat flow. In the simplest case, for a defect-free, infinitely-thick solid, the surface temperature vs. time plot, viewed on a double logarithmic scale, is a straight line with slope -0.5, indicating uninterrupted one-dimensional thermal diffusion. In the other case, the back wall of a slab with thickness L is adiabatically insulated such that there is no heat transfer through the back wall. The logarithmic temperature-time response begins as a straight line identical to the infinitely thick case, but transitions to a horizontal line that indicates that the transient diffusion process has terminated. The intersection of the extension of these 2 straight lines indicates the time t* at which the transition occurs, which is related to the thickness of the slab (L) by:

$$t^* = L^2 / \pi\alpha \qquad (5\text{-}1)$$

In Equation (5-1), α is the thermal diffusivity of the slab. Figure 4-42 shows this pictorially where the logarithmic surface temperature vs. time is plotted for a flash heated solid that is: 1) infinitely thick (gray), 2) contains an adiabatically insulated back wall (black), and 3) 2-layer solids with thermally insulating and conducting second layers (red, blue). Calculation of the 1st and 2nd derivatives of the pixel time history yields several significant results:

1. The 1st and 2nd derivatives of the infinitely thick solid are constants, with values -0.5 and 0, respectively.
2. The adiabatic slab 1st derivative transitions from a constant -0.5 to a constant 0 value.
3. The adiabatic slab 2nd derivative is zero everywhere except the vicinity of time around t*.
4. Derivative amplitudes are independent of the amount of excitation applied or material composition of the slab (the time scale may change but the amplitude will not).
5. For the non-adiabatic case, both derivatives turn in the positive direction when the thermal conductivity (k) of the buried layer is less than that of the surface layer (k2 < k1), and in the negative direction when k2 > k1.

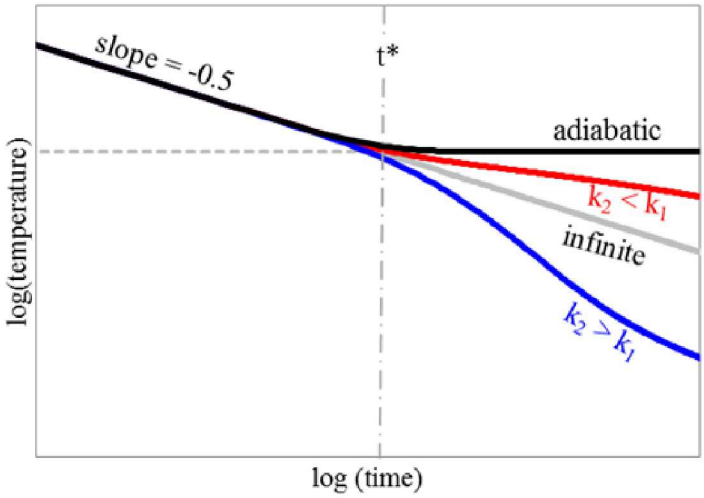

Figure 4-42: Surface Temperature Versus Time Plots for Different Flash-Heated Solids

Viewed as TSR 1st or 2nd derivatives, flash TNDI images have significantly more clarity, depth range and sensitivity to subtle features than the original image sequence. Furthermore, attributes of the derivative signals (e.g. peak amplitudes or the time at which they occur) can be used to automate the inspection process, or to flatten the entire sequence to a single image, analogous to an ultrasonic C-scan [4.17]. Figure

4-43 shows TSR 1st and 2nd derivatives for temperature vs. time plots of a solid that is infinitely thick (gray), adiabatically insulated back wall (black) and 2-layer solids with thermally insulating and conducting second layers (red, blue). Figure 4-44 shows the clarity produced via TSR by comparing unprocessed and TSR processed images from a flash TNDI of a 12-ply carbon fiber panel with polymer inserts embedded between plies 6 and 7.

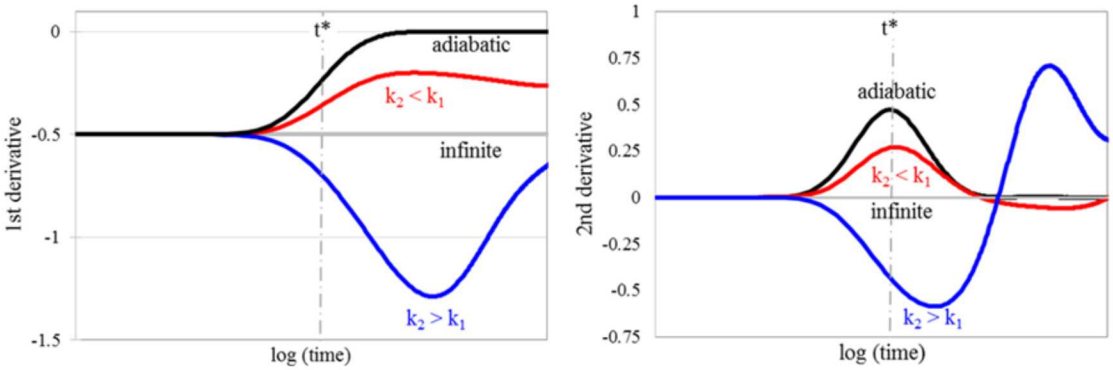

Figure 4-43: TSR 1st and 2nd Derivative Plots of Surface Temperature Versus Time for Different Flash-Heated Solids

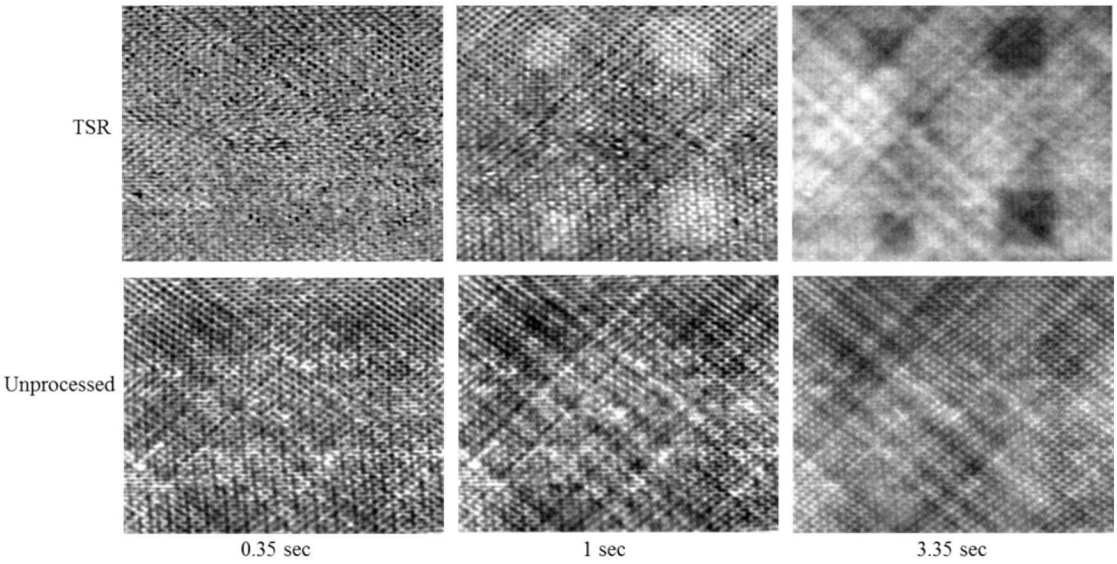

Figure 4-44: Comparison of Flash TNDI Images With and Without TSR to Demonstrate Enhanced Flaw Definition with TSR Processed Data
(IR images courtesy of Thermal Wave Imaging, Inc. [4.18])

4.2.2. Thermography Systems and Applications

Integrated flash TNDI systems using TSR processing are available commercially, and widely used in the aerospace and power generation industries for both manufacturing (QA) and maintenance (in-service NDI) applications [6]. Handheld units using heat

gun or lamp excitation and small, low-speed, low-resolution uncooled micro-bolometer IR cameras are routinely used to detect trapped water in honeycomb, impact damage or delamination in composite aircraft structures. More advanced measurement or material characterization systems, as well as automated systems for manufacturing quality assurance, use flash excitation and high-resolution, high-speed IR cameras that are cryogenically cooled. Figure 4-45 and Figure 4-46 show different TNDI systems ranging from portable to fixed-based operations including: (a) handheld system with optical step excitation for on-aircraft TNDI, (b) stationary flash system, (c) robotic QA system for aerospace composite manufacturing, and (d) projection system for TNDI of large structures.

Figure 4-45: Hand-Held Flash Thermography Systems with Roll-Around Data Acquisition Cart
(images courtesy of Thermal Wave Imaging, Inc.)

Figure 4-46: Gantry and Projection Thermography Systems for Manufacturing and Large Scale Structural Inspections
(images courtesy of Thermal Wave Imaging, Inc.)

Figure 4-47 and Figure 4-48 show sample results from thermographic inspections on bonded tear straps and composite honeycomb structure, respectively. Figure 4-47 shows how a disbond between an aircraft skin and the substructure tear strap affects the thermographic image by changing the heat transfer in that local region. Similarly, the IR image in Figure 4-48 indicates the various flaws that were engineered into the honeycomb panel.

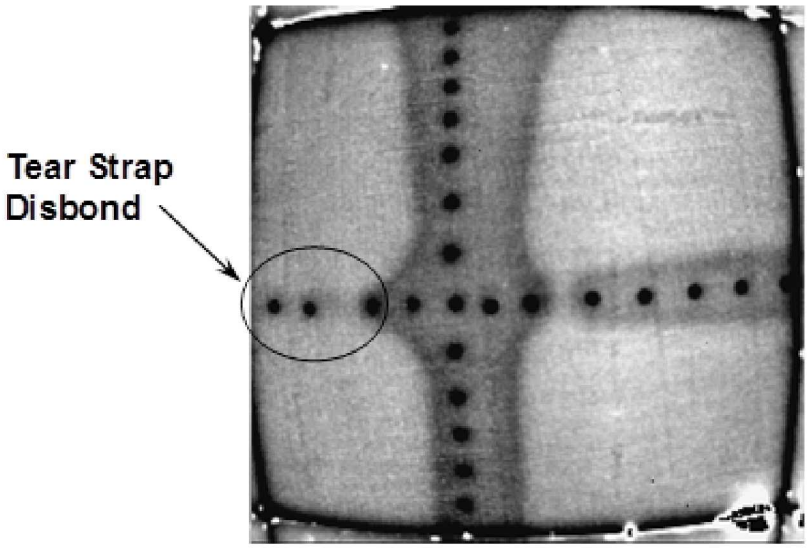

Figure 4-47: Sample Thermography Image Showing a Disbond in an Aluminum Fuselage-Tear Strap Structure

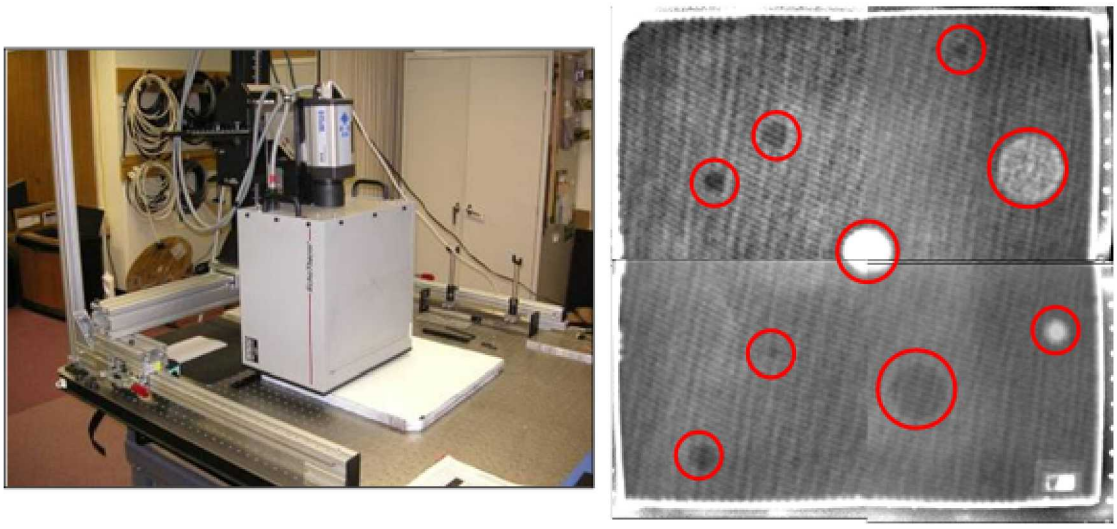

Figure 4-48: FLIR A40 Uncooled Camera Inspecting the Honeycomb Test Panels and a Sample IR Image from a Fiberglass Panel

Figure 4-49 and Figure 4-50 contain additional IR images of various flaws in composite honeycomb and composite laminate structures. One of the limitations of thermography is the depth of penetration of the inspection. For composite laminates, the inspection depth limit is in the range of 0.4" to 0.5" depending on a number of factors within the part and the heating method used. Only flaws that manifest themselves as variations in the surface temperature of the structure can be readily imaged by the infrared camera. Novel heating methods are currently being used to infuse higher levels of heat energy into the structure and improve the detection of deeper flaws.

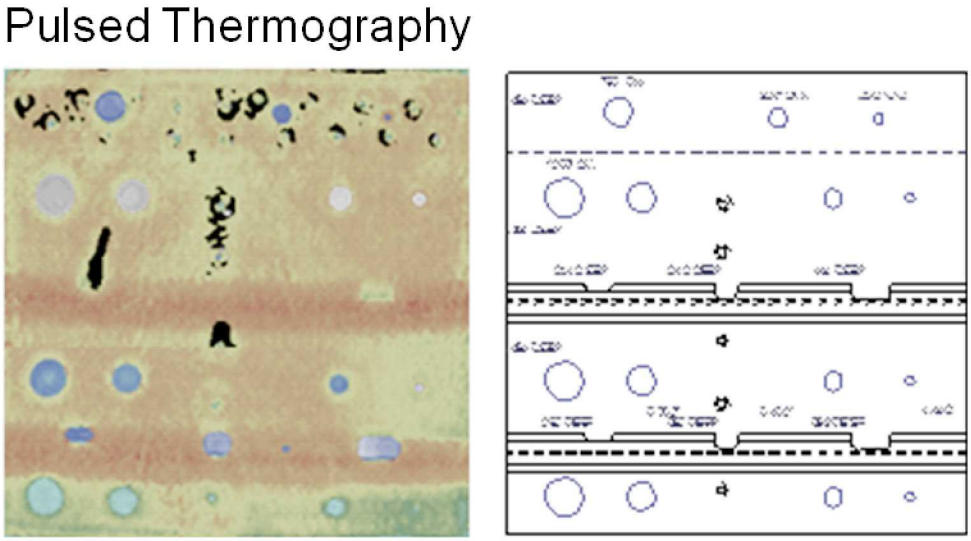

Figure 4-49: Thermography Image Produced from Inspection of Composite Laminate Panel with Flaw Profile as Shown in Drawing on the Right

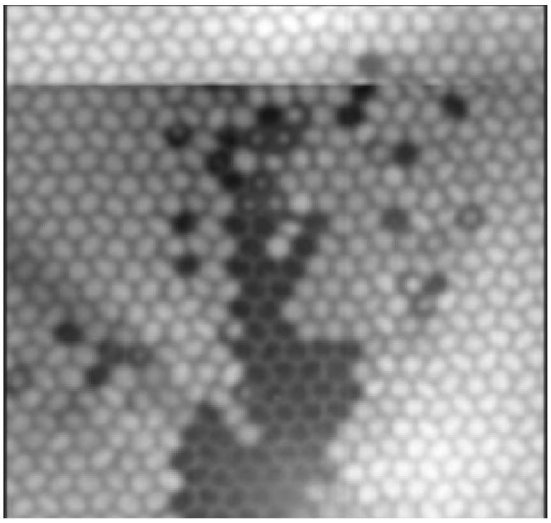

Water Ingress in a Composite Honeycomb Structure

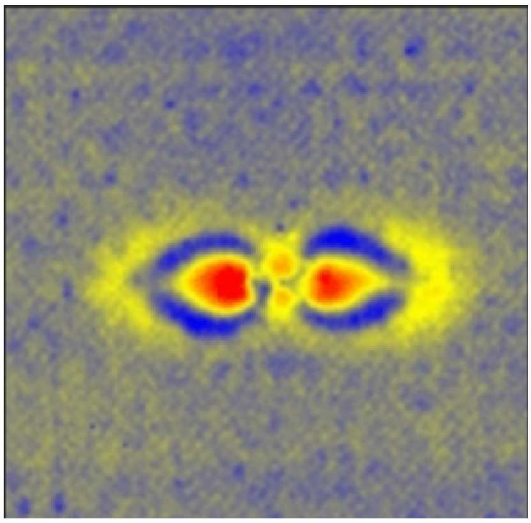

Impact Damage in a Solid Laminate Composite Structure

Figure 4-50: Sample Thermography Images Showing Trapped Water in a Composite Honeycomb Panel (left) and Impact Damage in a Composite Laminate (right)

Figure 4-51 Shows the use of TNDI and TSA to not only detect porosity in composite laminates but also to measure the level of porosity in the component. The Thermal Wave Imaging (TWI) system was also applied to a bonded, composite doubler repair which was installed on a DC-9 fuselage section in the Sandia Labs FAA Airworthiness Assurance hangar. Figure 4-52 shows a schematic of the 10 ply doubler highlighting the size, shape, and location of the embedded flaws. The resultant sequence of images produced by a TWI inspection is also contained in Figure 4-52. The features seen at early times are defects closest to the outside surface of the patch (note appearance of flaws #1 and #2 in the first few frames). The disbonds, located at the base of the doubler, and the deeper delaminations appear in the later frames corresponding to their delayed effect on the thermal field. All six embedded flaws were identified in the TWI images and flaws smaller than 0.5" in diameter could be detected.

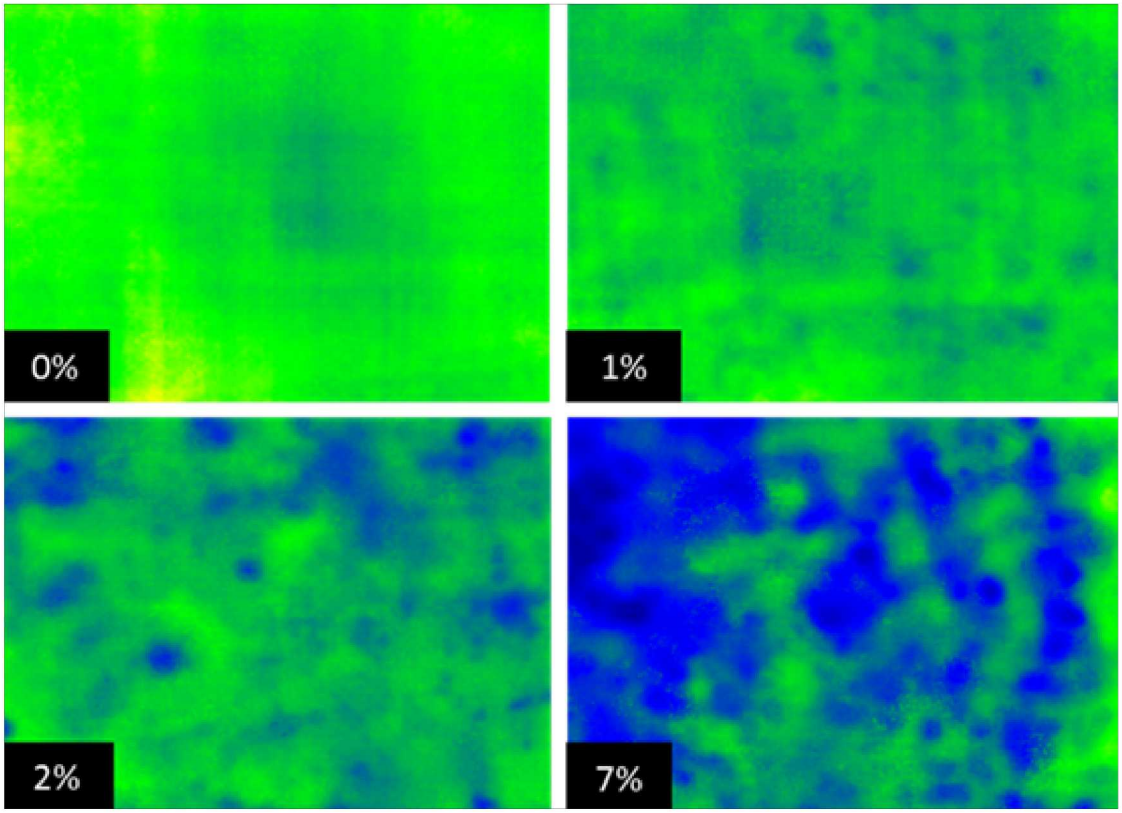

Figure 4-51: Use of TNDI to Measure Porosity Levels in a Composite Laminate
(images courtesy of Thermal Wave Imaging, Inc.)

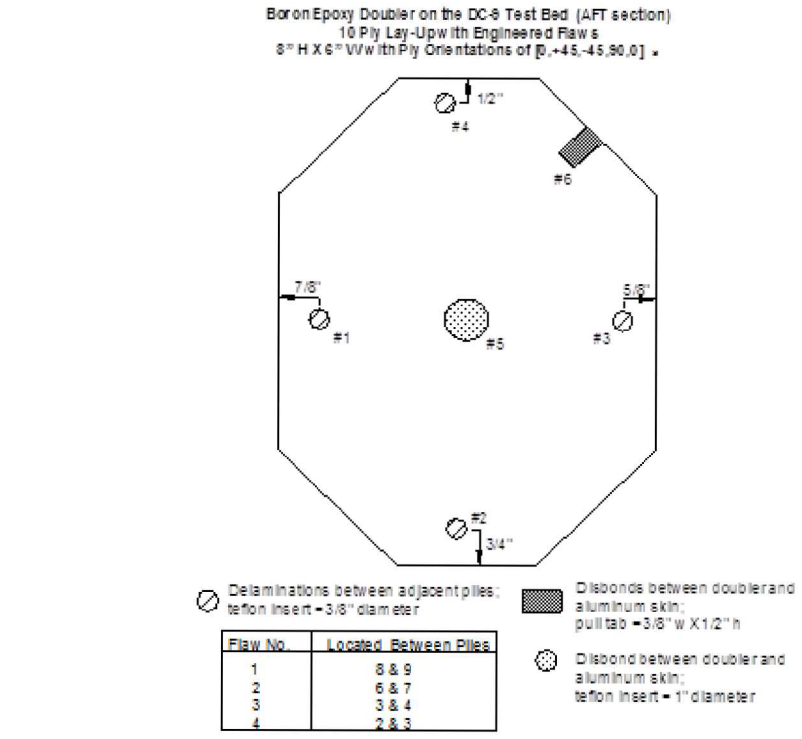

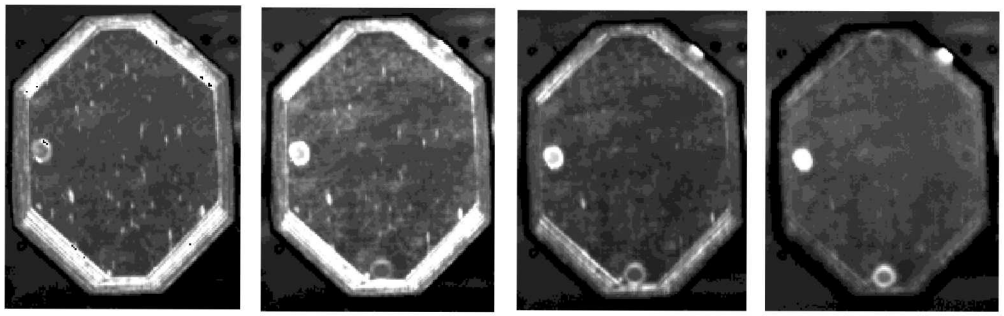

gate 1: 5 f | gate 2: 20 f | gate 3: 43 f | gate 5: 115 f

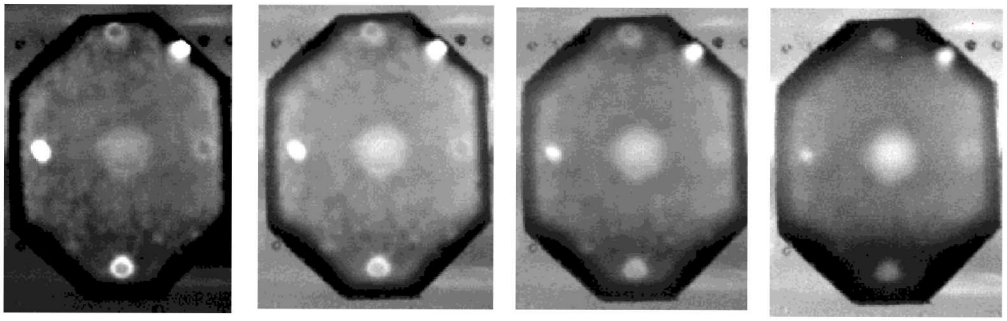

gate 7: 205 f | gate 9: 305 f | gate 11: 413 f | gate 14: 660 f

frame time ("f") = 1/60 of a second

Figure 4-52: Sequence of Thermal Wave Images from a DC-9 Composite Doubler Inspection

4.3. Microwave

Microwave inspection works by using a specialized transducer to bathe the material of interest in microwave energy of an essentially constant frequency. Several different system set-ups for Microwave inspection are shown in Figures 4-53 and 4-54. The energy is reflected from each interface between materials possessing differing dielectric constants within the specimen. The reflected energy is superimposed, creating a signal that is acquired as an analog voltage which is digitized. This signal is sampled at numerous discrete locations across the sample to create a two-dimensional image of the surface as shown in Figures 4-55 and 4-56.

The ability of microwaves to penetrate inside dielectric materials makes microwave inspections an NDT technique very suitable for interrogating structures made of non-conductive composites. Additionally, the sensitivity of microwaves to the presence of dissimilar layers in such materials allows for accurate thickness measurement and variation detection. The quality of the experimental images captured with these systems has demonstrated the potential of the technique for material NDT purposes. Basically, these systems utilize an antenna (a horn antenna used in the first experiments or open-ended rectangular waveguide used in recent years) to illuminate the composite with electromagnetic waves (for this particular applications the EM wavelength go from 1 up to 100 mm) and monitor the reflected waves. The EM waves penetrate deep into the dielectric material where they interact with its interior and reflect back to the antenna. The properties of the reflected wave will convey the needed information about the composite at hand. The Imaging mechanism is based on the idea that microwaves are very sensitive to discontinuities in the material space and the presence of water (the water reflects specularly with the wavelength of microwaves). Microwave NDT techniques may be conducted on a contact or non-contact basis. In addition, these techniques are conducted from only one side of the sample (reflection techniques). Furthermore, when compared with ultrasonic techniques, microwave NDT approaches require no coupling material and do not suffer from signal attenuation. Microwave techniques are able to detect voids, delaminations, porosity variation in a variety of materials as well as impact damage and water infiltration. These are all problems that affect composite materials and also provide the possibility of process control during the manufacturing. Finally, microwave NDT techniques do not require a high level of expertise from an operator and can be conducted in real time with simple, portable hardware. The main limitation of the Microwave method is that it is limited to non-conductive materials. Thus, it has been successfully applied to fiberglass composite structures but cannot be used to inspect carbon graphite composites.

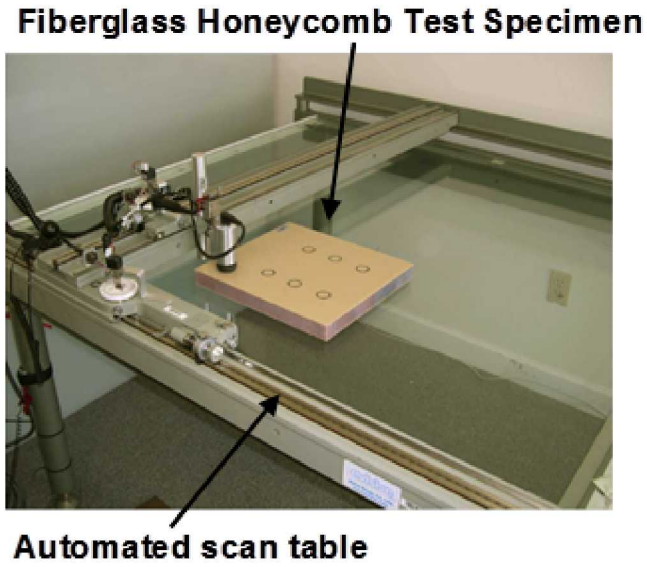

Figure 4-53: Configuration of Microwave Inspection System on a Laboratory Scan Table

Figure 4-54: Basic Equipment Set-up for Microwave Inspection

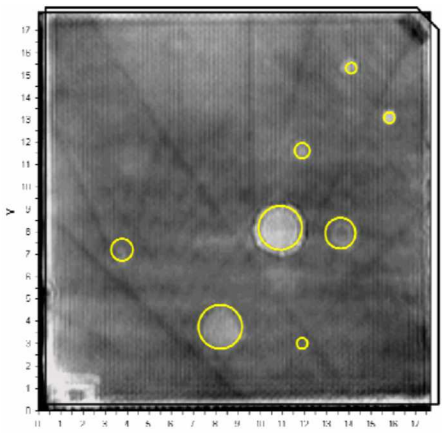

Figure 4-55: Sample Microwave Inspection Results for 3 Ply Fiberglass Panel with Engineered Flaws in the Laminate and Bond Line (Fiberglass Skin Bonded to Nomex Honeycomb)

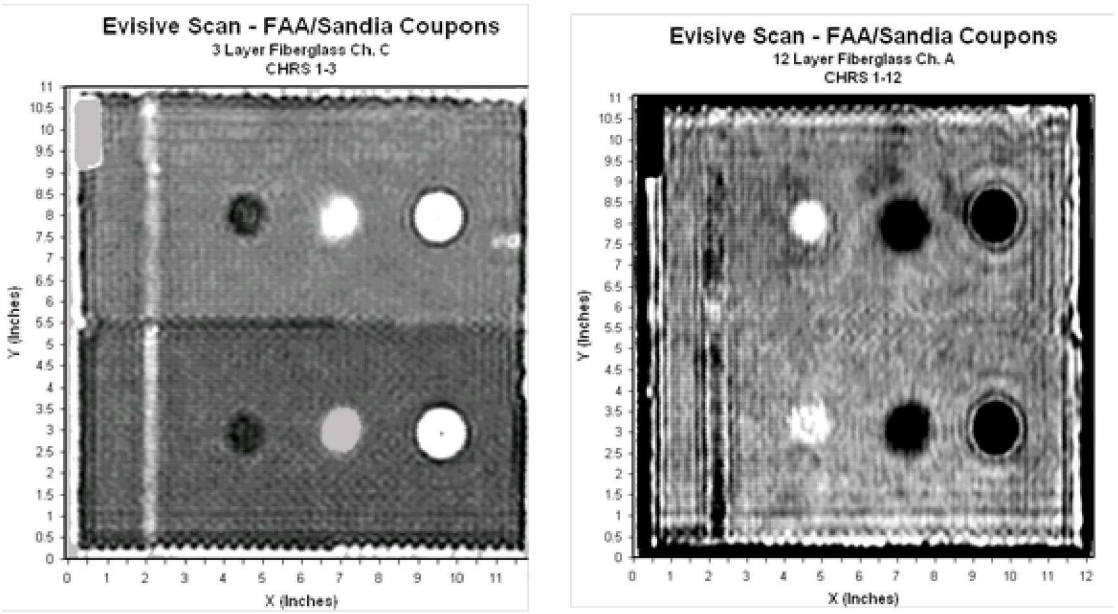

Figure 4-56: Sample Microwave Inspection Results for 3 Ply and 12 Ply Fiberglass Panels with Delamination, Disbonds, Potted Core and Core Splice

4.5. Shearography

Shearography is a wide area interferometric imaging technique that is capable of detecting micron-sized displacements in the surface of a structure. Shearography equipment, shown in Figure 4-57, monitors the surface of a structure for any changes in the surface strain field. Stressing the material in the appropriate way ensures that the subsurface anomalies are manifested on the surface of the structure. Shearography is implemented by comparing two interference patterns on a detector plane, typically "before" and "after" an object motion. If the motion, and subsequent out-of-plane deformations, cause changes in the optical path, then the speckle patterns differ. These images can be compared by subtraction or other algorithms to obtain an image of the object with fringe patterns superimposed. These fringe patterns can then be used to identify the presence, size, and depth of flaws in a structure.

Figure 4-57: LTI-5200 Portable Shearography System with Camera on Test Specimen

A typical shearography system uses a CCD (Charge-Coupled Device) camera with a shearing lens, which is completely integrated into a compact measurement head, to view laser light reflected from the surface under inspection. The object under test is illuminated with laser light and images from the object at different states of loading are taken. The loading of the surface is created by different excitation methods such as vacuum, thermal, vibration or mechanical load which induces some deformation of the outer surface. Such deformations are locally altered by the presence of sub-surface defects, e.g. disbonding or delaminations in composites. A comparison of the different images captured before and after loading allows a deformation gradient to be calculated. This deformation gradient can be a sensitive measure for identifying local defects. Overlapping sheared images are produced in the interferometric process. Two overlapped portions of the sheared images combine and interfere to produce a speckle pattern. When an applied stress deforms the specimen, the speckle pattern is slightly modified. A comparison of the two speckle patterns (stressed and unstressed)

produces a fringe pattern which depicts the relative displacement of the area being inspected. Figure 4-58 shows the basic principles of shearography.

Shearography inspections can detect anomalies such as disbonds, delaminations, voids, separation of structural components, wrinkles, kissing disbonds, impact damage, internal corrosion, crushed core, changes in sections and core splices [4.2]. With the use of the CCD-camera technique, no photo laboratory is required. This makes it possible to use shearography for real-time, nondestructive testing of structures. Laser Shearography views only the surface and does not penetrate into the material. As a result subsurface defects, must affect the surface strain field in order to be detectable.

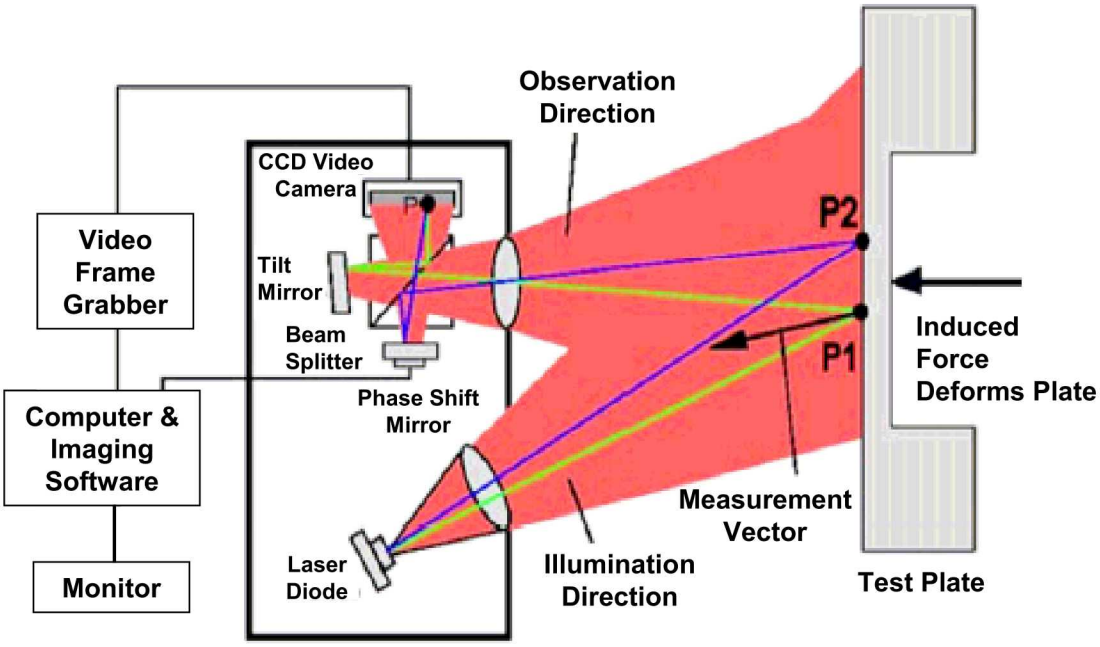

Figure 4-58: Basic Principal of Shearography

Laser Technology Inc. LTI-5200 System - The LTI-5200 is designed for large area inspection of bonded metallic or composite sandwich structures. Inspection rates of 14 m² per hour and the capability to inspect face sheet, core bond lines (near and far side), core splice joints and bonded repairs make this system well-suited for composite applications. Figure 4-59 shows the LTI5200 inspecting a composite honeycomb aircraft rudder assembly. Figure 4-60 shows a schematic of this set-up where detection of both near-side and far-side honeycomb disbonds are possible. Figures 4-61 through 4-63 show samples of shearography images that identify flaws in composite honeycomb panels. Figure 4-64 shows shearography images of a damaged, solid laminate composite structure.

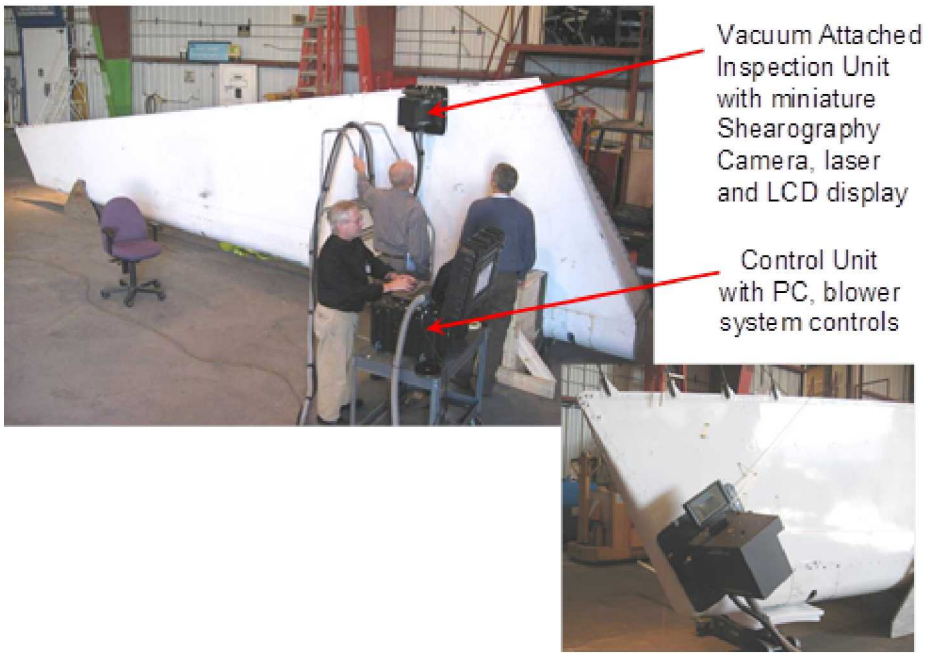

Figure 4-59: Composite Rudder Inspection Using LTI-5200 Portable Vacuum Shearography System

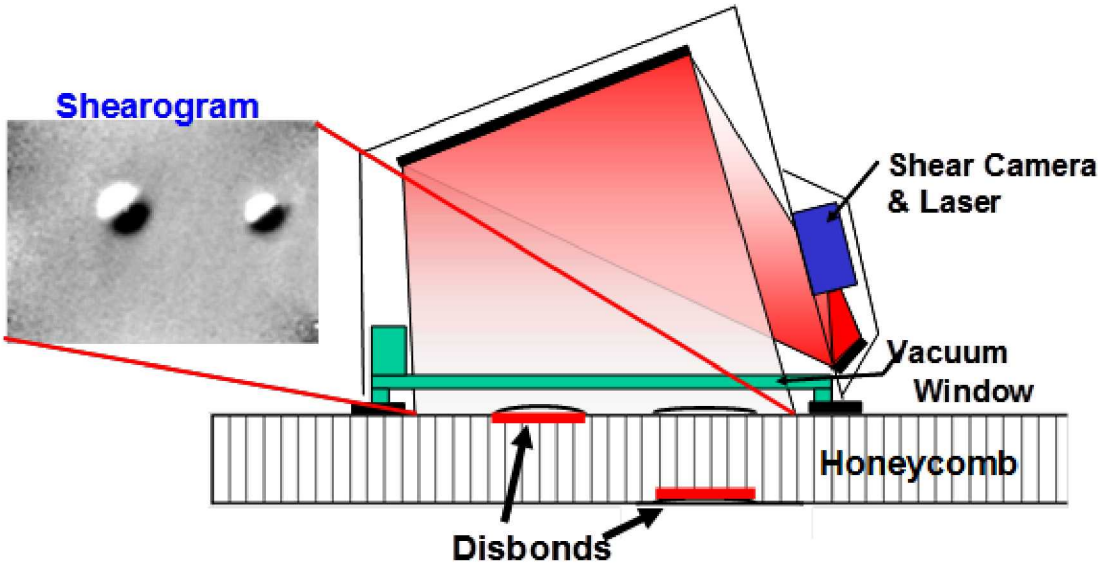

Figure 4-60: Schematic of Shearography Inspection for Near-Side and Far-Side Disbond Detection

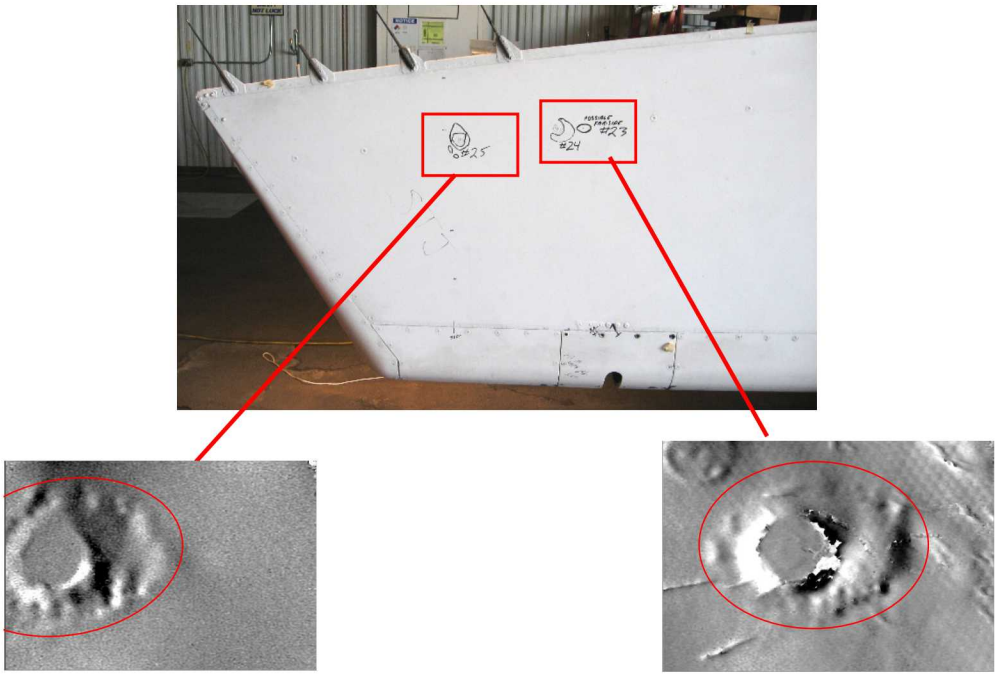

Figure 4-61: Near Side and Far Side Disbonds Detected by Shearography in A310 Composite Rudder

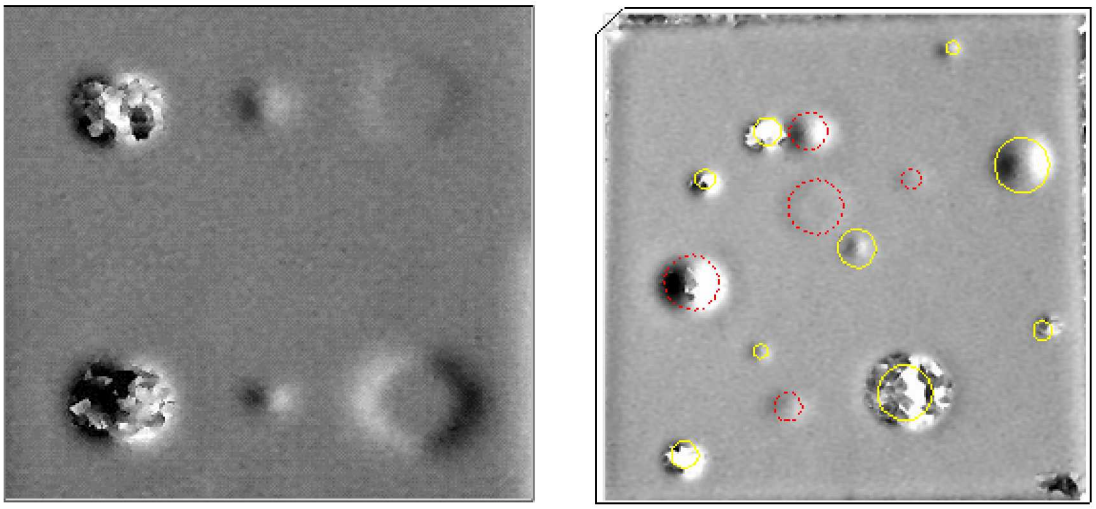

Figure 4-62: Close-Up View of Shearography Image Showing Flaws in a Composite Honeycomb Structure and a Sample Shearography Result for 6 Ply Fiberglass Panel Showing Near-Side and Far-Side Flaw Imaging

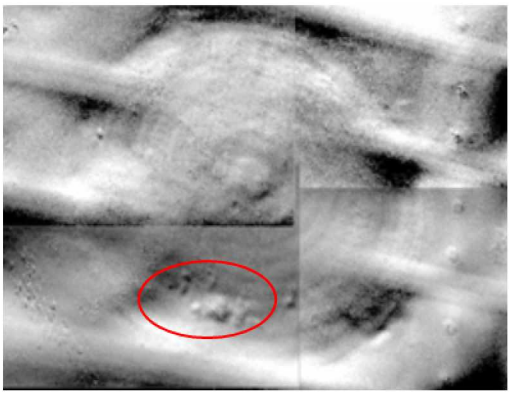

Figure 4-63: Shearographic Inspection Image of a Scarfed Repair to a Honeycomb Structure with Anomaly Indications in the Repair Plies

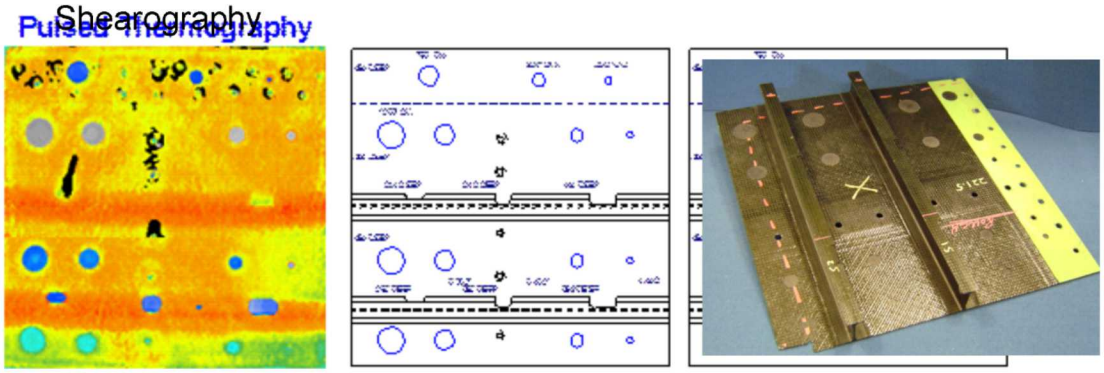

Figure 4-64: Shearography Image Produced from Inspection of Composite Laminate Panel (0.11" th. skin) with Flaw Profile as Shown in Drawing on the Right

Dantec Dynamics Q-810 Laser Shearography System - The Q-810 Laser Shearography System, shown in Figure 4-65, is oriented toward use on composite materials over large surface areas. It can detect defects such as delaminations, disbonds, kissing bonds, wrinkling, impact damage, and crushed core with no surface preparation. The turn-key optical systems are non-contact and full-field and will work on such materials as carbon-fiber, glass-fiber, laminates, honeycomb, foam, metal and Glare. The integrated systems are optimized for large surface area inspections. For example the system can be used on aircraft fuselages, wings, control surfaces, ship hulls, wind turbine blades and rocket components. The full-field inspection rate is approximately 300 mm x 200 mm every 10 seconds. With adaptive seals, the Q-810 can be used on flat as well as highly curved surfaces. The system operates independently of the local environmental conditions and can be used for production or in-field inspections. The interferometric technique measures microscopic surface deformations caused by internal flaws when a small loading is applied to the object. This can be done using thermal, pressure, vibration or mechanical excitation. The results are displayed live as the material responds to the excitation. Further image

processing is also available for export and reporting. Figure 4-66 shows a sample shearography image produced by the Q-810 system inspecting a composite laminate that contains wrinkles.

Figure 4-65: Q-810 Laser Shearography System

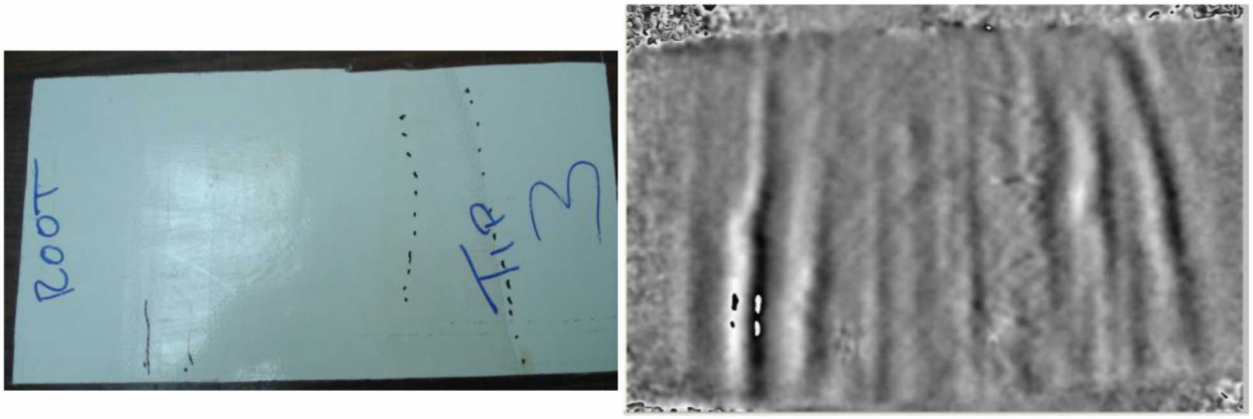

Figure 4-66: Test Specimen (left) and Q-810 Shearography Image of Wrinkles in a Composite Laminate

4.7. Acoustic Beamforming

Beamforming is a signal processing technique whereby signals from multiple sensors in an array are combined for directional signal reception. This is achieved by forming a beam via spatial filtering. In this way, beamforming can be used as a method to measure the relative strength of a signal coming from a particular direction. In general, this is achieved by combining signals from the array selectively such that those from desired and undesired directions experience constructive and destructive interference respectively.

All beamforming methods rely on the use of sensor redundancy in the form of a beamforming array. The spatial variation of each sensor position within the array enables the approach. A large variety of array structures have been proposed in literature and can be obtained from commercial vendors. Often, the size and shape of the array is specifically tailored for its intended application. This is motivated by the fact that the spatial form of the array directly correlates the to the quality of the algorithm results for a given application.

4.7.1. 2-D Delay Sum Beamforming

The most commonly employed method is time-domain delay-and-sum (DAS) beamforming. The basic operating principle of this method leverages the inherent relative delay between two measurements of a propagating sound based on differences in their relative distances to the source.

It is informative to begin with a description of the sound field generated by a simple acoustic source. The most basic sound source is a monopole—a source which radiates sound equally well in all directions. The acoustic field due to a monopole can be expressed simply with the 'free space' Green function:

$$p(t,r) = \frac{A}{4\pi r} e^{i(\omega t - kr)} \tag{1}$$

where r is the distance from the source, ω is the angular frequency of the source, and $k = \omega/c_0$ is the wave number with c_0 being the speed of sound. By looking at the expression given, it can be easily seen that both the magnitude and phase of the resulting sound field are functions of the distance from the source. This becomes the fundamental principle upon which the beamforming methods are developed.

Assume there are two simultaneous measurements, p_1 and p_2, of a single monopole acoustic source at distances r_1 and r_2 $(r_1 \neq r_2, r_1 < r_2)$ from the source respectively. Then

$$p(t,r_1) = \frac{A}{4\pi r_1} e^{i(\omega t - kr_1)} \tag{2}$$

$$p(t,r_2) = \frac{A}{4\pi r_2} e^{i(\omega t - kr_2)} \tag{3}$$

Given that the two measurements are taken at two different distances from the source, there exists a different acoustic wave propagation delay between them. Specifically, since it is located further away, the second measurement will be a smaller amplitude and delayed version of the first. Now, suppose that the source was located at an unknown distance from the two measurement locations. It would be possible to determine this distance by measuring the relative phase between the two measurements. Alternatively, this could be achieved by maximizing the following function

$$g(\tau) = \max_{\tau} \left(p(t,r_1) + p(t-\tau,r_2) \right) \tag{4}$$

Substituting the expression for the sound field at r_1 and r_2 from Eqs. (2) and (3), this can be expanded to

$$g(\tau) = \max_{\tau} Re \left\{ \frac{A}{4\pi r_1} e^{i(\omega t - kr_1)} + \frac{A}{4\pi r_2} e^{i(\omega(t-\tau) - kr_2)} \right\} \tag{5}$$

After some simplification, this becomes

$$g(\tau) = \max_{\tau} \left\{ \frac{A}{4\pi r_1} \cos\left(\omega t - kr_1\right) + \frac{A}{4\pi r_2} \cos\left(\omega t - [\omega\tau - kr_2]\right) \right\} \tag{6}$$

Thus, we can see that a maximum of $\frac{A(r_1 + r_2)}{4\pi r_1 r_2}$ occurs when

$$\omega\tau - kr_2 = kr_1 \tag{7}$$

$$\tau = \frac{k}{\omega}(r_1 + r_2) \tag{8}$$

Looking at the sum of the signals with the given delay, the two signals are said to be constructively interfering—their phase is such that their peaks are aligned in the time domain. Numerically, this would be accomplished by stepping through a range of phase values and deterministically measuring which phase produced the largest result.

This principle can be seen clearly with a simple example. Consider a linear microphone array with a single monopole acoustic source as shown in the following figure.

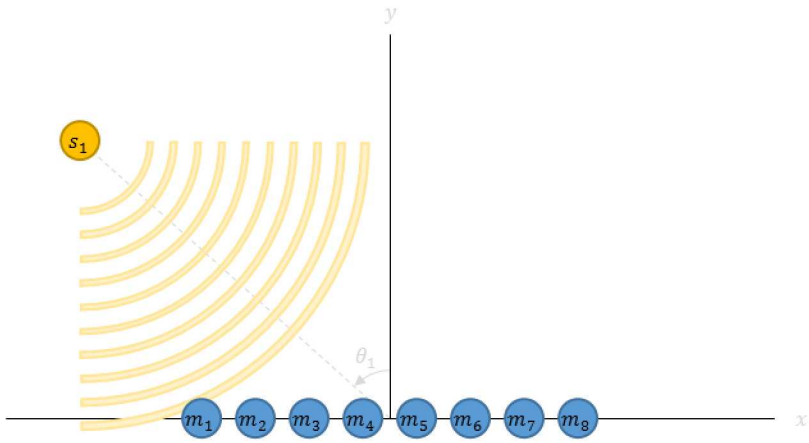

Figure 4-67: Schematic of 1-D Linear Microphone Array with Single Monopole Acoustic Source

In this hypothetical scenario, a sound emitted from the source will be seen first by the leftmost microphone, $^{m}1$. The adjacent microphones, $^{m}2$ to $^{m}8$, will see the same signal but with some additional delay due to the time it takes the sound to reach them. If we choose a simple haversine pulse as the emitted sound,

$$s_1(t) = \begin{cases} 1 - \cos(2\pi f t) & t \leq \frac{1}{f} \\ 0 & t > \frac{1}{f} \end{cases} \tag{9}$$

with an arbitrary selected frequency, $f = 200$, the response of each microphone can be seen in the figure below.

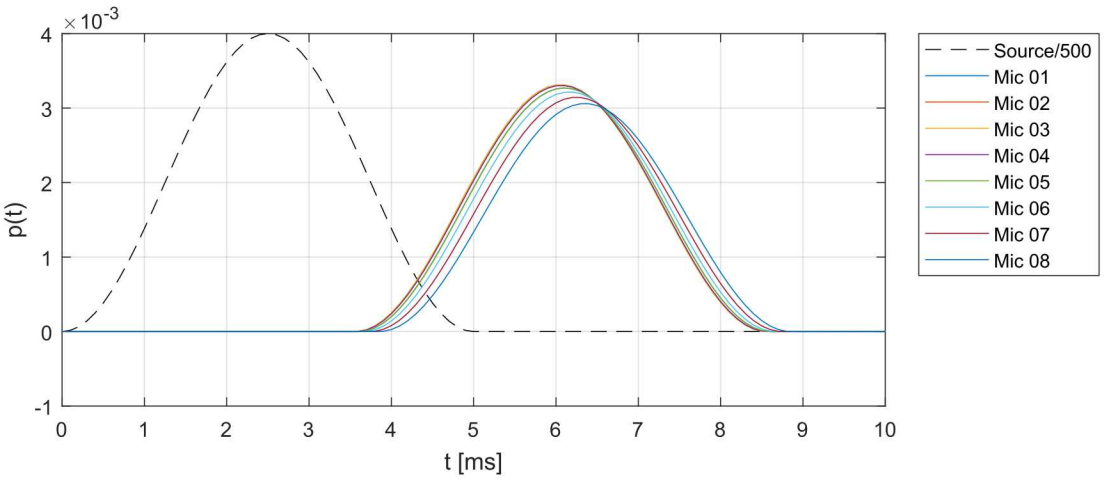

Figure 4-68: Microphone Array Response Due to Single Monopole Acoustic Source Pulse

As anticipated, each measurement is a delayed and scaled version of the original signal. In the context of our beamforming approach, by a suitable choice of delay these signals can be combined to form a signal of maximal constructive interference. Defining the delay based on the distance between each microphone relative to the location of the source, the resulting time shifted signals from each microphone can be obtained. This is shown in the figure below.

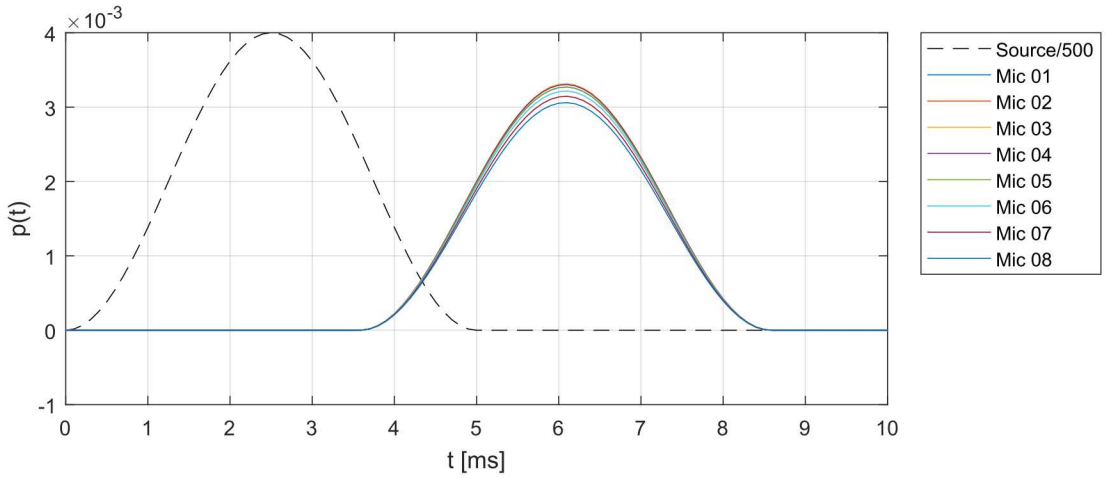

Figure 4-69: Time-Delayed Microphone Array Response Due to Single Monopole Acoustic Source Pulse

As seen in the figure, there exists a small amplitude difference in the time adjusted signals. For far field sources, the change in amplitude due to the small length scale between microphones is small and this difference is negligible. In the case of near-field sources, this difference is more critical. Accordingly, an additional compensation can be made to the microphone signals to account for this change in amplitude. This modified approach is generally referred to as filter-and-sum beamforming. After incorporating the magnitude adjustment in this idealized scenario, all the shifted microphone signals align perfectly with respect to both amplitude and time.

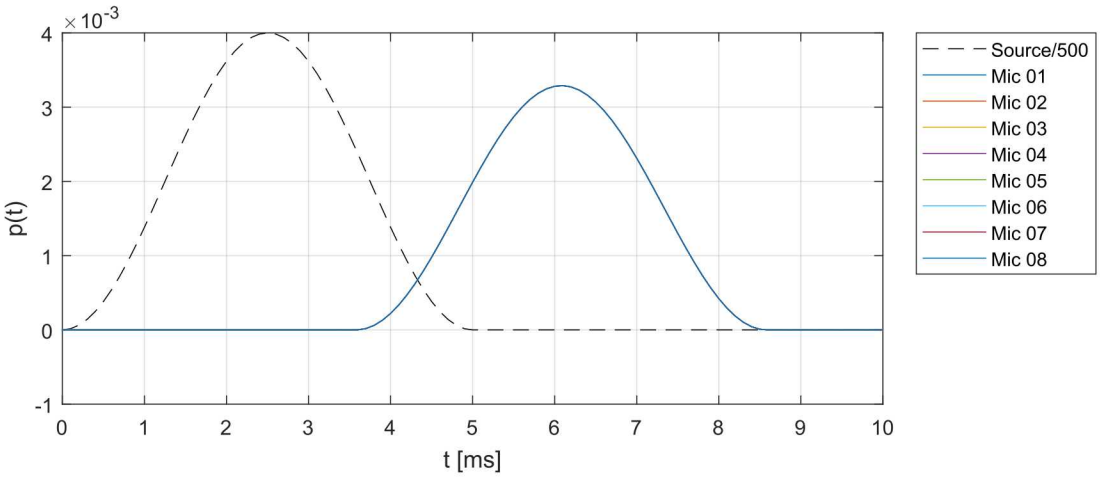

Figure 4-70: Time-Delayed and Magnitude Adjusted Microphone Array Response Due to Single Monopole Acoustic Source Pulse

In many applications, the delay and amplitude adjustment are made relative to the first microphone. For clarity of exposition, here it has been chosen to make all references relative to the origin of the microphone array, $\vec{r}_{m_0}$. Thus, they are all shifted virtually to a point at the origin of the microphone array.

The actual result of the beamforming is the summed response of all the adjusted microphone signals. The formal equations are given as follows,

$$b(t) = \sum_{n=1}^{N} \alpha_n p_n(t - \tau_n) \tag{10}$$

Where,

$$\tau_n = \frac{\omega}{c_0} d_{m_n} \tag{11}$$

$$\alpha_n = \frac{d_{m_n}}{d_{m_0}} \tag{12}$$

$$d_{m_n} = d_{m_n} - d_{m_0} \tag{13}$$

$$d_{m_0} = \left|\vec{r}_{m_0} - \vec{r}_s\right| \tag{14}$$

$$d_{m_n} = \left|\vec{r}_{m_n} - \vec{r}_{m_0}\right| \tag{15}$$

As a further demonstration of the beamforming concept, the preliminary example can be extended to the case of two sources. This is shown graphically in the figure below.

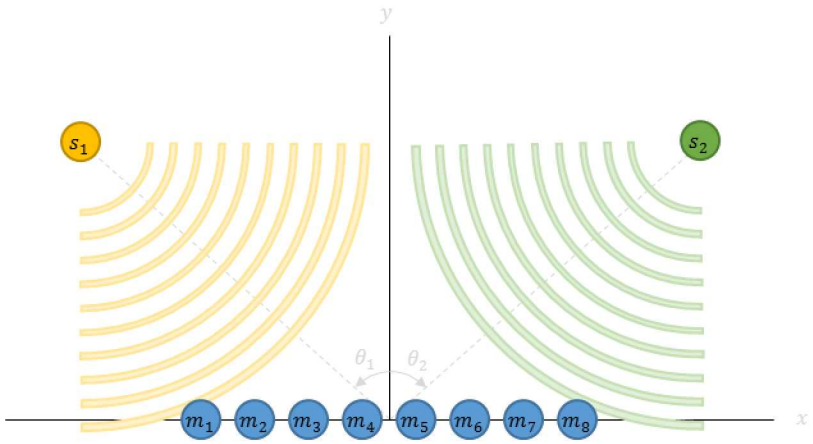

Figure 4-71: Schematic of 1-D Linear Microphone Array with Two Monopole Acoustic Sources

In this modified scenario, when the signals are delayed and scaled there are two possible beam angles for which the signal could be maximized. When the beam is focused on the first and second source positions respectively, the following two sets of adjusted microphone signals are obtained. Note however, that for illustration purposes no amplitude scaling has been applied to either case.

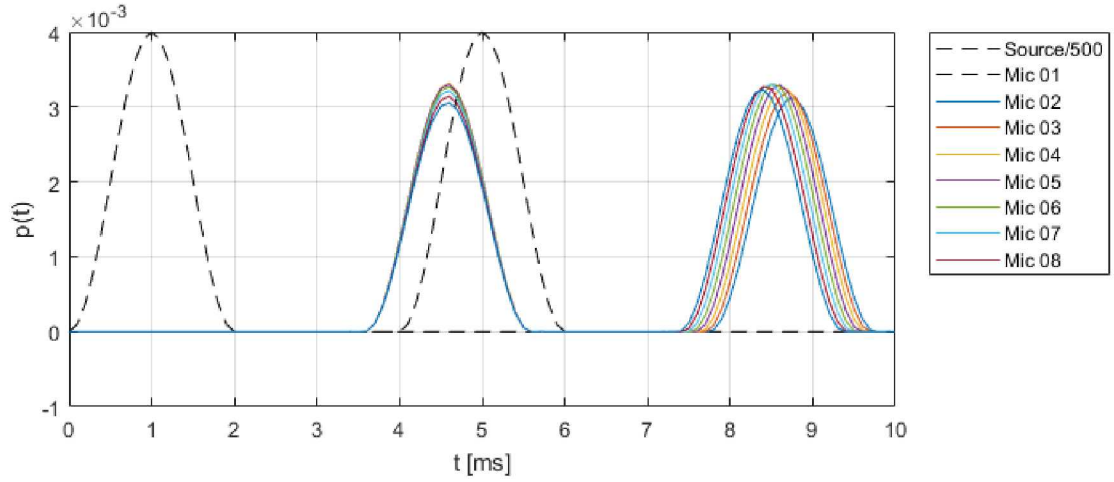

Figure 4-72: Optimally Time-Delayed Microphone Array Response for Source 1

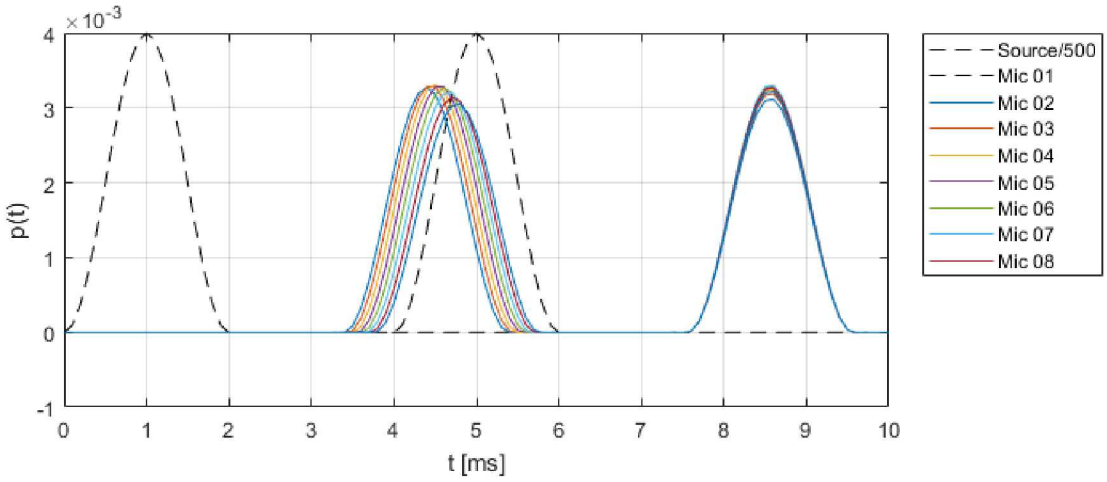

Figure 4-73: Optimally Time-Delayed Microphone Array Response for Source 2

As shown in the first figure, the delay which maximized the constructive interference of the sound from source one, s_1, does not maximize the sound coming from the second source, s_2, and vice versa. Thus, by sweeping through a grid of potential source positions, local maxima can be obtained and sources identified.

4.7.2. 3-D Delay Sum Beamforming

So far, the analysis plane (both sources and microphones) have been constrained to exist in a 2-dimensional space. If the analysis is extended to 3-dimensions, the example microphone array previously given will be inadequate. Consider the case where there exist two sources at the same relative distance along the x-y plane but with an associated elevation in the z-axis. This can be seen in the figure below.

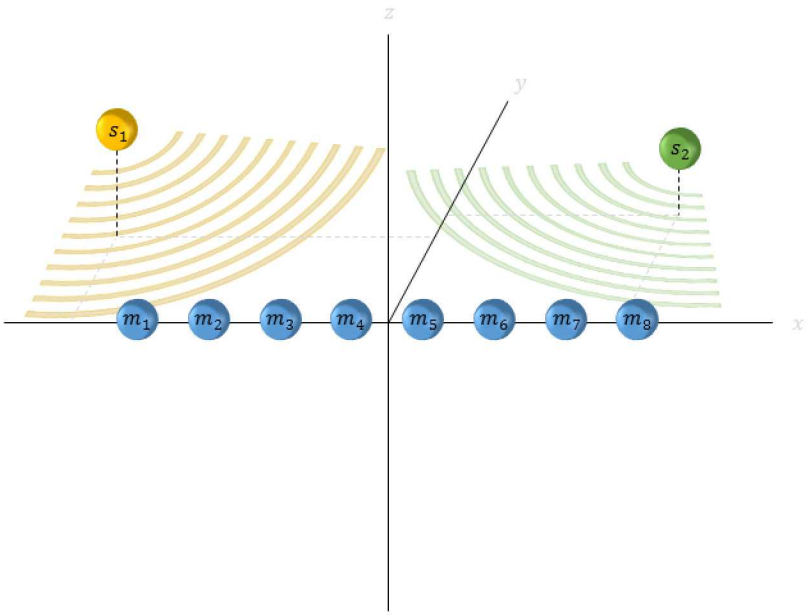

Figure 4-74: Schematic of 1-D Linear Microphone Array with Two Monopole Acoustic Sources in 3-D Field

The change in the relative delay between microphones for each source signal is largely independent of the z-axis height. Specifically, two sources at the same x-y coordinate with different z-axis heights will be nearly indistinguishable from one another. Therefore, to make 3-dimensional analysis possible, the microphone array itself must be modified to enable improved beams along this new dimension. As a simple solution, an additional set of microphones can be added to the array along an axis perpendicular to the original.

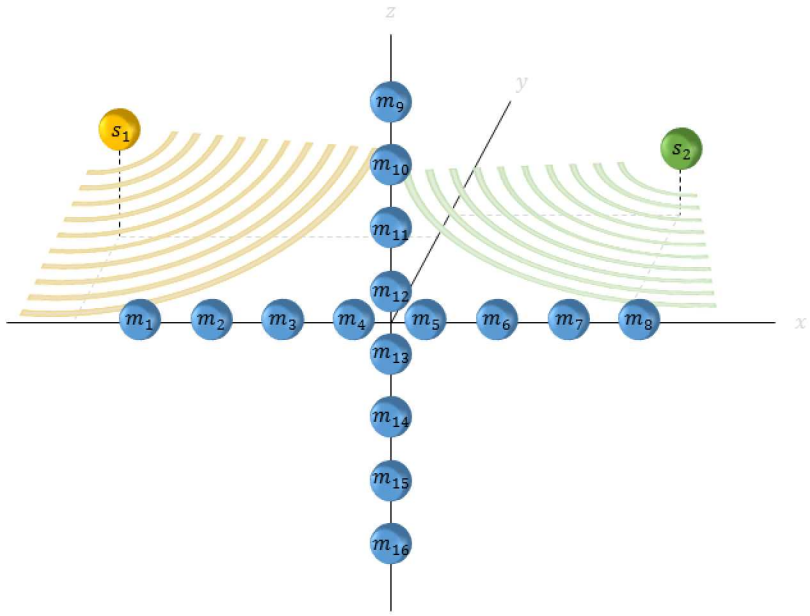

Figure 4-75: Schematic of 2-D Linear Microphone Array with Two Monopole Acoustic Sources in 3-D Field

With the modified array, the beam can be focused along both the horizontal and vertical axes. Applying a haversine pulse at each source location, the following microphone signals are obtained.

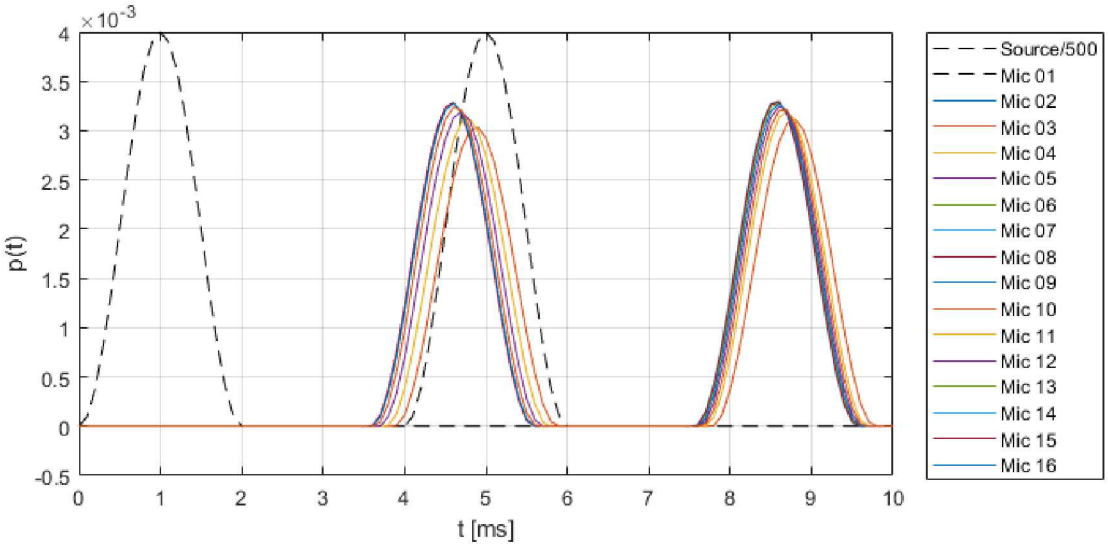

Figure 4-76: Microphone Array Response Due to Two Monopole Acoustic Source Pulses

To form a simple beamforming map, choose an analysis grid and iterate through all possible source locations. Let the beamforming solution be defined as the peak amplitude of the summed microphone responses.

$$B(x,y,z) = \max_{t} b(t|x,y,z) \tag{16}$$

In many applications, the region of interest is limited to a known surface or plane located some distance away from the array. Therefore, in the example given, the analysis plane has been reduced to a 2-d plane at a prescribed distance from the microphone array. The resulting beamformer estimate is shown in the following figure. Here, we can see that the peak value for each candidate x-z coordinate is plotted on a color scale. Regions of high magnitude (indicated by yellow) can be identified as the locations of the sources.

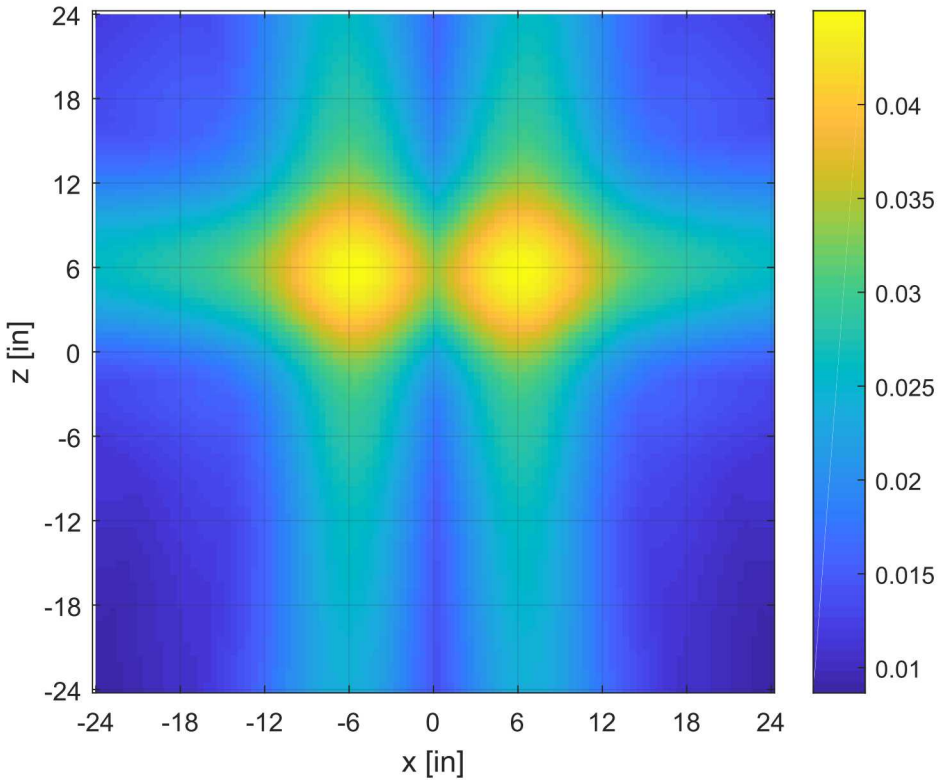

Figure 4-77: Beamforming Analysis Map Due to Two Monopole Acoustic Source Pulses

4.7.3. Frequency Domain Delay-Sum Beamforming

Until now, no discussion has been given as to the practical aspects of applying the necessary delay to each measured microphone signal. In actuality, a continuous measurement $p(t)$ of the instantaneous pressure at each microphone is not available. Instead, the measured response is a discrete sampled measurement $p[k]$ of the pressure. Thus, a defined phase delay will correspond to a discrete shift of the measured signal by $F_s\tau_n$ samples, where F_s is the sampling frequency. Given that non-integer sample delays are not possible, the signal must be up-sampled via a suitable interpolation in order to perform the desired time shift. This motivates the use of an alternate form of the beamforming algorithm—one in which non-integer delays are no longer an issue.

This is accomplished by moving into the frequency domain. The shift into the frequency domain is justified by the fact that a time delay in the time-domain corresponds to a phase shift in the frequency-domain.

$$F\{x(t-\tau)\} = F\{x(t)\}e^{-i2\pi f\tau} \tag{17}$$

Therefore, an arbitrary time delay can be implemented in the frequency domain without the need for interpolation or other advanced computation. The result beamforming solution is given by the following equation.

$$B(f) = \sum_{n=1}^{N} \alpha_n P_n(f) e^{-j2\pi f\tau_n} \tag{18}$$

where P_n is the Fourier transform of the original microphone signal.

As presented here, the result of the frequency domain beamforming is a frequency dependent beamforming map (intensity level) for each analysis coordinate. Depending on the application, the frequency range of interest may vary. When no specific frequency range has been identified, a first approach can be based on the overall sound pressure level (OASPL)—the total energy contained in the spectrum—at each analysis point.

$$OASPL(x,y) = 10\log_{10} \int B(x,y,f)df \tag{19}$$

The result of standard delay-and-sum beamforming techniques is an estimate of the source intensity on an analysis plane. Returning to Figure 11, it can be seen that the source intensity has been smeared along the analysis plane outward from the source location even though the original source was located at exactly a point. This effect is a direct result of the beamformer's directional characteristics—main lobe width and side lobe attenuation. Given knowledge of the beamformer's sensor arrangement, these effects can be characterized apriori. Subsequently, it is possible to account for these effects in the analysis by using deconvolution techniques. These methods have been shown to achieve higher spatial resolution than standard methods.

In order to illustrate the fundamental concept of this approach, consider the following beamforming map obtained from two point sources with broadband random excitation.

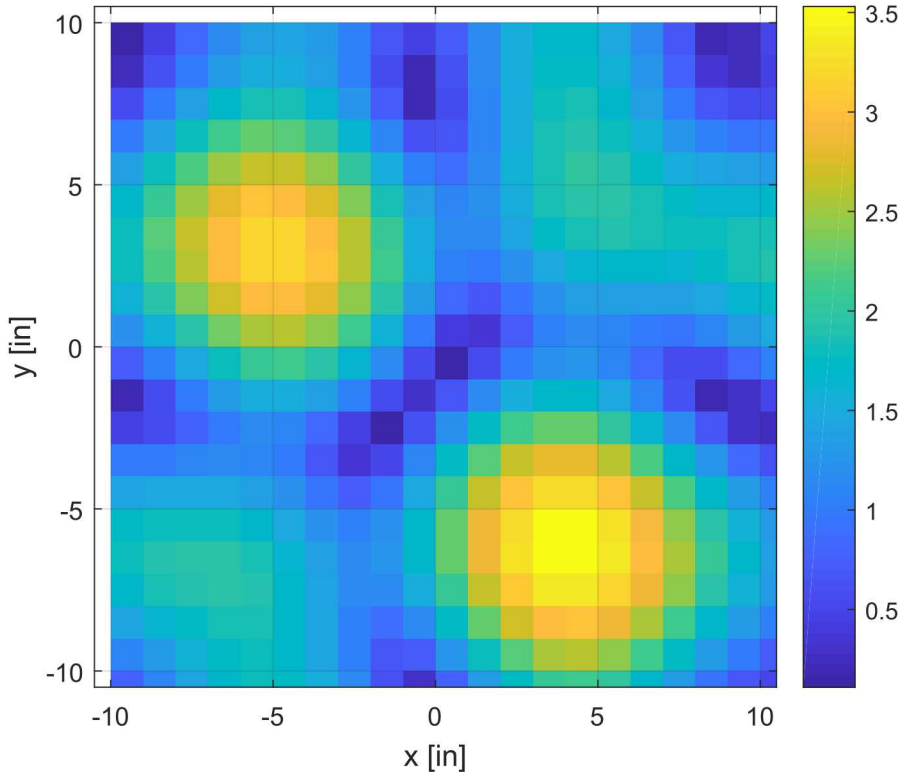

Figure 4-78: Beamforming Analysis Map Due to Two Broadband Random Monopole Acoustic Sources

In this hypothetical scenario suppose there are only three possible candidate locations for a monopole source. Thus, one can predict the hypothetical map which would be obtained for a monopole at each candidate location. Each map is scaled to have unity amplitude at the analysis point on the map which corresponds to the candidate location. The resulting unit maps are referred to as Point-Spread Functions (PSFs). The deconvolution approach is based on the assumption that the actual beamforming map must consist of some combination of scaled versions of these PSFs. The only challenge which remains is determined what scaling factor, $a_i \geq 0$, needs to be applied to each PSF to obtain the measured beamforming map.

$$B = a_1 B_1 + a_2 B_2 + a_3 B_3 \tag{20}$$

Traditionally, this is accomplished by collapsing each map into vector form and solving the resulting linear equation.

$$vec[B] = \begin{bmatrix} vec[B_1] & vec[B_2] & vec[B_3] \end{bmatrix} \begin{bmatrix} a_1 \\ a_2 \\ a_3 \end{bmatrix} \tag{21}$$

The value obtained for each scale factor becomes the magnitude associated with the corresponding point on the analysis plane. By plotting each PSF as a surface alongside

the original beamforming map, one can visually determine that some contribution must be due to both candidate locations one and two—scaled versions of these surfaces are visible in the original beamforming map.

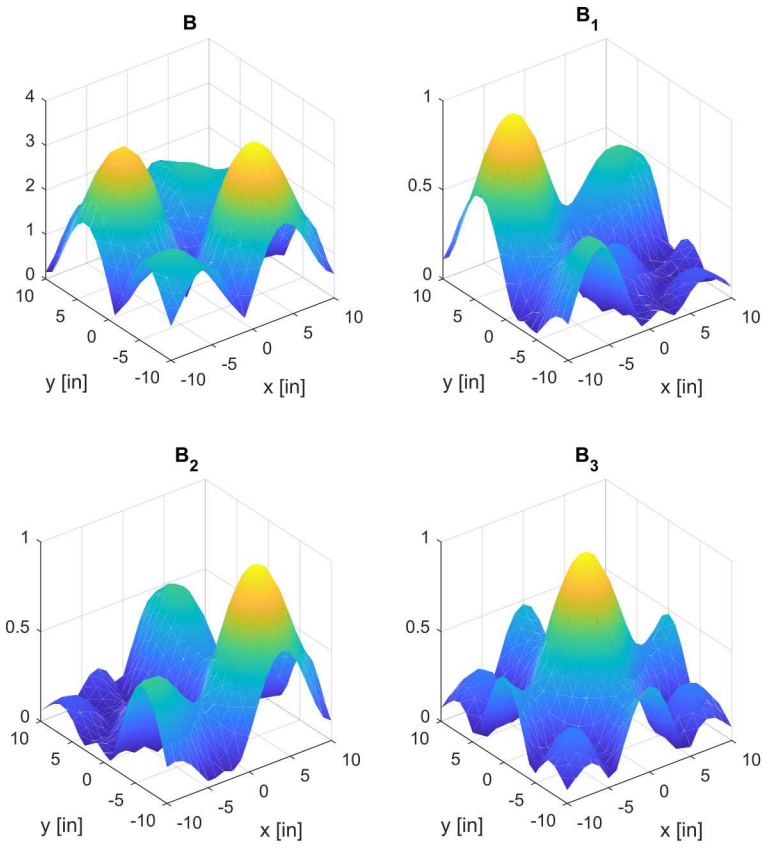

Figure 4-79: Beamforming Analysis Map and Point Spread Functions for Monopole Sources

Using the nonnegative least-squares approach, the following solution was obtained.

$$B = 2.43 * B_1 + 2.82 * B_2 + 0 * B_3$$

Thus, assigning the scale factors for each PSF to their corresponding locations, the deconvolved solution becomes the following beamforming map.

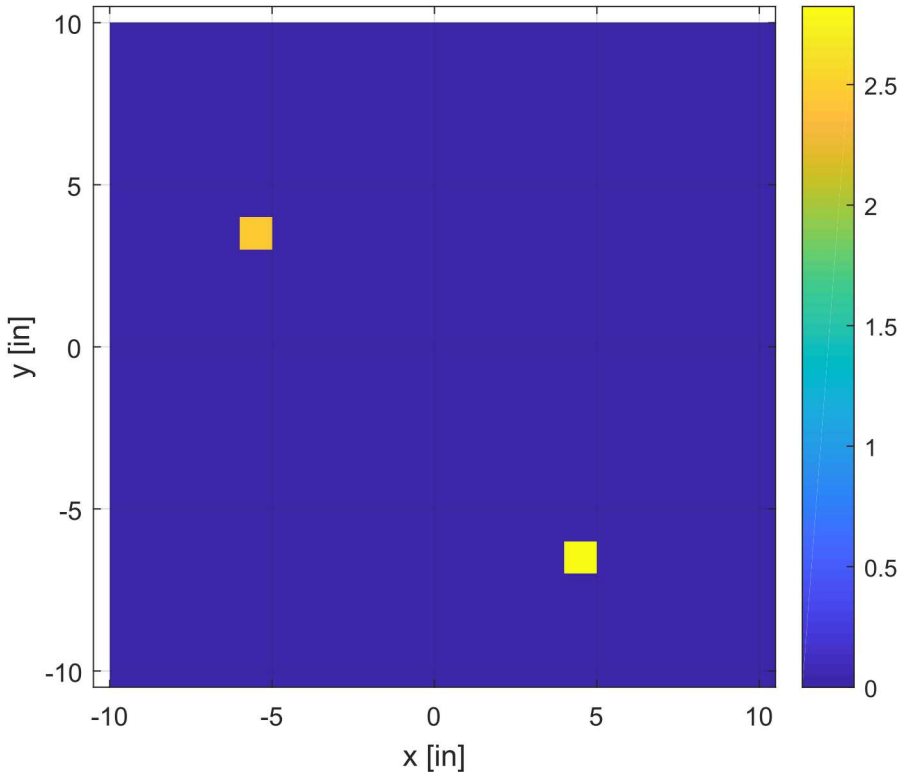

Figure 4-80: De-Convolution Beamforming Analysis Map Results for Two Monopole Sources

As shown in the figure, the location of each source can now be described with greater accuracy. In practice, the PSFs for all candidate locations would need to be considered. In this case, the resulting map may not be as distinct as the hypothetical situation presented here. However, as demonstrated by other others, the spatial resolution of the resulting map is improved.

4.7.4. Non-Contact Damage Detection via Acoustic Beamforming Methods

The application of acoustic beamforming for non-contact damage detection has been investigated by multiple authors. Many of these methods rely on comparisons between a healthy (i.e. damage free) structure and a structure with potential damage. In practice, this would be accomplished by obtaining a nominal beamforming map of a healthy structure and comparing later measurements on the same structure to this baseline data. Locations which exhibit high source intensity relative to their nominal characteristics can be identified as locations of potential damage—locations where something has changed within the structure to increase the sound radiation/transmission.

These comparison metrics can be implemented on a frequency dependent basis or as a cumulative metric across all frequencies. In applications where damage is known to have specific frequency domain characteristics, detection can be limited to these

bandwidths. In the absence of apriori knowledge of the critical bandwidths for damage detection, the beamforming ought to be conducted on response data due to broadband random excitation—excitation with energy across all frequencies. In the ideal scenario, this analysis could be performed by leveraging the natural acoustic emission of the target structure in operation. However, in many applications, the radiated sound pressure level is insufficient to guarantee reliable operation of the beamformer. In these applications, an external excitation method must be provided.

Previous authors have explored the use of both external piezo-patches and internal speakers to provide the necessary excitation required for damage detection beamforming methods. In the case of speaker excitation, a sound source is imbedded into the structure under examination and acoustic transmission/radiation from the structure is used for beamforming. The benefit of these methods is the possibility to improve the signal-to-noise ratio (SNR). The higher the SNR, the greater the performance of beamforming methods. The use of external excitation also enables additional signal processing techniques which can be used to further improve performance. In one of such approaches, the microphone response data can be pre-processed prior to beamforming to include only energy which is correlated to the known excitation.

In the application under investigation here, the beamforming array is constrained by the desire to make it compact enough to enable mobile deployment on a drone for remote operation. Due to the large size of a wind turbine, it is not feasible to design a ground based array with sufficient accuracy along the surface of its blades. By equipping a drone with a mobile array, the array can be positioned closer to the blade surface and enable greater potential for damage detection. The drone could then be programmed to fly a pre-determined flight scanning the surface of the wind turbine blade. Scans from subsequent frames of data (i.e. positions along the surface) could then be stitched together into a larger beamforming map.

4.8. References

4.1 Roach, D., Neidigk, S., Rice, T., Duvall, R., Paquette, J., "Blade Reliability Collaborative: Development and Evaluation of Nondestructive Inspection Methods for Wind Turbine Blades," Sandia DOT Report, SAND2014-16965, September 2014.

4.2 Mayer,T. Scherling, D., Sun, J., "Shearography Testing on Aerospace CFRP Components," *J. of Inspection Physics*, June 2002.

4.3 Hsu, D., Barnard, D., Peters, J., Kommareddy, V., Dayal, V., "Aerospace NDT Using Piezoceramic Air-Coupled Transducers,"

4.4 Buckley, J., "Air-coupled Ultrasound - A Millennial Review,"

4.5 Strycek, J., Loertscher, H., "Ultrasonic Air-Coupled Inspection of Advanced Material,"

4.6 Kommareddy, V., Peters, J., Hsu, D.," Air-Coupled Ultrasonic Measurements in Composites,"

4.7 Roach, D.P., Moore, D., and Walkington, P., "Nondestructive Inspection of Bonded Composite Doublers for Aircraft", Proceedings of SPIE Conference on Nondestructive Evaluation of Aging Aircraft, December 1996.
4.8 Roach, D., Beattie, A., Dahlke, L., Gieske, J., Hansche, B., Phipps, G., Shagam, R., and Thompson, K., "Emerging Nondestructive Inspection Methods for Aging Aircraft"; Dept. of Energy SAND Report 92-2732, March 1994; Dept. of Transportation Report No. DOT/FAA/CT-94/11, October 1994.
4.9 Palmer, D.D., Wood, N.O., "Development of MAUS Enhancements for Large Area Wing Inspections," Air Force Structural Integrity Conf., Dec. 1999.
4.10 Thomas, R., Favro, L., Han, X. and Zhong, O. “Thermal Methods Used in Composite Inspection,” Comprehensive Composite Materials, vol. 5 Pergamon/Elsevier Science, Oxford, 2000.
4.11 Favro, L., Han, X. and Thomas, R.,"Quantitative Thermal-wave measurement of defects in composite aircraft structures", 44th International SAMPE Symposium and Exhibition, 1999.
4.12 Shepard S.M. and Maldague X.P.V., “Infrared and Thermal Testing”, in Aerospace NDT ASNT Industry Handbook, Ch. 11, Bossi R., ed, ASNT; 2014.
4.13 Roach, D.P., “A Quantitative Assessment of Conventional and Advanced NDI Techniques For Detecting Flaws In Composite Honeycomb Aircraft Structures”, DOT/FAA/TC-15/63, Dec 2016.
4.14 Shepard, S., Roach, D., “Signal Enhancement and Noise Reduction Strategies for Thermographic Inspections,” FAA/DOD/NASA Aging Aircraft Conference, May 2009.
4.15 Roach, D.P. and Rice, T.M, “A Quantitative Assessment of Advanced NDI Techniques for Detecting Flaws In Composite Laminate Aircraft Structures”, DOT/FAA/TC-15/4, Mar 2016.
4.16 Balageas, D. L. Defense and illustration of time-resolved pulsed thermography for NDE. QIRT J. 1–1 (2012). doi:10.1080/17686733.2012.723243.
4.17 Shepard S.M., Hou Y.L., Lhota, J.R., Golden J.M., Automated processing of thermographic derivatives for quality assurance. Optical Engineering 2007;46:051008. doi:10.1117/1.2741274.
4.18 Thermal Wave Imaging, Inc., Ferndale, MI, www.thermalwave.com
4.19 Roach, D., Rice, T., Paquette, J., “Probability of Detection Study to Assess the Performance of Nondestructive Inspection Methods for Wind Turbine Blades,” Sandia DOT Report, SAND2017-8032, August 2017.
4.20 Aizawa, K., Poozesh, P., Niezrecki, C., Baqersad, J., Inalpolat, M., and Heilmann, G., “An acoustic-array based structural health monitoring technique for wind turbine blades,” Proc. SPIE 9437, Structural Health Monitoring and Inspection of Advanced Materials, Aerospace, and Civil Infrastructure, Apr 2015.

THIS PAGE INTENTIONALLY LEFT BLANK

5. NONDESTRUCTIVE INSPECTION METHODS DESIGN DOWN SELECTION

Based on the scope of the project (i.e., duration and funding), the team decided to focus on 1 or 2 of the NDI methods previously described in Section 0. The emphasis was to select method(s) that fit into the framework of SkySpecs' existing drone platform and inspection methodology. With this in mind, Sandia and SkySpecs worked together to develop a set of design criteria, as described in Section 5.1. Then, using these criteria, Sandia used a combination of research and experience to score each NDI method in Section 5.2. Adjustments were made to these scores, as needed, based on SkySpecs' expertise. Based on these final scores, thermography was selected as the primary NDI method for testing and integration, as detailed in Section 5.3. Additionally, in Section 5.4, a number of NDI methods that showed promise but were deemed outside the scope of this project, due to various barriers to entry, were selected for some level of additional research.

5.1. Design Criteria and Weighting

In order to successfully deploy a NDI method on SkySpecs' drone, a set of design criteria were developed. These criteria focused on the team's ability to integrate and test the NDI sensor with minimal drone modifications, as well as the NDI method's ability to compliment optical surface inspections and detect subsurface flaws in wind blade structures. Based on these needs, the following list was developed:

- Weight: The drone's payload is limited and a significant amount of its weight capacity is used by the existing custom-built rig and LiPo batteries. Additionally, any added weight decreases the maximum flight time. If the weight is added to the gimbal, that requires additional battery power to operate the gimbal motors and decreases the maximum flight time.
- Cost: Because the NDI sensor would be added to multiple drones, the cost of the sensor and any associated hardware should not be prohibitive.
- Data Storage: The existing custom-built rig contains a multi-TB solid state hard drive which should be sufficient for any inspection method as long as the NDI method does not require exceptionally large files.
- Integration Complexity: Due to the scope of the project, priority should be given to methods that can be easily added to the drone and/or wind turbine.
- Scan Speed (Scan Area / Scan Time): The maximum flight time of the drone is limited and inspection time should be minimized to limit operating costs. Therefore, priority should be given to methods that can inspect large areas quickly.
- Coupling Reliability: Some methods (e.g., ultrasonics) require coupling between the sensor and inspection surface; however, the drone is limited in its ability to fly near the blade or to directly make contact with the blade. Priority should be given to methods that do not require coupling that interferes with the drone's controls.

- Automated Flaw Detection Performance: This criterion measures the ability of an NDI method to successfully detect flaws, given the various inspection challenges of a wind turbine blade (e.g., near surface flaws, full penetration flaws, thick fiberglass laminates, sandwich structures). This criterion also gives weight to the need to quickly identify damage and the desire to avoid lengthy analysis of the NDI data.
- Risk: Due to the time and budget limitations of the project, priority should be given to an NDI method that can be successfully integrated and tested before the end of the project. For the scope of this trade study, risk is an assessment of the likelihood of successfully integrating and testing an inspection method, given factors such as maturity level and expected integration challenges.

5.2. Pugh Matrix

A Pugh matrix approach was selected to quantitatively compare each of the candidate NDI methods. Sandia developed initial weights for each design criteria based on experience and preliminary conversations with SkySpecs. These initial weights were then discussed by the entire team and adjusted, as needed. For example, the weights assigned to data storage and cost were decreased after receiving feedback from SkySpecs. The final weights assigned to each design criteria are listed in Table 5-1.

Table 5-1: Weights Assigned to Design Criteria

Category	Weight
Weight	0.10
Cost	0.05
Data Storage	0.05
Integration Complexity	0.10
Scan Speed	0.20
Coupling Reliability	0.10
Automated Flaw Detection Performance	0.20
Risk	0.20
Total	1.00

After assigning the weights, each category was assigned a score of 1-5, where 5 is the best. For example, for weight, the lightest NDI methods, which fit within the existing drone payload requirements, receiving a score of 5. Then, for each score, a brief rationale was provided. The resulting scores for each method are provided in Tables 5-2 to 5-8.

Table 5-2: Pulsed Thermography Pugh Matrix Results

Category	Weight	Score	Rationale
Weight	0.10	5.0	Lightweight IR cameras are designed for UAVs

Cost	0.05	4.0	Miniature IR cameras are available for < $5k
Data Storage	0.05	4.0	IR video files are expected to be < 10 GB
Integration Complexity	0.10	4.0	Concerns with availability/consistency of a heat source
Scan Speed (Scan Area ÷ Scan Time)	0.20	3.0	Medium scan area needs to be inspected for several seconds at a time
Coupling Reliability	0.10	5.0	No coupling required
Automated Flaw Detection Performance	0.20	3.0	Excellent for sandwich structure and good for near surface flaws, otherwise limited
Risk	0.20	3.0	Effectiveness of heat sources will need to be tested
Total	1.00	3.6	

Table 5-3: Phased Array Ultrasonics Pugh Matrix Results

Category	Weight	Score	Rationale
Weight	0.10	2.0	UT module (such as OmniScan) and water for coupling add significant weight
Cost	0.05	3.0	Estimated ROM cost of a phased array system is $60k
Data Storage	0.05	5.0	File sizes approximately 100's of MBs
Integration Complexity	0.10	2.0	Requires a boom, coupling system, and significant work on automating UT system
Scan Speed (Scan Area ÷ Scan Time)	0.20	2.0	Small scan area needs to be rastered at a limited speed
Coupling Reliability	0.10	1.0	Constant physical contact causes UAV control issues
Automated Flaw Detection Performance	0.20	5.0	Best performance with deeper penetration
Risk	0.20	2.0	No strategy currently exists for maintaining contact for coupling
Total	1.00	2.7	

Table 5-4: Air Coupled Ultrasonics Pugh Matrix Results

Category	Weight	Score	Rationale
Weight	0.10	4.0	Probe weight is relatively low; Dependent on limiting onboard electronics
Cost	0.05	3.0	Estimated ROM cost of an inspection system is $100k, could be significantly more to design custom electronics
Data Storage	0.05	5.0	File sizes approximately 100's of MBs
Integration Complexity	0.10	3.0	Requires a boom and significant work on automating UT system
Scan Speed (Scan Area ÷ Scan Time)	0.20	2.0	Small scan area needs to be rastered
Coupling Reliability	0.10	3.0	No coupling required, distance to blade needs to be held constant to high precision
Automated Flaw Detection Performance	0.20	3.5	Good overall performance; Attenuation concerns when compared to directly coupled UT methods
Risk	0.20	3.0	Moderate maturation level, likely requires custom electronics
Total	1.00	3.1	

Table 5-5: Microwave Pugh Matrix Results

Category	Weight	Score	Rationale
Weight	0.10	4.0	Probe weight is relatively low; Dependent on limiting onboard electronics
Cost	0.05	3.0	Estimated ROM cost of an inspection system is $100k
Data Storage	0.05	5.0	File sizes approximately 100's of MBs
Integration Complexity	0.10	3.0	Requires a boom and significant work on automating microwave system
Scan Speed (Scan Area ÷ Scan Time)	0.20	2.0	Small scan area needs to be rastered
Coupling Reliability	0.10	3.0	No coupling required, distance to blade needs to be held constant to high precision
Automated Flaw Detection Performance	0.20	3.0	Good overall performance, except spar cap-to-shear web bond line and leading and trailing edges, does not work on carbon fiber

Risk	0.20	3.0	Moderate maturation level
Total	1.00	3.0	

Table 5-6: Shearography Pugh Matrix Results

Category	Weight	Score	Rationale
Weight	0.10	2.0	Equipment is moderately sized; vacuum attachment and pump could add considerable weight
Cost	0.05	2.0	Estimated ROM cost of an inspection system is $200k
Data Storage	0.05	4.0	Files sizes are expected to be < 10 GB
Integration Complexity	0.10	2.0	Requires applied strain, perhaps from wind and significant work on automating shearography system
Scan Speed (Scan Area ÷ Scan Time)	0.20	3.0	Medium scan area needs to be inspected for several seconds at a time
Coupling Reliability	0.10	1.0	Would likely require vacuum attachment to maintain exact position
Automated Flaw Detection Performance	0.20	2.0	Excellent for sandwich structure and good for near surface flaws, otherwise limited
Risk	0.20	2.0	Moderate maturation level; attachment concerns
Total	1.00	2.2	

Table 5-7: Pulse-Echo Ultrasonics Pugh Matrix Results

Category	Weight	Score	Rationale
Weight	0.10	2.0	Counterweights and water for coupling add significant weight
Cost	0.05	3.0	Estimated ROM cost of an inspection system is $100k
Data Storage	0.05	5.0	File sizes approximately 100's of MBs
Integration Complexity	0.10	2.0	Requires a boom, coupling system, and significant work on automating UT system
Scan Speed (Scan Area ÷ Scan Time)	0.20	1.5	Small scan area needs to be rastered, scan area is smaller than PA-UT
Coupling Reliability	0.10	1.0	Constant physical contact causes UAV control issues

Automated Flaw Detection Performance	0.20	5.0	Best performance with deeper penetration
Risk	0.20	2.0	No strategy exists for maintaining contact for coupling
Total	1.00	2.6	

Table 5-8: Acoustic Beamforming Pugh Matrix Results

Category	Weight	Score	Rationale
Weight	0.10	4.0	Microphone weight is relatively low; Dependent on limiting onboard electronics
Cost	0.05	4.0	Equipment costs are expected to be low; Potentially labor intensive to program algorithms
Data Storage	0.05	5.0	File sizes approximately 100's of MBs
Integration Complexity	0.10	3.0	Requires a method for transmitting sound inside the blade (e.g., a speaker near the root)
Scan Speed (Scan Area ÷ Scan Time)	0.20	5.0	Excellent theorectical scan speed, full coverage may be possible
Coupling Reliability	0.10	4.0	No coupling required, distance to blade needs to be held constant (probably to low precision)
Automated Flaw Detection Performance	0.20	3.0	Hypothesized based on expectation that near flaws and deeper flaws could both be detected; Resolution is a potential concern
Risk	0.20	1.0	Very low maturation level; Has not been tested for flaws other than through holes
Total	1.00	3.4	

After reviewing the results of each Pugh matrix, pulsed thermography and acoustic beamforming received the highest total score by a significant margin. Due to its lower risk, pulsed thermography was selected as the primary NDI method for further evaluation. The ability to field a lightweight inspection technique without changes to SkySpecs controls strategy (i.e., flying 4-8 m from the blade) were particularly desirable attributes. Integration considerations for this technique are provided in the subsequent sections.

During the down selection process, it became apparent that a number of techniques, in addition to thermography, warranted additional consideration. In some cases, the NDI method was particularly promising for detecting defects but simply presented too

many integration challenges (e.g., phased array ultrasonics). In other cases, the NDI method showed considerable upside but presented too much risk based on its technology maturation level (e.g., acoustic beamforming). Based on this additional review, acoustic beamforming and a number of other NDI methods were identified for additional work. Multiple promising techniques require close proximity or direct contact with the blade which requires significant changes to the drone controls and associated technical risk. Phase array ultrasonics, in particular, has demonstrated the ability to produce accurate full-penetration inspections of wind blade spar caps and bond lines. Therefore, these methods were highlighted in the following sections, including some preliminary design concepts.

Acoustic beamforming was another technique that was extremely promising, namely due to its fast scan speed and low weight. However, the technique has a very low maturation level, which made it a high risk for primary integration testing. Some initial simulations were performed that demonstrated this this could be a potential up and coming technique that SkySpecs should consider for future work.

Finally, while X-Ray inspections were not included in the original down selection process, SkySpecs requested that the method receive some consideration. Therefore, some initial design concepts and considerations are provided.

5.3. Primary Nondestructive Inspection Method Selected – Thermography

5.3.1. Thermography Integration Concepts

Based on the results of the down selection process, thermography was selected as the most promising method for NDI implementation on a drone platform. The following sections provide a detailed description of the team's considerations for implementing this capability, including hardware selection, flight strategies, thermal gradient sources, and data processing.

5.3.1.1. Thermography Hardware

A large number of IR cameras are available, providing various combinations of specifications. While evaluating these options, the following criteria were determined to be the most important:

- Wavelength – Mid-wave or Longwave IR cameras are appropriate for our temperature range (i.e., near room temperature)
- Thermal Sensitivity – Metric of IR camera's signal-to-noise ratio, typically in mK, lower is better
- Resolution – 640x512 is common in many cameras, although higher and lower resolutions are available, higher is better
- Field of View – Determines the viewable area at a set distance from the area of interest, dependent on the lens selected, should be determined based on the drone's distance from the wind blade

- Weight – Lower is better for drone's payload constraints and battery life, < 450 g is desired based on current SkySpecs drone platform
- Power Consumption – Lower is better for drone battery life
- Frame Rate – A higher frame rate is critical for near surface flaws in materials with high thermal diffusivities, for our application (i.e., fiberglass with low thermal diffusivity) high speed cameras should not be required, 30-60 Hz should be sufficient
- Post-Processing Features – The team plans to perform their own modified thermographic signal reconstruction, as documented in Section 5.3.1.4, so post-processing features are not required, camera must provide access to the raw 16 bit grayscale video feed

Based on the weight and power consumption constraints of drone-deployment, the team focused on miniature longwave IR cameras with uncooled Vandium Oxide (VOx) microbolometer sensors. While these cameras sacrifice some thermal sensitivity when compared to mid-wave IR cameras with cooled Indium Antimonide (InSb) sensors, the miniature IR cameras represented an impressive balance between thermal sensitivity, weight, and power consumption. Examples of these cameras include the FLIR Tau 2 and FLIR Boson series.

The selected IR camera should be mounted to a gimbal to enable the drone to perform thermography inspections from a number of different drone and wind blade orientations. Ideally, the IR camera should be mounted on the same gimbal as the visual inspection camera to allow both cameras to inspect the same area of interest.

5.3.1.2. Thermography Flight Strategies

The capabilities of the drone platform and the flight path both play critical roles in the implementation of a drone-deployed thermography system. The ability of the drone to position itself in an area of interest along the blade and maintain position is critical. Fortunately, autonomous drone positioning is one of the greatest strengths of the SkySpecs drone platform. This gives the team flexibility in selecting methods for performing thermography inspections and post-processing the results.

Typically, thermography inspections are performed with a stationary part and stationary IR camera. This assumption simplifies data processing because each pixel of the IR camera always references the same area of the inspection surface. Conversely, with drone-deployed thermography, both the wind blade and drone are moving relative to the ground and each other. Even though the turbine is stopped prior to beginning inspections, the wind blade can still deflect and move due to the wind, especially near the tip. Also, while the drone has controls in place to maintain position, it still moves slightly, especially in higher winds. Therefore, to mimic a traditional thermography inspection, these movements need to be subtracted out. SkySpecs uses a combination of GPS and LiDAR position data as well as IR camera gimbal orientation data that could potentially be used to subtract out these movements and to link the data to an area of interest along the blade. While this capability was

not implemented during this project, concepts for future work are explored in Section 8.1.2.

Using this near-stationary approach, the drone-deployed thermography system could be deployed for a number of target inspections. The team developed the following list of potential inspections:

- Systemic defects, as noted by the OEM and/or wind farm operator
- Visual indication from the SkySpecs visual inspection data
- Planned repairs, to estimate sizing
- Existing repairs
- High stress and high suspect areas, as noted by the OEM and/or wind farm operator
- Suspected water ingress in the wind blade tip

While this list is not intended to be exhaustive, it provides a good foundation for identifying areas where the drone-deployed thermography system can provide value. Note that all of these proposed inspection areas require *a priori* knowledge of where to perform an inspection. Because each inspection takes approximately a minute and the inspection area (i.e., IR camera field of view) is relatively small, the time required to perform stationary inspection of the entire blade isn't feasible. The battery life required and the opportunity cost of deploying the drone asset for that much time do not fit into the current business model.

The focus of SkySpecs' inspection strategy is rapid, automated inspections of wind turbine blades. Therefore, the proposed near-stationary thermography inspections would likely function as an add-on inspection for specific, known concerns. While these add-on inspections have value, there's also significant interest in using thermography to find unknown subsurface damage as part of SkySpecs' automated flight pattern. As such, two additional "moving" concepts were generated:

- Perform thermography inspections during "standard" flight path
    1. The current "standard" flight path for visual inspection includes a number of start/stop motions, as the drone flies along each side of the blade.
    2. Results are based on instantaneous IR images/video frames. Without accumulated temperature vs. time data on the surface of interest, post-processing techniques, such as the modified Thermographic Signal Reconstruction analysis described in Section 5.3.1.4, cannot be performed.
    3. Depending on the severity of the flaw and the timing of the flight, some flaws should be detectable; however, the sensitivity is expected to be considerably lower than the near-stationary tests.

- Perform thermography inspections during an augmented flight path
    1. Adjust the current "standard" flight path to include relatively fast back and forth movement, as shown in Figure 5-1.
    2. Results are based on a combination of instantaneous IR images/video frames, as well as some accumulated temperature vs. time data on the surface of interest. Based on this approach, a limited version of the modified Thermographic Signal Reconstruction analysis described in Section 5.3.1.4, may be feasible.
    3. The flaw detection sensitivity is expected to be somewhere between near-stationary testing and "standard" flight path testing.

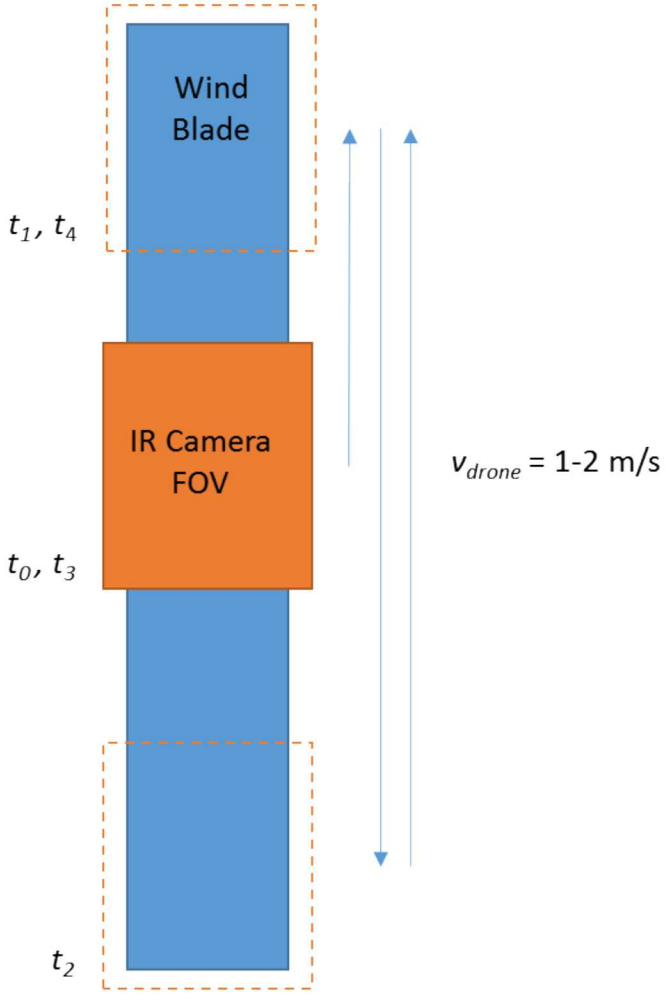

Figure 5-1: Notional Example of an Augmented Flight Pattern Showing Back and Forth Drone Movement

While this project focused on near-stationary thermography testing, thoughts and recommendations on the potential implementation of these flight strategies are provided in Section 8.1.2.

5.3.1.3. Thermography Thermal Gradient Source Concepts

As described in Section 4.2, active thermography requires thermal gradients to detect potential flaws. A common source of these thermal gradients is a thermal impulse applied to the inspection surface using flash tubes or other impulse heating method. For the interest of this project, a variety of heating sources were considered, including:

- Flash Tubes
- Solar Radiation
- Frictional Heating
- Strain Heating
- Forced Air Heating

From these potential heating sources, four thermal gradient source concepts were generated:

- Flash Tube Heating – Use drone-deployed flash tubes with a LiPo battery and capacitor energy source.
- Solar Radiation Heating – Pitch blades into and out of the sun (see Figure 5-2).
- Operational Heating – Generate frictional and/or strain heating of flaws during normal operation and then stop the turbine for IR inspections.
- Internal Forced Air Heating – Use a forced hot air heater to warm the air mass inside the blade (see Figure 5-3).

Figure 5-2: Solar Radiation Thermal Gradient Source Concept

Figure 5-3: Internal Forced Air Heating Thermal Gradient Source Concept

Table 5-9 documents the advantages and disadvantages of each of these concepts. Because each concept contains some significant risks, all four concepts were evaluated to some degree in benchtop and/or drone integration testing. The results of these tests are documented in Sections 6 and 0.

Table 5-9: Advantages and Disadvantages of Thermal Gradient Source Concepts

Concept	Advantages	Disadvantages
Flash Tubes	• Controlled, repeatable energy levels • Precise timing • Not dependent on weather • Easily tested in a laboratory environment • Requires very short temperature soaks	• Relatively large amount of energy required – battery and weight concern • Close proximity to blade required – drone controls concern • Low total energy – depth of penetration concern
Solar Radiation	• Relatively high total energy – good depth of penetration • Does not require any	• Uncontrolled energy levels • Imprecise timing

	additional equipment onboard the drone • Easily tested in a laboratory environment • Requires relatively short temperature soaks	• Dependent on weather conditions
Operational	• Does not require any additional equipment onboard the drone • Potentially high total energy – good depth of penetration	• Uncontrolled energy levels • Imprecise timing • Difficult to test in a laboratory environment • Limited research on the types of flaws that can be detected
Internal Forced Air	• Does not require any additional equipment onboard the drone • Semi-controlled energy levels • Easily tested in a laboratory environment • High total energy – good depth of penetration	• Imprecise timing • Requires access to blade root • Requires relatively long temperature soaks • Less sensitive to near surface flaws • Only effective on solid laminates (e.g., spar cap)

5.3.1.4. Thermography Data Processing Strategy

As described in Section 4.2.1, Thermographic Signal Reconstruction (TSR) is an effective method for processing thermographic NDI data. Thermal Wave Imaging developed and patented this approach and provided approval for the team to use TWI's technology for the research purposes of this project.

The following section briefly describes a modified TSR approach based off TSR basics [5.1] that was utilized by this project for near-stationary flight strategies. This summary is not intended to be exhaustive and assumes knowledge of the TSR basics, as briefly described in Section 4.2.1 and associated references. A MATLAB integration of this process is provided in Appendix B.2. The modified TSR approach uses the following process:

1. Rotate and crop each IR video frame, as needed, to select a Region of Interest (ROI).

a. Assume test specimen and IR camera are stationary.

b. Display one frame of the IR video.

c. Employ a user interface to select rotation and crop image.

d. Store variables for rotating and cropping image.

2. Save 16 bit grayscale values (corresponding to signal intensity and surface temperature) for each pixel within the (ROI) for each frame.

3. Mimic $\Delta T = T_{Surf}(t) - T_{Surf}(0^-)$ by subtracting 97% of the minimum value of each pixel from each frame of the IR video, where T_{Surf} is the front surface temperature and t is time.
(Note: The purpose of this step is to generate a temperature-time history for each pixel value that resembles an exponential temperature decay that approaches zero. This is less representative of the specimen response than subtracting the pixel values prior to applying the heat input, but it provides additional flexibility for the purposes of this project, which includes testing a variety of heat inputs. Ultimately, it provides a similar shape as a "true" TSR analysis and enables the user to examine the results using the same methods. Also, the 97% value is somewhat arbitrary and is intended to demonstrate that the final surface temperature has increased when compared to the initial surface temperature, prior to heating.)

4. Take the natural log of "ΔT".

5. Take the natural log of time.

a. Determine $t = 0$

i. Assume the maximum pixel value occurs at t_0 (e.g., peak temperature achieved when the flash tubes provide a heat impulse to the specimen).

b. Time is considered the time elapsed from t_0 of each frame, based on the frame rate.

c. Take the $ln(t)$ for each frame.

6. Select a subset of frames to fit a polynomial to the temperature-time history of each pixel.
(Note: The goal of this step is to select a subset of training points based on approximately equally spaced $ln(t)$ values rather than equally spaced t values.)

a. Select a target number of training points n_{input} for each pixel.

i. Create n_{input} linear spaces between frame $ln(t_0)$ and the $ln(t_{Final})$.

ii. Select $ln(t)$ values that approximately equal each of these linear spaces.

7. Create the TSR functions by fitting a polynomial, using least squares regression to determine the values of each coefficient, for each pixel using the selected training points.
(Note: Polynomials of degree 6 were used, based on trial and error.

8. Calculate the 1st derivative (1D) polynomial functions for each pixel by using the Power Rule to differentiate the TSR polynomial functions.

9. Calculate the 2nd derivative (2D) polynomial functions for each pixel by using the Power Rule to differentiate the 1st derivative polynomial functions.

10. Create a vector of linearly spaced $ln(t)$ values for plotting the output values of the TSR, 1D, and 2D polynomial functions.

11. Calculate and save the values for each pixel for each $ln(t)$ value using the TSR, 1D, and 2D polynomial functions.

12. Save the TSR, 1D, and 2D results.

a. Reassemble the pixels into frames.

b. Scale the frames to 8 bit values, taking up the maximum range of 0 to 255. (Note: While this removes the temperature-time history of the pixels, it enables the user to observe contrast between different areas of the specimen, which typically corresponds with flaws.)

c. Save each frame as a .tiff image.

d. Save all the frames as a .tiff stack.

The end result of this process is three .tiff stacks for the TSR, 1D, and 2D analyses. Each image of these stacks is auto-contrasted. This enables the user to identify differences in the thermal response at different pixel locations. The differences are considered flaw indications, which the user can further evaluate to determine their root cause. Figure 5-4 shows an example of .tiff images generated using this modified TSR approach.

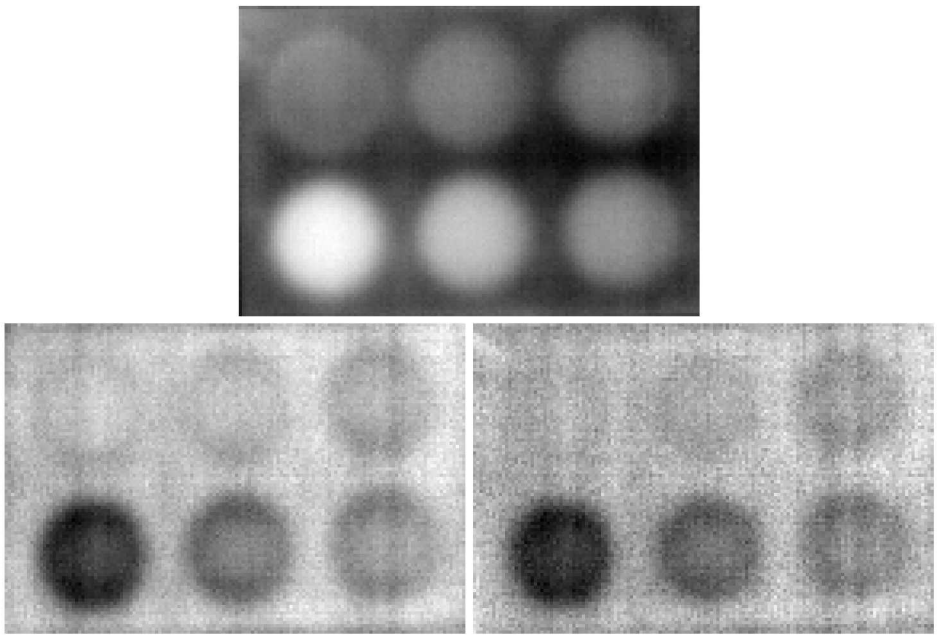

Figure 5-4: Example Results for TSR, 1D, and 2D Analyses

5.4. Promising Nondestructive Inspection Methods Considered for Future Work

After completing the down selection process, it became apparent that a number of techniques, in addition to thermography, warranted additional consideration. In some cases, the NDI method was particularly promising for detecting defects but simply presented too many integration challenges (e.g., phased array ultrasonics). In other cases, the NDI method showed considerable upside but presented too much risk based on its technology maturation level (e.g., acoustic beamforming).

This section documents the work that was performed to begin to address some of the concerns surrounding these methods, such as integration design concepts, simulations, and experiments. Additionally, this section provides a brief summary of the remaining work or technological breakthroughs required in order to pursue their future implementation.

- Design concepts for other promising NDI methods (i.e., ultrasonic, X-Ray, acoustic beamforming)
- NDI methods that had 1 or 2 significant limitations (e.g., microwave with sensitive standoff distance, more suitable for crawler robot technologies)
- NDI methods to keep an eye on in the future (e.g., air-coupled UT, including a design concept)

5.4.1. Ultrasonic Inspection

Previous research [5.2, 5.3] has shown that low frequency (i.e., 0.5 or 1.0 MHz) phased array ultrasonic inspection is the best overall NDI technique for wind blade inspections and is the only NDI technique that is capable of full penetration of thick spar cap structures. However, due to integration concerns, namely the ability of the drone to make consistent contact with the blade, ultrasonic inspections were not selected for primary evaluation on this project. Nevertheless, as technology advances, opportunities to include ultrasonic inspection capabilities should always be carefully considered.

The following subsections provide some initial concepts for the integration of ultrasonic inspection systems on a drone platform, along with some thoughts on the known challenges that need to be addressed. While all of these concepts require an extended boom, the team decided not to include a counterweight based on SkySpecs' feedback. The expectation is that the drone is able to compensate for some shift in the center of gravity. Before fielding any of these concepts, it's recommended that the user performs calculations on the mass and length of the boom to validate the assumption that the drone can accommodate this center of mass offset.

5.4.1.1. Phased Array Ultrasonics Integration Concepts

Phased array ultrasonics (UT) is currently the most promising of the ultrasonic inspection techniques. In general, UT requires direct coupling with the inspection surface, including some form of couplant, such as water or gel. Figure 5-5 shows an example integration concept with an ultrasonic probe extended out from the drone on a

boom. The sensor would need to make direct contact with the wind blade surface, and any momentary loss of contact would result in a corresponding signal loss. Additionally, some type of couplant dispensing system would be required, such as a water reservoir and a mister or weep hole located near the sensor. Spring loading at the end of the boom could allow for some motion of the drone while still maintaining sensor contact.

The main disadvantages of this concept are drone controls issues, weight concerns, sensor location encoding logistics, and data transfer needs. The SkySpecs drone is currently controlled with GPS and LiDAR which enables it to fly around the blade from a safe distance of 4-8 m. Additional work would be required to reduce this distance. Between the accuracy of the sensors and the relative movement of both the drone and blade, direct contact presents a number of controls issues.

Ultrasonic inspections can also present a number of weight concerns. The ultrasonic transducer, boom, water reservoir, mister, and transducer controller/computer (e.g., Olympus Focus PX) are expected to add up to a sizeable weight. Optimization of these features along with an increase in drone size (e.g., Alta Freefly 8) would likely be required to keep the system within payload limits.

Another consideration is the need for a method to track sensor movement, such as encoders or detailed GPS and LiDAR information. This information on sensor movement is required to successfully convert the ultrasonic A Scans into C Scans.

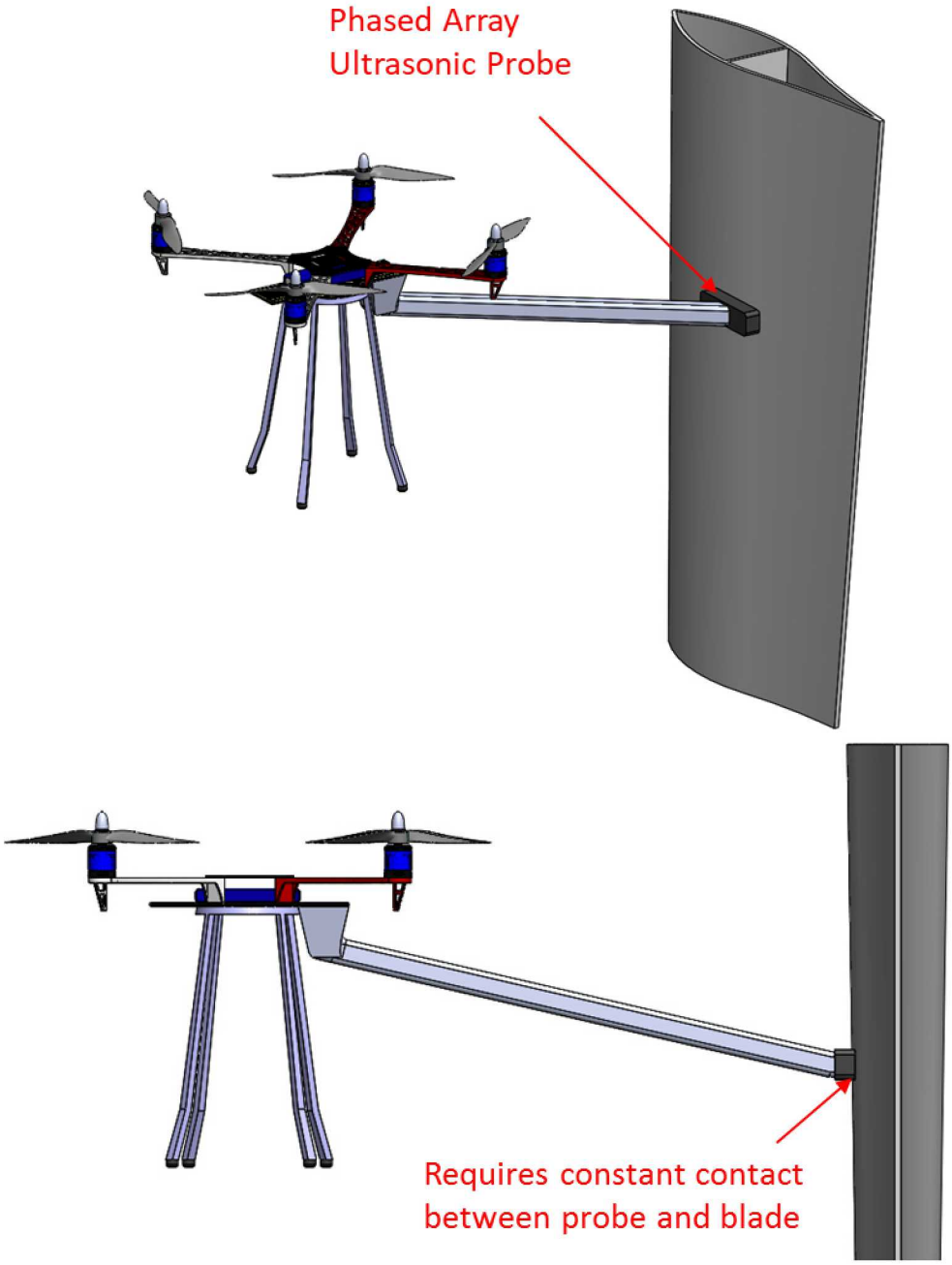

Figure 5-5: Phased Array Ultrasonics Drone Integration Concept

5.4.1.2. Air-Coupled Pulse-Echo Ultrasonics Integration Concepts

Air-coupled pulse-echo ultrasonics (AC-UT) share most of the same design considerations as the previously discussed directly-coupled ultrasonics. The main difference is that the air-coupled ultrasonics require a consistent air gap for coupling rather than direct contact. Figure 5-6 illustrates an example concept of drone-deployed air-coupled ultrasonics.

By eliminating the need for a couplant system, this design would require less complexity and weight. However, flying in consistently close proximity to the wind blade still presents substantial drone control challenges. In fact, without additional research, it's not clear whether this technique would be more or less difficult to implement than direct contact.

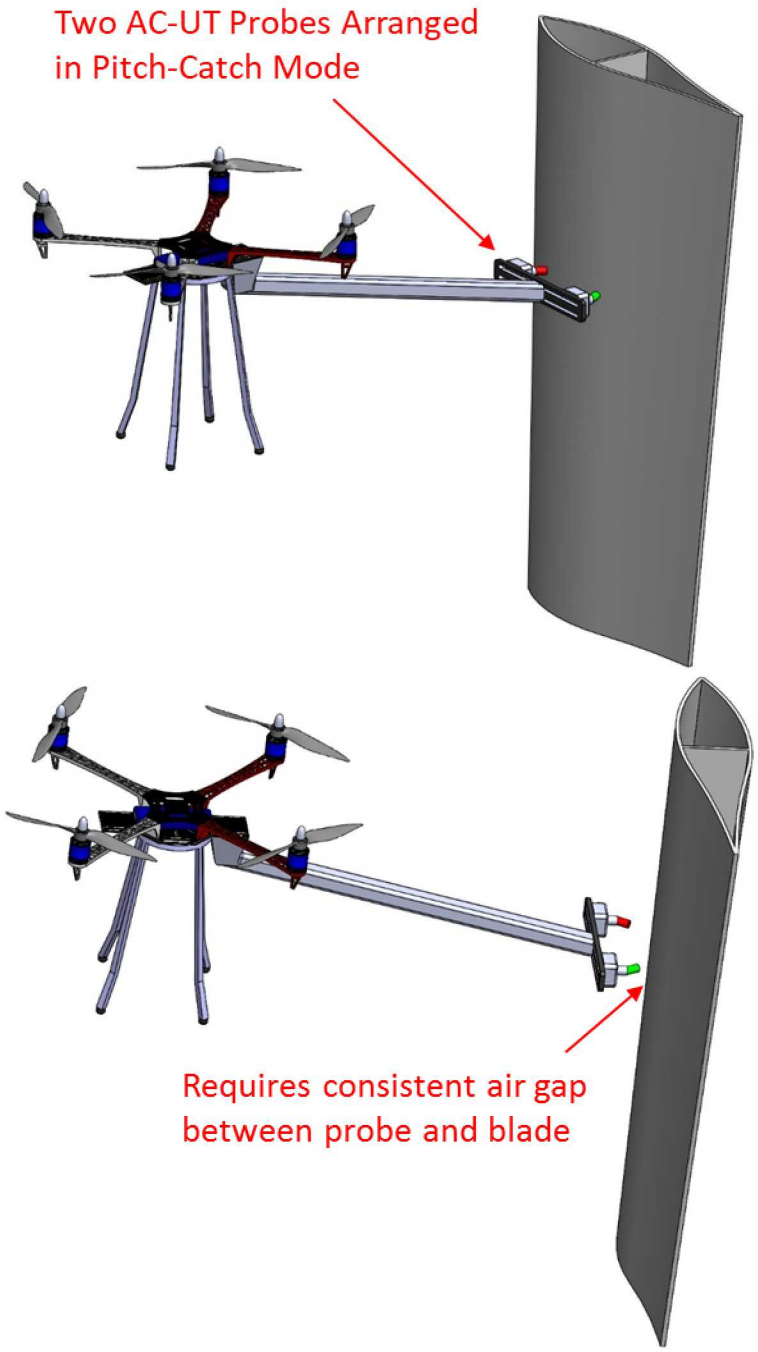

Figure 5-6: Air-Coupled Pulse-Echo Ultrasonics Drone Integration Concept

Another consideration is that air-coupled ultrasonics are currently less effective than direct coupled ultrasonics due to the signal attenuation in air. The technology may require additional maturation before it can be considered for drone integration.

5.4.1.3. Air-Coupled Through Transmission Ultrasonics Integration Concepts

The final ultrasonic inspection concept is air-coupled through transmission ultrasonics. The concept is similar to air-coupled pulse-echo ultrasonics, except the ultrasonic signal is passed through the material instead of reflected off a back wall. In general, the concept for integrating the transducer is the same except the through transmission limits the capability to thin sections, such as the trailing edge, where the two mating transducers can be positioned on opposite sides of the structure to be inspected. Figure 5-7 shows a design concept.

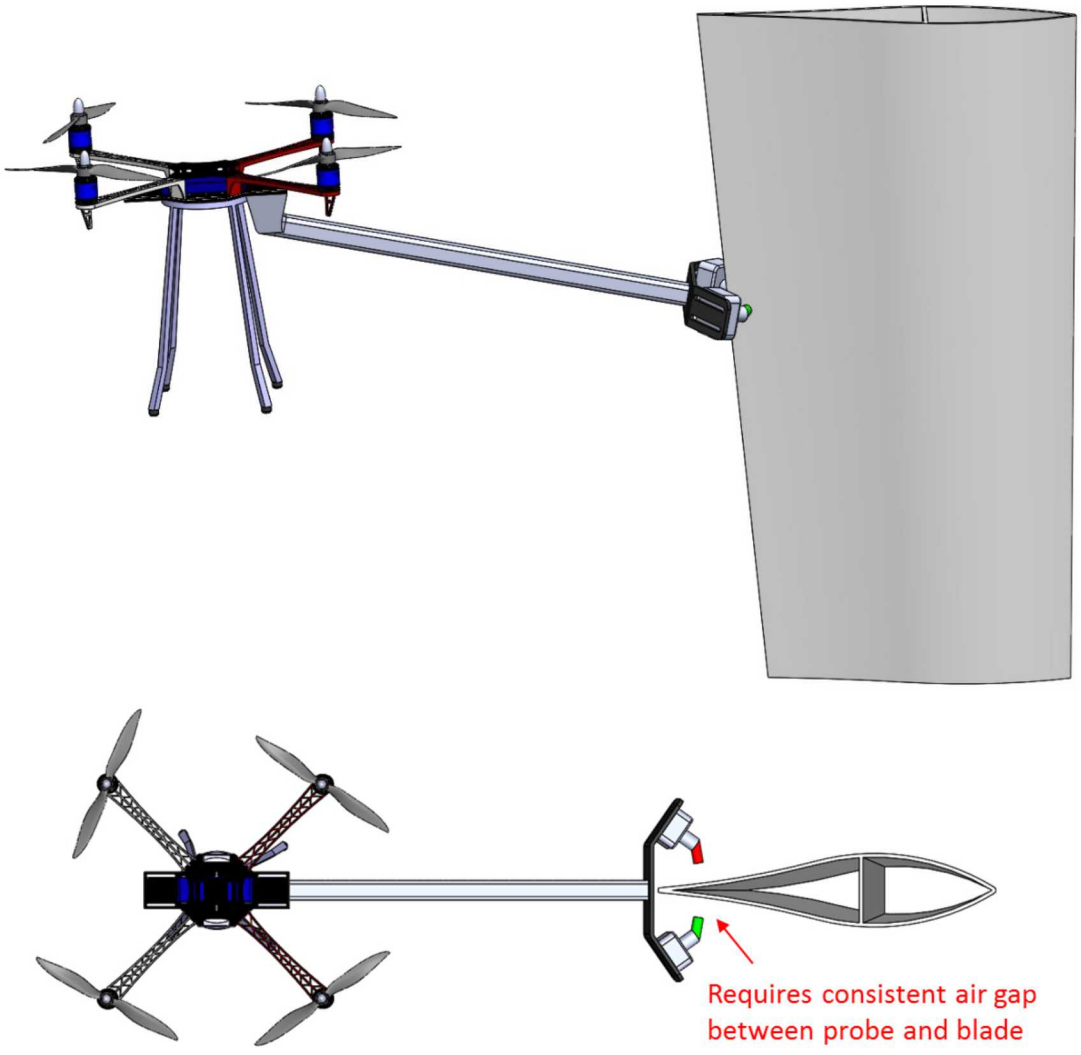

Figure 5-7: Air-Coupled Through Transmission Ultrasonics Drone Integration Concept

5.4.2. Acoustic Beamforming Inspection

5.4.2.1. Acoustic Beamforming Integration Concepts

Based on some initial computational results, it was determined that an acoustic beamforming design would require at least two rows (i.e., booms) of microphones to provide spatial information on the location of defects. A concept using two horizontal rows of microphones is provided in Figure 5-8. A key consideration is the drone propeller noise, which would need to be isolated from the sound source of interest. This isolation may be able to be performed physically (e.g., strategic microphone location) or computationally. Finally, this method requires a noise source inside the blade (e.g., speakers in the blade root), which presents integration challenges that may be more conducive to gross, known damage or manufacturing inspections.

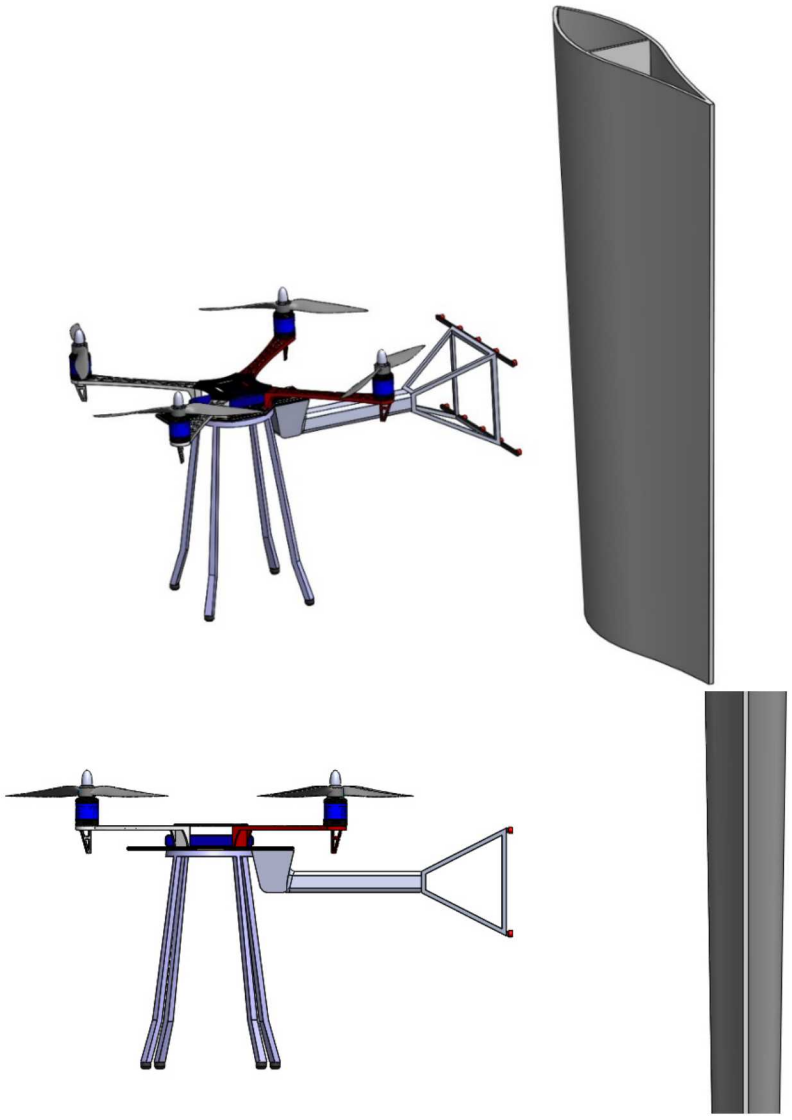

Figure 5-8: Acoustic Beamforming Drone Integration Concept

While this concept has promising attributes, additional research and integration was outside the scope of this project.

5.4.3. X-Ray Inspections

5.4.3.1. X-Ray Integration Concepts

SkySpecs approached Sandia with the concept of lowering an X-Ray source down inside of the wind blade for inspections. After consideration of this concept, a similar alternative idea was proposed. Because the X-Ray detector (i.e., film or digital receivers) needs to be held still in relation to the inspection surface, the detector should be lowered down into the blade or adhered to the backside of the blade. Then, the X-Ray source could be mounted on the drone and flown within close proximity of the blade, as shown in Figure 5-9.

A potential X-Ray source is the Golden Engineering XRS3 shown in Figure 5-10. The XRS3 weighs 11.8 lbs and has a maximum photon energy of 270 kV. While considered portable by X-Ray source standards, the weight is relatively high for drone deployment and would likely require substantial reconfiguration of the SkySpecs drone (or a second, specialized drone platform). Because fiberglass composites are nearly transparent to X-Rays, a relatively low energy level should be used. Additional work would be required to characterize X-Ray performance using Sandia's Wind Blade NDI Test Specimen Library.

Meanwhile, an X-Ray detector would be required on the backside of the inspection surface of interest. A high resolution digital detector is recommended. This detector could be lowered down inside the blade from the root or adhered to the backside of the blade. Additional consideration is required to determine the most appropriate method for positioning the source, such as a drone, climber robot, or human inspector that repels down blades.

Due to the obvious integration challenges, X-Ray inspection was not pursued beyond these initial design concepts and considerations.

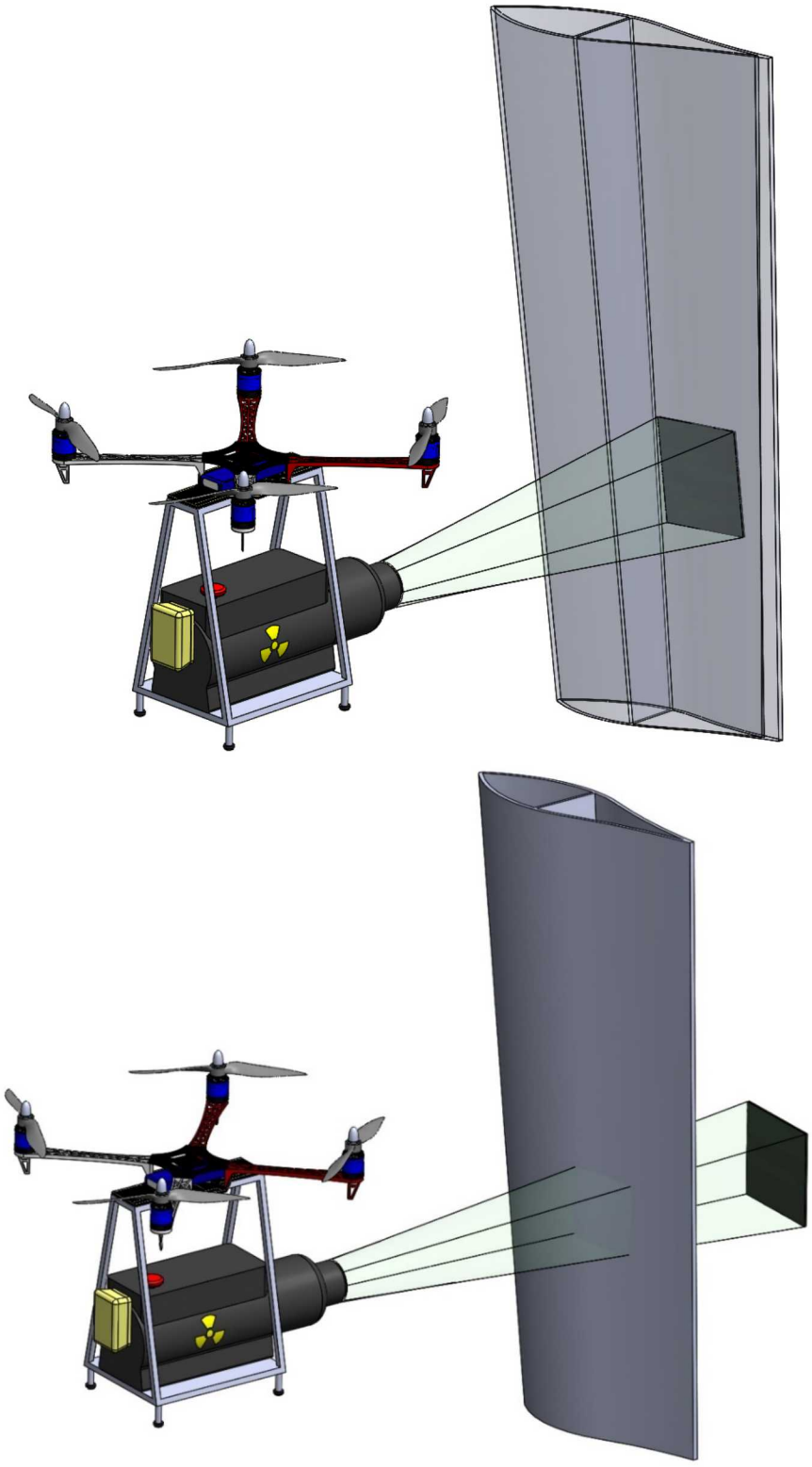

Figure 5-9: X-Ray Drone Integration Concept

Figure 5-10: Golden Engineering XRS3 X-Ray Source

5.5. References

5.1 Shepard, S., Jou, J., Lhota, J.R., Golden, J.M., "Automated processing of thermographic derivatives for quality assurance," Optical Engineering 46(5), May 2007.

5.2 Roach, D., Neidigk, S., Rice, T., Duvall, R., Paquette, J., "Blade Reliability Collaborative: Development and Evaluation of Nondestructive Inspection Methods for Wind Turbine Blades," Sandia DOT Report, SAND2014-16965, September 2014.

5.3 Roach, D., Rice, T., Paquette, J., "Probability of Detection Study to Assess the Performance of Nondestructive Inspection Methods for Wind Turbine Blades," Sandia DOT Report, SAND2017-8032, August 2017.

6. THERMOGRAPHY BENCHTOP TESTING

Based on the design down select performed in Section 5, a lightweight thermography system was developed and tested. The following sections describe the initial thermography benchtop testing that was performed to verify the potential effectiveness of this system and ascertain the parameters that will be critical for deploying a thermography system on a drone platform. In particular, this test plan had the following goals:

- Characterize the effectiveness of the heat sources proposed in Section 5.3.1.3 to generate a temperature gradient sufficient for inspecting flaws in fiberglass wind blades. This characterization includes the following:
    1. How much thermal gradient is required (i.e., how long does the surface need to be heated for)?
    2. What duration of IR video is required (i.e., how does this inspection technique affect SkySpecs' flight strategy)?
- Establish the viability, depth-of-penetration, and usage space for thermography inspections of solid laminate and sandwich construction regions of a blade.

6.1.1. Thermography System

A FLIR Vue Pro R 640x512 resolution IR camera with a 19mm lens was initially selected for the thermography system. The camera is a miniature lightweight 30 Hz Vandium Oxide (VOx) microbolometer longwave IR camera based on FLIR's Tau core with features specifically designed for drones (e.g., USB power, SD card, smartphone app control). The 19mm lens was selected because it has the narrowest available field of view (FOV), which is desirable based on the approximately 6m distance that the SkySpecs drone flies from the blades. However, after completing initial exploratory testing, it was determined that the added Vue Pro R features limited complete control of the Tau core. In particular, the camera did not allow the user to access the pre-automatic gain control (AGC) data. The resulting post-AGC data would periodically update the thermal contrast of an image, which adversely affected the temperature vs. time history, as shown in Figure 6-1.

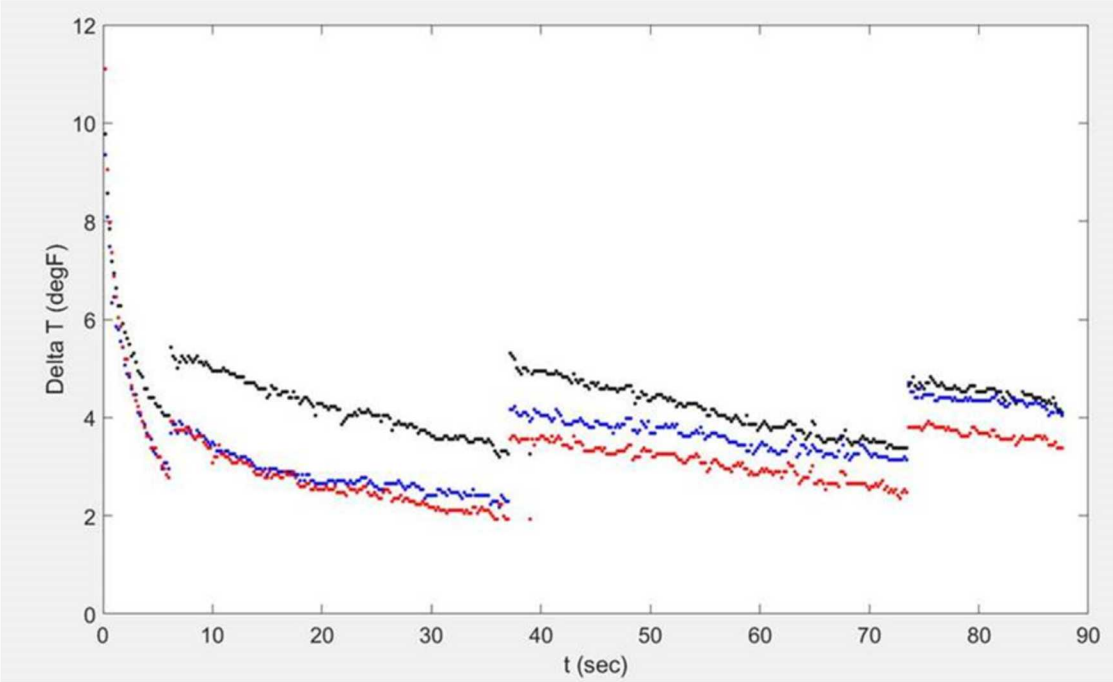

Figure 6-1: Example of Inadequate Temperature vs. Time History on the FLIR Vue Pro R

After determining that the FLIR Vue Pro R would not work for this application, alternative options were reviewed. The FLIR Tau 2, without the undesirable added capabilities, and FLIR Boson cores were both considered. Ultimately, the new FLIR Boson was selected for its size, weight, and power consumption properties. The FLIR Boson is a new, even smaller VOx microbolometer longwave IR camera core. Currently, only the 320x256 resolution option is available, although a 640x512 resolution should be considered in the future. A 9.1 mm lens was selected as a balance between FOV and lens weight. The incredibly small size of the Boson is of particular interest and may enable SkySpecs to place the IR camera on the same gimbal as their existing visible spectrum camera. Also, because the Boson does not include the extra module for drone features, Sandia and SkySpecs will be able to use additional features, such as tapping into the cores raw, pre-AGC video feed.

6.1.1.1. Infrared Camera Settings

For our benchtop testing, the FLIR Boson is controlled by the Windows FLIR Boson Application, version 1.3.0. Both the camera settings and video capture is controlled by this utility, which is available for Windows, macOS, and Linux. Note that newer versions of the software appear to have limited access to a number of camera settings and should be used with caution.

To install the program (and the camera's drivers), the software needs to be downloaded from the following page and installed *before* connecting the camera with a USB cable.

https://groupgets.com/manufacturers/flir/products/boson

Once installed, connect the camera and open the FLIR Boson Application. Select the appropriate Port and Device, as highlighted in Figure 6-2.

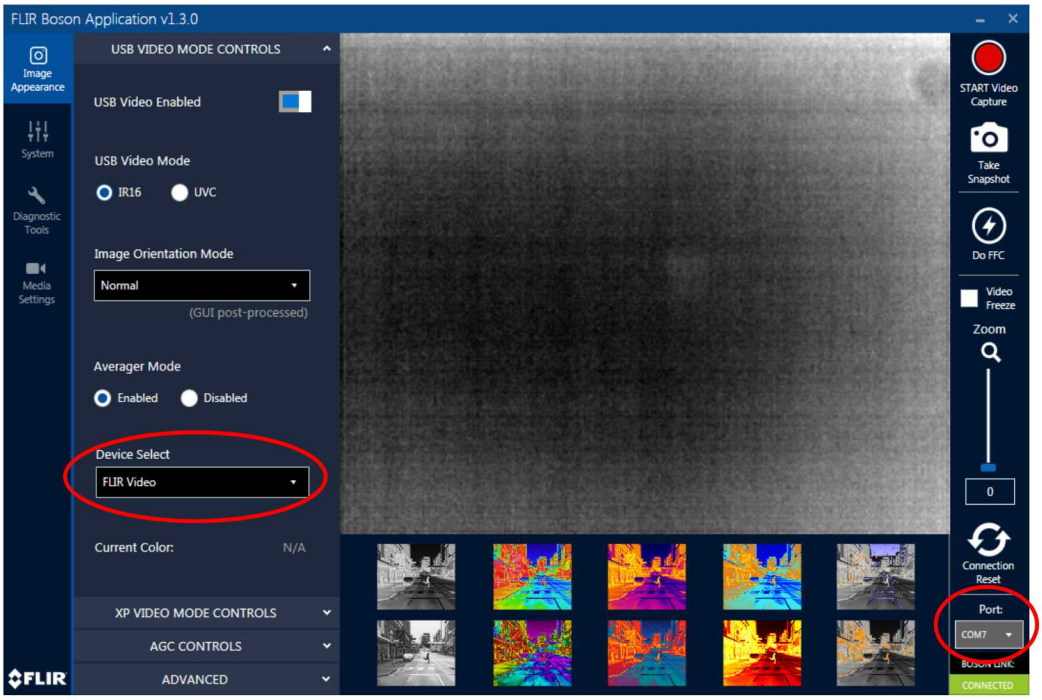

Figure 6-2: Screenshot of FLIR Boson Application Highlighting Port and Device Selections

After connecting the camera, several settings need to be changed or confirmed to ensure the video is captured correctly. The objective is to capture video in the highest quality (16-bit TIFF sequence) and prior to the software applying Automatic Gain Control (AGC). The AGC applies various video processing such as real-time contrast adjustment that can affect the temperature vs. time history. Another important setting to verify is the Flat Field Correction (FFC). FFC compensates for temporal drift and pixel non-uniformity by closing a shutter to provide a flat field for adjusting the nominal value of each pixel. To prevent this from occurring mid-inspection, it's important to set the FFC to manual and perform the operation immediately prior to testing. A 16 frame FFC integration period is selected to achieve the maximum reduction of spatial noise. Note that while a 16 frame integration period requires the greatest amount of time, this is inconsequential because it is performed prior to inspection.

The settings to change or confirm are:

- USB Video Mode: IR16 (see Figure 6-3)
- XP Video Tap Point: Pre-AGC (see Figure 6-4)
- FFC Mode: Manual (see Figure 6-5)
- FFC Integration Period: Sixteen Frames (see Figure 6-5)

- Frame Rate: 60 FPS (see Figure 6-6)
- Quality: N/A (grayed out for IR16 USB Video Mode) (see Figure 6-6)
- File Save Path: Set to User's Preference (see Figure 6-6)
- File Name Prefix: Set to Test Specimen ID (see Figure 6-6)

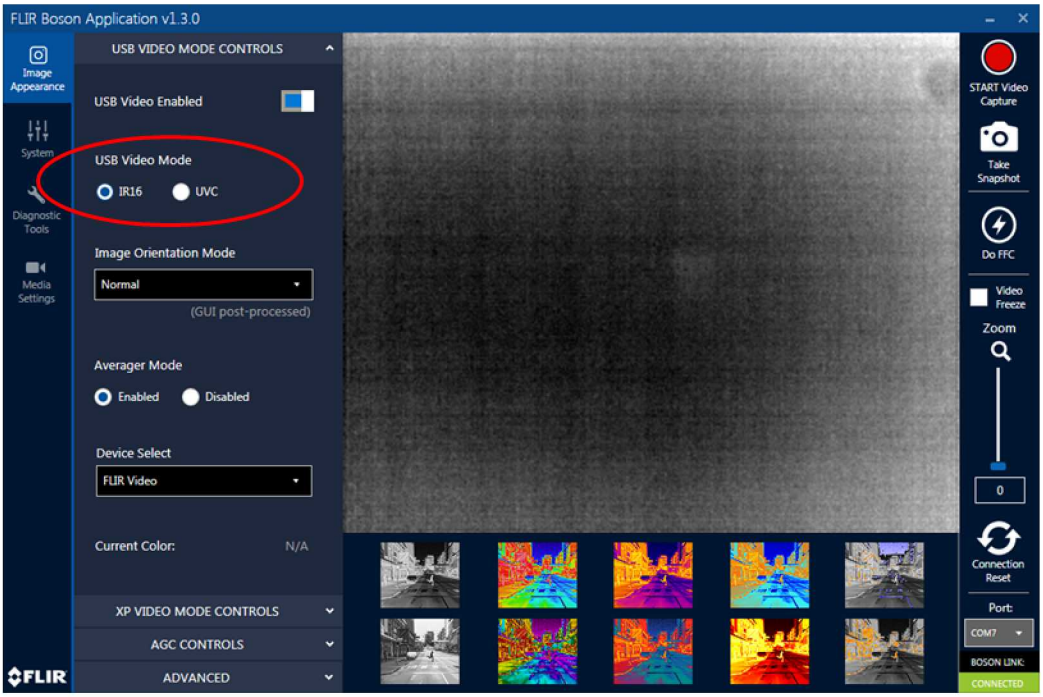

Figure 6-3: Screenshot of FLIR Boson Application Highlighting USB Video Mode Selection

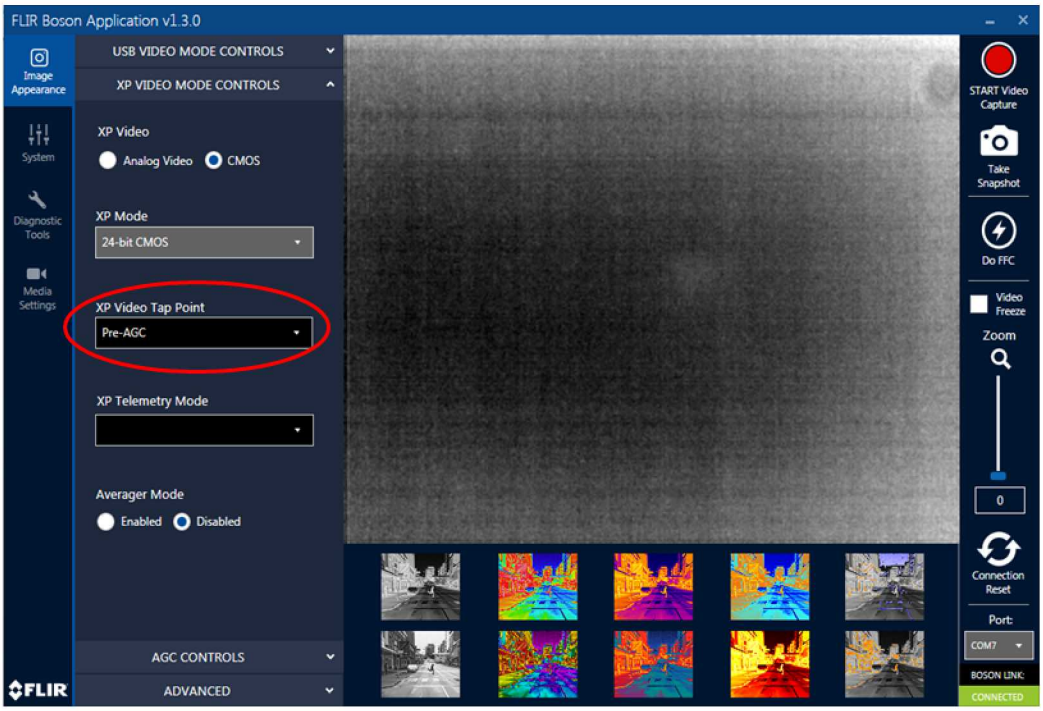

Figure 6-4: Screenshot of FLIR Boson Application Highlighting XP Video Tap Point Selection

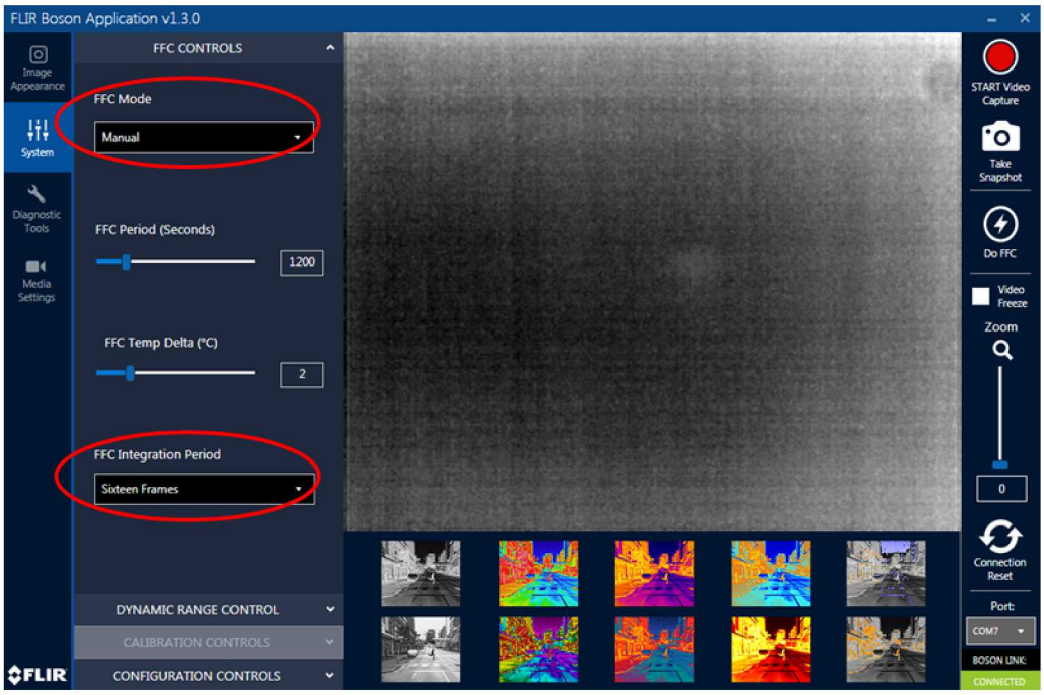

Figure 6-5: Screenshot of FLIR Boson Application Highlighting FFC Selections

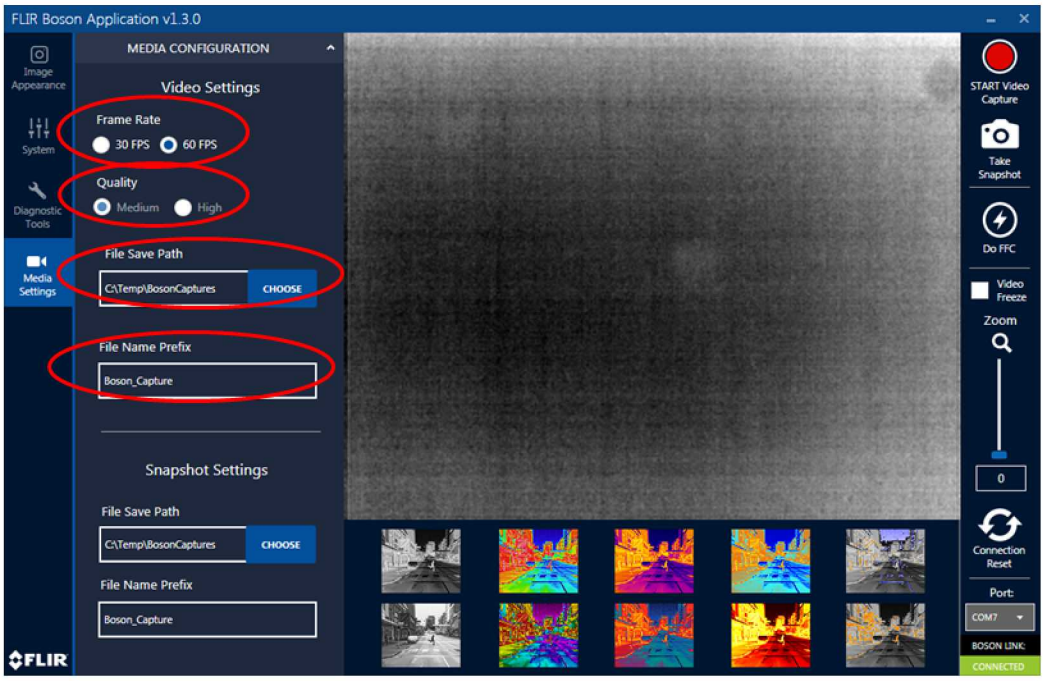

Figure 6-6: Screenshot of FLIR Boson Application Video Settings Selections

6.2. Heating Methods and Test Specimens

6.2.1. Heating Sources

Thermography requires a temperature gradient to identify the presence of flaws. Typically, this heat gradient is generated by heating and then cooling the part (or vice versa). As described in Section 5.3.1.3, the following heating methods were selected for testing:

- Internal Forced Air – Heat Gun or hot air supply directed at the "inside" of panel; panel must be part of an enclosure as in an actual blade [6.1, Figs. 7-104 and 7-108]
- Solar Radiation – Sun/shade directed at the "outside" of the panel, horizontal to the ground
- Flash Tubes – Thermal Wave Imaging's flash tubes system directed at the "outside" of panel

Turbine operational heating was also considered, but the team determined that it would be difficult to accurately test in a benchtop environment. Instead, it was evaluated during drone integration testing in Section 0. Heating generated by the heat gun directed to the "outside" of the panel was also considered, depending on the effectiveness of the other methods. After initial testing, the concept was dropped due to the effectiveness of the other methods, and in particular, the sun/shade method.

6.2.2. *Test Specimens*

The following test specimens were selected in order to evaluate the effectiveness of the thermography system in a benchtop configuration. The specimens are existing fiberglass and fiberglass sandwich construction specimens designed with engineered flaws [6.1]. Figure 6-7 shows an example of these specimens. Details about the design of each of these specimens are provided in 0.

- Sandwich construction – Specimen REF-STD-1-150-TPI-1
- Laminate "bricks" with flat bottom holes of controlled depth – actual wind blade fiberglass laminate specimens (FGB-X) and G11 fiberglass laminates (G11-STD-X)
- Actual wind blade specimens with added flat bottom holes – Specimens WIND-1-029, WIND-2-044, WIND-3-110-SPAR-140, WIND-4-161
- Thin skin-foam core specimens from an aviation program but similar to wind construction

Figure 6-7: Front and Back Photos of G11 Solid Laminate Set with Flat Bottom Holes

6.3. Testing Procedures and Results

6.3.1. Flash Tube Heating Testing

While not realistic from an integration standpoint, flash tube testing provides a controlled setup that enables us to benchmark the FLIR Boson camera. The goal of these tests was to evaluate the effectiveness of the IR camera and gain some preliminary insights into the system's depth of penetration.

For the flash tube tests, Sandia's existing Thermal Wave Imaging EchoTherm system was utilized. The MOSAIQ software was used to control the flash duration, and the FLIR Boson IR Camera was mounted to the flash hood, as shown below in Figure 6-8 and Figure 6-9. Note that the Raytheon Radiance HS IR Camera remained installed, for simplicity, to prevent an error with the Thermal Wave Imaging MOSAIQ software. The EchoTherm system uses two 5000 Joule xenon flash tubes, with adjustable power and flash truncation options, that are triggered in conjunction with the Raytheon IR camera.

Figure 6-8: FLIR Boson Installed on TWI EchoTherm Flash Tube System

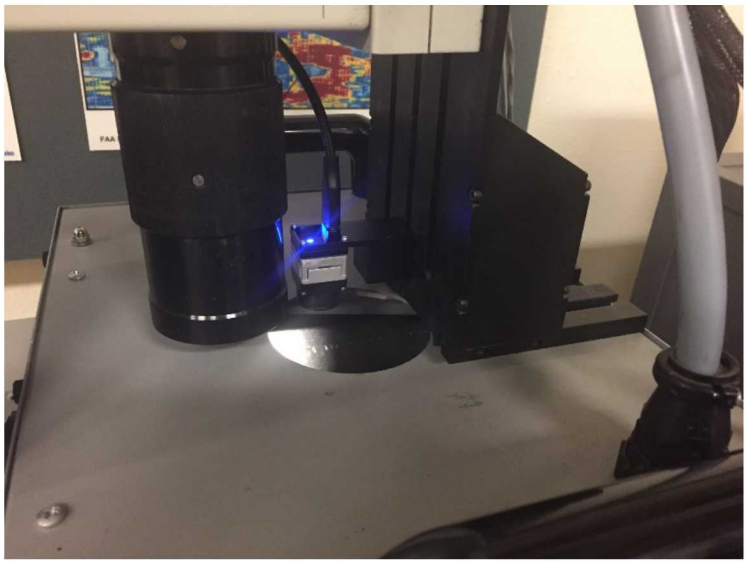

Figure 6-9: FLIR Boson Installed with Tripod Accessory and 1/4"-20 Screw

In addition to the IR thermal data, thermocouples were also used to measure the temperature increase of the front and rear surface of the specimens, as well as the ambient temperature. Figure 6-11 shows an image of the Omega HH1384 4-channel thermocouple datalogger, which logs the temperature values of K-type thermocouples at a 1 Hz sampling frequency.

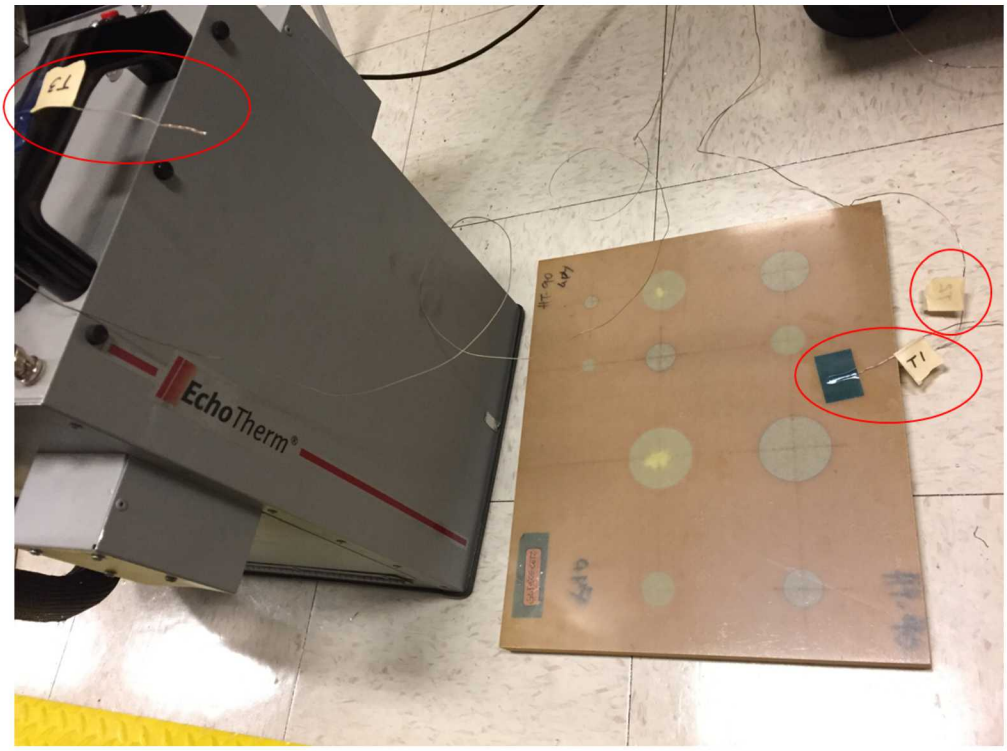

Figure 6-10: Thermocouple Locations: TC1 on the Front of Specimen, TC2 on the Rear of Specimen, TC3 on EchoTherm Flash Tubes Unit (Measuring Ambient Temperature)

Figure 6-11: Omega HH1384 4-Channel Thermocouple Datalogger with K-Type Thermocouples

Because the EchoTherm system is not setup to trigger the flash tubes and FLIR Boson camera simultaneously, synchronizing the timing of the thermocouples, flash tubes, and IR camera are important for post-processing the data. For this series of tests, the synchronization was performed as follows.

- The IR camera is manually instructed to perform a FFC event, using FLIR Boson Application.
- The IR camera is manually instructed to begin videoing, using FLIR Boson Application.
- The flash tubes are initiated manually using the MOSAIQ software.
- A timer is started to measure the approximate IR camera data acquisition duration.
- After the data acquisition duration is achieved, the IR camera is manually instructed to stop videoing, using FLIR Boson Application.

Because all these operations are manually performed, the timing is synchronized during post-processing as follows.

- Thermocouples: Assume T_{max} occurs at $t = 0$
- IR Video: Assume T_{max} (i.e., highest pixel value) occurs at $t = 0$

Note that the video duration is approximate and subject to human error. The target video durations are based on the following equation for the time required for the heat to reach to rear surface, as described in Section 4.2.1, plus approximately 50% margin.

$$t^* = \frac{L^2}{\pi\alpha}$$

where L is the thickness of the part at the location of the deepest flaw and α is the thermal diffusivity. The thermal diffusivity is governed by the following equation.

$$\alpha = \frac{k}{\rho c_p}$$

where k is the thermal conductivity, ρ is the density, and c_p is the specific heat capacity. For fiberglass, these values are k = 0.288 W/m-°K, ρ = 1.8 g/cm^3, and c_p = 0.999 J/g-°K at 300 °K (from MATWEB for G11 fiberglass and http://materialdatabase.magnet.fsu.edu/G10.htm). This yields α = 0.0016 cm^2/s.

6.3.1.1. Test Matrix

In order to get the maximum depth of penetration, maximizing the heat input was a priority. Therefore, the TWI EchoTherm system was set to 100% power for each test, and the maximum flash duration of 30 ms was used. These settings are appropriate for thick fiberglass specimens where maximum heat input is desired. Note that these settings may not be appropriate for thin materials with high thermal diffusivities (e.g., thin sheets of aluminum), where long flash durations can oversaturate the IR video frames of interest.

The decision was made not to improve the emissivity of the specimens by painting the front surface matte black. While this would have improved the test results, it was considered an unrealistic case because the current drone integration concepts do not have plans for painting the surface of the wind blades.

For the flash tubes, the goal was to measure the maximum depth of penetration in thick fiberglass composites, using thick specimens with flat bottom holes set at various depths. Also, as a secondary goal, the plan was to confirm that the benchtop thermography system, using the FLIR Boson IR camera, was proficient at observing flaws in sandwich construction, which previous work [6.1] has demonstrated that thermography is well suited for.

Based on these considerations, the test matrix in Table 6-1 was developed.

Table 6-1: Flash Tubes Test Matrix

Specimen	Comments
G11-STD-1	
G11-STD-2	
G11-STD-3	
G11-STD-4	Contain deeper flaws. Decide whether to test based on G11-STD-3 test results
G11-STD-5	
FGB-1	
FGB-2	
FGB-3	
FGB-4	
REF-STD-1-050-TPI-1	
WIND-1-029	
WIND-2-044	
WIND-3-110-SPAR-140	Contain deeper flaws. Decide whether to increase duration based on G11-STD-3 test results
WIND-4-161	
WIND-5-180	
WIND-6-180-SPAR-220	
GLF-S05-C4T2	Use experience on timing from REF-STD-1-050-TPI-1
GLF-S05-C4T2-P5-02	
GLF-S04-C4T2	
GLF-S05-C6T2	
GLF-S06-C4T2	

6.3.1.2. Data Acquisition

The following data for the flash tube testing was recorded.

- Date/Time
- Test Location (e.g., Building 894/Room 157)
- Location of Thermocouples

- Test Specimen ID
- Test Number
- IR Camera Information – model, resolution, frame rate, serial number
- IR camera settings – file format and quality, automatic gain control (AGC) settings, flat field correction (FFC) settings, target video duration
- Heat Source (i.e., TWI EchoTherm system with 2x 5000 Joule flash tubes)
- Flash Tubes Settings – power, duration
- Ambient Temperature in lab, per thermocouple reading
- Test notes

Screenshots of the flash tube testing template are shown in Figure 6-12.

Date	Time	Location	Temp Data (Location of Thermocouples)	Test Specimen ID	Test #	IR Camera	IR Camera Settings
		894/157	TC1 (K Type): Front, Top Left TC2 (K Type): Back, Top Left TC3 (K Type): Air	G11-STD-1		FLIR Boson Resolution: 320x256 Frame Rate: 60 Hz S/N: 2338	Format: 16-bit TIFF sequence AGC Settings: Pre-AGC FFC: Manual, 16 frames integration, performed immediately before test Target Video Duration: TBD

Heat Source	Heat Source Settings	Air Temperature	Notes
TWI EchoTherm Flash Tubes	Flash Duration: 30 ms Flash Power Level: 100%	Recorded by TC3 prior to test	

Figure 6-12: Screenshots of Flash Tube Testing Data Acquisition Form

6.3.1.3. Test Procedure

1. Apply thermocouples TC1 and TC2 to front and rear surfaces (as shown in Figure 6-13 and Figure 6-14) with flash breaker tape.
2. Connect thermocouples to Omega HH1384 4-channel thermocouple datalogger, including TC3 for ambient temperature.
3. Turn on laptop, thermocouple datalogger, TWI EchoTherm flash tube system, and FLIR Boson IR Camera (plug the USB cable into the laptop).
4. Open FLIR Boson Application, connect to IR Camera (e.g., COM7), and double check camera settings.
5. Open D4IThermoMeter software and connect to thermocouple datalogger (e.g., COM6).

6. Wait approximately 15 minutes for IR Camera to warm up and thermocouples to stabilize.
7. Open MOSAIQ software and set up a flash of the intended duration.
8. Start recording thermocouple data.
9. Perform a manual FFC event, using the FLIR Boson Application.
10. Start recording video, using the FLIR Boson Application.
11. Start timer to measure the approximate IR video duration.
12. Provide power to flash tubes in MOSAIQ.
13. Stop recording video in the FLIR Boson Application when the timer approximately reaches the target video duration.
14. Stop recording thermocouple data and save file to laptop.

Figure 6-13: Approximate Location of TC1

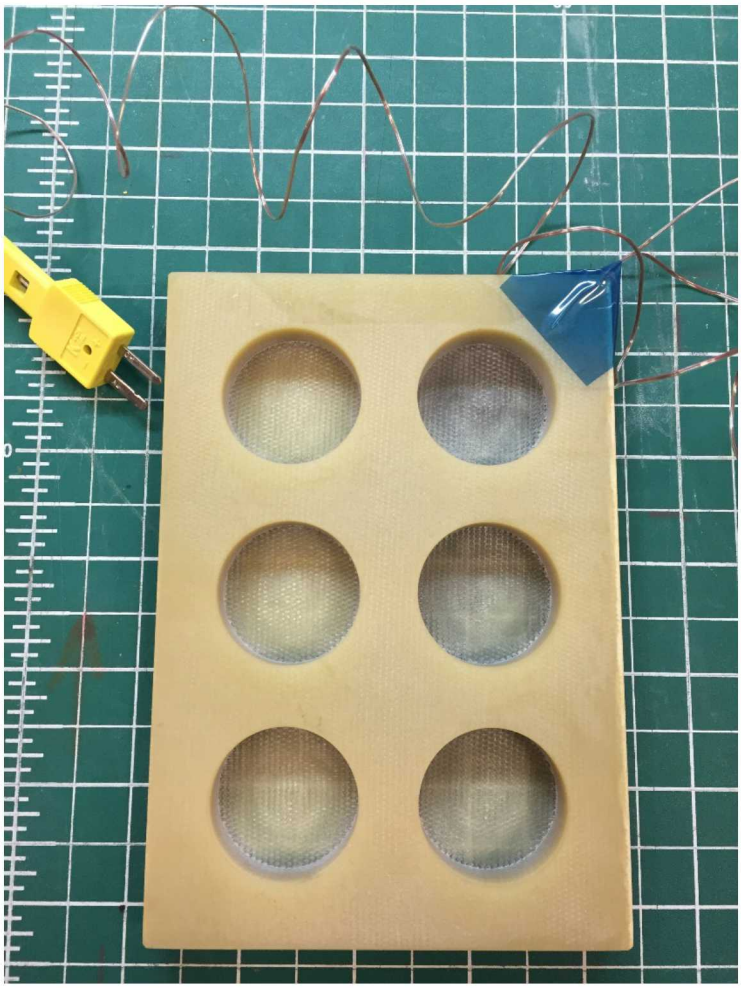

Figure 6-14: Approximate Location of TC2

6.3.1.4. Post-Processing Procedure

The post-processing procedure was based on the modified TSR algorithm that was described in Section 5.3.1.4 using the MATLAB function in Appendix B.2. The MATLAB function takes the FLIR Boson's .tiff files as an input and outputs the following:

- TIFF stack of TSR data (200 frames)
- TIFF stack of 1st Derivative TSR data (200 frames)
- TIFF stack of 2nd Derivative TSR data (200 frames)
- Log File (see Figure 6-15)

These TIFF stacks can then be manually reviewed to look for contrast between the areas with flaws and the surrounding "clean" area. Examples of these results are

provided in the next section. More advanced automated analyses may be possible with future work, as described in Section 8.1.2.

Additionally, a log file is generated to provide the information required to repeat the same post-processing parameters. The Region of Interest values are of particular interest because these are manually selected with a cursor and are therefore difficult to reproduce.

```
Filename: Boson_Capture_35.tiff

Date/Time Processed: 31-Oct-2017 10:43:14

TSR Skipped Frames: 0
Calculated Flash Bulb Frame Number: 1
Framerate: 60
Polynomial Degree: 6
Rotation (Degrees): 0

Selected Region of Interest (pixels):
xmin   ymin   width   height
  38     53     250      170

Elapsed Time: 64.6 sec
```

Figure 6-15: Example Log File

6.3.1.5. Results

Overall, the flash tube test series yielded excellent results. The G11-STD-X and wind blade test specimens provided information on the maximum depth of penetration of the flash tube system with FLIR Boson IR camera. As shown in Figures 6-16 through 6-22 and summarized in Table 6-2, the maximum discernable depth of penetration is approximately .25 inches, including one case as high as .330 inches. The .260 inch deep flaw on G11-STD-3 may have been barely visible and could likely be found with some optimization of the system and specimen (e.g., reducing surface reflection, removing the black lines and text). Likewise, the performance on WIND-2-044-SPAR-085 likely could be further optimized to mitigate some reflection issues caused by the glossy surface.

The other goal of the study was to evaluate the flash tube system's ability to find flaws in fiberglass and foam sandwich construction specimens. As expected, the system performed extremely well at finding all the flaws in the sandwich construction as shown in Figures 6-23 through 6-30. This result was particularly encouraging because fiberglass and foam or balsa core sandwich structures represent a large area of the total wind blade structure.

While the team does not plan to integrate a flash tube system on a drone platform, this test series demonstrated that the FLIR Boson along with the modified TSR algorithm are capable of finding similar defects as commercial systems with much larger and more expensive IR cameras.

Table 6-2: Flash Tubes Solid Laminate Depth of Penetration Results

Specimen ID	All Flaws Visible?	Deepest Flaw Observed (in)
G11-STD-1	Yes	.050
G11-STD-2	Yes, but barely	.180
G11-STD-3	No	.220, possibly .260
WIND-1-029	Yes	.256
WIND-2-044-SPAR-085	No	.164, some issues with reflection
WIND-3-110-SPAR-150	No	.240
WIND-4-161	No	.330, but barely

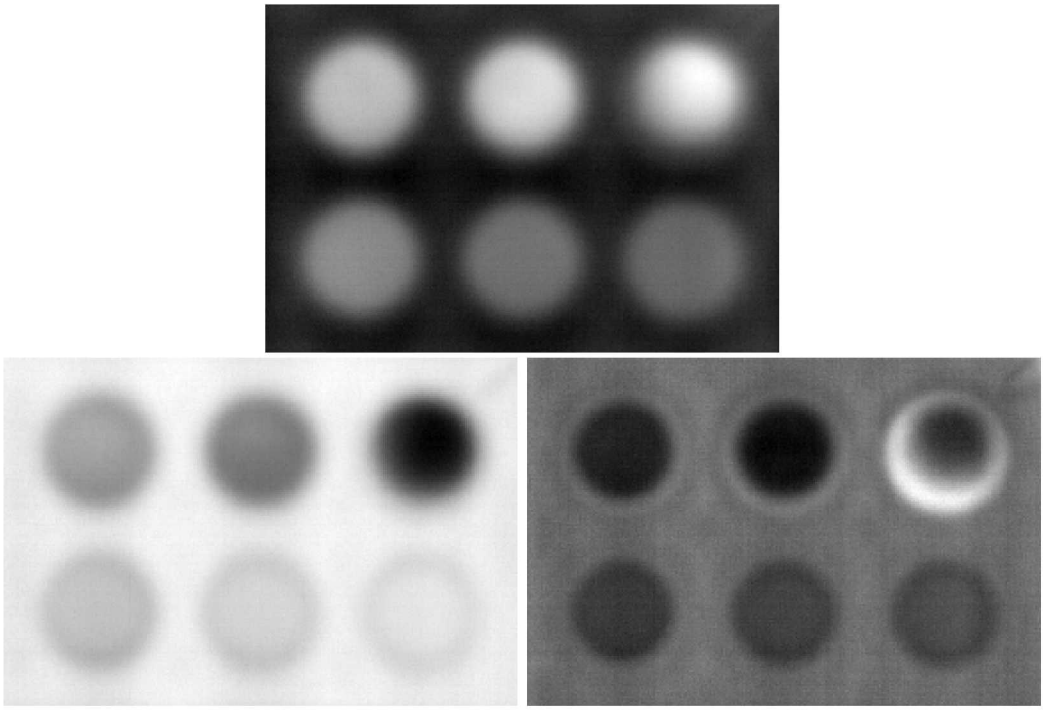

Figure 6-16: G11-STD-1 Flash Tubes Test 1 Results for TSR (at 180 frames), 1D (at 189 frames), and 2D (at 180 frames)

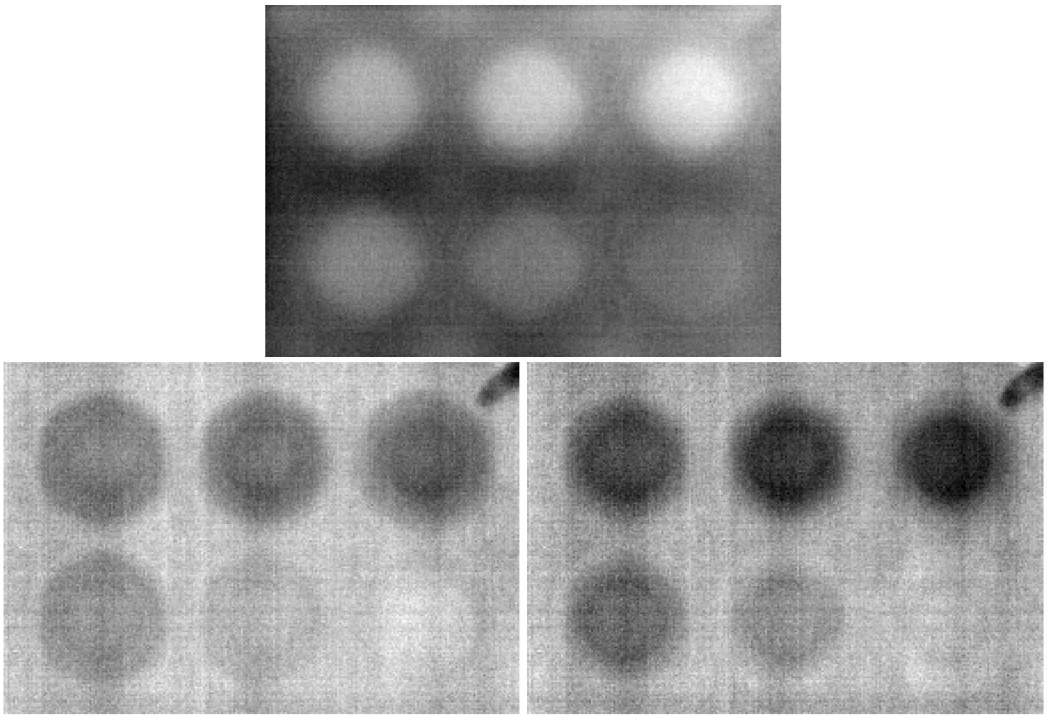

Figure 6-17: G11-STD-2 Flash Tubes Test 1 Results for TSR (at 195 frames), 1D (at 200 frames), and 2D (at 184 frames)

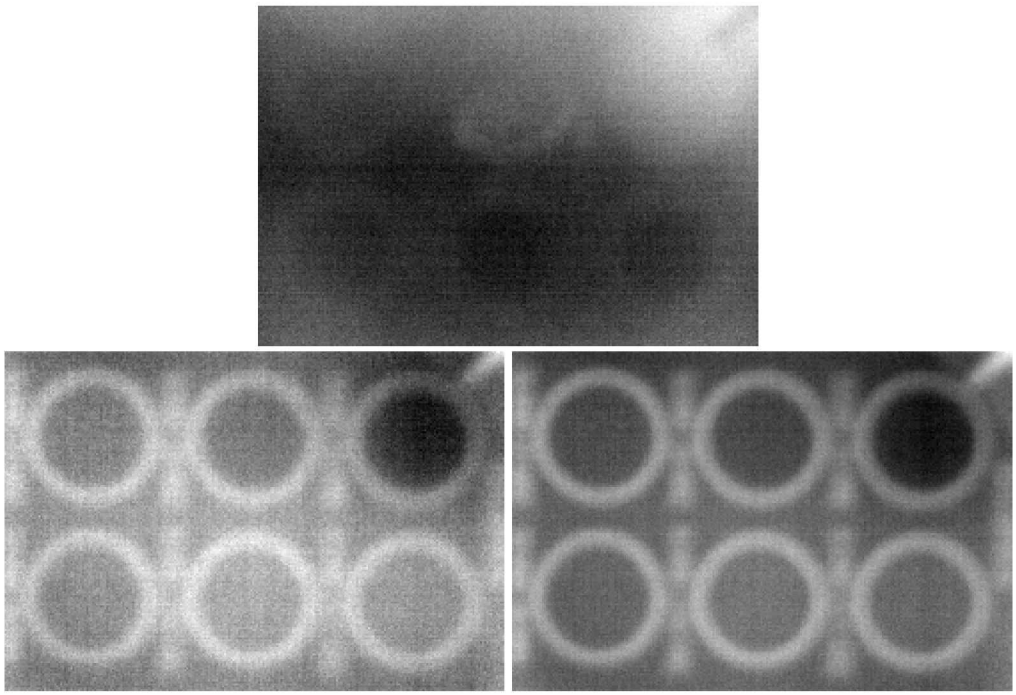

Figure 6-18: G11-STD-3 Flash Tubes Test 1 Results for TSR (at 165 frames), 1D (at 190 frames), and 2D (at 172 frames)

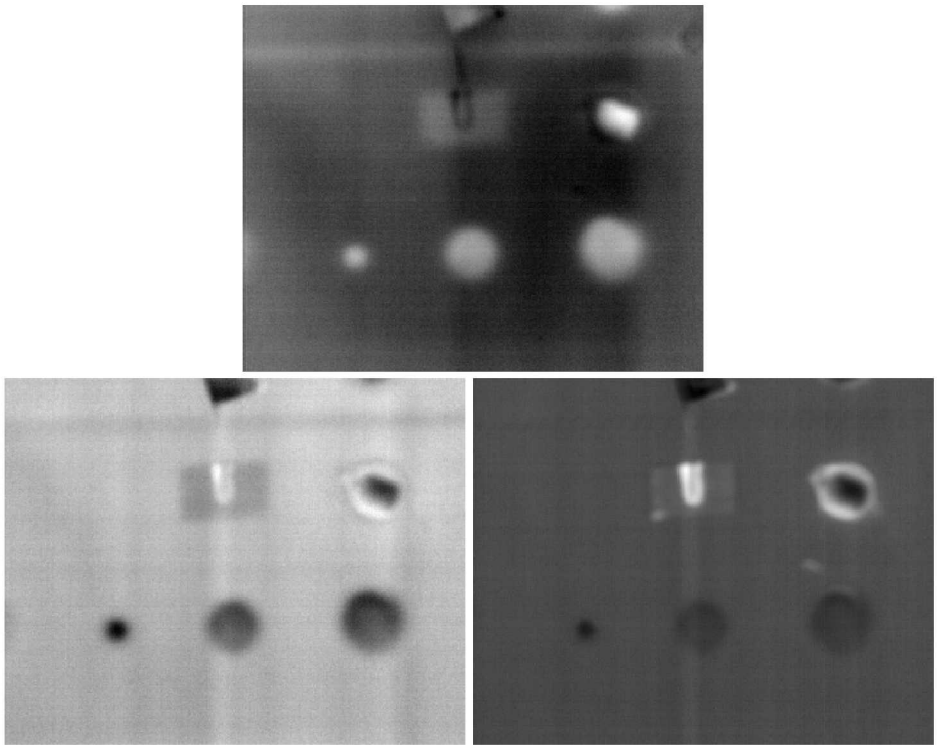

Figure 6-19: WIND-1-029 Flash Tubes Test 3 Results for TSR (at 164 frames), 1D (at 185 frames), and 2D (at 149 frames)

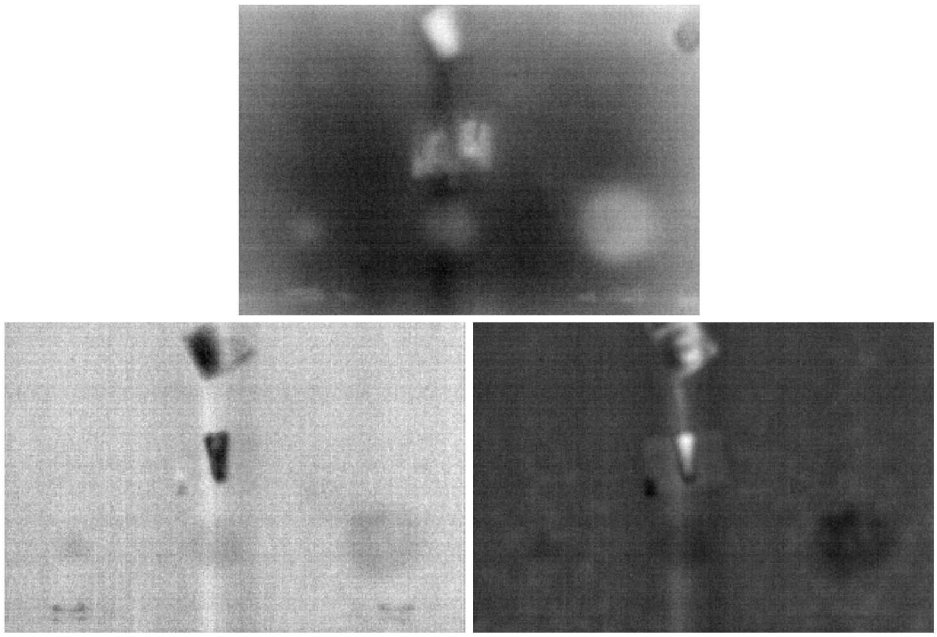

Figure 6-20: WIND-2-044-SPAR-085 Flash Tubes Test 2 Results for TSR (at 182 frames), 1D (at 194 frames), and 2D (at 176 frames)

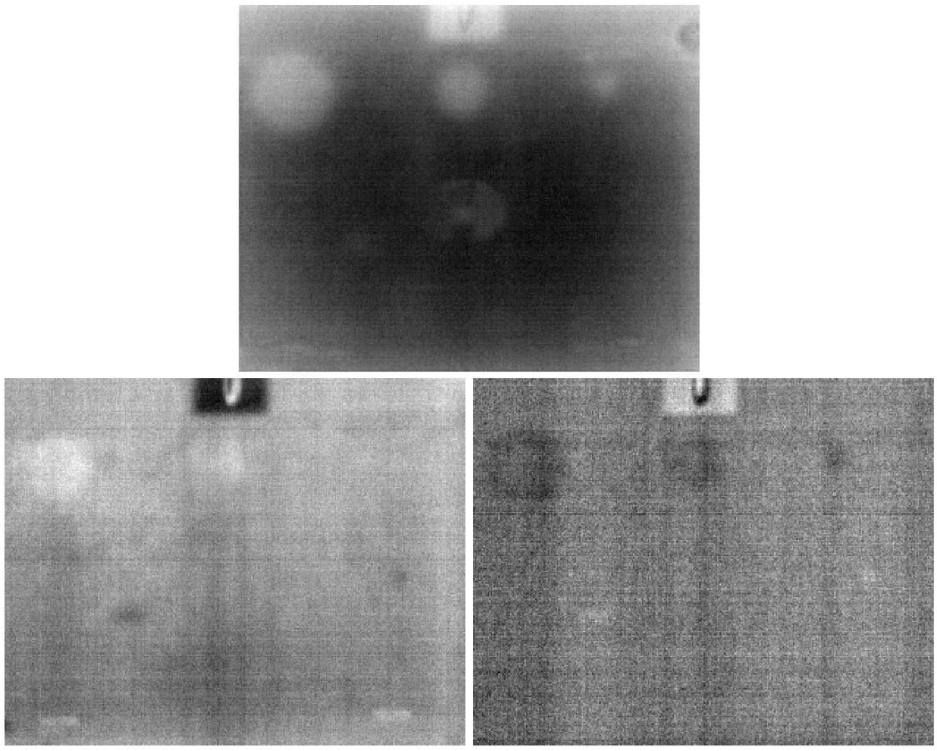

Figure 6-21: WIND-3-110-SPAR-150 Flash Tubes Test 1 Results for TSR (at 161 frames), 1D (at 172 frames), and 2D (at 177 frames)

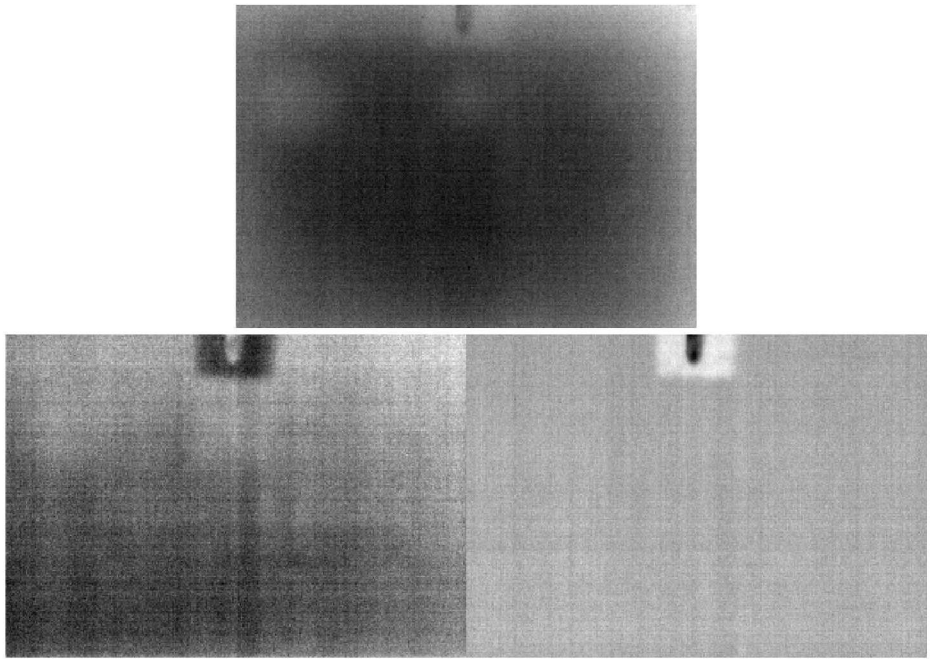

Figure 6-22: WIND-4-161 Flash Tubes Test 1 Results for TSR (at 200 frames), 1D (at 184 frames), and 2D (at 200 frames)

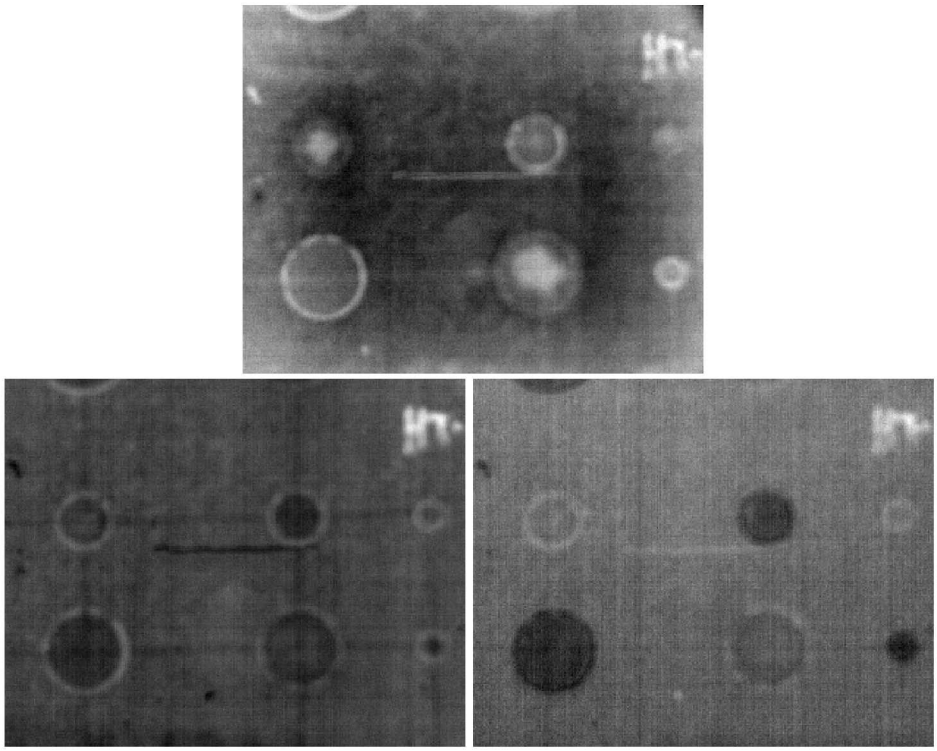

Figure 6-23: GLF-S05-C4T2 Flash Tubes Test 3 Results for TSR (at 91 frames), 1D (at 73 frames), and 2D (at 61 frames)

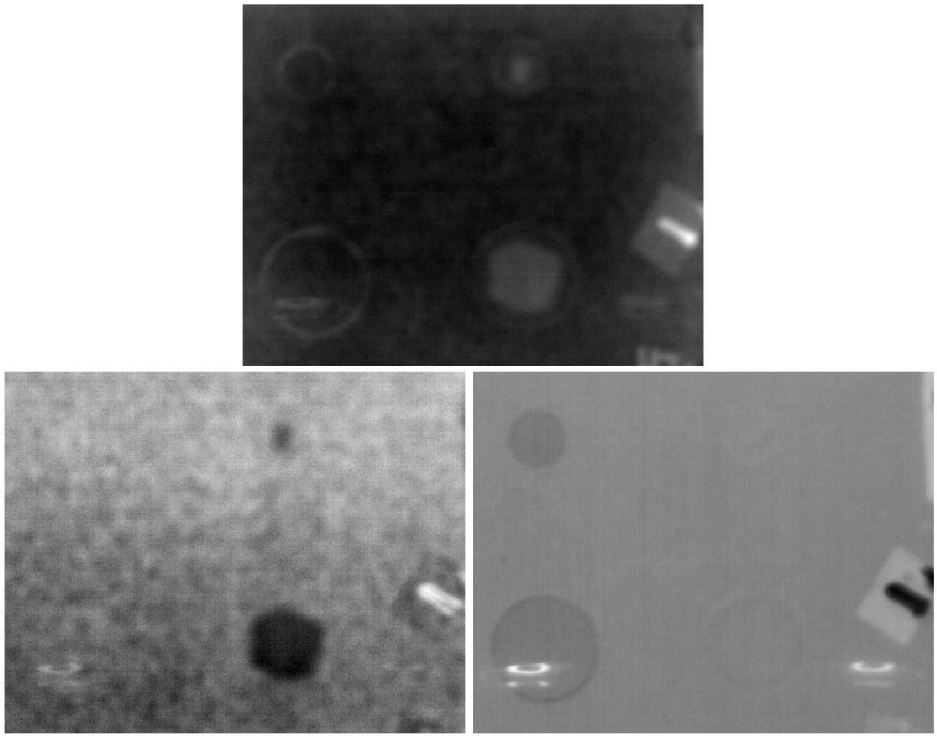

Figure 6-24: GLF-S05-C4T2 Flash Tubes Test 4 Results for TSR (at 123 frames), 1D (at 173 frames), and 2D (at 68 frames)

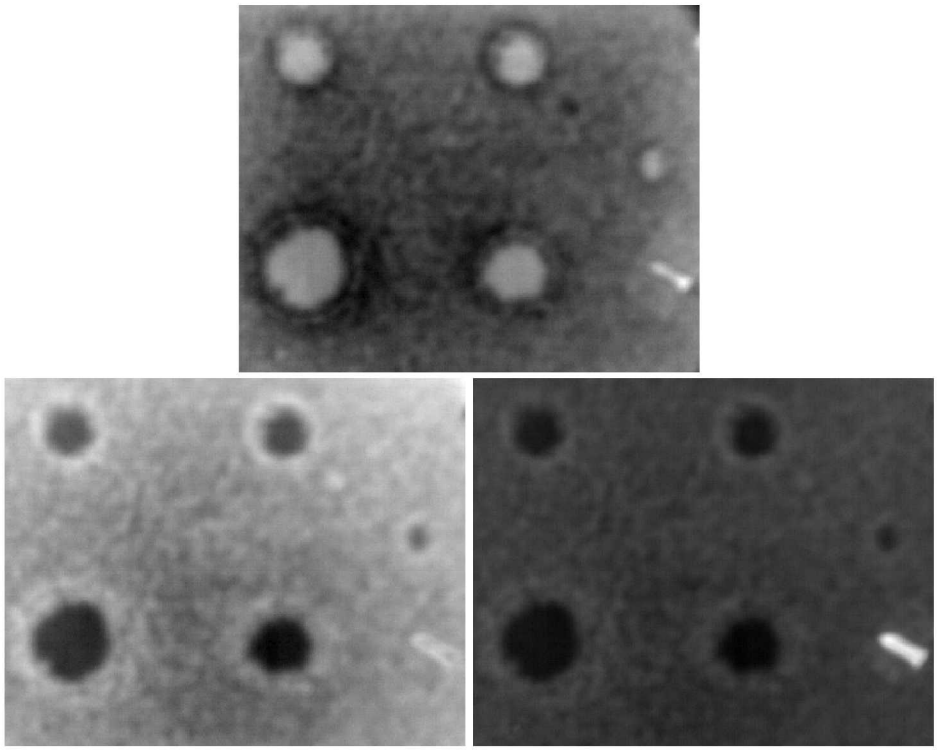

Figure 6-25: GLF-S04-C4T2 Flash Tubes Test 1 Results for TSR (at 114 frames), 1D (at 152 frames), and 2D (at 120 frames)

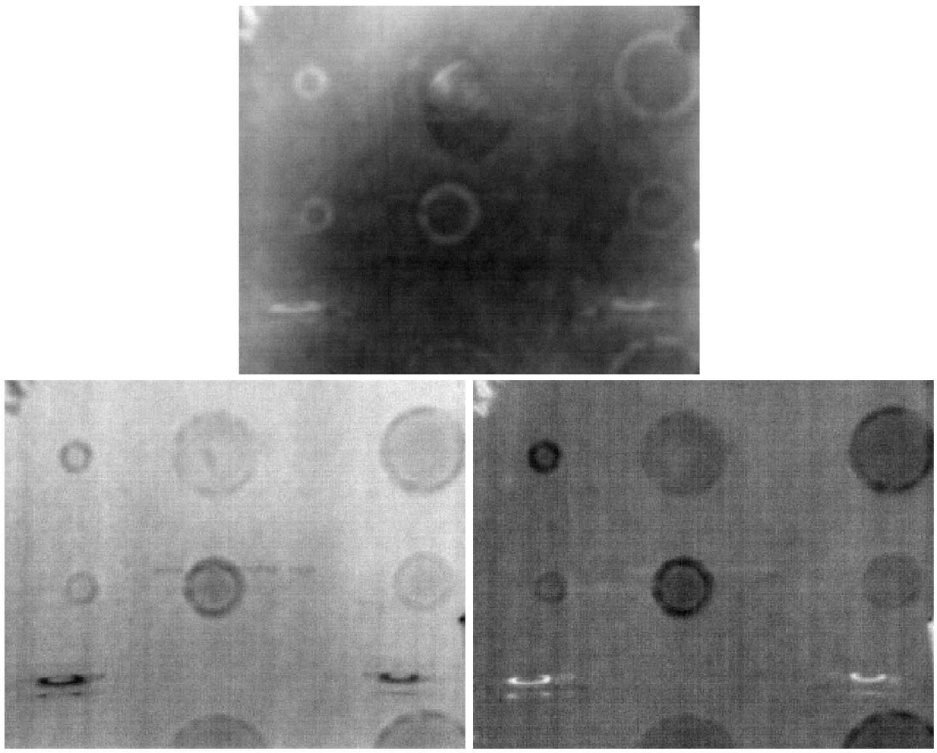

Figure 6-26: GLF-S05-C6T2 Flash Tubes Test 1 Results for TSR (at 120 frames), 1D (at 141 frames), and 2D (at 93 frames)

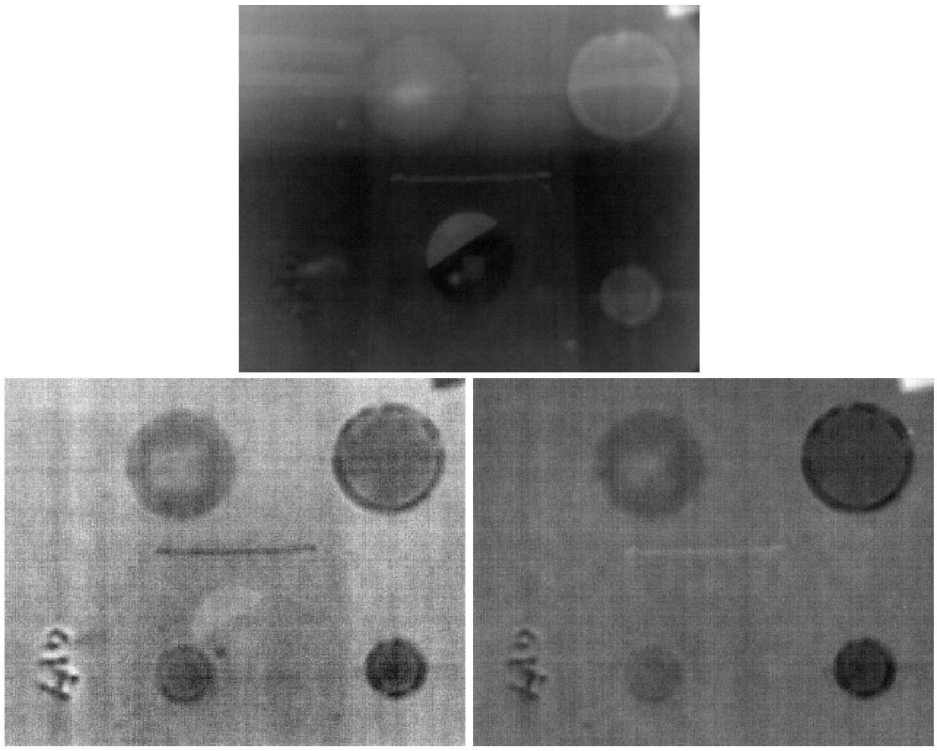

Figure 6-27: GLF-S05-C6T2 Flash Tubes Test 2 Results for TSR (at 77 frames), 1D (at 134 frames), and 2D (at 87 frames)

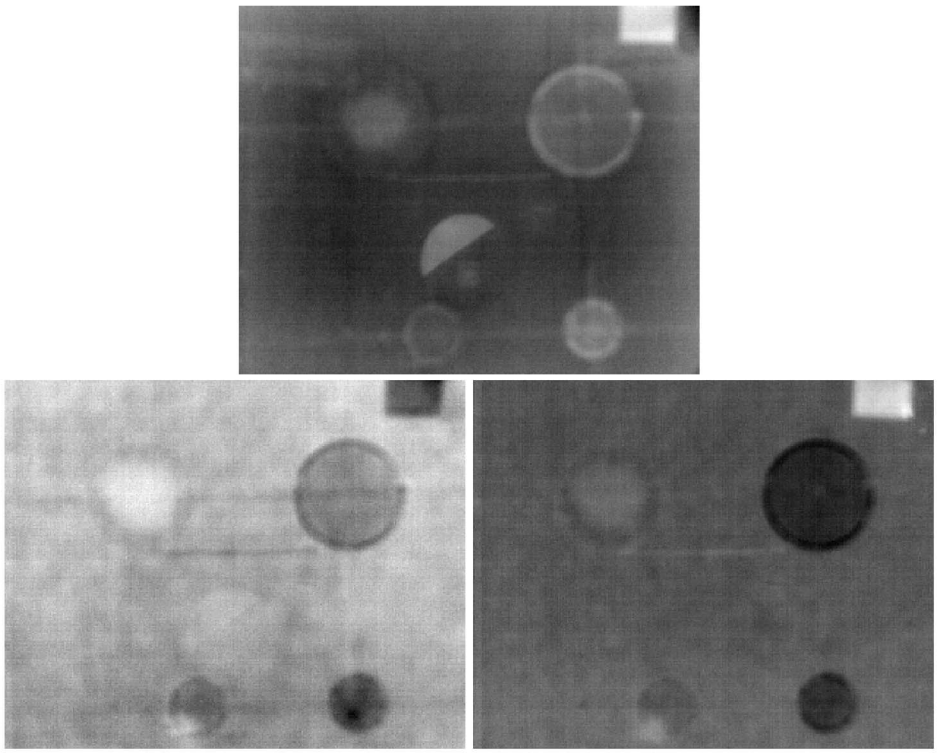

Figure 6-28: GLF-S06-C4T2 Flash Tubes Test 1 Results for TSR (at 106 frames), 1D (at 138 frames), and 2D (at 85 frames)

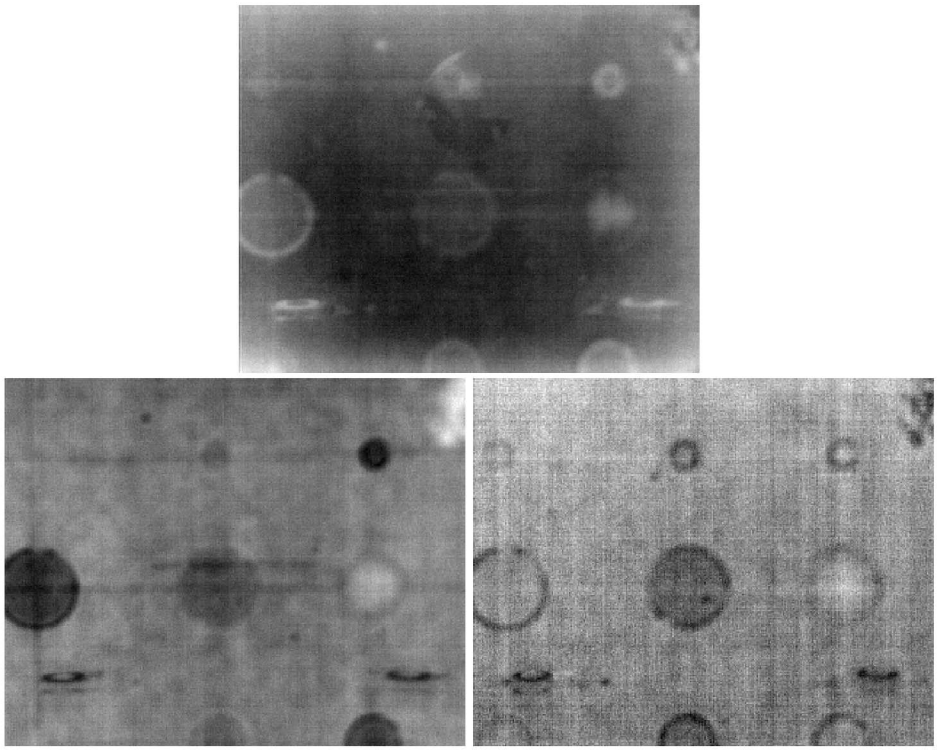

Figure 6-29: GLF-S06-C4T2 Flash Tubes Test 2 Results for TSR (at 116 frames), 1D (at 122 frames), and 2D (at 112 frames)

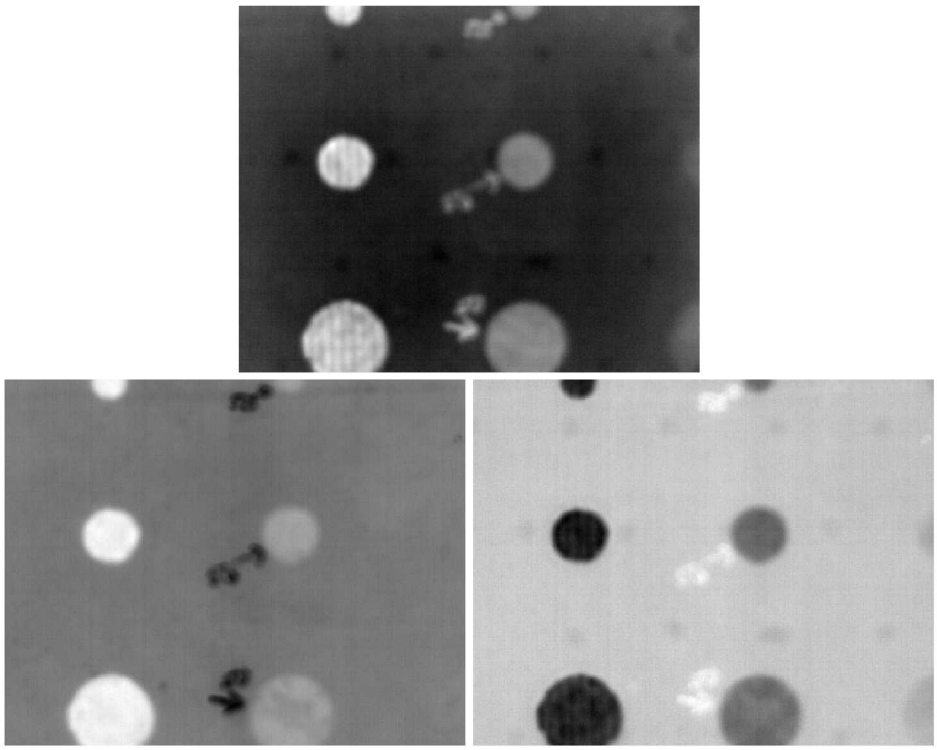

Figure 6-30: REF-STD-1-050-TPI-1 Flash Tubes Test 1 Results for TSR (at 89 frames), 1D (at 67 frames), and 2D (at 87 frames)

6.3.2. *Internal Forced Air (Heat Gun) Heating Testing*

Internal forced air heating provided a unique set of attributes compared to the other methods. A diverse set of heating methods was desirable to mitigate the risk of that all of the heating techniques proved to be infeasible. In particular, internal heating provided a backup plan for solar radiation, which prior to testing was a significant technical risk, and flash tube heating, which has substantial integration challenges. The goal of these tests was to evaluate the heating gradient (i.e., the internal blade temperature – ambient external blade temperature) required as well as an opportunity to compare and contrast front and rear surface heating, with respect to depth of penetration. Because of the difficulty in heating foam or balsa core sandwich structures with low thermal conductivities, only solid laminate structures were considered.

To emulate the internal heating of a wind blade, an insulated structure was required that would enable the rear surface of a specimen to be heated while the front surface was subjected to ambient temperature. The solution that was selected was a double cardboard box with an internal cavity that can be heated with a hot air gun (see Figure 6-31). This internal cavity was thermally insulated from ambient temperatures by a layer of denim insulation as shown in Figures 6-32 to 6-34. A rectangular hole that was sized slightly smaller than the test specimen enabled the rear surface of the specimen to be subjected to the heated internal cavity. Figure 6-35 depicts this rectangular hole, and Figure 6-36 shows the thermocouple location used to measure the internal temperature of the cavity. Meanwhile, Figure 6-37 shows the complete experimental setup, including the FLIR Boson IR camera mounted on a tripod, the thermocouple datalogger, the heat gun, and an installed test specimen.

Figure 6-31: Master Appliance Corp. H6501L 14 Amp Heat Gun

Figure 6-32: Insulated Double Box Construction

Figure 6-33: Heat Gun Installation

Figure 6-34: Final Insulation Installation

Figure 6-35: Access to Hot Air Cavity to Expose the Rear Surface of the Test Specimens

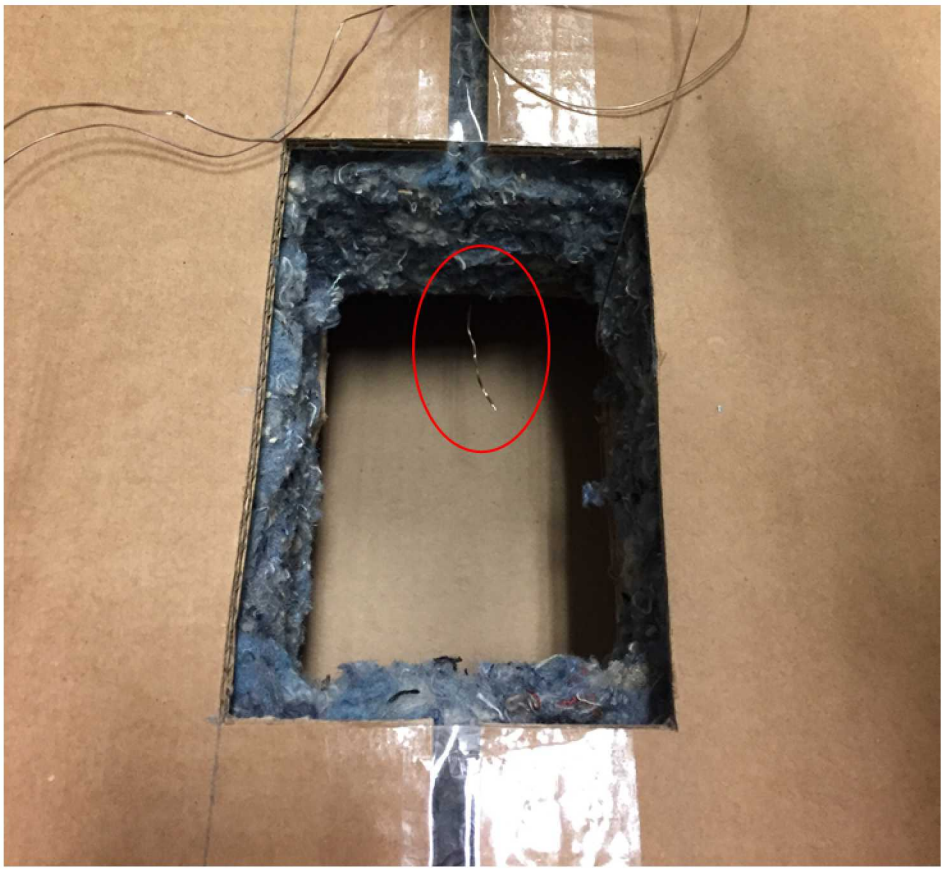

Figure 6-36: Location of Thermocouple TC3

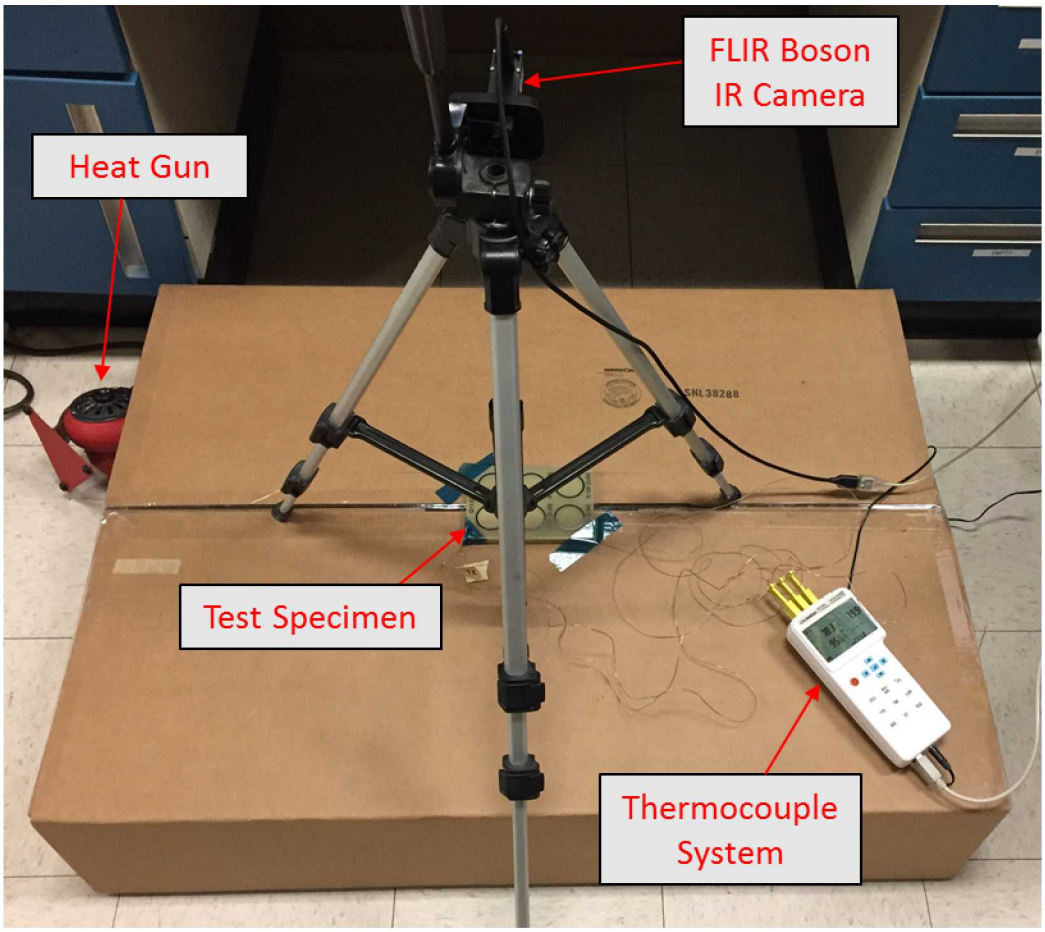

Figure 6-37: Internal Forced Air (Heat Gun) Heating Experimental Setup

As described later in Section 6.3.2.5, the rear surface heating provided unique challenges. One of these challenges was the design of the flat bottom holes. By machining the flat bottom holes from the rear surface, they typically simulate a disbond when inspected from the front surface. However, when heated from the rear surface, the thinner fiberglass above the flat bottom hole heated significantly quicker than the full thickness regions. In order to achieve a more accurate disbond-representative flaw, aluminum tape was added to the rear surface side of each flat bottom hole, as shown in Figure 6-38.

Figure 6-38: Aluminum Tape Added to Rear Surface Over Flat Bottom Holes

6.3.2.1. Test Matrix

In order to get the maximum depth of penetration, maximizing the rear surface temperature, without damaging the fiberglass specimens, was a priority. In order to determine the thermography system's sensitivity to temperature gradient, a number of scoping tests were performed to identify an appropriate range of heating durations.

For the internal force air heating, the goal was to measure the maximum depth of penetration in thick fiberglass composites, using thick specimens with flat bottom holes set at various depths. Therefore, only the G11-STD-X and FGB-X specimens were selected for testing. Similar to the other benchtop tests, the decision was made not to improve the emissivity of the specimens by painting the front surface matte black.

Based on these considerations, the test matrix in Table 6-3 was developed.

Table 6-3: Internal Forced Air Heating Test Matrix

Specimen	Comments
G11-STD-1	
G11-STD-2	
G11-STD-3	

G11-STD-4	Contain deeper flaws. Decide whether to test based on G11-STD-3 test results
G11-STD-5	
FGB-1	
FGB-2	
FGB-3	
FGB-4	

6.3.2.2. Data Acquisition

The following data for the internal forced air testing was recorded.

- Date/Time
- Test Location (e.g., Building 894/Room 157)
- Location of Thermocouples
- Test Specimen ID
- Test Number
- IR Camera Information – model, resolution, frame rate, serial number
- IR camera settings – file format and quality, automatic gain control (AGC) settings, flat field correction (FFC) settings, target video duration
- Heat Gun Settings
- Heating Duration
- Heating Box Air Temperature, per thermocouple reading
- Ambient Temperature in lab, per thermocouple reading
- Test notes

Screenshots of the flash tube testing template are shown in Figure 6-39.

Date	Time (approx. time specimen is placed in the heat gun box, to the minute)	Location	Temp Data (Location of Thermocouples)	Test Specimen ID	Test #	IR Camera
5/31/2017	4:06pm	Heating: 894/157 Cooling: 894/157	TC1 (K Type): Front, Top Left TC2 (K Type): Back, Top Left TC3 (K Type): Box TC4 (K Type): Room	G11-STD-2	1	FLIR Boson Resolution: 320x256 Frame Rate: 60 Hz S/N: 2338

IR Camera Settings	Heat Gun Settings	Heating Duration (s)	Heating Box Air Temperature (°F)	Inside Air Temperature (°F)	Notes (Peak Temperatures are approximate)
Format: 16-bit TIFF sequence (IR16) AGC Settings: Pre-AGC FFC: Manual, 16 frames integration, performed immediately before test Video Duration (after heating): 65	Hot	15	Recorded by TC3 peak temperature during heating	Recorded by average TC4 temp during heating and cooling/videoing	Video File: Boson_Capture_13.tiff Peak Temp: 108° F

Figure 6-39: Screenshots of Internal Forced Air Testing Data Acquisition Form

6.3.2.3. Test Procedure

1. Apply thermocouples TC1 and TC2 to front and rear surfaces (as shown in Figure 6-13 and Figure 6-14) with flash breaker tape.
2. Connect thermocouples to Omega HH1384 4-channel thermocouple datalogger, including TC3 for ambient temperature and TC4 for internal box temperature.
3. Turn on laptop, thermocouple datalogger, TWI EchoTherm flash tube system, and FLIR Boson IR Camera (plug the USB cable into the laptop).
4. Open FLIR Boson Application, connect to IR Camera (e.g., COM7), and double check camera settings.
5. Open D4IThermoMeter software and connect to thermocouple datalogger (e.g., COM6).
6. Wait approximately 15 minutes for IR Camera to warm up and thermocouples to stabilize.
7. Start recording thermocouple data.
8. Perform a manual FFC event, using the FLIR Boson Application.
9. Start timer to measure the approximate heating and IR video duration.
10. Start recording video, using the FLIR Boson Application.
11. Turn on heat gun on hot mode.
12. Turn off the heat gun after reaching the target heating duration.
13. Stop recording video in the FLIR Boson Application when the timer approximately reaches the target video duration.
14. Stop recording thermocouple data and save file to laptop.

6.3.2.4. Post-Processing Procedure

Unlike the other heating methods, which provided front surface heating, the internal forced air heating tests were not post-processed using our modified TSR algorithm. That algorithm is specifically designed to observe the front surface temperature decay after subjecting the front surface to a heat source. While this testing method would benefit from a similar type of analysis (e.g., noise smoothing from polynomial fitting), the derivation of the thermal equations and post-processing algorithm is outside of this project.

Instead, the post-processing procedure focused on optimizing the contrast of the raw data images by cropping the region of interest and converting the 16 bit IR camera pixel values to 8 bit images that utilized the full 8 bit grayscale range (i.e., 0 to 255). The MATLAB function used to process these results and save log files is provided in Appendix B.3.

6.3.2.5. Results

Overall, the internal forced air heating test series yielded positive results. An interesting early result was the difference in how the flat bottom holes responded to rear surface heating. As shown in Figure 6-40, without the addition of aluminum tape, the flat bottom holes provided hot (i.e., white) regions. This is because the flat bottom holes created a thinner fiberglass region, which were easier to heat, compared to the full thickness of the rest of the specimen. To correct this issue, aluminum tape was added to each flat bottom hole to isolate an air pocket that was more representative of a disbond. This change resulted in colder (i.e., darker) regions, as expected.

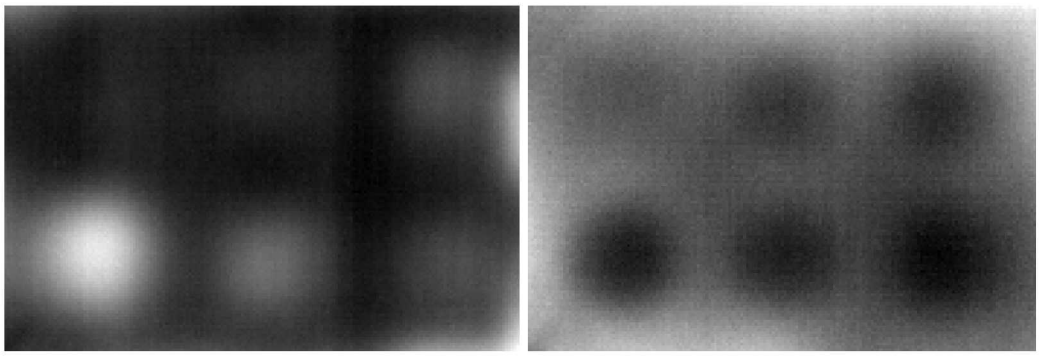

Figure 6-40: G11-STD-3 Internal Forced Air Test Results for Test 3 (No Aluminum Tape), and Test 4 (Aluminum Tape Added)

The G11-STD-X specimens provided information on the maximum depth of penetration of the flash tube system with FLIR Boson IR camera. As shown in Figures 6-43 through 6-44 and summarized in Table 6-4, the maximum discernable depth of penetration is at least .900 inches, which was the maximum flaw depth tested. This excellent depth of penetration is attributed to the large thermal gradient that is possible using rear surface forced air heating. The heating durations were also worth

noting. For even the deepest flaws, only approximately 120 seconds of heating was required.

While the team does not plan to integrate an internal forced air heating system within the scope of this project, this test series demonstrated that internal forced air heating is capable of identifying deep subsurface flaws in the spar cap structure of a wind turbine blade. If the integration challenges can be addressed, this type of system has significant benefits.

Table 6-4: Internal Forced Air Heating Solid Laminate Depth of Penetration Results

Specimen ID	All Flaws Visible?	Deepest Flaw Observed (in)
G11-STD-1	Yes	.050
G11-STD-2	Yes	.180
G11-STD-3	Yes	.450
G11-STD-4	Yes	.900 (1.000 inch does not include a flat bottom hole)

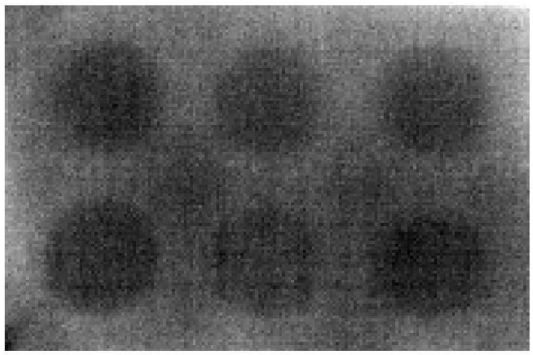

Figure 6-41: G11-STD-1 Internal Forced Air Test Results for Test 2 (15s) of Heating

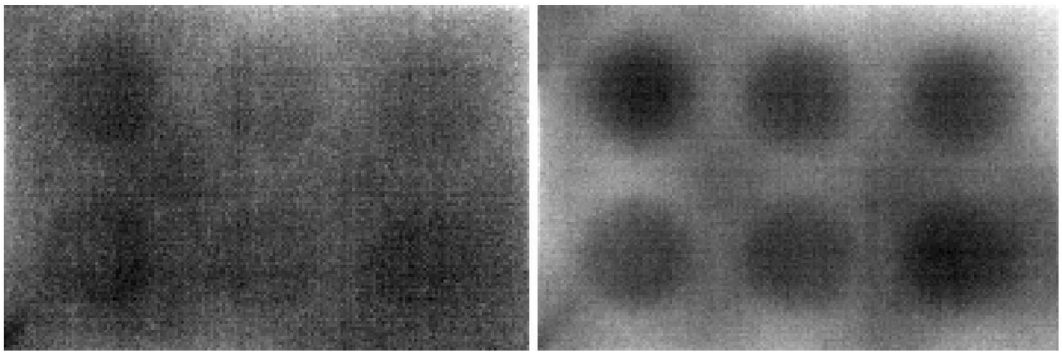

Figure 6-42: G11-STD-2 Internal Forced Air Test Results for Test 3 (15s) and Test 4 (30s) of Heating

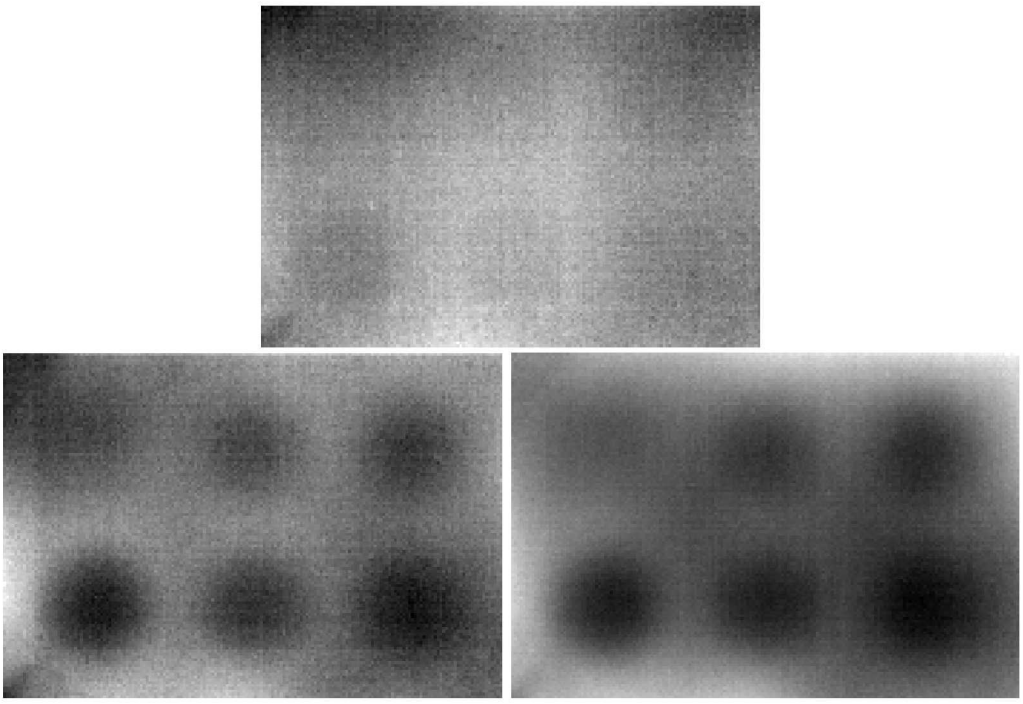

Figure 6-43: G11-STD-3 Internal Forced Air Test Results for Test 7 (15s), Test 6 (30s), and Test 4 (60s) of Heating

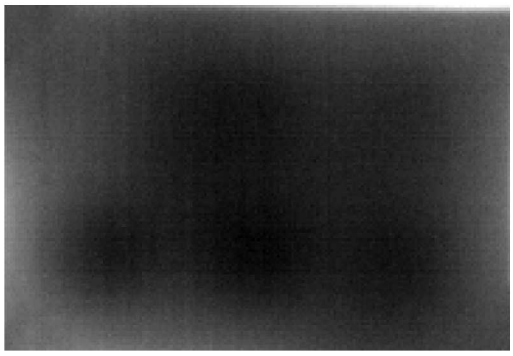

Figure 6-44: G11-STD-4 Internal Forced Air Test Results for Test 3 (120s) of Heating

6.3.3. Solar Radiation (Sun/Shade) Heating Testing

One of the most promising sources of thermal gradients is solar radiation. Because solar radiation has the potential to provide high input energy to the surface of the part, the concept is basically a higher heat, longer duration version of the flash tubes concept. The proposed method for generating the thermal gradient is:

- Stabilize wind blade temperatures at near ambient temperature by exposing them to forced convection due to normal turbine operation.
- Provide heat to the surface of the blade by stopping the turbine and pitching the blade surface into direct sunlight.
- Remove heat source by pitching the blade out of direct sunlight.
- Observe the change in surface temperature as the heat diffuses down into the blade.

To recreate this testing in a benchtop environment, specimens were thermally soaked until they reached approximately ambient indoor temperature. Then, the specimen was exposed to direct sunlight for a predetermined duration. After that, the heat source was removed by blocking the direct sunlight with a shade. Once the heat source was removed, the FLIR Boson IR camera was used to observe the temperature diffusing down into the specimen. Figure 6-45 and Figure 6-46 show examples of the experimental setup in direct sunlight and shade.

The goal of these tests was to demonstrate the solar radiation concept on a small scale and decide if the concept was feasible. Also, these experiments were designed to help establish guidelines on the required heating durations. Finally, these experiments were designed to assess if this approach is compatible with our modified TSR data processing strategy.

Figure 6-45: Solar Radiation Experimental Setup

Figure 6-46: Solar Radiation "Shade" Testing

The strategy for thermocouple data acquisition and IR data acquisition duration are the same as Section 6.3.1. In addition to these data requirements, the solar irradiance was also recorded by using Sandia's onsite Photovoltaic Systems Evaluation Laboratory. A MATLAB function was developed to record the global normal solar irradiance for each thermography test by recording data from the Sandia Photovoltaic website (http://photovoltaics.sandia.gov/weather/Weather.htm). A copy of this MATLAB function is provided in Appendix B.4.

Because this is an open setup, synchronizing the timing of the thermocouples, sun/shade, and IR camera are important for post-processing the data. For this series of tests, the synchronization was performed as follows.

- The IR camera is manually instructed to perform a FFC event, using FLIR Boson Application.
- The IR camera is manually instructed to begin videoing, using FLIR Boson Application.

- The specimen is exposed to direct sunlight, by rolling the cart into the sun.
- A timer is started to measure the approximate exposure to direct sunlight.
- After the specified duration of direct sunlight exposure, a cardboard sheet is used to shade the specimen.
- After the data acquisition duration is achieved, the IR camera is manually instructed to stop videoing, using FLIR Boson Application.

Because all these operations are manually performed, the timing is synchronized during post-processing as follows.

- Thermocouples: Assume T_{max} occurs at $t = 0$
- IR Video: Assume T_{max} (i.e., highest pixel value) occurs at $t = 0$
- Solar Irradiance: Average global normal solar irradiance values for the hour that testing occurred.

6.3.3.1. Test Matrix

In order to maximize the depth of penetration for the solar radiation concept, a balanced approach to the duration of direct sunlight exposure was required. Additional time in direct sunlight increases the total heat input, which increases the depth of penetration. However, too much time in the sun allows the heat to begin diffusing down into the part prior to performing the inspection. This premature thermal diffusion results in data loss, particularly near the surface. In our case, the low thermal diffusivity of fiberglass allows us to provide a relatively high total heat input without sacrificing too much data. Also, less heating time requires less turbine stoppage time, which is more cost efficient. In the end, it was determined that scoping experiments should be performed to ascertain what durations of heat input work best.

Like the other benchtop tests, the decision was made not to improve the emissivity of the specimens by painting them matte black. While this would have improved the test results, it was considered an unrealistic case because the current drone integration concepts do not have plans for painting specimens.

For the solar radiation tests, the primary goal was to measure the maximum depth of penetration in thick fiberglass composites, using thick specimens with flat bottom holes set at various depths. Also, as a secondary goal, the plan was to find a suitable range for the duration of direct sunlight exposure.

Based on these considerations, the test matrix in was developed.

Table 6-5: Solar Radiation Test Matrix

Specimen	Comments
G11-STD-1	
G11-STD-2	
G11-STD-3	
G11-STD-4	Contain deeper flaws. Decide whether to test based on G11-STD-3 test results
G11-STD-5	
FGB-1	
FGB-2	
FGB-3	
FGB-4	
REF-STD-1-050-TPI-1	
DRY-SPOTS	
WIND-1-029	
WIND-2-044	
WIND-3-110-SPAR-140	Contain deeper flaws. Decide whether to increase duration based on G11-STD-3 test results
WIND-4-161	
WIND-5-180	
WIND-6-180-SPAR-220	
GLF-S05-C4T2	Use experience on timing from REF-STD-1-050-TPI-1
GLF-S05-C4T2-P5-02	
GLF-S04-C4T2	
GLF-S05-C6T2	
GLF-S06-C4T2	

6.3.3.2. Data Acquisition

The following data for the flash tube testing was recorded.

- Date/Time
- Test Location (e.g., Building 894/Room 157)

- Location of Thermocouples
- Test Specimen ID
- Test Number
- IR Camera Information – model, resolution, frame rate, serial number
- IR camera settings – file format and quality, automatic gain control (AGC) settings, flat field correction (FFC) settings, target video duration
- Global Normal Solar Irradiance – recording method, data filename
- Heating Duration
- Ambient Outside Temperature near specimen, per thermocouple reading
- Test notes

Screenshots of the flash tube testing template are shown in Figure 6-47.

Date	Time (approx. time specimen is placed on outside table, to the minute)	Location	Temp Data (Location of Thermocouples)	Test Specimen ID	Test #	IR Camera
6/14/2017	2:35pm	Heating: Outside (West) of 894/157 Cooling: 894/157	TC1 (K Type): Front, Top Left TC2 (K Type): Back, Top Left TC3 (K Type): Air	G11-STD-2	1	FLIR Boson Resolution: 320x256 Frame Rate: 60 Hz S/N: 2338

IR Camera Settings	Global Normal Solar Irradiance	Heating Duration (s)	Outside Air Temperature	Inside Air Temperature	Notes (Transition Time is the approx. time required to move the part into the shade)
Format: 16-bit TIFF sequence (IR16) AGC Settings: Pre-AGC FFC: Manual, 16 frames integration, performed immediately before test Video Duration (after heating): 30	Recorded by MATLAB PV_Website_Read function every 1 minute File: Solar Irradiance Data 6-14-17.xlsx	30	Recorded by TC3 peak temperature during heating Also recorded by MATLAB PV_Website_Read function every 1 minute	Recorded by TC3 after test	Video File: Boson_Capture_74.tiff Thermocouple File: 051 Transition Time: 9s Part placed on plastic rails to provide an airgap under the part After this test this rails were moved in slightly to prevent them from contacting TC2

Figure 6-47: Screenshots of Solar Radiation Testing Data Acquisition Form

6.3.3.3. Test Procedure

1. Start collecting solar irradiance data by running MATLAB function PV_Website_Read.
2. Apply thermocouples TC1 and TC2 to front and rear surfaces (as shown in Figure 6-13 and Figure 6-14) with flash breaker tape.
3. Connect thermocouples to Omega HH1384 4-channel thermocouple datalogger, including TC3 for ambient temperature.

4. Turn on laptop, thermocouple datalogger, TWI EchoTherm flash tube system, and FLIR Boson IR Camera (plug the USB cable into the laptop).
5. Open FLIR Boson Application, connect to IR Camera (e.g., COM7), and double check camera settings.
6. Open D4IThermoMeter software and connect to thermocouple datalogger (e.g., COM6).
7. Wait approximately 15 minutes for IR Camera to warm up and thermocouples to stabilize.
8. Start recording thermocouple data.
9. Move the specimen outside into direct sunlight.
10. Start timer to measure the approximate heating duration.
11. After reaching the target heating duration, perform a manual FFC event, using the FLIR Boson Application.
12. Start recording video, using the FLIR Boson Application.
13. Start timer to measure the approximate IR video duration.
14. Stop recording video in the FLIR Boson Application when the timer approximately reaches the target video duration.
15. Stop recording thermocouple data and save file to laptop.

6.3.3.4. Post-Processing Procedure

The general solar radiation testing post-processing strategy was the same as flash tubes testing. In effect, the solar radiation replaced the flash tubes, and the strategy for observing the subsequent temperature decay of the front surface of the specimen remains the same. The main difference is that the testing was performed in a more open environment than the TWI EchoTherm flash hood. This required special consideration to ensure that outside influences, such as reflections, did not disrupt the data and/or post-processing algorithm (e.g., a reflection could cause the algorithm to incorrectly determine the frame with the maximum temperature).

6.3.3.5. Results

Overall, the solar radiation test series produced excellent results. The G11-STD-X, FGB-X and wind blade test specimens provided information on the maximum depth of penetration of the solar radiation concept. As shown in Figures 6-48 through 6-57 and summarized in Table 6-6, the maximum discernable depth of penetration approaches one inch for long (e.g., several minutes) IR video durations. These results are particularly encouraging and suggest that a solar radiation heating method could inspect the majority of the wind blade structure, with the exception being deep subsurface flaws in the spar cap or bond line.

Also, similar to flash tubes, the thermography system performed extremely well at finding all the flaws in the sandwich construction as shown in Figures 6-59 through 6-61. One caveat with these results is that the system had issues with the GLF series of specimens, due to their glossy surface. This is not expected to be a significant issue with the more matte finish of the wind blade paint.

The solar radiation intensity values were fairly consistent throughout testing, as shown in Appendix D. Additional work will be required to demonstrate that wind farm locations and/or times of the year with less solar radiation are adequate to provide results of a consistently high quality.

Table 6-6: Solar Radiation Solid Laminate Depth of Penetration Results

Specimen ID	All Flaws Visible?	Deepest Flaw Observed (in)
G11-STD-2	Yes	.180
G11-STD-3	No	.350
G11-STD-4	No	.500
FGB-1	Yes	.650
FGB-2	Yes, after long video duration	.950
WIND-1-029	Yes	.256
WIND-2-044-SPAR-085	Yes (not counting bondline flaws)	.328
WIND-3-110-SPAR-150	No	.480
WIND-4-161	No	.660

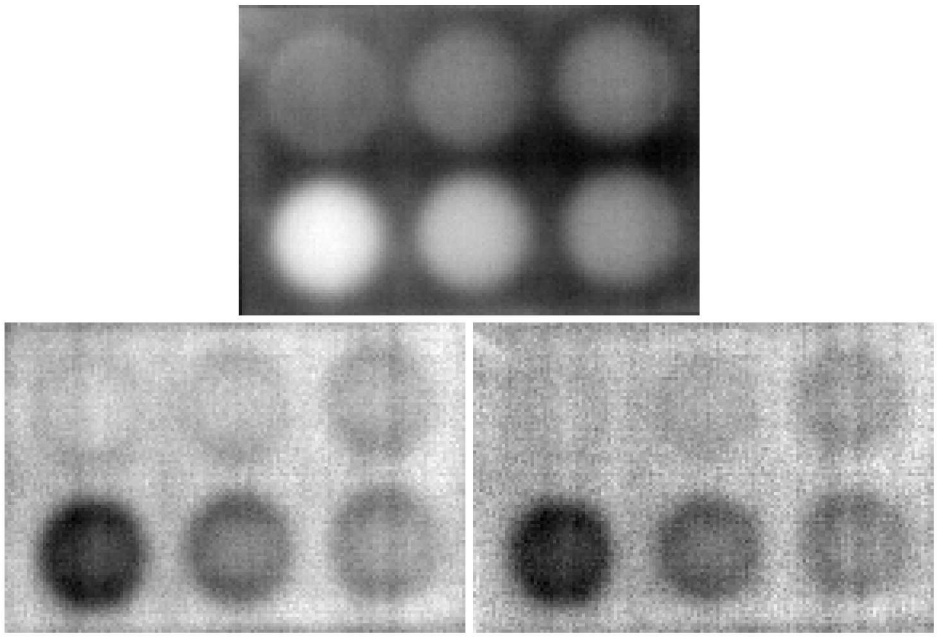

Figure 6-48: G11-STD-2 Solar Radiation Test 1 Results for TSR (at 1 frames), 1D (at 188 frames), and 2D (at 168 frames)

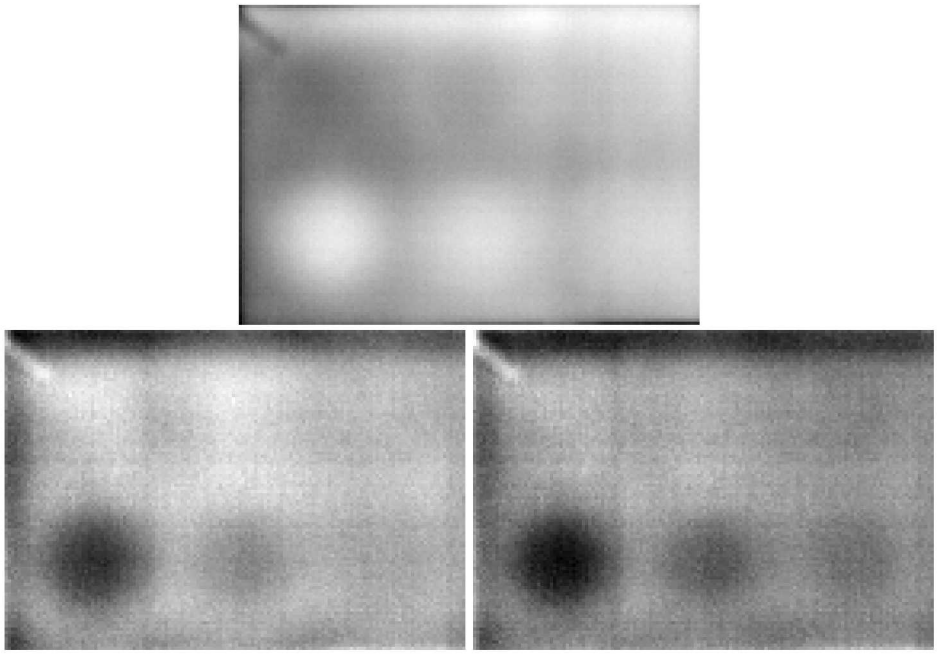

Figure 6-49: G11-STD-3 Solar Radiation Test 2 Results for TSR (at 170 frames), 1D (at 190 frames), and 2D (at 172 frames)

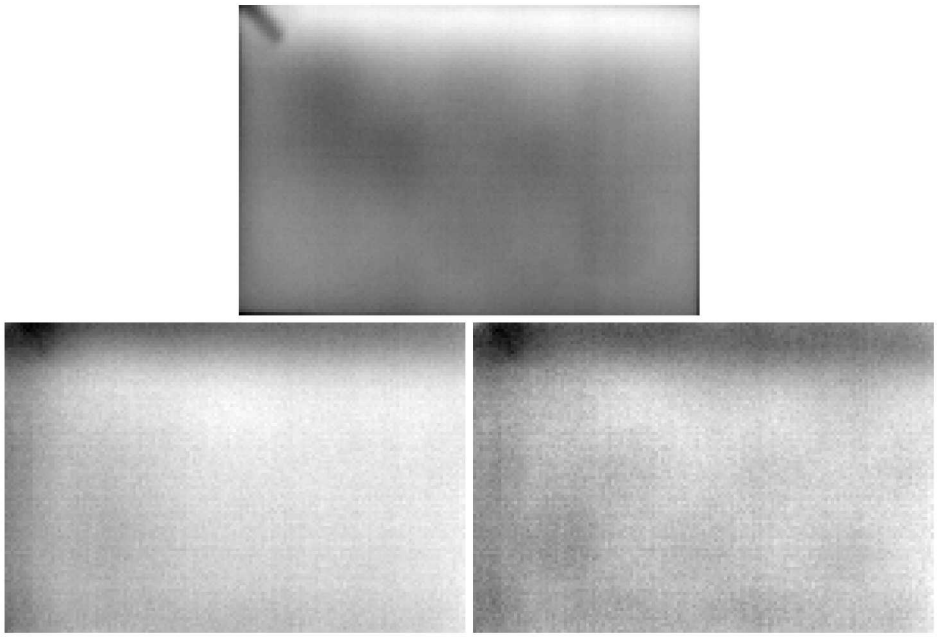

Figure 6-50: G11-STD-4 Solar Radiation Test 2 Results for TSR (at 161 frames), 1D (at 193 frames), and 2D (at 181 frames)

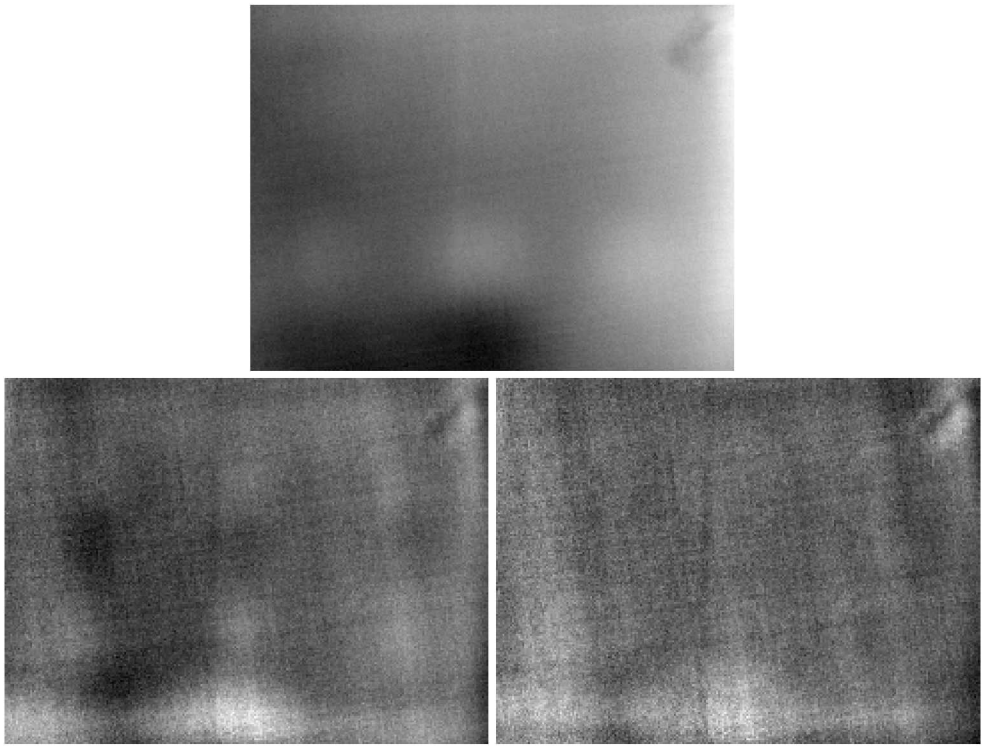

Figure 6-51: FGB-1 Solar Radiation Test 2 Results for TSR (at 200 frames), 1D (at 200 frames), and 2D (at 200 frames)

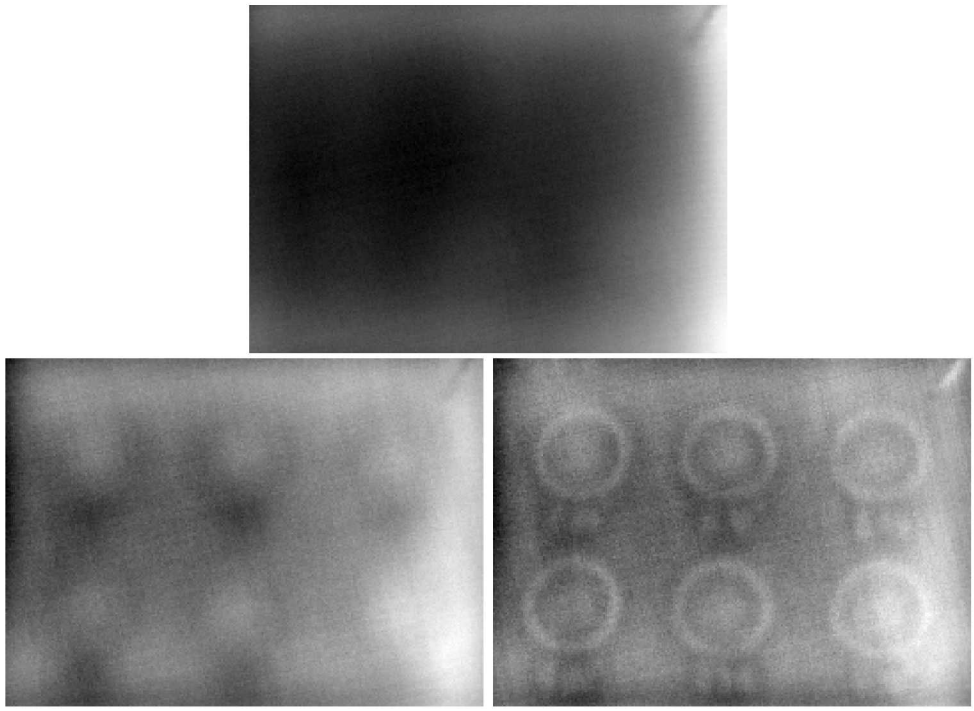

Figure 6-52: FGB-2 Solar Radiation Test 1 Results for TSR (at 200 frames), 1D (at 187 frames), and 2D (at 167 frames)

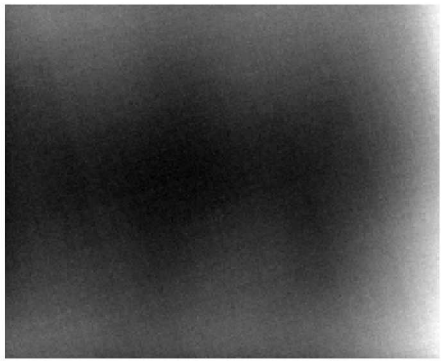

Figure 6-53: FGB-2 Solar Radiation Results – Screenshot of Raw Video Several Minutes After Test 1

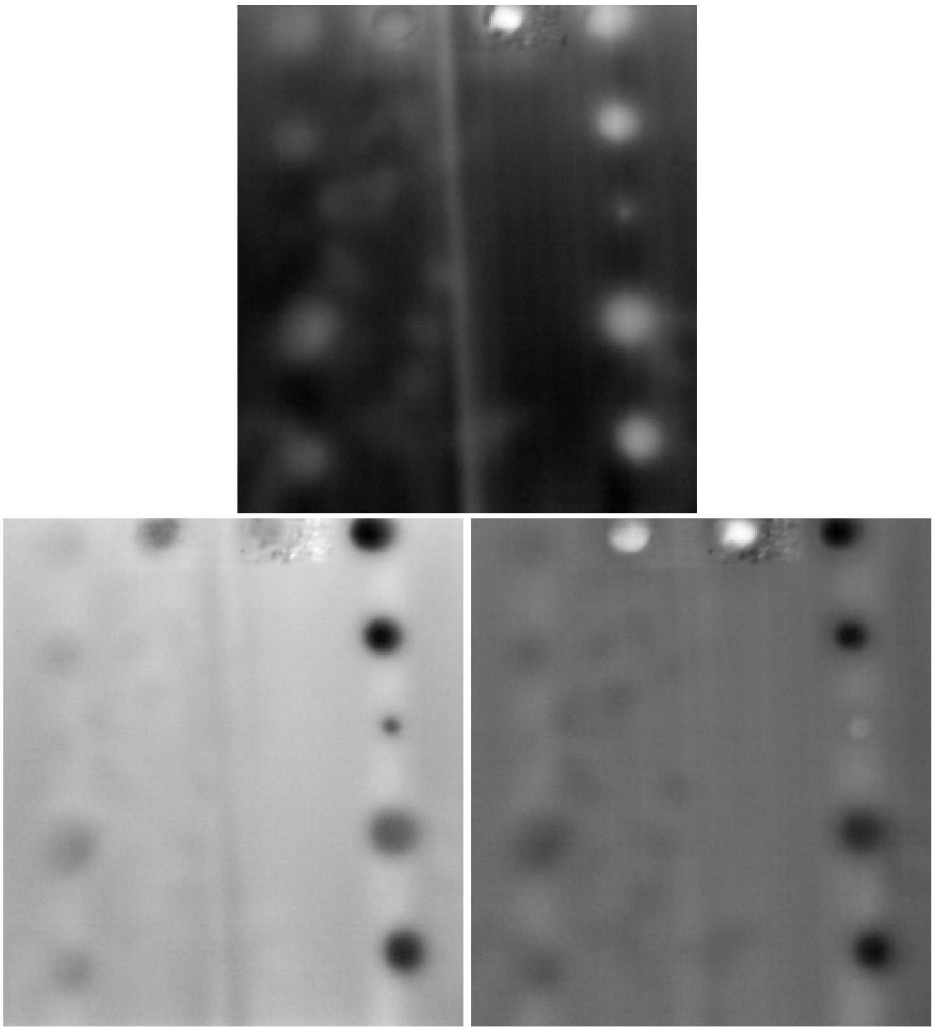

Figure 6-54: WIND-1-029 Solar Radiation Test 2 Results for TSR (at 132 frames), 1D (at 181 frames), and 2D (at 172 frames)

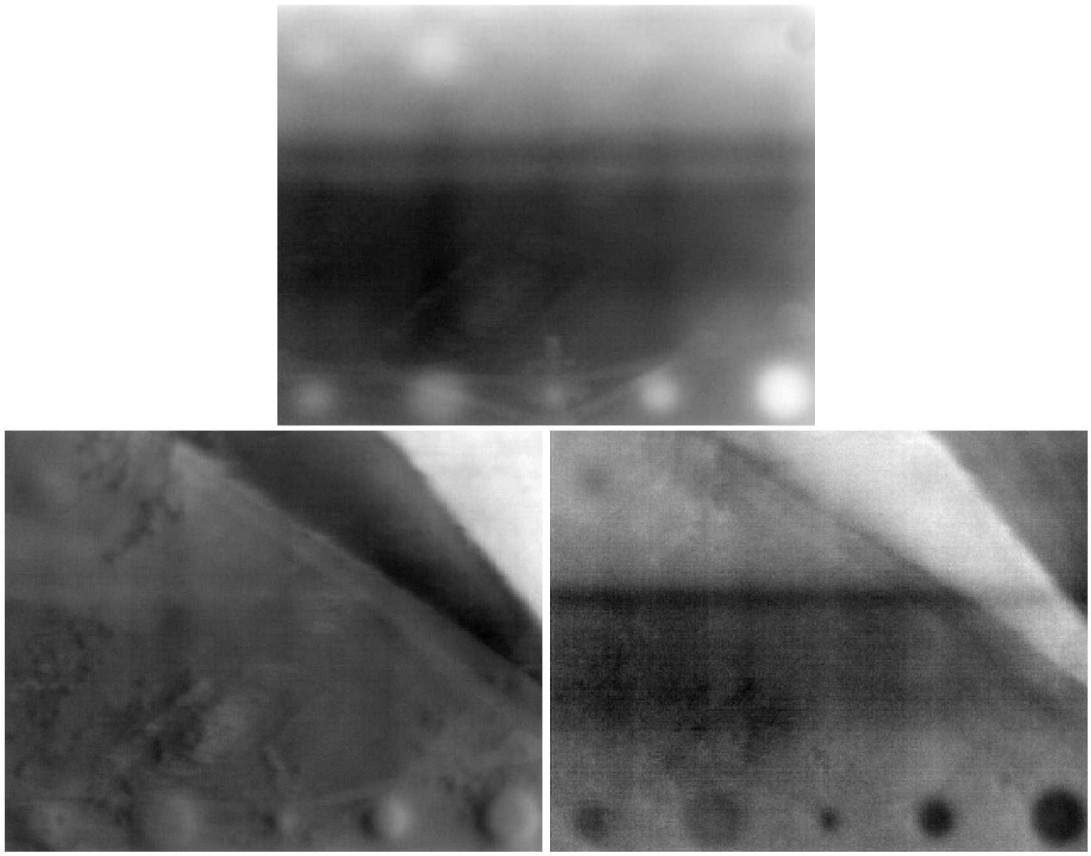

Figure 6-55: WIND-2-044-SPAR-085 Solar Radiation Test 1 Results for TSR (at 176 frames), 1D (at 135 frames), and 2D (at 172 frames)

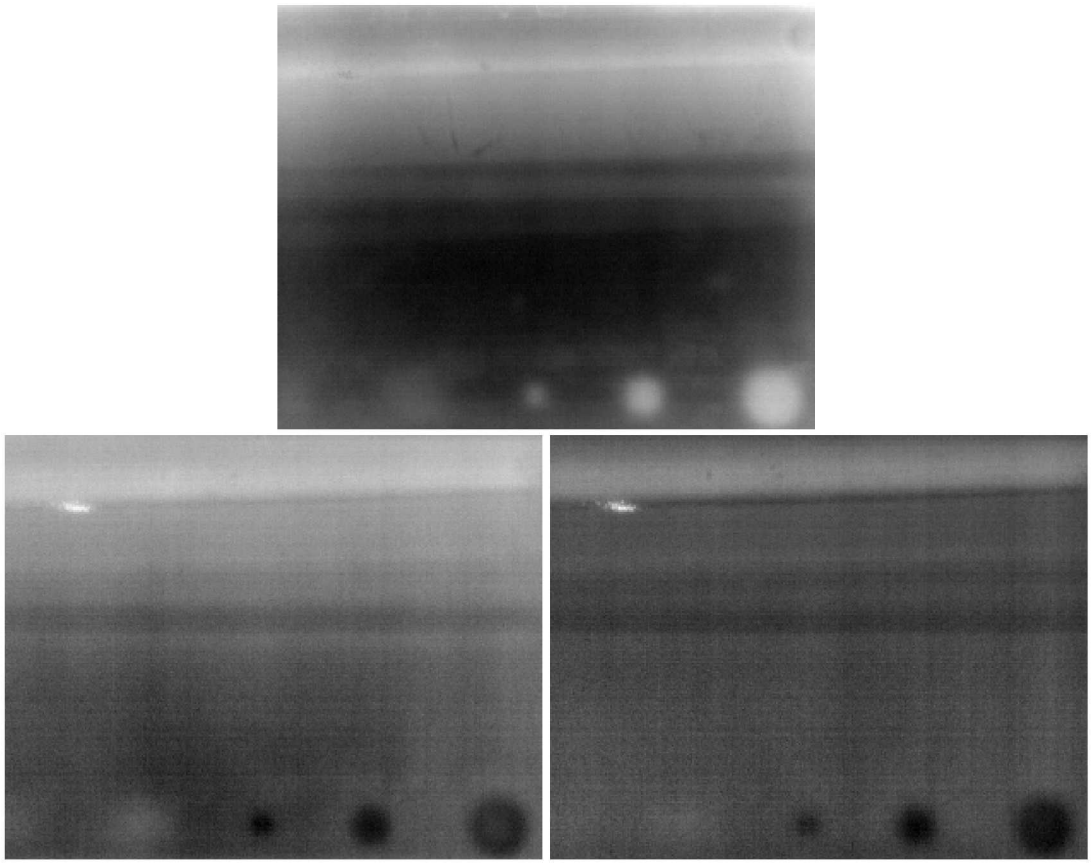

Figure 6-56: WIND-3-110-SPAR-140 Solar Radiation Test 1 Results for TSR (at 105 frames), 1D (at 185 frames), and 2D (at 174 frames)

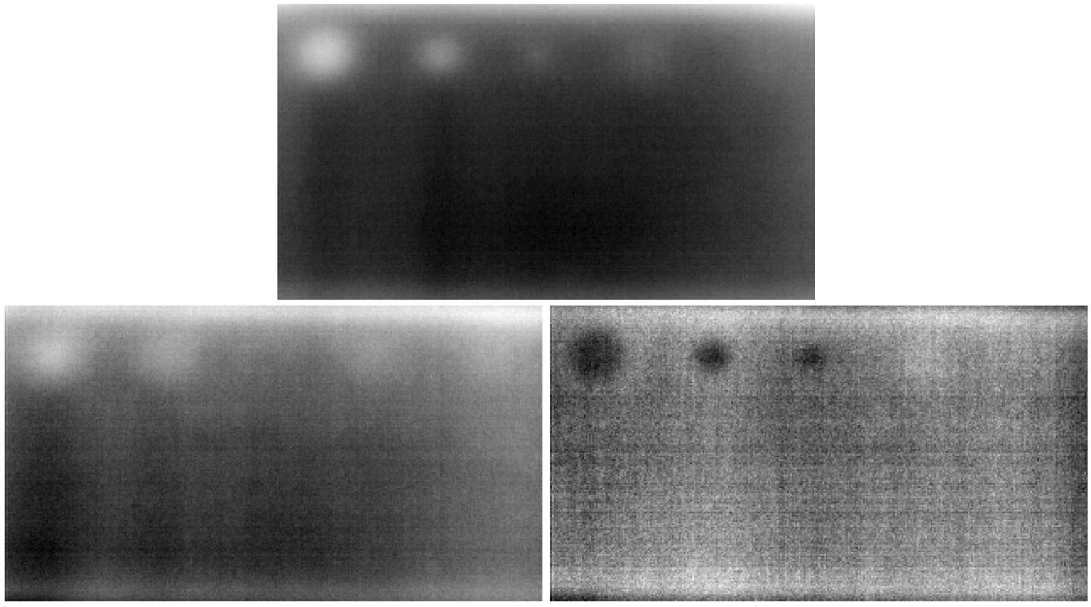

Figure 6-57: WIND-4-161 Solar Radiation Test 1 Results for TSR (at 200 frames), 1D (at 177 frames), and 2D (at 173 frames)

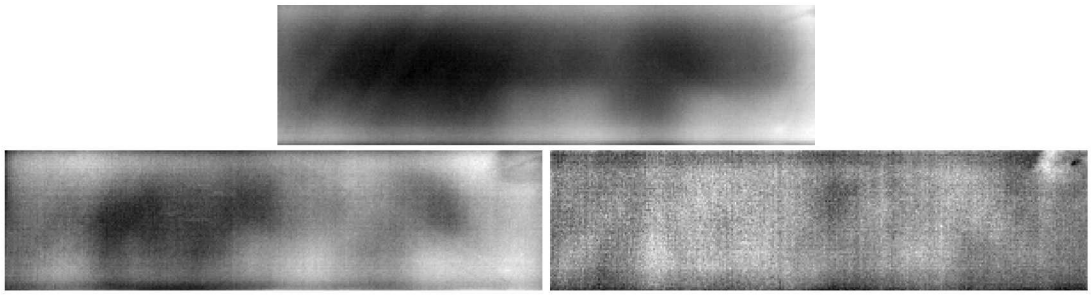

Figure 6-58: DRY-SPOTS Solar Radiation Test 2 Results for TSR (at 170 frames), 1D (at 167 frames), and 2D (at 200 frames)

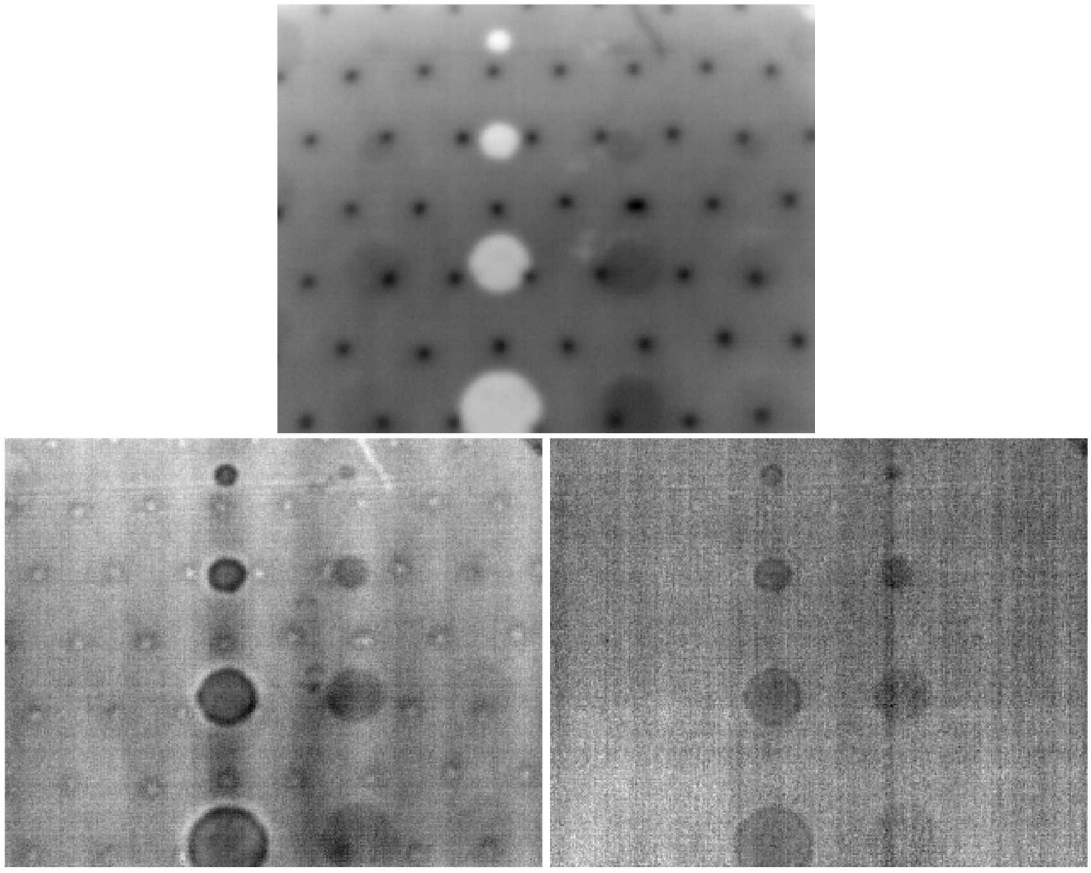

Figure 6-59: REF-1-STD-050-TPI-1 Solar Radiation Test 1 Results for TSR (at 1 frames), 1D (at 122 frames), and 2D (at 79 frames)

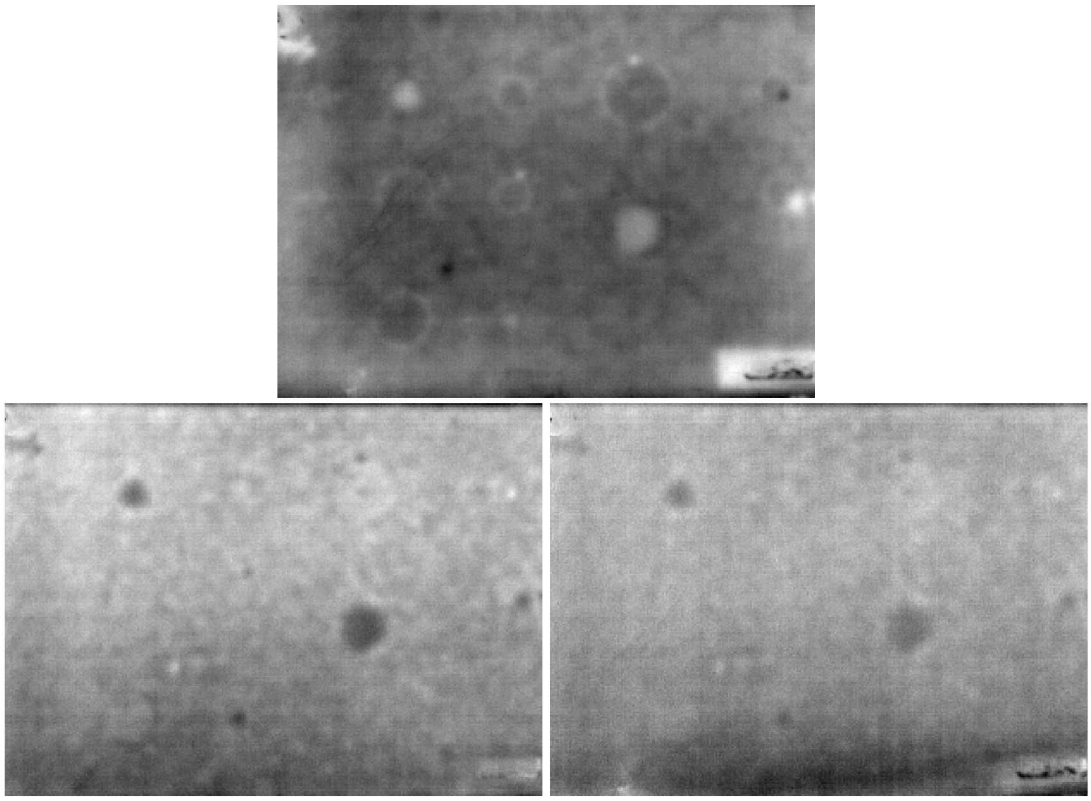

Figure 6-60: GLF-S06-C4T2 Solar Radiation Test 2 Results for TSR (at 71 frames), 1D (at 156 frames), and 2D (at 132 frames)

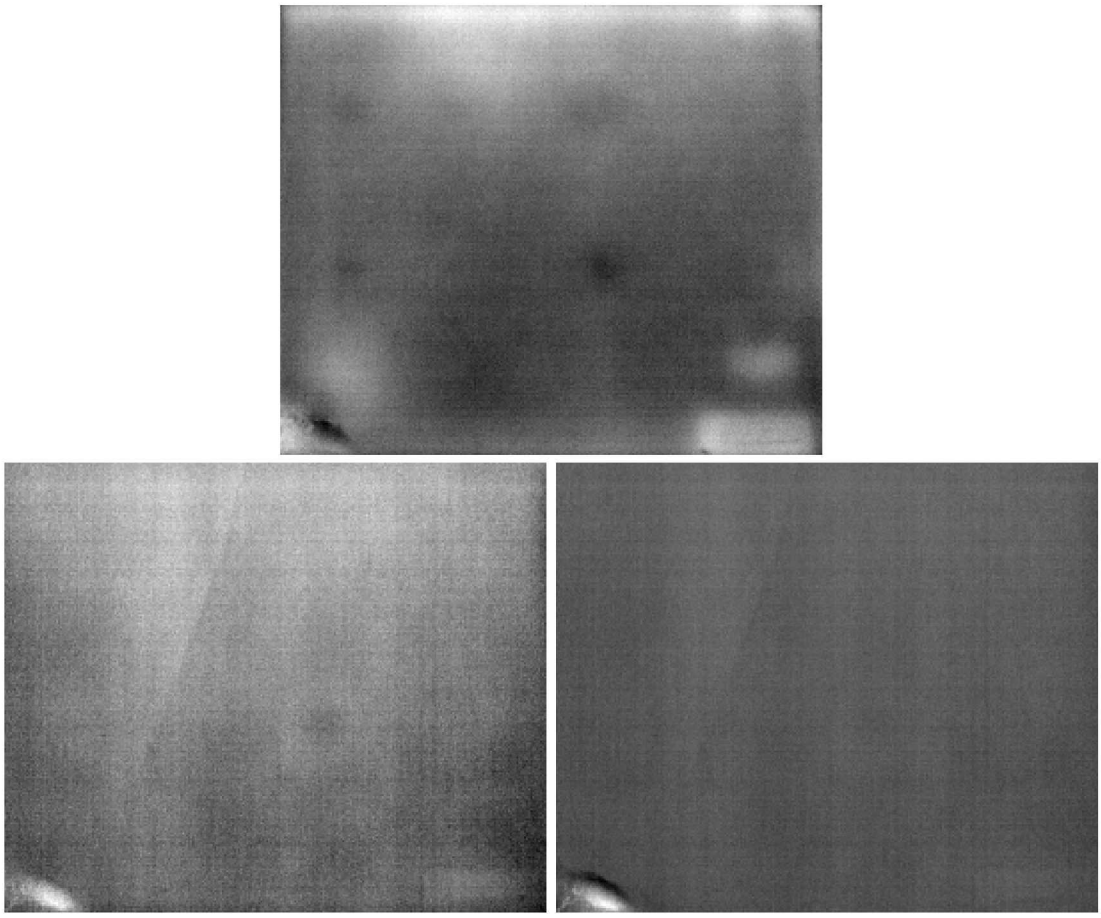

Figure 6-61: GLF-S05-C6T2 Solar Radiation Test 1 Results for TSR (at 157 frames), 1D (at 187 frames), and 2D (at 178 frames)

6.4. Conclusions

All three testing methods were successful in identifying engineered flaws in wind blade specimens. While flash tubes and internal forced air showed promise, solar radiation was selected as the most promising technique for drone integration testing. The method consistently detected flaws greater than .500 inches deep, and in one case, detected a flaw as deep as .950 inches. In addition to providing good depth of penetration and successful inspection of both solid laminates and sandwich structures, solar radiation is also the most feasible concept for immediate integration. Section 0 provides details on the initial integration of this technique.

Finally, some concepts for future work as well as lessons learned from these tests are provided in Section 0.

6.5. References

6.1. Roach, D., Neidigk, S., Rice, T., Duvall, R., Paquette, J., “Blade Reliability Collaborative: Development and Evaluation of Nondestructive Inspection Methods for Wind Turbine Blades,” Sandia DOT Report, SAND2014-16965, September 2014.

THIS PAGE INTENTIONALLY LEFT BLANK

7. THERMOGRAPHY DRONE INTEGRATION TESTING

Based on successful benchtop testing, the team identified solar radiation as the most promising concept for drone integration tests. The team also performed some evaluations on turbine operational heating, which could not be evaluated during benchtop testing. The following sections detail the team's thermography system integration efforts as well as the results of these tests.

7.1. IR Camera Integration

7.1.1. Hardware Integration

The FLIR Boson was selected in part due to its small size which allows it to fit on the existing gimbal. For initial testing, attaching the Boson required replacing the digital camera, as shown in Figure 7-1. The Boson was attached to the gimbal using the Boson tripod mount accessory with a standard ¼"-20 thread (Figure 7-2). The power supply and data connection was achieved using the USB connector on the Boson VPC kit (Figure 7-3).

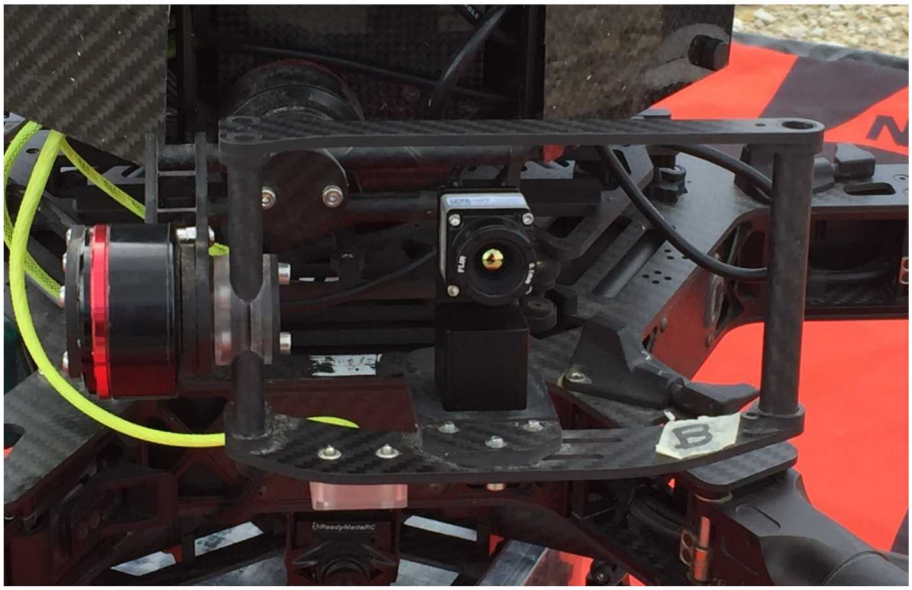

Figure 7-1: FLIR Boson Mounted on Gimbal Using Boson Tripod Mount Accessory

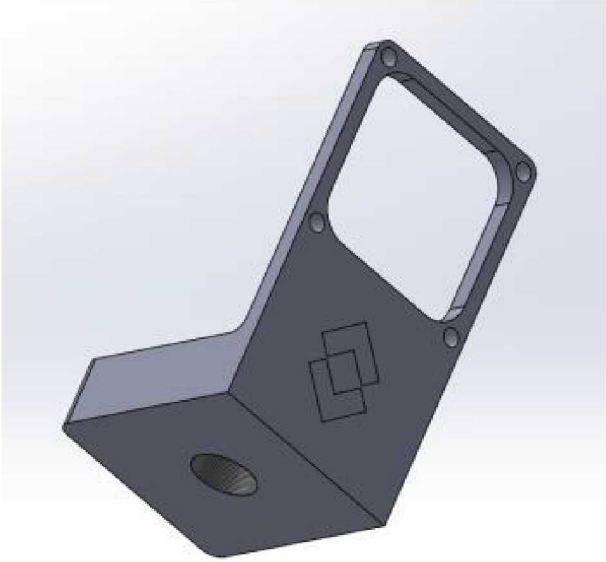

Figure 7-2: FLIR Boson Tripod Mount Accessory

Figure 7-3: FLIR Boson VPC Kit

Moving forward, the plan is to simultaneously use the digital camera and IR camera. In this case, the digital camera would be fastened in its usual location in the center of the gimbal, and the Boson would be fastened to the side of the camera with Velcro. The Boson tripod mount accessory would no longer be required and could be removed to save weight.

7.1.2. Software Integration

For the benchtop testing described in Section 6, the Boson was controlled through the Windows FLIR Boson Application GUI. However, in order to use the Boson on the drone, we needed to control the video operations through additions to SkySpecs'

software or the Linux command line. The team initially tried to use the FLIR Boson Software Development Kit (SDK) to control the camera settings and capture video. However, during initial attempts, the SDK appeared to be limited to capturing single images rather than video at the full 60 Hz framerate.

Due to limitations with the SDK, the team transitioned to using the guvcview Linux application which enables the user to record video from a wide range of camera types. After encountering some initial issues with the configuration file not saving the camera settings, the team was able to record the pre-AGC 16-bit video feed as a .raw binary file. As expected, the binary files started with a set number of bits to document header information (e.g., camera settings). These extra bits are easily removed. However, the binary files also included an inconsistent number of bits between frames that needed to be removed to process the IR data. In order to remove those bits, we wrote a MATLAB function that is provided in Appendix B.1.

For the initial integration tests, the guvcview application was not incorporated into autonomous drone control software. Therefore, for these initial tests, SkySpecs connected a laptop to the sensor rig and used the command line to manually start capturing video. The laptop was then disconnected prior to flying the drone toward the wind turbine of interest.

Moving forward, multiple improvements should be made to software integration strategy. First, the IR video capture software should be folded into the existing sensor rig software. This will make it a repeatable operation and tie the results to the other drone date such as position and orientation. Next, the SDK should be used to perform a manual FFC operation immediately prior to beginning inspections to reduce signal noise. Finally, the .raw output files need to be better understood in order to perform a more robust method of accessing the IR data (i.e., understand and removing the bits between frames).

7.2. Integration Testing

After performing hardware and software integration activities, the team progressed to the initial drone integration testing. This initial integration test was a critical milestone for the program and included the following goals:

- Demonstrate that the hardware and software integration strategy was effective.
- Evaluate IR camera performance in real life conditions (e.g., wind, sun/glare).
    1. Determine if the lens selection and corresponding FOV are adequate.
- Perform an initial assessment of the effectivity of the solar radiation heating method in real life conditions.
- Evaluate the merits of the turbine operational heating concept, which was not included in benchtop testing.

Ideally, this testing would be performed at a controlled wind farm environment, where we would have prior information about wind blade flaw locations and repair history.

Additionally, we would prefer follow-on access to the wind farm, in order to perform detailed follow-up nondestructive inspections at a later time. Due to these priorities, our first choice was to use the Department of Energy funded Sandia Scaled Wind Farm Technology (SWiFT) facility in Lubbock, TX. This facility includes the use of scaled (i.e., reduced size) blades to perform various research projects. As such, the blades are occasionally removed from the turbine, which would enable us to perform detailed nondestructive inspections on the ground, included phased array ultrasonic inspections.

The team also considered various wind farms near the SkySpecs office. Close proximity to SkySpecs and existing relationships between the wind farms and SkySpecs would have provided a number of options for follow-on activities.

Ultimately, a constraint on the number of available drone assets limited our ability to test at the SWiFT and sites local to SkySpecs. The team decided that the most practical solution was for Sandia to join SkySpecs during one of their scheduled inspection jobs at a wind farm site in Iowa. Note, that due to proprietary agreements between SkySpecs and the wind farm, the exact site cannot be specified. However, it is worth noting that the wind farm consists of fairly new turbines, which means that they are unlikely to contain any damage.

7.2.1. Test Planning

In order to accomplish our test goals, we planned to perform two primary tests – solar radiation heating and operational turbine heating. Focusing on these two tests would enable us to evaluate the two most promising techniques heating sources. Then, while we perform those two tests, we could also assess the other performance goals highlighted in the previous section.

As previously discussed in Section 7.1.2, the IR camera needs to be run in manual mode. We also do not have access to view the live output from the IR camera. Therefore, we need to set the IR camera to record data for a predetermined duration and plan a flight strategy that fits within that time window.

Solar Radiation Heating Test Plan

The main goal of the solar radiation tests was to demonstrate that the IR camera is able to capture the thermal changes on the surface of the wind blade. Given that the wind blades are relatively new and unlikely to have many defects, the team decided to focus on a region of the blade with the highest likelihood of exhibiting temperature gradients that are different than the surrounding blade surface. Because the lightning receptor is made out of a metallic material with significantly different thermal properties than the surrounding fiberglass, it was selected as the focal point for the solar radiation tests.

Based on the solar radiation heating benchtop testing, we decided to pitch the blade into the sun for approximately 2 minutes. Then, we would pitch the blade into the shade and start collecting IR video of the lightning receptor. Because of the limitations with recording manual IR video as well as the benefit of capturing the

initial cooling, we planned to fly the drone near the blade while it was heating. That way, once the blade was pitched into the shade, the drone would be nearby to begin filmed as soon as possible.

Operational Turbine Heating Test Plan

The primary goal of the operational heating tests was to assess whether the operational heating would generate a detectable temperature difference. Since we are not aware of any existing damage or stress "hot spots", we decided to focus on the vortex generators (VGs) because the difference in air flow around the VGs should result in different temperatures.

We decided to run the turbine for at least several minutes prior to testing to ensure the blade surface temperatures had reached a steady state. Then, we would stop the turbine as quickly as possible (i.e., expected to be less than one minute) and then start collecting IR video. Similar to the solar radiation heating test plan, we planned to fly the drone near the blade, prior to stopping the turbine. This would enable us to start filming the VGs as soon as possible.

7.2.2. Test Procedure

As described in the previous section, the test plan included both solar radiation heating and turbine operational heating test series. Unfortunately, the solar radiation heating required sunny or at least partly cloudy conditions, and we experienced very cloudy conditions. Because of this limitation, we were only able to perform the operational heating tests.

For turbine operational heating, the following procedure was developed:

1. Attach the FLIR Boson to the gimbal and connect the VPC Kit USB cable to the sensor rig.
2. Connect a laptop to the sensor rig with an ethernet cable and use the command line to start recording IR video for five minutes (see Figure 7-4).
3. Start a timer to monitor how much IR video time we have remaining.
4. Disconnect the ethernet cable from the sensor rig.
5. Manually fly the drone near the turbine but at a safe distance (see Figure 7-5).
6. Use the turbine controls on the tower to stop the turbine (see Figure 7-6).
7. Manually fly the drone into position and begin filming the VGs (see Figure 7-7).
8. Manually control the drone to attempt to hold a constant position for remainder of the video duration (i.e., approximately 3 minutes).
9. Manually land the drone.
10. Use the turbine controls on the tower to restart the turbine.
11. Connect a laptop to the sensor rig and verify that the IR video file was saved.

Figure 7-4: Using the Laptop to Start Collecting IR Video

Figure 7-5: Flying the Drone in Manual Mode

Figure 7-6: Stopping the Wind Turbine Prior to Inspection

Figure 7-7: Manually Holding the Drone's Position Near the Wind Blade Tip

7.2.3. Results

During the first day of testing, the team successfully integrated the FLIR Boson IR camera and collected our first IR video of a stopped wind turbine. Upon reviewing the data, we realized that the IR camera recorded a .mkv file using the H.264 codec. The .mkv file is an 8-bit video of IR data taken after the Boson's AGC feature is applied. While this wasn't what we intended, it was a good first chance to assess how well the FLIR Boson performs in real-life conditions. Figure 7-8 shows a screenshot of this video which shows an overall good level of detail. Note that you can see the VGs on the left side of the blade. Potential improvements would be to use a lens with a narrower field of view (e.g., 18mm lens with a 12° HFOV) and switching to the 640x512 resolution, which was not available at the time this project started.

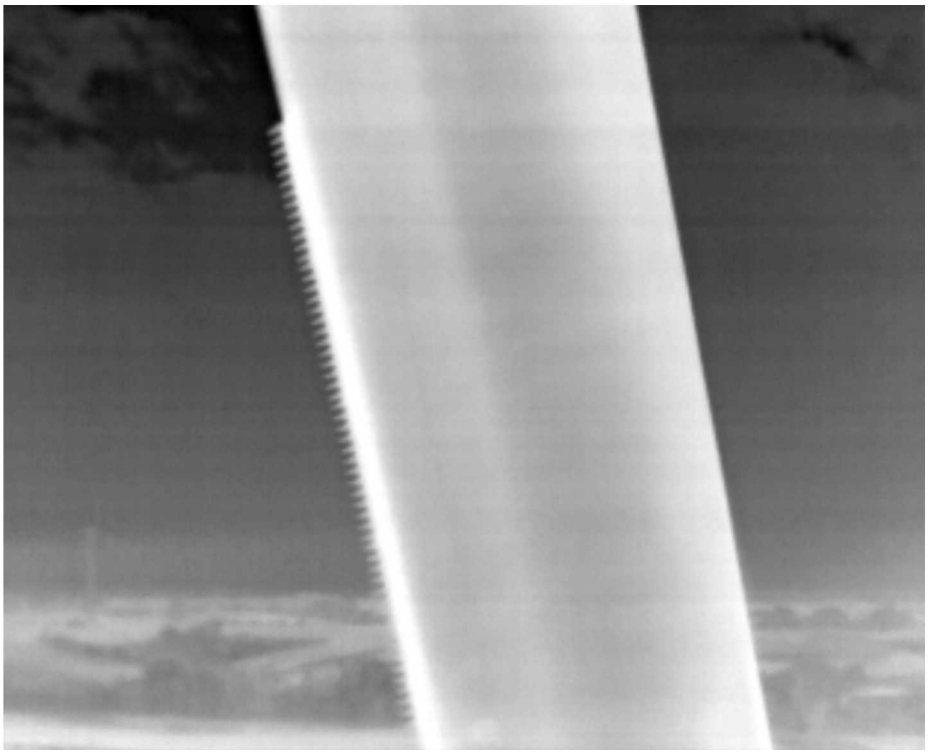

Figure 7-8: Screenshot of First Drone-Deployed IR Video

Troubleshooting revealed that the guvcview Linux application was not properly saving the GUI settings into the configuration file. After some changes to ensure that we were accessing the desired pre-AGC 16-bit data from the Y12 feed, the IR camera was ready to save .raw files. With the IR camera properly configured, another test was performed on a stopped wind turbine.

Figure 7-9 and Figure 7-10 show screenshots of the results of the test, after post-processing in MATLAB to convert the binary .raw file into TIFF stacks (see Appendix B.1) and opening them in ImageJ. The 8-bit TIFF stacks have the benefit of automatic contrast post-processing on each video frame, which enables the user to clearly identify features on the wind blade. Meanwhile, the 16-bit TIFF stacks retain all the original pixel values, which enables the user to perform various thermography post-processing techniques such as TSR.

In both images, the VGs are still visible and the lightning receptor near the blade tip is easy to differentiate from the surrounding fiberglass. Based on these results, the team determined that we were ready to proceed the next day with the scheduled solar radiation heating and operational turbine heating.

Figure 7-9: Screenshot of First Pre-AGC IR Video (After Post-Processing in MATLAB and Saving as a 8-bit TIFF Stack)

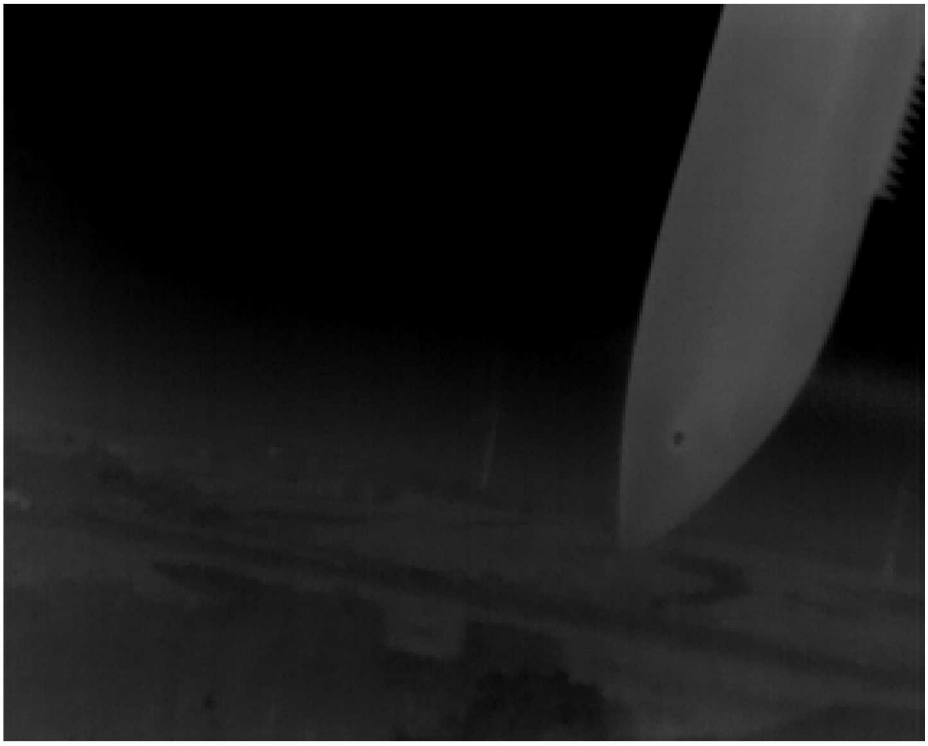

Figure 7-10: Screenshot of First Pre-AGC IR Video (After Post-Processing in MATLAB and Saving as a 16-bit TIFF Stack)

Unfortunately, the weather was much more challenging on the second day of testing. Because of the clouds, the team made the decision to postpone the solar radiation heat testing until a later testing opportunity. Instead, we would focus on the operational turbine heating tests. The wind was also a complicating factor, which drove the pilot to fly at a slightly further distance from the blade to ensure the drone and blade were safe.

As planned, the pilot flew the drone in manual mode near the turbine while we used the wind turbine controls to stop the turbine. Then, when the turbine was stopped, the pilot flew the drone closer to record IR video of the wind blade. We were ultimately able to perform two tests using this method. A sample of the results from these two tests is provided in Figure 7-11 and Figure 7-12. As shown in the images, the results are less clear than the first day of testing, which makes it difficult to determine if any temperature changes are occurring. The loss of clarity was due to two factors – the larger distance between the IR camera and blade as well as a higher level of noise in the images. The increased level of noise was likely due to the timing of the FFC event. Preferably, a manual FFC would be performed immediately prior to collecting IR video. However, since we were operating in manual mode, the last FFC event was likely performed when the USB cable was connected to the IR camera, and this timing was not tightly controlled during these two tests. This was previously acknowledged in Section 7.1.2 but timing constraints limited the team's ability to integrate FFC controls during this initial test series.

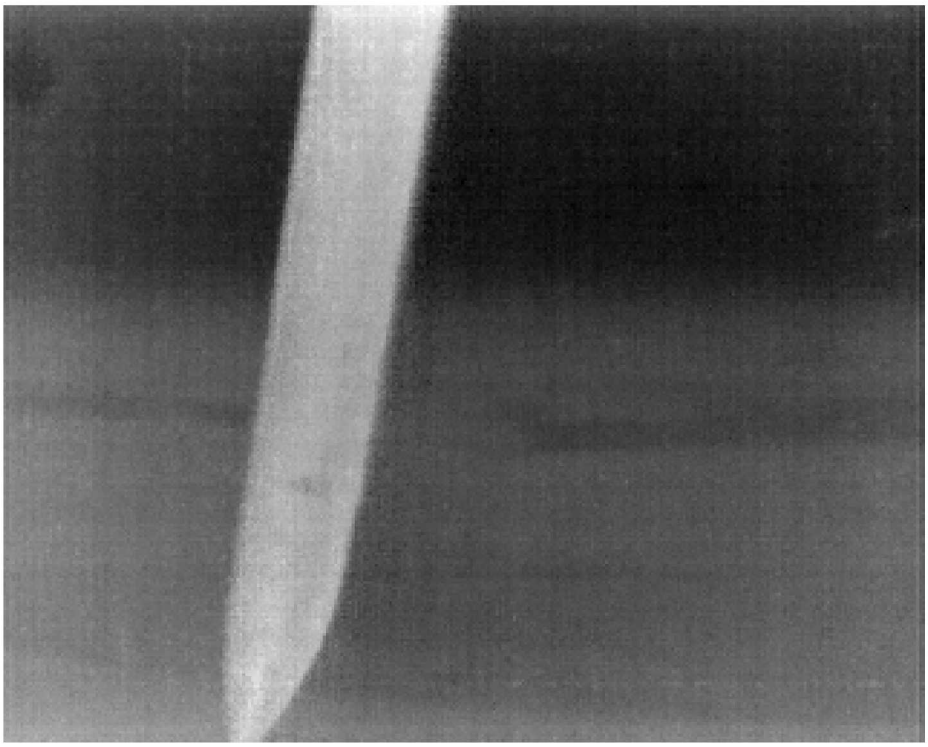

Figure 7-11: Screenshot of First Operational Turbine Heating Test (After Post-Processing in MATLAB and Saving as a 8-bit TIFF Stack)

Figure 7-12: Screenshot of Second Operational Turbine Heating Test (After Post-Processing in MATLAB and Saving as a 8-bit TIFF Stack)

7.2.4. Conclusions

Overall, the first round of integration testing was very successful and enabled the team to identify a clear set of next steps for follow-on testing and integration activities. Unfortunately, SkySpecs' busy inspection schedule and the conclusion of the project prevented us from performing any additional tests under the scope of this Small Business Voucher program. By including a detailed list of recommended future work in Section 8.1, SkySpecs will have a strong foundation to continue this work in the future.

The main conclusions from these tests were the following:

- The FLIR Boson is a good choice for a drone-deployed thermography camera. The Boson is easy to integrate and includes the features that we need for data collection and data processing (e.g., manual FFC control, access to pre-AGC data).
    1. Switching to a newly available 640x512 resolution FLIR Boson would improve the quality of the data significantly.
    2. SkySpecs should consider flying closer to the wind blades and/or getting a different lens with a narrower FOV.

- We were successfully able to record IR video using the Linux command line. Therefore, in the future, SkySpecs should be able to fold this capability into their existing sensor rig code.
    1. The sensor rig code should include a manual FFC event immediately before inspecting the blade to reduce IR video noise.
    2. Additional work is needed to understand the bits between the IR video frames. Then, the software used to convert the .raw binary files to TIFF stacks should be improved.
- Despite weather affecting our ability to properly test solar radiation heating, it remains the most promising heating method and warrants additional testing.
    1. Focusing on lightning receptor is still recommended as a good place to start performing inspections. Initial testing demonstrated that the metallic material is easy to identify compared to the surrounding fiberglass material.
- Additional work needs to be performed to assess the effectiveness of operational turbine heating. Based on testing to date, the method should be considered a secondary priority when compared to solar radiation heating.
- In order to perform more advanced postprocessing, such as Thermal Wave Imaging's thermographic signal reconstruction (TSR), SkySpecs would need to record accurate 6 DOF position and orientation data. This 6 DOF data would enable them to track features on the blade and analyze the temperature versus time data for the pixels of interest.
    1. Without 6 DOF position and orientation data, SkySpecs could still use solar radiation heating and monitor the IR video for any obvious areas of contrast. While this method is expected to have lower sensitivity than the TSR method, its simplicity offers an appealing first approach.

THIS PAGE INTENTIONALLY LEFT BLANK

8. CONCLUSIONS

As the wind industry market share grows and the need for advanced maintenance capabilities increases, rapid and effective inspections of both surface and subsurface damage will be required. The combination of the effectiveness of advanced NDI and flexibility of drone-deployed inspection systems have an opportunity to fulfill this market need. By combining these technologies, drone-deployed NDI can help wind blades reach their design life and efficiently provide the necessary life management tasks that maximizes wind farm operations.

The current state-of-the-art for wind blade inspections is primarily ground based visual inspections. These inspections are performed using a high resolution camera on a tripod to inspect the blades on stopped turbines. Typically, the turbine needs to be repositioned (i.e., rotor rotated, blades pitched) multiple times to complete the full set of inspections. SkySpecs is disrupting this industry by performing much faster and more repeatable autonomous drone-deployed visual inspections. Moving forward, there is increased value to the customer in adding nondestructive inspection techniques to monitor blades for subsurface damage.

In order to assess the feasibility of incorporating nondestructive inspection techniques on a drone, a down selection study was performed. Based on the results of this down selection process, thermography was selected as the most promising method for NDI implementation on a drone platform. Considerations were compiled for implementing this capability, including hardware selection, flight strategies, thermal gradient sources, and data processing.

Based on the weight and power consumption constraints of drone-deployment, the team focused on miniature longwave IR cameras with uncooled Vandium Oxide (VOx) microbolometer sensors. While these cameras sacrifice some thermal sensitivity when compared to mid-wave IR cameras with cooled Indium Antimonide (InSb) sensors, the miniature IR cameras represented an impressive balance between thermal sensitivity, weight, and power consumption. The FLIR Boson was ultimately selected for integration and mounted to the drone's gimbal.

Thermography requires a temperature gradient to identify the presence of flaws. Typically, this heat gradient is generated by heating and then cooling the part (or vice versa). Three heating methods were selected for benchtop testing – internal forced air, solar radiation, and flash tubes. Turbine operational heating was also considered, but the team determined that it would be difficult to accurately test in a benchtop environment.

All three testing methods were successful in identifying engineered flaws in wind blade specimens. While flash tubes and internal forced air showed promise, solar radiation was selected as the most promising technique for drone integration testing. The method consistently detected flaws greater than .500 inches deep, and in one case, detected a flaw as deep as .950 inches. In addition to providing good depth of penetration and successful inspection of both solid laminates and sandwich structures, solar radiation is also the most feasible concept for immediate integration.

Initial hardware and software integration was performed to pair the FLIR Boson camera with SkySpecs' custom sensor rig. Once this integration was completed, the team prepared for flight testing. Based on the benchtop testing, solar radiation and operational turbine heating were selected for these drone integration tests. The main conclusions from these tests were the following:

- The FLIR Boson is a good choice for a drone-deployed thermography camera. The Boson is easy to integrate and includes the features that we need for data collection and data processing (e.g., manual FFC control, access to pre-AGC data).
    1. Switching to a newly available 640x512 resolution FLIR Boson would improve the quality of the data significantly.
    2. SkySpecs should consider flying closer to the wind blades and/or getting a different lens with a narrower FOV.
- We were successfully able to record IR video using the Linux command line. Therefore, in the future, SkySpecs should be able to fold this capability into their existing sensor rig code.
    1. The sensor rig code should include a manual FFC event immediately before inspecting the blade to reduce IR video noise.
    2. Additional work is needed to understand the bits between the IR video frames. Then, the software used to convert the .raw binary files to TIFF stacks should be improved.
- Despite weather affecting our ability to properly test solar radiation heating, it remains the most promising heating method and warrants additional testing.
    1. Focusing on lightning receptor is still recommended as a good place to start performing inspections. Initial testing demonstrated that the metallic material is easy to identify compared to the surrounding fiberglass material.
- Additional work needs to be performed to assess the effectiveness of operational turbine heating. Based on testing to date, the method should be considered a secondary priority when compared to solar radiation heating.
- In order to perform more advanced postprocessing, such as Thermal Wave Imaging's thermographic signal reconstruction (TSR), SkySpecs would need to record accurate 6 DOF position and orientation data. This 6 DOF data would enable them to track features on the blade and analyze the temperature versus time data for the pixels of interest.
    1. Without 6 DOF position and orientation data, SkySpecs could still use solar radiation heating and monitor the IR video for any obvious areas of contrast. While this method is expected to have lower sensitivity than the TSR method, its simplicity offers an appealing first approach.

Overall, the first round of integration testing was very successful and enabled the team to identify a clear set of next steps for follow-on testing and integration activities. Unfortunately, SkySpecs' busy inspection schedule and the conclusion of the project prevented us from performing any additional tests under the scope of this Small Business Voucher program. By including a detailed list of recommended future work in the subsequent section, SkySpecs will have a strong foundation to continue this work in the future.

8.1. Future Work

8.1.1. Damage Classification Future Work

Automated damage detection with detailed recommendations for wind farm operators are expected to add great value to SkySpecs' business model. In order to continue progressing towards this capability, the following future work is recommended:

- Continue training and testing the damage classification engine to mature its capabilities.
- Consider adding nondestructive inspection data, such as thermography, to the damage classification engine.
- Perform data fusion to combine data from multiple inspection techniques to correlate damage indications and provide evidence to wind farm operators of the extent of subsurface damage.

8.1.2. Thermography Future Work

Based on the work documented in this report, thermography is the most promising nondestructive inspection technique for drone-deployed wind blade inspections. In particular, solar radiation heating showed great promise with good depth of penetration capabilities. Additional work is still required to bring this capability to market including:

- Switching to a newly available 640x512 resolution FLIR Boson would improve the quality of the data significantly.
- Consider flying closer to the wind blades and/or getting a different lens with a narrower FOV.
- The sensor rig code should include a manual FFC event immediately before inspecting the blade to reduce IR video noise.
- SkySpecs should fold the IR video capture capability into their existing sensor rig code.
- Additional work is needed to understand the bits between the IR video frames. Then, the software used to convert the .raw binary files to TIFF stacks should be improved.
- Despite weather affecting our ability to properly test solar radiation heating, it remains the most promising heating method and warrants additional testing.

1. Focusing on lightning receptor is still recommended as a good place to start performing inspections. Initial testing demonstrated that the metallic material is easy to identify compared to the surrounding fiberglass material.

- Additional work needs to be performed to assess the effectiveness of operational turbine heating. Based on testing to date, the method should be considered a secondary priority when compared to solar radiation heating.
- In order to perform more advanced postprocessing, such as Thermal Wave Imaging's thermographic signal reconstruction (TSR), SkySpecs would need to record accurate 6 DOF position and orientation data. This 6 DOF data would enable them to track features on the blade and analyze the temperature versus time data for the pixels of interest.

    1. Without 6 DOF position and orientation data, SkySpecs could still use solar radiation heating and monitor the IR video for any obvious areas of contrast. While this method is expected to have lower sensitivity than the TSR method, its simplicity offers an appealing first approach.

- Develop a GUI for plotting Temperature vs. time curves using the TSR data described in Section 5.3.1 Step 11.
- Develop automated flaw detection tools. Figure 8-1 shows an example of a method for determining if damaged regions of a part deviate from the expected thermography results of a sound region [8.1].

    1. The concept is based on the fact that the TSR 2nd derivative peak is determined by a theoretically unobstructed back wall (e.g., internal surface of a spar cap). Any time or magnitude shift of this peak is expected to be caused by a flaw, such as a disbond, that disrupts the heat flow. By setting the bounds represented by the red box, any significant changes in time or magnitude of the peak can be flagged for further review.
    2. As previously discussed in Section 6.3.1, $t^* = \frac{L^2}{\pi\alpha}$ is the approximate time required for the heat to reach the unobstructed back wall of a part (i.e., the TSR 2nd derivative peak). Therefore, if the thermal diffusivity is known, time shifts in t^* are a good starting point for estimating the depth of a flaw that represents an unobstructed back wall.

        - Note that additional considerations may be required due to the longer heating duration of the solar radiation method as compared to the flash tubes method. Without additional work, any shifts in t^* should be considered qualitative.
        - This method also has potential for determining changes in thermal diffusivity. The most promising application is

water ingress in wind blade tips. While closed cell foams are not expected to absorb much water, balsa wood cores could absorb enough water to cause an observable change in thermal diffusivity.

- Perform additional flight tests to determine the merits of the flight strategies described in Section 5.3.1.2. Preferably, these tests would be performed by inspecting wind blades with known damage and assessing the ability of the thermography system to find defects with three different methods, as follows.
    1. Static drone IR video with full TSR analysis, including automated processing of 2nd derivative peaks
    2. Moving drone IR video with partial TSR analysis (i.e., using drone position and orientation data to piece together multiple Temperature vs. Time data points), including automated processing of 2nd derivative peaks
    3. Moving drone IR video without TSR analysis (i.e., scanning the surface for areas of high thermal contrast)

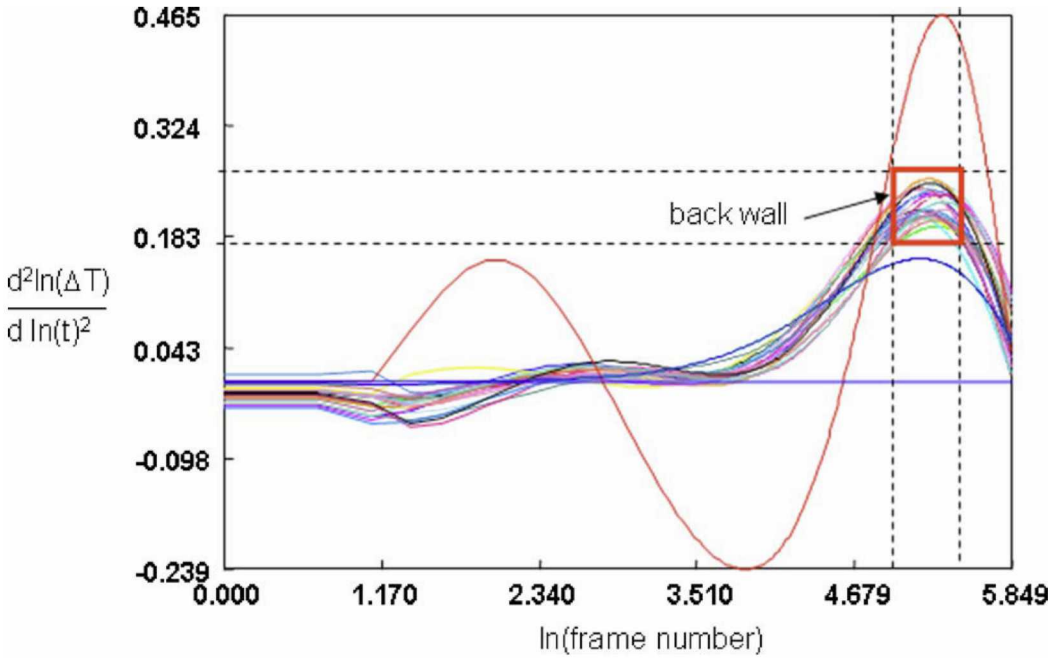

Figure 8-1: Plot of TSR 2nd Derivative Showing Bounds (in Red) on Time and Amplitude Shifts [8.1]

8.1.3. Other NDI Methods Future Work

As both drone and nondestructive inspection technologies mature, a number of additional NDI methods may warrant additional investigation. Most notably, phased array ultrasonic inspections have been demonstrated as the best inspection method for full-penetration of thick wind blade spar caps. If the coupling issues described in

Section 5.4.1 can be resolved (e.g., improve drone controls to enable contact with the blade, mature air-coupled ultrasonics), then ultrasonic inspection methods have the ability to be a strong complement to visual inspection and thermography.

Other NDI methods, such as acoustic beamforming and microwave inspections, also have significant potential if they can be matured and properly integrated onto a drone platform.

8.2. Lessons Learned

At the conclusion of a project, capturing the lessons learned is a good practice. For this project, the results were generally successful. The main drawback is that time limitations prevented the team from progressing the project further. Some reasons that the team noted for the time limitations are:

- The change from Windows to Linux for acquiring IR data required more effort than anticipated. The team could have started switched operating systems sooner to ensure that the software integration went smoothly.
- More joint testing and knowledge transfer would have enabled the team to perform more integration prior to the field testing at the wind farm in Iowa.
- Scheduling more field testing time would have given the team more flexibility to accommodate the cloudy weather and would have enabled us to collect additional data.
- Assessing the results of the drone integration tests were difficult because the blades did not include known damage or repairs. Performing preliminary integration tests on specimens with engineered damage prior to performing inspections on blades would have been a potential solution.
- Initially selecting the wrong IR camera caused some delays in the benchtop testing. Note, that this should not technically be considered a lesson learned because the FLIR Vue Pro R's features were incorrectly listed in its documentation; however, the error did cause a significant schedule impact to the project.

8.3. References

8.1 Shepard S.M., Hou Y.L., Lhota, J.R., Golden J.M., Automated processing of thermographic derivatives for quality assurance. Optical Engineering 2007;46:051008. doi:10.1117/1.2741274.

THIS PAGE INTENTIONALLY LEFT BLANK

APPENDIX A. TEST SPECIMENS

A.1 Laminate “Bricks” Drawings

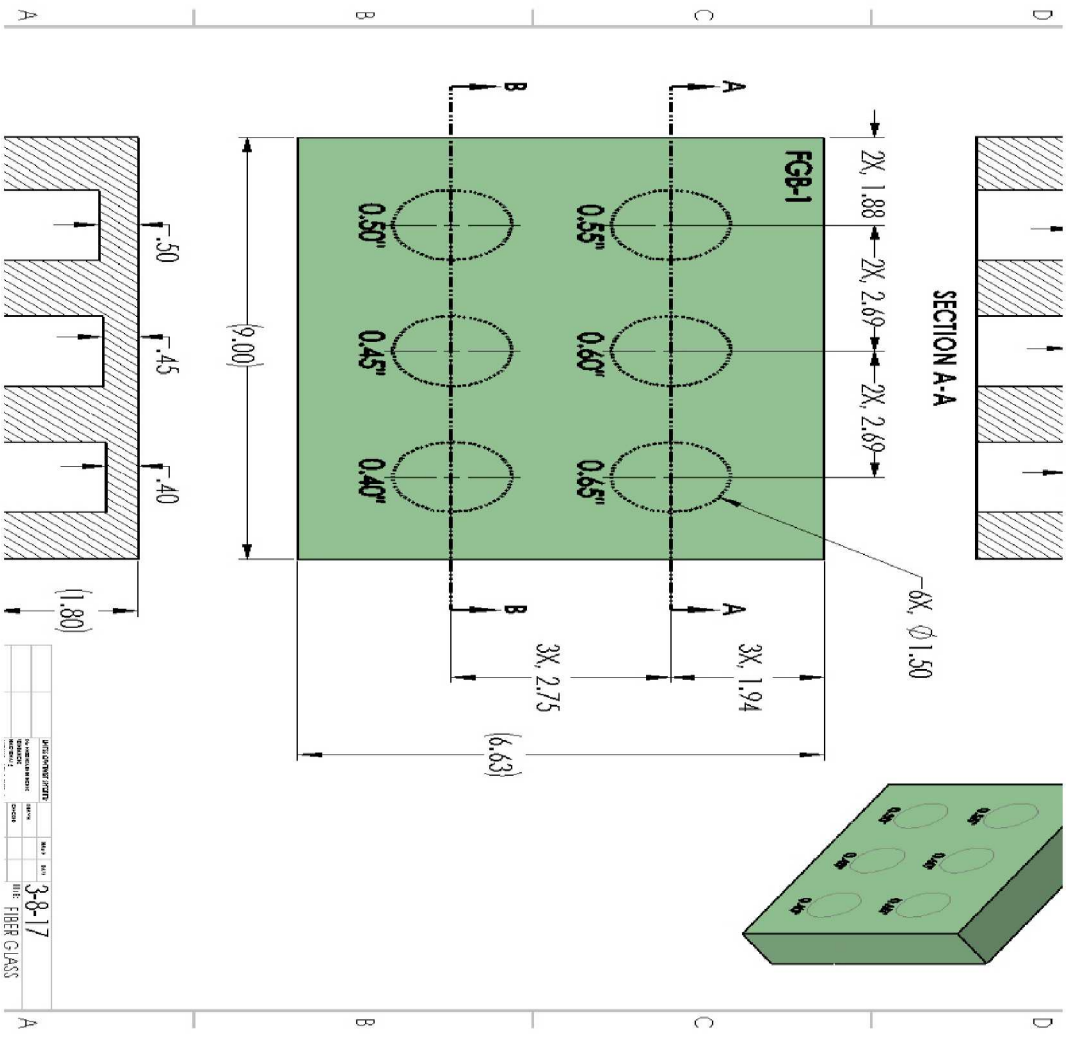

Figure A-2: Wind Blade Fiberglass Reference FGB-1

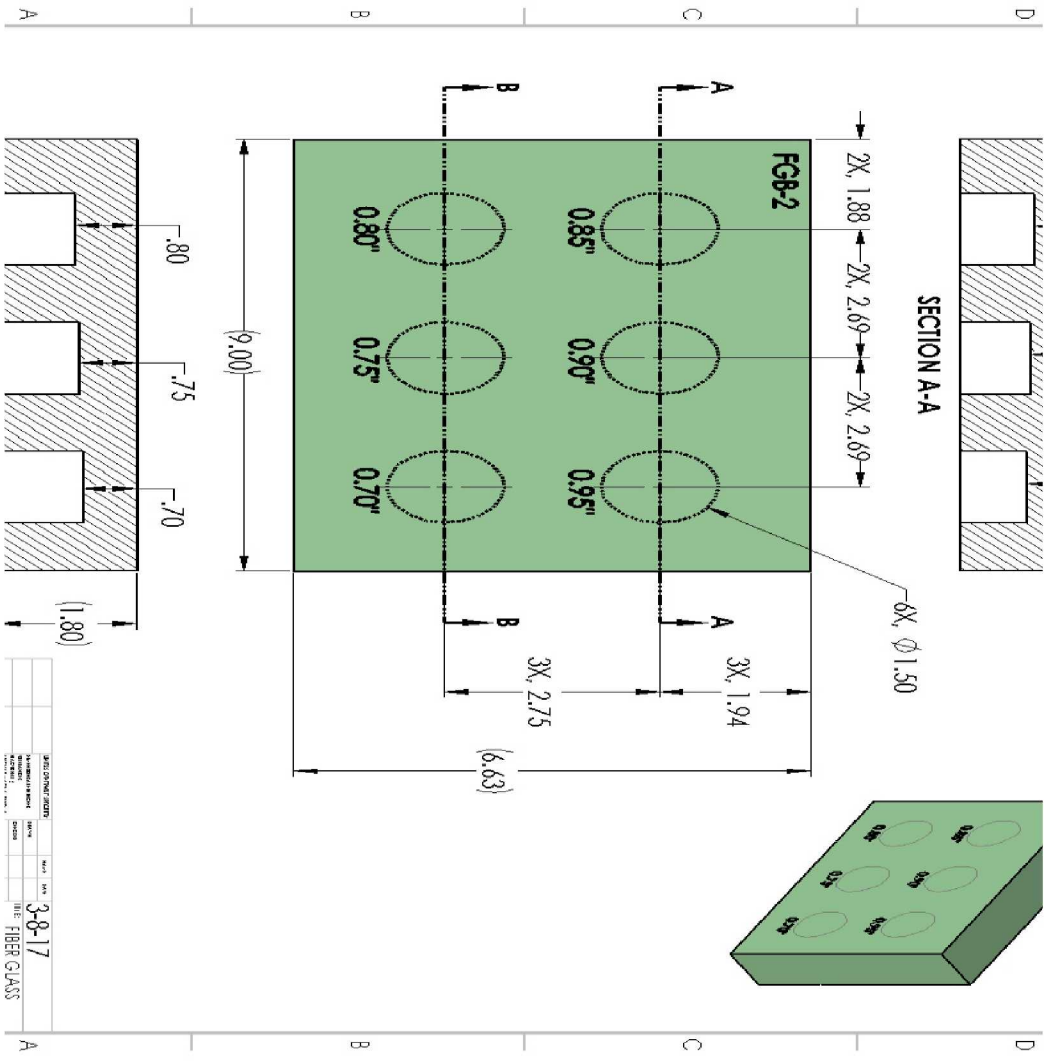

Figure A-3: Wind Blade Fiberglass Reference Block FGB-2

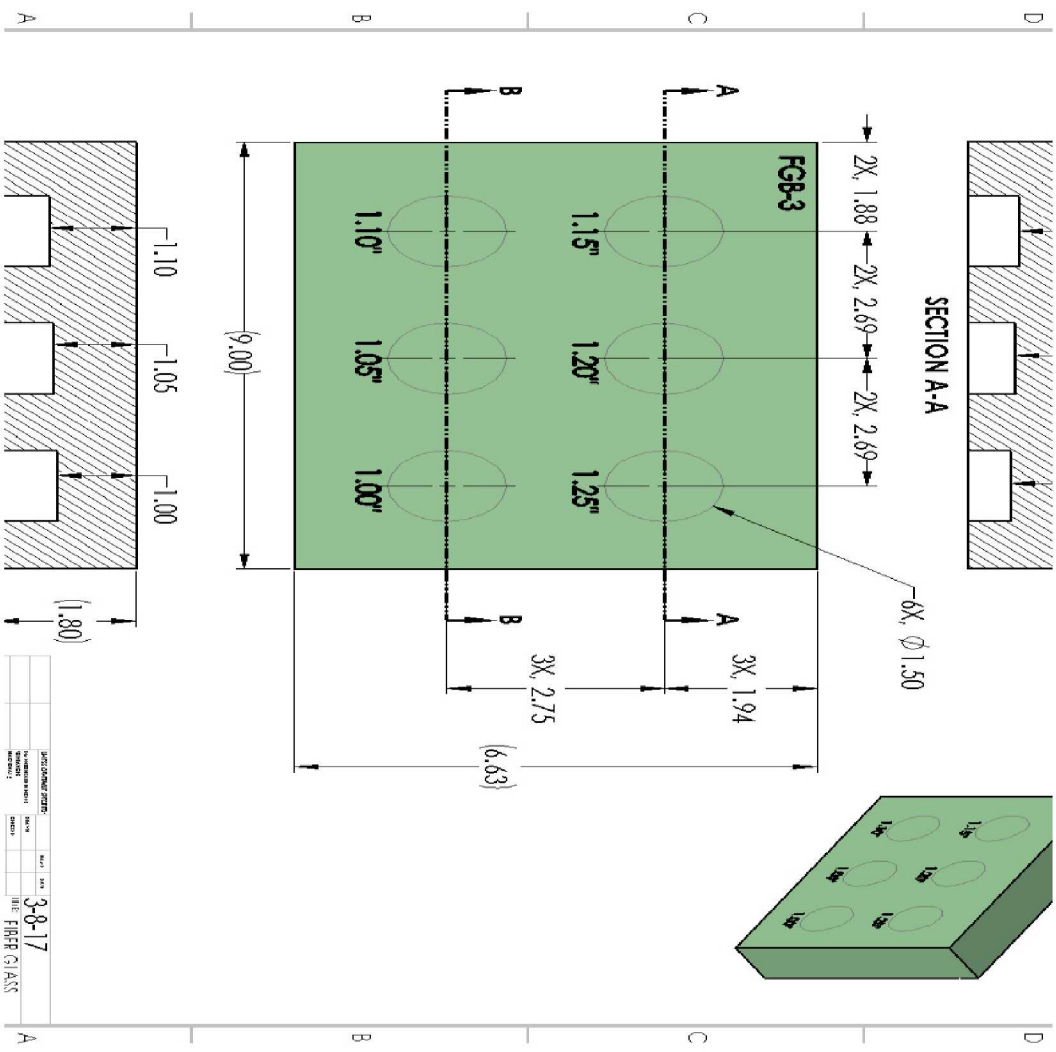

Figure A-4: Wind Blade Fiberglass Reference Block FGB-3

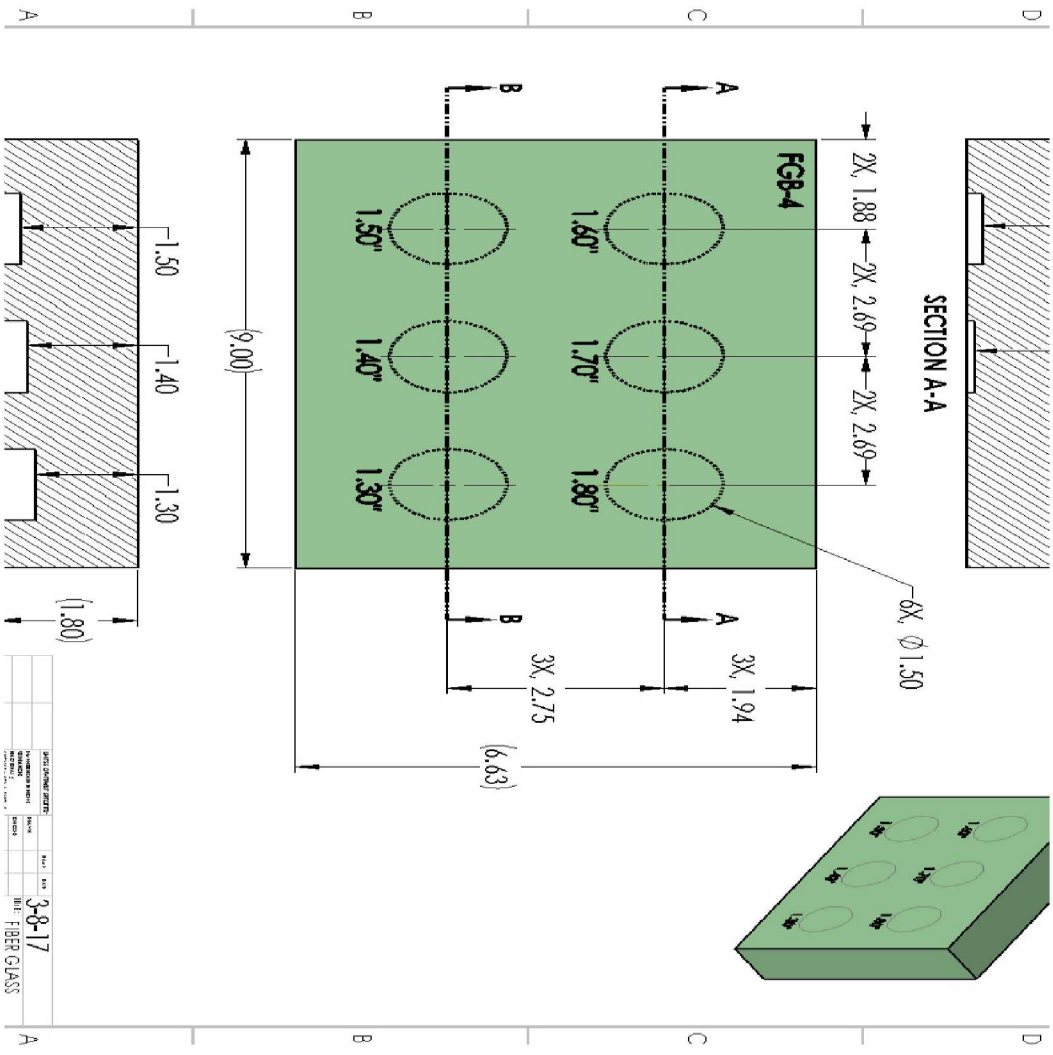

Figure A-5: Wind Blade Fiberglass Reference Block FBG-4

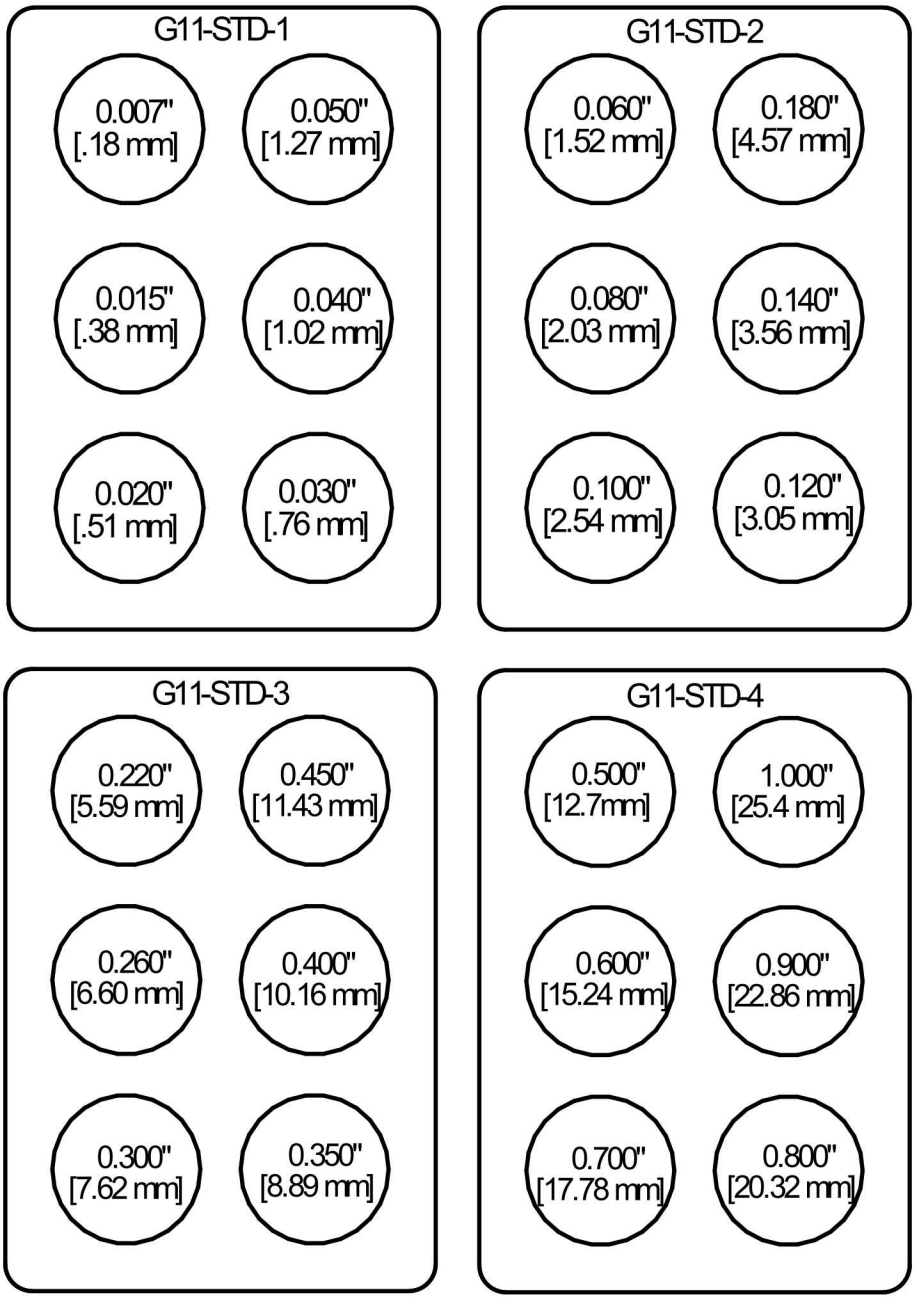

Figure A-6: G11 Solid Laminate Standard Set
(dimensions represent skin thickness of each flat bottom hole)

Figure A-7: Front and Back Photos of G11 Solid Laminate Set

A.2 Fiberglass and Foam Sandwich Specimen Drawings

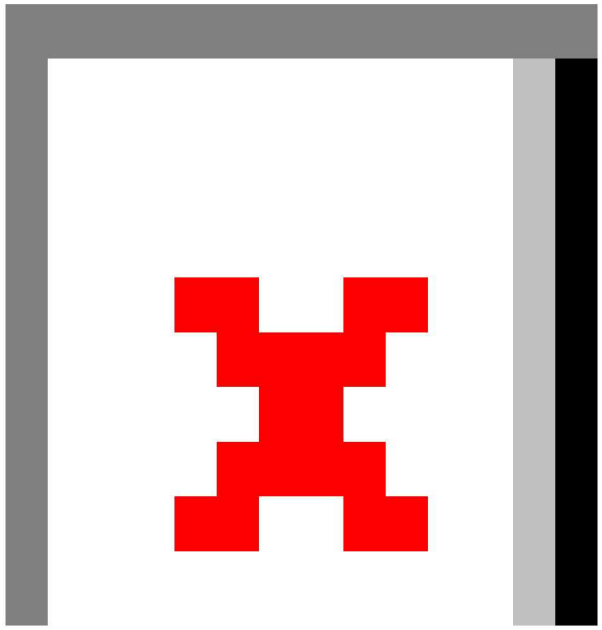

Figure A-8: Laminate Skin and Foam Core Specimen
NDI Feedback Specimen No. 1 (REF-STD-1-050-TPI-1)

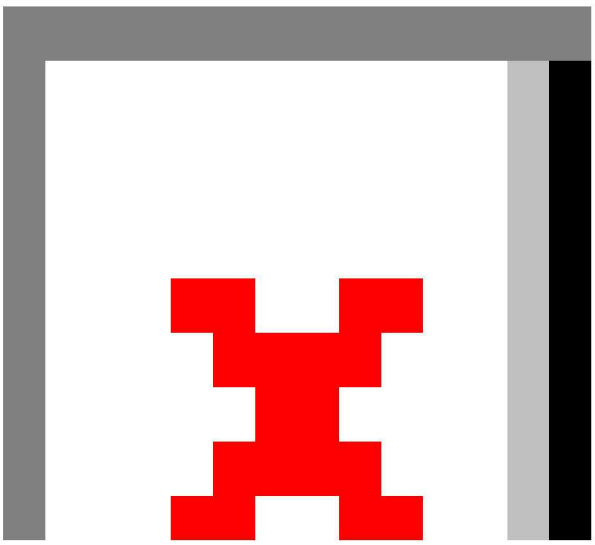

Figure A-9: Additional Information on How Flaws Were Engineered Into REF-STD-1-050-TPI-1

Figure A-10: Photos of WINDIE Specimen REF-STD-1-050-TPI-1

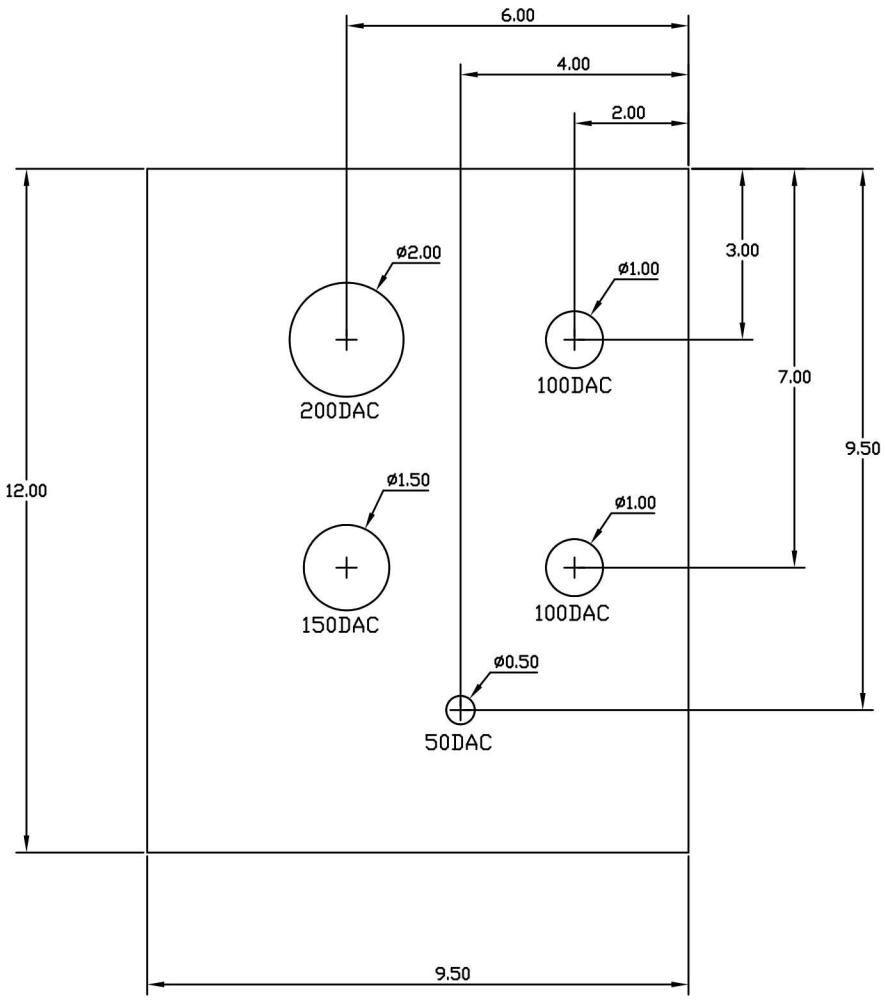

Figure A-11: Layout of Sandwich Standard GLF-S04-C4T2

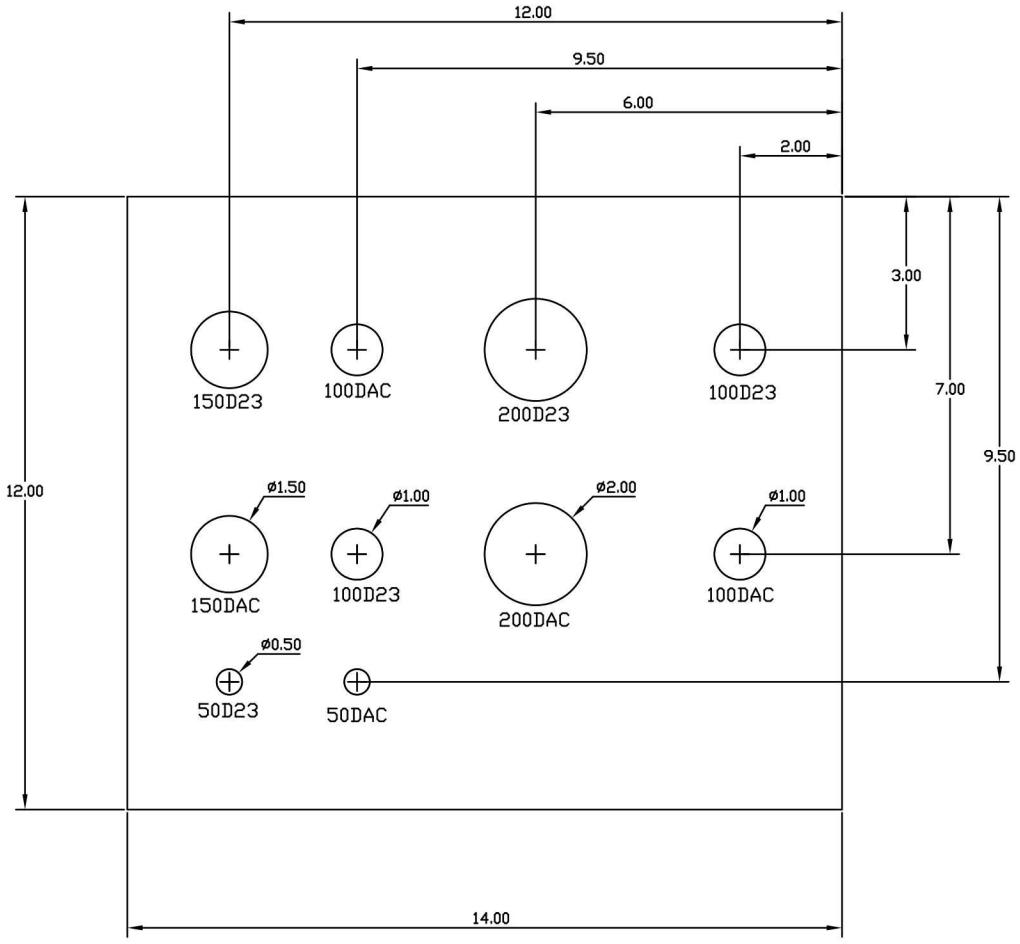

Figure A-12: Layout of Sandwich Standards GLF-S05-C4T2, GLF-S05-C5T2 & GLF-S05-C6T2.

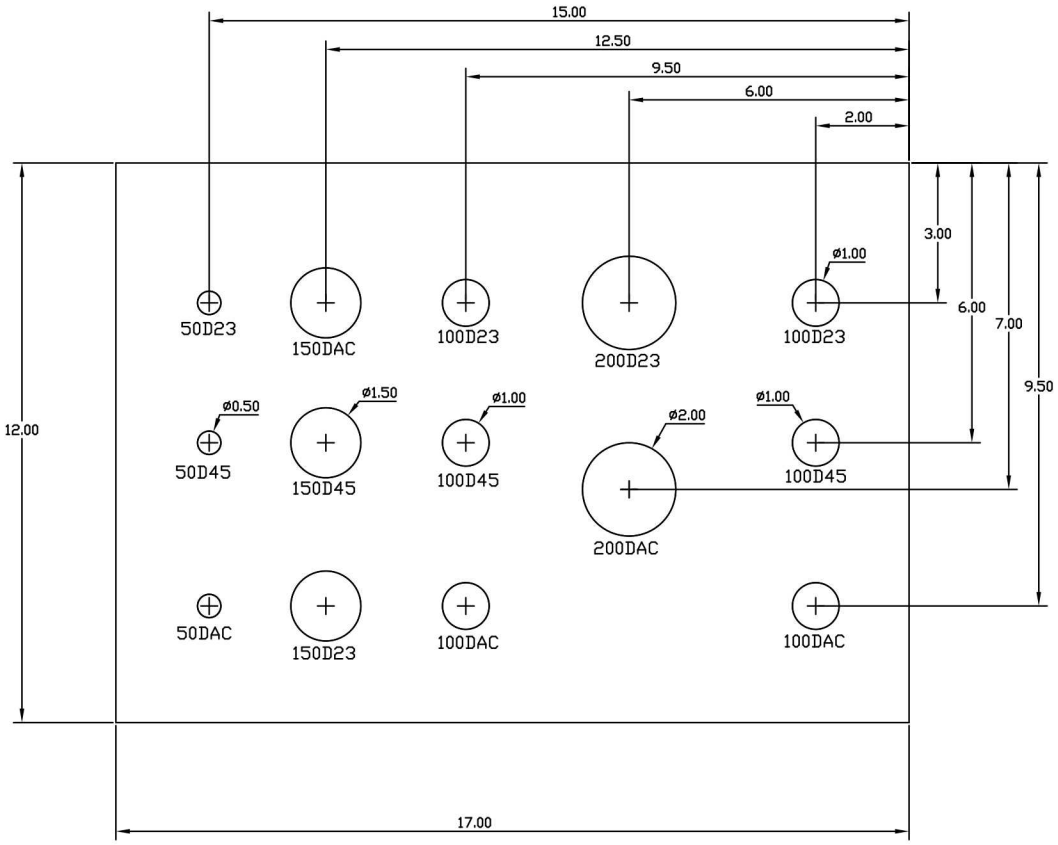

Figure A-13: Layout of Sandwich Standard GLF-S06-C4T2

A.3 Wind Blade Specimens Drawings

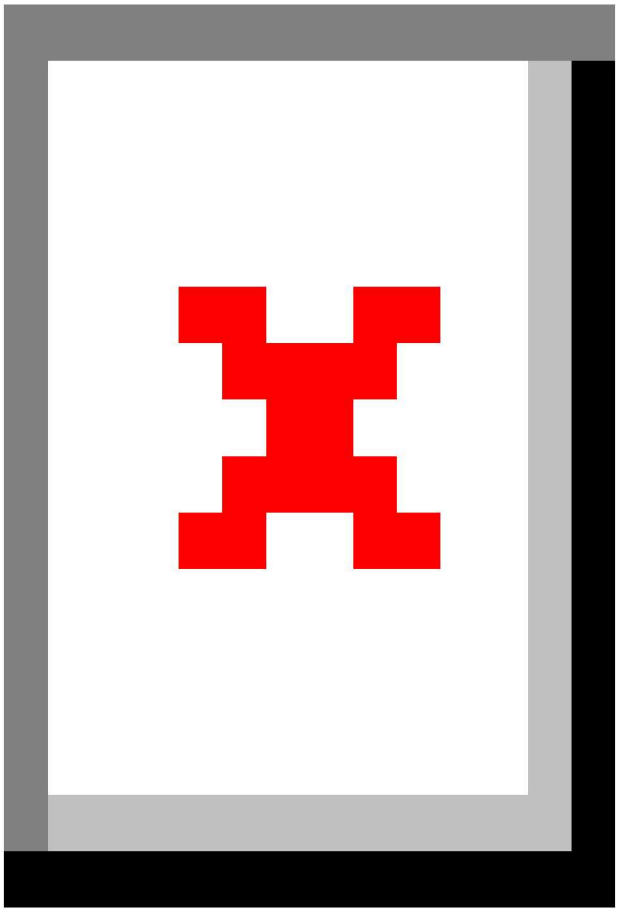

Figure A-14: WIND-1-029 Thin Spar Cap (0.29" th.) Specimen with Flat Bottom Holes

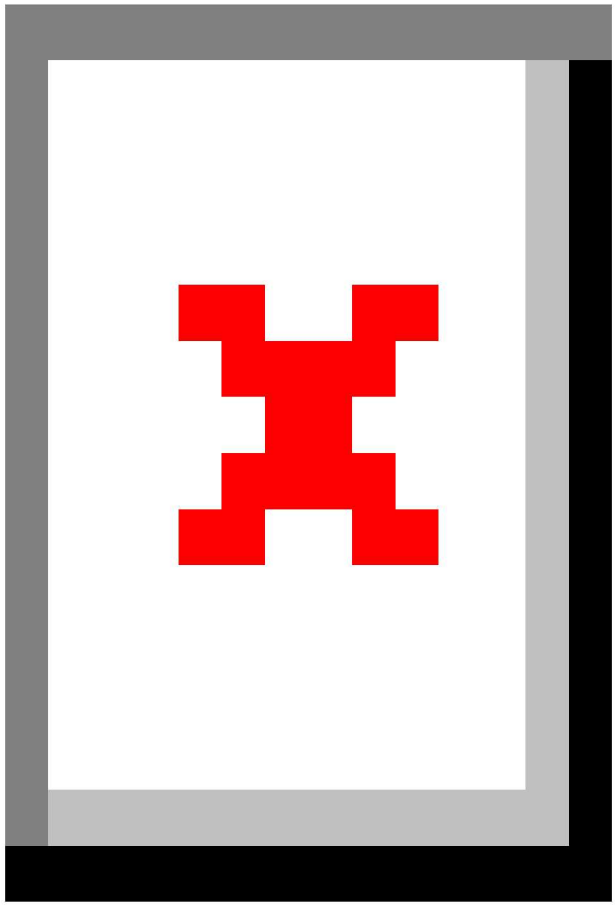

Figure A-15: WIND-2-044-SPAR-085 Spar Cap (0.44" th.) and Shear Web (0.85" th. at bond line) Specimen with Flat Bottom Holes

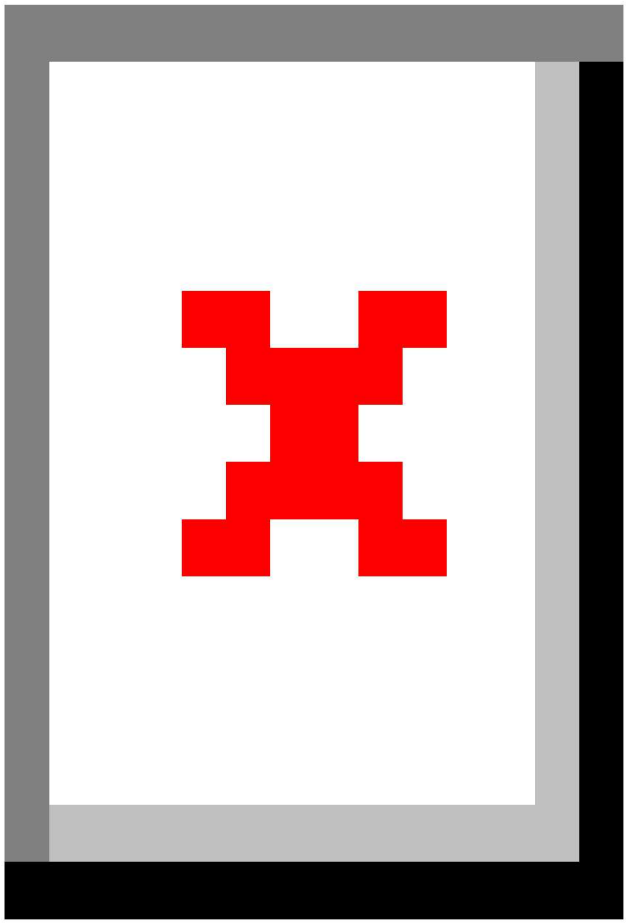

Figure A-16: WIND-3-110-SPAR-140 Spar Cap (1.1" th.) and Shear Web (1.4" th. at bond line) Specimen with Flat Bottom Holes

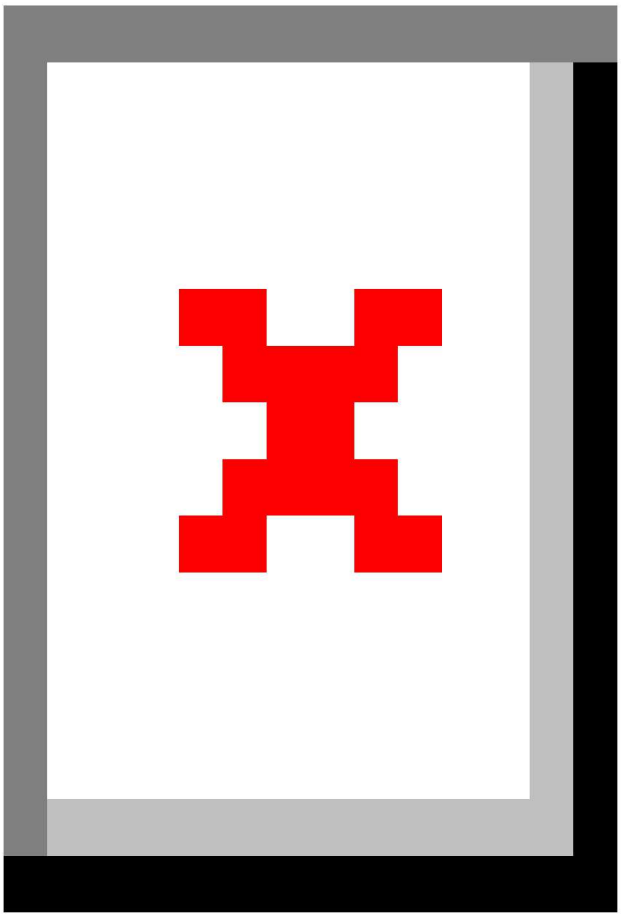

Figure A-17: WIND-4-161 Spar Car (1.61" th.) Specimen with Flat Bottom Holes

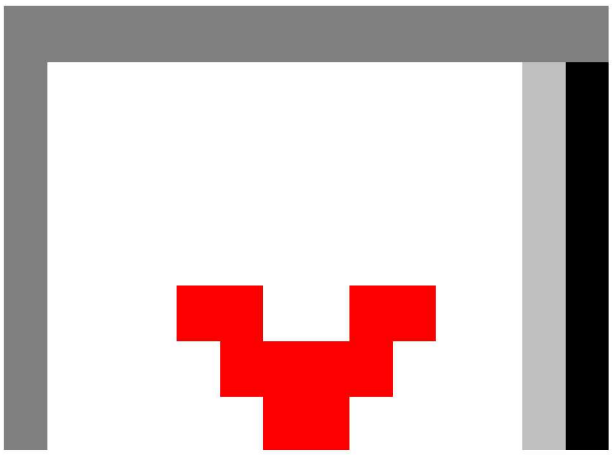

Figure A-18: WIND-5-180 Spar Cap (1.80" th.) Specimen with Flat Bottom Holes

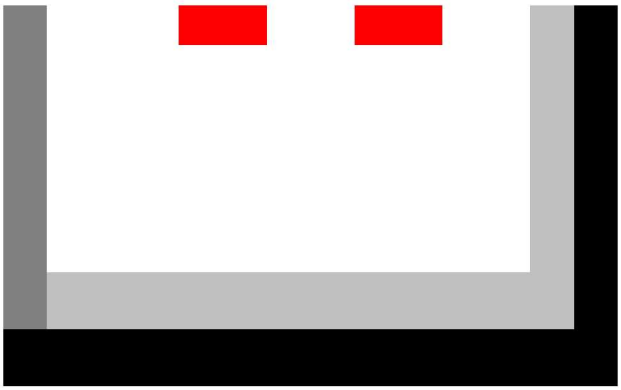

Figure A-19: WIND-6-180-SPAR-220 Spar Cap (1.8" th.) and Shear Web (2.2" th. at bond line) Specimen with Flat Bottom Holes

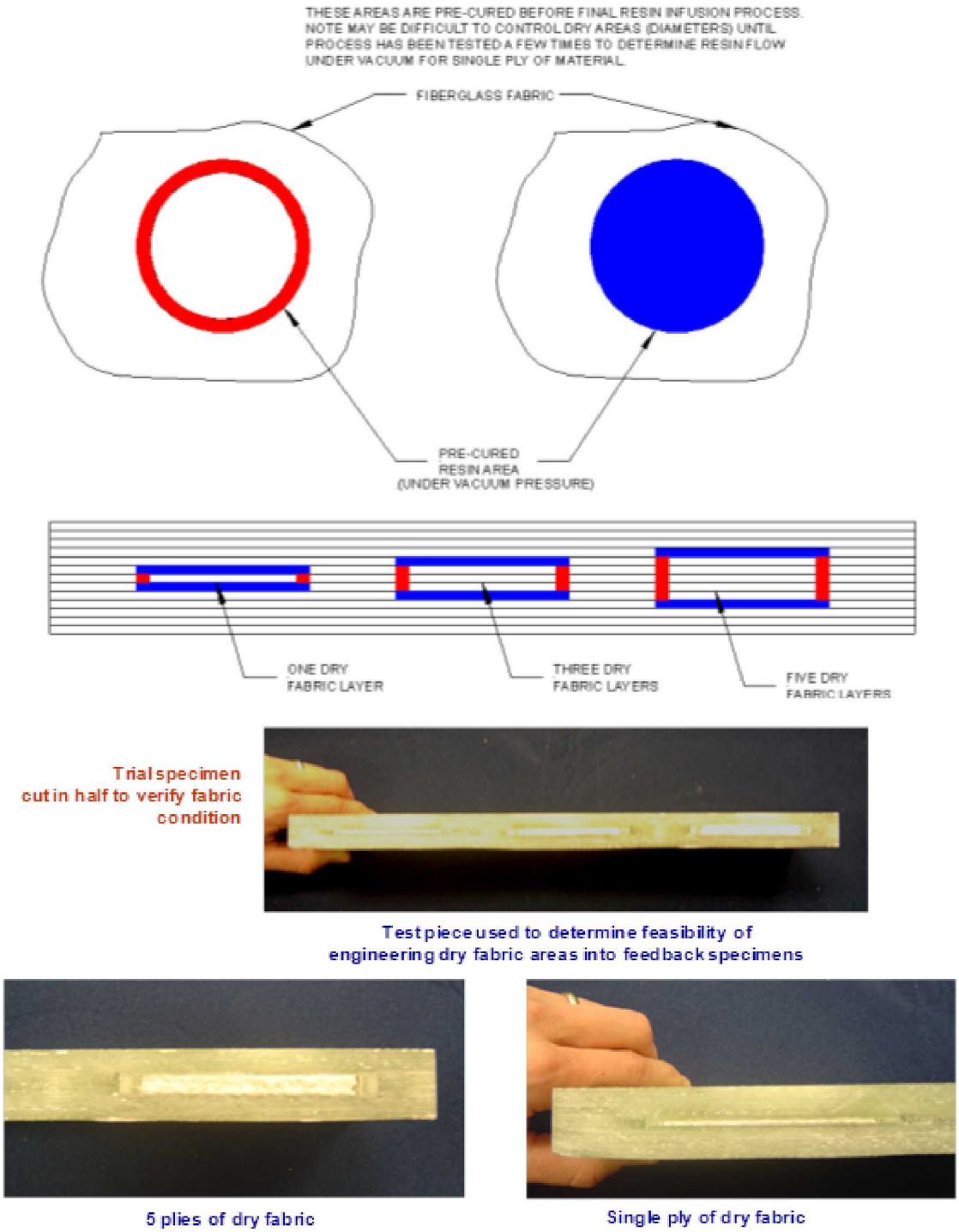

Figure A-20: Cross Section Views of DRY-SPOTS Showing Successful Engineering of Dry Fabric Flaws in Wind Blade NDI Specimens

APPENDIX B. THERMOGRAPHY PROCESSING CODE AND ALGORITHM

B.1 FLIR Boson RAW (.raw) File Processing Code

```
function [skipped_indices] = processRawVid16(filename)

%{
function to convert .raw 16 bit data from FLIR Boson to .tiff stacks
G. Ray Ely, Sandia National Labs, Org. 06621, grely@sandia.gov
v1.0, 10/31/17

%}


%% load 16 bit data
fid = fopen(filename);
raw_data_16bit_even = fread(fid,'*uint16');
fclose(fid);

%% load 16 bit data after skipping the first 8 bits
fid = fopen(filename);
fread(fid,1,'*uint8');
raw_data_16bit_odd = fread(fid,'*uint16');
fclose(fid);

%% find indices of arrays with value of "33028" which shows up 3 8 bit values before
each frame
ind_even = find(raw_data_16bit_even == 33028)*2;  % multiply by 2 to convert to 8
bit
ind_odd = find(raw_data_16bit_odd == 33028)*2+1;   % multiply by 2 and add 1 to
convert to 8 bit
ind = sort([ind_even; ind_odd]);  % combine and sort indices

%% clear arrays to save memory
clear raw_data_16bit_even raw_data_16bit_odd

%% load 8 bit data
fid = fopen(filename);
raw_data_8bit = fread(fid,'*uint8');
fclose(fid);

%% initialize vector to store false frames
skipped_indices = [];

for i = 1:length(ind)
   %% save 8 bit data for next frame
```

```
    tmp = raw_data_8bit(ind(i)+4:ind(i)+3+320*256*2);

    %% convert 8 bit data to 16 bit data and reshape into a 320x256 array
    img = reshape(typecast(tmp, 'uint16'),[320,256]);

    %% check if current data is an actual image (pixel values < 1000 is fairly arbitrary)
    if min(img(:))< 1000
        %% increment counter
        skipped_indices = [skipped_indices; ind(i)];

        %% skip writing current data to .tiff stack
        continue
    end

    %% write data to .tiff stack
    imwrite(img,['Processed\16bit\',filename(1:end-4),'.tiff'],'WriteMode','append')

    %% print completion status
    if mod(i,100) == 0
        fprintf('%.1f%% Complete\n',i*100/length(ind))
    end
end

end
```

B.2 Thermal Signal Reconstruction (TSR) Processing Code

```
function
TIFF_TSR_1D_2D_Processing_v3_7(filename,existing_logfile,heat_event_frame)

%% Program to process thermography TIFF sequence files
%% G. Ray Ely, Sandia National Labs, Org. 06621, grely@sandia.gov
%% v3.7, 7/19/17
%% input: TIFF image sequence of raw IR camera video, existing log file (for
repeating settings from a previous analysis, optional), heat frame (for manually
selecting the heating frame number, optional)
%% outputs: TIFF image sequences of Thermographic Signal Reconstruction (TSR),
1st derivative of TSR, and 2nd derivative of TSR, log file

%% uses least squares to fit a polynominal to the ln(temperature) vs. ln(time)
%% uses mldivide (\) to provide a least squares solution to A*x = B
%% x = A\B,  where x is the vector of least squares polynomial coefficients, A is the
matrix of ln(time) values raised to each polynominal value, where B is
ln(temperature),
%% requires copying tifflib.mexw64 from C:\Program
Files\MATLAB\R2016a\toolbox\matlab\imagesci\private to current folder


%% start timer
tic

%% determine number of images in input TIFF sequence
info = imfinfo(filename);
numFiles = numel(info);

%% number of frames to include in the output TIFF sequence
output_frames = 200;

%% approximate number of frames to use to fit polynomial functions
approx_input_frames = 140;


mImage=info(1).Width;
nImage=info(1).Height;
FileID = tifflib('open',filename,'r');
rps = tifflib('getField',FileID,Tiff.TagID.RowsPerStrip);
Temp_Matrix_temp = zeros(nImage,mImage,'double');

%% determine settings based on whether a previous log file or heat frame is specified
switch nargin
   case 2
```

```
        [~,~,~,TSR_skip_frames] = textread(existing_logfile,'%s %s %s %u',1,
'headerlines',4);
        [~,~,~,~,~,heat_event_frame] = textread(existing_logfile,'%s %s %s %s %s
%u\r\n',1, 'headerlines',5);
        [~,framerate] = textread(existing_logfile,'%s %u',1, 'headerlines',6);
        [~,~,poly_degree] = textread(existing_logfile,'%s %s %u',1, 'headerlines',7);
        [~,~,angle] = textread(existing_logfile,'%s %s %u',1, 'headerlines',8);
        [xmin,ymin,pixel_width,pixel_height] = textread(existing_logfile,'%u %u %u
%u',1, 'headerlines',12);
    case 3
        [~,~,~,TSR_skip_frames] = textread(existing_logfile,'%s %s %s %u',1,
'headerlines',4);
        [~,framerate] = textread(existing_logfile,'%s %u',1, 'headerlines',6);
        [~,~,poly_degree] = textread(existing_logfile,'%s %s %u',1, 'headerlines',7);
        [~,~,angle] = textread(existing_logfile,'%s %s %u',1, 'headerlines',8);
        [xmin,ymin,pixel_width,pixel_height] = textread(existing_logfile,'%u %u %u
%u',1, 'headerlines',12);
    otherwise
        %% skip frames for TSR functionality, currently set to 0, consider doing more
research on this number
        TSR_skip_frames = 0;

        %% polynominal degree (degree 6 selected based on literature and limited trial
and error)
        poly_degree = 6;

        %% IR camera framerate (frames/second)
        framerate = 60;

        %% select region of interest by drawing a rectangle with the mouse, image
displayed for rectangle selection is the middle frame of the video
        ROI_image = mat2gray(imread(filename, round(numFiles/2), 'Info', info));
        imshow(ROI_image)
        prompt = 'Rotate Image? (positive values = counter clockwise, 0 = no rotation): ';
        angle = input(prompt);
        angle2 = angle;
        while angle2 ~= 0
            close all
            imshow(imrotate(ROI_image,angle))
            angle2 = input(prompt);
            angle = angle + angle2;
        end
        display('Use cursor to select Region of Interest')
        ROI = getrect;
        xmin = round(ROI(1));
        ymin = round(ROI(2));
```

```
    pixel_width = round(ROI(3));
    pixel_height = round(ROI(4));
    close all  %% closes figure



    %% find frame with the maximum temperature (consider changing to look only
in the ROI)
    %% initialize maximum pixel value
    max_pixel = 0;

    %% loop to find frame with the maximum temperature value (consider swapping
out if statement for find function)
    for i = 1:numFiles
       tifflib('setDirectory',FileID,i-1);
       rps = min(rps,nImage);

       for r = 1:rps:nImage
          stripNum = tifflib('computeStrip',FileID,r);
          current_strip = tifflib('readEncodedStrip',FileID,stripNum-1);   %% save
current image/frame
          max_pixel_current = max(current_strip(:));
          if max_pixel_current > max_pixel
             heat_event_frame = i;
          end

       end
    end
end

%% total number of frames to skip
skip_frames = heat_event_frame + TSR_skip_frames;

%% total remaining frames to analyze after subtracting out the skipped frames
frames_remaining = numFiles-skip_frames;

%% create an error if any negative pixel values exist (prevents natural log of pixel
values creating complex values)
if(frames_remaining == 0)
   error('Heat Frame Selection Error (Last Frame is hottest)')
end

%% Create a 1D array of time data based on framerate
t = (1:frames_remaining)/framerate;

%% Take natural log (ln) of time
```

```
ln_t = log(t);

%% spacing between ln(time) inputs
delta_t = (ln_t(end)-ln_t(1))/approx_input_frames;

%% loop to select frames for fitting polynomial functions
%% initialize variables
index_vector = [];
running_diff = 0;

%% loop to find the indices for the selected frames
diff_ln_t = diff(ln_t);
for i = 1:frames_remaining-1
   if diff_ln_t(i) > delta_t
      index_vector = [index_vector; i];
   else
      running_diff = running_diff + diff_ln_t(i);
      if running_diff > delta_t
         index_vector = [index_vector; i];
         running_diff = 0;
      end
   end
end

%% actual number of input frames for fitting the polynomial functions
input_frames = length(index_vector);

%% remove ln(time) values that are not part of the input frames
ln_t = ln_t(index_vector);

%% initialize temperature matrix (to speed up script)
%% use double (rather than single) for temperature matrix to prevent a matrix rank
error
Temp_Matrix = zeros(pixel_height, pixel_width, input_frames,'double');  %% matrix
of all temperature pixel values for each input frame, after cropping, starting after the
skipped frames


%% save grayscale values for each pixel for each image of TIFF sequence
if angle ~= 0
   for i = 1:input_frames
      tifflib('setDirectory',FileID,skip_frames+index_vector(i)-1);
      rps = min(rps,nImage);

      for r = 1:rps:nImage
         row_inds = r:min(nImage,r+rps-1);
```

```
            stripNum = tifflib('computeStrip',FileID,r);
            Temp_Matrix_temp(row_inds,:) =
double(tifflib('readEncodedStrip',FileID,stripNum-1));   %% save current image/frame
        end
        Temp_Matrix_temp2 = imrotate(Temp_Matrix_temp,angle);  %% rotate image
        Temp_Matrix(:,:,i) = Temp_Matrix_temp2(ymin:ymin+pixel_height-
1,xmin:xmin+pixel_width-1);  %% crop current image/frame and add it to the
temperature matrix
    end
else
    for i = 1:input_frames
        %% save grayscale values and append data for image number "i" to a matrix for
all images/frames
        %% use variable type "double" (convert from type uint16)
        tifflib('setDirectory',FileID,index_vector(i)-1);
        rps = min(rps,nImage);

        for r = 1:rps:nImage
            row_inds = r:min(nImage,r+rps-1);
            stripNum = tifflib('computeStrip',FileID,r);
            Temp_Matrix_temp(row_inds,:) =
double(tifflib('readEncodedStrip',FileID,stripNum-1));   %% save current image/frame
        end
        Temp_Matrix(:,:,i) = Temp_Matrix_temp(ymin:ymin+pixel_height-
1,xmin:xmin+pixel_width-1);  %% crop current image/frame and add it to the
temperature matrix
    end
end


%% find 97% * min grayscale value for the last frame and subtract from each pixel for
each frame
%% trial and error showed this worked well as a scaling value (subtracting less than
the minimum prevents negative values and natural log errors, smaller values provide
larger differences in natural log values)
min_Temp_t_end = min(min(Temp_Matrix(:,:,end)))*.97;
Temp_Matrix = Temp_Matrix - min_Temp_t_end;

%% create an error if any negative pixel values exist (prevents natural log of pixel
values creating complex values)
if(min(Temp_Matrix(:))<=0)
    error('Negative Temperature Pixel Values Error')
end

%% Take natural log (ln) of temperature matrix
ln_Temp_Matrix = log(Temp_Matrix);
```

```
%% clear original time vector and temperature matrix (without ln) to save memory
clear t Temp_Matrix

%% create single type version of ln(t) for evaluating the output frames
sing_ln_t = single(linspace(min(ln_t),max(ln_t),output_frames));

%% initialize variables (to speed up script)
%% use singles to save space
ln_y = zeros(pixel_height, pixel_width, output_frames,'single');        %% matrix of the
natural log of all temperature pixel values for each output frame
ln_y_1D = zeros(pixel_height, pixel_width, output_frames,'single');     %% matrix of
the 1st derivative of a polynominal fit of the natural log of all temperature pixel values
for each output frame

%% create vectors for operations prior to starting for loop
r = (poly_degree:-1:1)';
s = (poly_degree-1:-1:1)';
v = poly_degree:-1:0;
y = zeros(size(sing_ln_t),'single');

%% create matrix for polynomial fit
M = repmat(ln_t',1,poly_degree+1);
A = bsxfun(@power,M,v);

%% fit poly_degree order polynomial to ln_Temp_Matrix and calculate ln(T) values
from polynomial
%% calculate 1st and 2nd derivatives
for j = 1:pixel_height
   for k = 1:pixel_width
      %% fit a poly_degree order polynomial to ln(T) vs. ln(t)
      %% x = A\B, where x is a vector of the polynomial contants and B is vector of
ln(T) values
      x = single(A\(ln_Temp_Matrix(pixel_height*(k-
1)+j:pixel_height*pixel_width:end))');

      %% take 1st and 2nd derivatives using the power rule
      x_1D = x(1:poly_degree).*r;
      x_2D = x_1D(1:poly_degree-1).*s;

      %% calculate ln(T) with new polynomial (using stripped down polyval function)
      y(:) = x(1);
      for a = 2:poly_degree+1
         y = sing_ln_t .* y + x(a);
      end
```

```
        ln_y(j,k,:) = y;

        %% calculate 1st derivative with new polynomial (using stripped down polyval
function)
        y(:) = x_1D(1);
        for b = 2:poly_degree
            y = sing_ln_t .* y + x_1D(b);
        end
        ln_y_1D(j,k,:) = y;

        %% calculate 2nd derivative with new polynomial (using stripped down polyval
function)
        y(:) = x_2D(1);
        for c = 2:poly_degree-1
            y = sing_ln_t .* y + x_2D(c);
        end
        ln_y_2D(j,k,:) = y;
    end

    %% displays progress based on what iteration of the loop it's on
    display(['Analyzing Data: ',num2str(j*100/pixel_height,'%.0f'),'% Complete'])
end


%% clear matrices to save memory
clear M A ln_Temp_Matrix

%% save grayscale values for each pixel for every 15 seconds * 60 frames/sec of TIFF
sequence
frame_spacing = 15*60;
counter = 1;
if angle ~= 0
    for i = skip_frames+1:frame_spacing:numFiles
        tifflib('setDirectory',FileID,i);
        rps = min(rps,nImage);

        for r = 1:rps:nImage
            row_inds = r:min(nImage,r+rps-1);
            stripNum = tifflib('computeStrip',FileID,r);
            Temp_Raw_Matrix_temp(row_inds,:) =
double(tifflib('readEncodedStrip',FileID,stripNum-1));   %% save current image/frame
        end
        Temp_Raw_Matrix_temp2 = imrotate(Temp_Raw_Matrix_temp,angle);  %%
rotate image
```

```
        Temp_Raw_Matrix(:,:,counter) =
Temp_Raw_Matrix_temp2(ymin:ymin+pixel_height-1,xmin:xmin+pixel_width-1);
%% crop current image/frame and add it to the temperature matrix
        counter = counter + 1;
    end
else
    for i = skip_frames+1:frame_spacing:numFiles
        %% save grayscale values and append data for image number "i" to a matrix for
all images/frames
        %% use variable type "double" (convert from type uint16)
        tifflib('setDirectory',FileID,i);
        rps = min(rps,nImage);

        for r = 1:rps:nImage
            row_inds = r:min(nImage,r+rps-1);
            stripNum = tifflib('computeStrip',FileID,r);
            Temp_Raw_Matrix_temp(row_inds,:) =
double(tifflib('readEncodedStrip',FileID,stripNum-1));   %% save current image/frame
        end
        Temp_Raw_Matrix(:,:,counter) =
Temp_Raw_Matrix_temp(ymin:ymin+pixel_height-1,xmin:xmin+pixel_width-1);
%% crop current image/frame and add it to the temperature matrix
        counter = counter + 1;
    end
end

for m = 1:output_frames
    %% convert matrices to 8 bit grayscale images, scales min value to 0 and max value
to 255 (does not preserve temperature data)
    C = mat2gray(reshape(ln_y(:,:,m),[pixel_height, pixel_width]));
    D = mat2gray(reshape(ln_y_1D(:,:,m),[pixel_height, pixel_width]));
    E = mat2gray(reshape(ln_y_2D(:,:,m),[pixel_height, pixel_width]));

    %% save images as 8 bit grayscale TIFF sequences
    if m == 1
        imwrite(C,['Processed\',filename(1:end-5),' TSR.tiff'])
        imwrite(D,['Processed\',filename(1:end-5),' 1D.tiff'])
        imwrite(E,['Processed\',filename(1:end-5),' 2D.tiff'])
    else
        imwrite(C,['Processed\',filename(1:end-5),' TSR.tiff'],'WriteMode','append')
        imwrite(D,['Processed\',filename(1:end-5),' 1D.tiff'],'WriteMode','append')
        imwrite(E,['Processed\',filename(1:end-5),' 2D.tiff'],'WriteMode','append')
    end

    %% displays progress based on what iteration of the loop it's on
    display(['Saving Output: ',num2str(m*100/output_frames,'%.0f'),'% Complete'])
```

```
end

for n = 1:size(Temp_Raw_Matrix,3)
   %% convert matrices to 8 bit grayscale images, scales min value to 0 and max value
to 255 (does not preserve temperature data)
   F = mat2gray(Temp_Raw_Matrix(:,:,n));

   %% save images as 8 bit grayscale TIFF sequences
   if n == 1
      imwrite(F,['Processed\',filename(1:end-5),' Raw.tiff'])
   else
      imwrite(F,['Processed\',filename(1:end-5),' Raw.tiff'],'WriteMode','append')
   end
end


%% stop timer and display
total_time = toc;
display(['Time Elapsed: ',num2str(total_time,'%.1f'),' sec'])

%% save log file
fileID = fopen(['Processed\',filename(1:end-5),' log.txt'],'w');
fprintf(fileID,'%s %s\r\n\r\n','Filename:',filename);
fprintf(fileID,'%s %s\r\n\r\n','Date/Time Processed:',datetime);
fprintf(fileID,'%s %u\r\n','TSR Skipped Frames:',TSR_skip_frames);
fprintf(fileID,'%s %u\r\n','Calculated Flash Bulb Frame
Number:',min(heat_event_frame));
fprintf(fileID,'%s %u\r\n','Framerate:',framerate);
fprintf(fileID,'%s %u\r\n','Polynomial Degree:',poly_degree);
fprintf(fileID,'%s %.0f\r\n\r\n','Rotation (Degrees):',angle);
fprintf(fileID,'%s\r\n','Selected Region of Interest (pixels):');
fprintf(fileID,'%4s %6s %7s %8s\r\n','xmin','ymin','width','height');
fprintf(fileID,'%4u %6u %7u %8u\r\n\r\n',xmin,ymin,pixel_width,pixel_height);
fprintf(fileID,'%s %.1f %s','Elapsed Time:',total_time,'sec');
fclose(fileID);
```

B.3 Internal Forced Air Heating Image Processing Code

```
function TIFF_Heat_Gun_Processing_v1(filename,existing_logfile)

%% Program to process thermography TIFF sequence files
%% G. Ray Ely, Sandia National Labs, Org. 06621, grely@sandia.gov
%% v1.0, 11/10/17
%% input: TIFF image sequence of raw IR camera video, existing log file (for
repeating settings from a previous analysis, optional)
%% outputs: 8 bit cropped and scaled TIFF image sequences, log file

%% requires copying tifflib.mexw64 from C:\Program
Files\MATLAB\R2016a\toolbox\matlab\imagesci\private to current folder


%% start timer
tic

%% determine number of images in input TIFF sequence
info = imfinfo(filename);
numFiles = numel(info);

%% number of frames to include in the output TIFF sequence
output_frames = 200;

%% determine image size
mImage=info(1).Width;
nImage=info(1).Height;

%% open TIFF stack
FileID = tifflib('open',filename,'r');
rps = tifflib('getField',FileID,Tiff.TagID.RowsPerStrip);

%% initialize variable for temporarily saving each frame
Temp_Matrix_temp = zeros(nImage,mImage,'double');

%% determine settings based on whether a previous log file or heat frame is specified
switch nargin
   case 2
      [~,framerate] = textread(existing_logfile,'%s %u',1, 'headerlines',4);
      [~,~,angle] = textread(existing_logfile,'%s %s %u',1, 'headerlines',5);
      [xmin,ymin,pixel_width,pixel_height] = textread(existing_logfile,'%u %u %u
%u',1, 'headerlines',9);
   otherwise
      %% IR camera framerate (frames/second)
      framerate = 60;
```

```
    %% select region of interest by drawing a rectangle with the mouse, image
displayed for rectangle selection is the middle frame of the video
    ROI_image = mat2gray(imread(filename, round(numFiles/2), 'Info', info));
    imshow(ROI_image)
    prompt = 'Rotate Image? (positive values = counter clockwise, 0 = no rotation): ';
    angle = input(prompt);
    angle2 = angle;
    while angle2 ~= 0
       close all
       imshow(imrotate(ROI_image,angle))
       angle2 = input(prompt);
       angle = angle + angle2;
    end
    display('Use cursor to select Region of Interest')
    ROI = getrect;
    xmin = round(ROI(1));
    ymin = round(ROI(2));
    pixel_width = round(ROI(3));
    pixel_height = round(ROI(4));
    close all  %% closes figure
end



%% initialize temperature matrix (to speed up script)
Temp_Matrix = zeros(pixel_height, pixel_width, output_frames,'double');  %% matrix
of all temperature pixel values for each input frame, after cropping, starting after the
skipped frames

output_frame_numbers = round((1:output_frames)*(numFiles/output_frames))-1;

%% save grayscale values for each pixel for each image of TIFF sequence
if angle ~= 0
   for i = 1:output_frames
    %% save grayscale values and append data for image number "i" to a matrix for
all images/frames
    %% use variable type "double" (convert from type uint16)
    tifflib('setDirectory',FileID,output_frame_numbers(i));
    rps = min(rps,nImage);

    for r = 1:rps:nImage
       row_inds = r:min(nImage,r+rps-1);
       stripNum = tifflib('computeStrip',FileID,r);
       Temp_Matrix_temp(row_inds,:) =
double(tifflib('readEncodedStrip',FileID,stripNum-1));   %% save current image/frame
    end
```

```
        Temp_Matrix_temp2 = imrotate(Temp_Matrix_temp,angle);  %% rotate image
        Temp_Matrix(:,:,i) = Temp_Matrix_temp2(ymin:ymin+pixel_height-
1,xmin:xmin+pixel_width-1);  %% crop current image/frame and add it to the
temperature matrix
    end
else
    for i = 1:output_frames
        %% save grayscale values and append data for image number "i" to a matrix for
all images/frames
        %% use variable type "double" (convert from type uint16)
        tifflib('setDirectory',FileID,output_frame_numbers(i));
        rps = min(rps,nImage);

        for r = 1:rps:nImage
            row_inds = r:min(nImage,r+rps-1);
            stripNum = tifflib('computeStrip',FileID,r);
            Temp_Matrix_temp(row_inds,:) =
double(tifflib('readEncodedStrip',FileID,stripNum-1));   %% save current image/frame
        end
        Temp_Matrix(:,:,i) = Temp_Matrix_temp(ymin:ymin+pixel_height-
1,xmin:xmin+pixel_width-1);  %% crop current image/frame and add it to the
temperature matrix
    end
end



for m = 1:output_frames
    %% convert matrices to 8 bit grayscale images, scales min value to 0 and max value
to 255 (does not preserve temperature data)
    A = mat2gray(reshape(Temp_Matrix(:,:,m),[pixel_height, pixel_width]));

    %% save images as 8 bit grayscale TIFF sequences
    if m == 1
        imwrite(A,['Processed\',filename(1:end-5),' Processed.tiff'])
    else
        imwrite(A,['Processed\',filename(1:end-5),' Processed.tiff'],'WriteMode','append')
    end
end


%% stop timer and display
total_time = toc;
display(['Time Elapsed: ',num2str(total_time,'%.1f'),' sec'])

%% save log file
```

```
fileID = fopen(['Processed\',filename(1:end-5),' log.txt'],'w');
fprintf(fileID,'%s %s\r\n\r\n','Filename:',filename);
fprintf(fileID,'%s %s\r\n\r\n','Date/Time Processed:',datetime);
fprintf(fileID,'%s %u\r\n','Framerate:',framerate);
fprintf(fileID,'%s %.0f\r\n\r\n','Rotation (Degrees):',angle);
fprintf(fileID,'%s\r\n','Selected Region of Interest (pixels):');
fprintf(fileID,'%4s %6s %7s %8s\r\n','xmin','ymin','width','height');
fprintf(fileID,'%4u %6u %7u %8u\r\n\r\n',xmin,ymin,pixel_width,pixel_height);
fprintf(fileID,'%s %.1f %s','Elapsed Time:',total_time,'sec');
fclose(fileID);

end
```

B.4 Solar Irradiance Data Logging Code

```
function [solarIrradiance] = PV_Website_Read(~,~)

%{
function to save Global Normal Solar Irradiance, date, time, and air temperature every
minute
G. Ray Ely, Sandia National Labs, Org. 06621, grely@sandia.gov
v1.1, 6/21/17

Saves data from Sandia Photovoltaic Systems Evaluation Laboratory in Albuquerque,
NM
Latitude: 35.05 N Longitude: 106.54 W Altitude: 1657 m (5436 ft)
Data is updated every minute on the website
http://photovoltaics.sandia.gov/weather/Weather.htm

to use, call:
t = timer('TimerFcn', {@PV_Website_Read}, 'Period', 60.0, 'ExecutionMode',
'fixedRate');
start(t)

to stop, call:
stop(t)
%}

%% save data from Sandia PhotoVoltaic website
raw_data = urlread('http://photovoltaics.sandia.gov/weather/Weather.htm');

%% search for general location of Global Normal (Solar Irradiance), date, time, and
air temp (degF) in html code
startIndex_solar = regexp(raw_data,'Global Normal');
startIndex_date = regexp(raw_data,'---');
startIndex_time = regexp(raw_data,'---');
startIndex_temp = regexp(raw_data,'Air Temp');

%% search for values of variables and save indices
[solar_start_index, solar_end_index] = regexp(raw_data(startIndex_solar(1):end),'[0-
9]{3}');
[date_start_index, date_end_index] =
regexp(raw_data(startIndex_date(1):end),'(?<month>\d+)/(?<day>\d+)/(?<year>\d+)');
[time_start_index, time_end_index] = regexp(raw_data(startIndex_time(1):end),'[0-
9]{1}:[0-9]{1}');
[temp_start_index, temp_end_index] = regexp(raw_data(startIndex_temp(1):end),'[0-
9]{1}\.[0-9]{1}');

%% save value of variables based on indices
```

```
solarIrradiance = (strcat((raw_data((startIndex_solar(1) + solar_start_index(1) - 1) :
(startIndex_solar(1) + solar_end_index(1))))));
date = strcat((raw_data((startIndex_date(1) + date_start_index(1) - 1) :
(startIndex_date(1) + date_end_index(1)))));
time = strcat((raw_data((startIndex_time(1) + time_start_index(1) - 2) :
(startIndex_time(1) + time_end_index(1)))));
temp = (strcat((raw_data((startIndex_temp(1) + temp_start_index(2) - 2) :
(startIndex_temp(1) + temp_end_index(2))))));

%% header for Excel file
header = {'Date', 'Time (24hr)', ['Air Temp (', char(176), 'F)'], 'Global Normal Solar
Irradiance (W/m^2)'};

%% save filename with date pulled from website (replace "/" with "-" in date)
filename = ['Solar Irradiance Data ', strrep(date, '/', '-'), '.xlsx'];

%% save data to Excel file

%% if file already exists for this date (if it's appending data)
if exist(filename, 'file')
   %% save existing data
   [~,~,old_data] = xlsread(filename);

   %% find next available row to append data to
   my_cell = sprintf('A%s',num2str(size(old_data,1)+1));

   %% write current data to the next available row
   xlswrite(filename,{date, time, temp, solarIrradiance},1,my_cell)

%% if file doesn't exist yet
else
   %% save header to the first row
   xlswrite(filename,header,1,'A1')

   %% save current data to the 2nd row
   xlswrite(filename,{date, time, temp, solarIrradiance},1,'A2')

   %% adjust column widths in Excel to fit header titles
   hExcel = actxserver('Excel.Application');
   hWorkbook =
hExcel.Workbooks.Open(['C:\Users\grely.SANDIA\Documents\MATLAB\',filename]
);
   hWorksheet = hWorkbook.Sheets.Item(1);
   hWorksheet.Columns.Item(1).columnWidth = 9; %first column
   hWorksheet.Columns.Item(2).columnWidth = 10.5; %second column
   hWorksheet.Columns.Item(3).columnWidth = 12; %second column
```

```
    hWorksheet.Columns.Item(4).columnWidth = 36; %second column
    hWorkbook.Save
    hWorkbook.Close
    hExcel.Quit
    hExcel.delete
end
```

APPENDIX C. TEST NOTES

C.1 Flash Tube Heating Test Notes

Date	Time (approx. time specimen is placed in the flash bulbs box, to the minute)	Location	Temp Data (Location of Thermocouples)	Test Specimen ID	Test #	IR Camera
6/5/2017	10:33am	894/157	TC1 (K Type): Front, Top Left TC2 (K Type): Back, Top Left TC3 (K Type): Room Temp	G11-STD-1	1	FLIR Boson Resolution: 320x256 Frame Rate: 60 Hz S/N: 2338
6/5/2017	10:46am	894/157	TC1 (K Type): Front, Top Left TC2 (K Type): Back, Top Left TC3 (K Type): Room Temp	G11-STD-2	1	FLIR Boson Resolution: 320x256 Frame Rate: 60 Hz S/N: 2338
6/5/2017	10:55am	894/157	TC1 (K Type): Front, Top Left TC2 (K Type): Back, Top Left TC3 (K Type): Room Temp	G11-STD-3	1	FLIR Boson Resolution: 320x256 Frame Rate: 60 Hz S/N: 2338
6/5/2017	11:12am	894/157	TC1 (K Type): Front, Top Left TC2 (K Type): Back, Top Left TC3 (K Type): Room Temp	GLF-S05-C4T2	1	FLIR Boson Resolution: 320x256 Frame Rate: 60 Hz S/N: 2338
6/5/2017	11:30am	894/157	TC1 (K Type): Front, Top Left TC2 (K Type): Back, Top Left TC3 (K Type): Room Temp	GLF-S05-C4T2	2	FLIR Boson Resolution: 320x256 Frame Rate: 60 Hz S/N: 2338
6/5/2017	1:20pm	894/157	TC1 (K Type): Front, Top Left TC2 (K Type): Back, Top Left TC3 (K Type): Room Temp	GLF-S05-C4T2	3	FLIR Boson Resolution: 320x256 Frame Rate: 60 Hz S/N: 2338
6/5/2017	1:29pm	894/157	TC1 (K Type): Front, Top Left TC2 (K Type): Back, Top Left TC3 (K Type): Room Temp	GLF-S05-C4T2	4	FLIR Boson Resolution: 320x256 Frame Rate: 60 Hz S/N: 2338
6/5/2017	1:43pm	894/157	TC1 (K Type): Front, Top Left TC2 (K Type): Back, Top Left TC3 (K Type): Room Temp	GLF-S05-C4T2-P5-02	1	FLIR Boson Resolution: 320x256 Frame Rate: 60 Hz S/N: 2338
6/5/2017	1:48pm	894/157	TC1 (K Type): Front, Top Left TC2 (K Type): Back, Top Left TC3 (K Type): Room Temp	GLF-S05-C4T2-P5-02	2	FLIR Boson Resolution: 320x256 Frame Rate: 60 Hz S/N: 2338
6/5/2017	2:00pm	894/157	TC1 (K Type): Front, Top Left TC2 (K Type): Back, Top Left TC3 (K Type): Room Temp	GLF-S04-C4T2	1	FLIR Boson Resolution: 320x256 Frame Rate: 60 Hz S/N: 2338
6/5/2017	3:24pm	894/157	TC1 (K Type): Front, Top Left TC2 (K Type): Back, Top Left TC3 (K Type): Room Temp	GLF-S04-C4T2	2	FLIR Boson Resolution: 320x256 Frame Rate: 60 Hz S/N: 2338
6/5/2017	3:33pm	894/157	TC1 (K Type): Front, Top Left TC2 (K Type): Back, Top Left TC3 (K Type): Room Temp	GLF-S05-C6T2	1	FLIR Boson Resolution: 320x256 Frame Rate: 60 Hz S/N: 2338

Figure C-21: Flash Tubes Heating Test Notes 1

IR Camera Settings	Heat Source	Heat Source Settings	Air Temperature (°F)	Notes (see photos for part orientation)
Format: 16-bit TIFF sequence (IR16) AGC Settings: Pre-AGC FFC: Manual, 16 frames integration, performed immediately before test Video Duration (after heating): 30s	TWI EchoTherm 2x 5000 J Flash Tubes	Flash Duration: 30 ms Flash Power Level: 100%	Recorded by TC3 prior to test	Video File: Boson_Capture_33.tiff Thermocouple File: 008
Format: 16-bit TIFF sequence (IR16) AGC Settings: Pre-AGC FFC: Manual, 16 frames integration, performed immediately before test Video Duration (after heating): 65s	TWI EchoTherm 2x 5000 J Flash Tubes	Flash Duration: 30 ms Flash Power Level: 100%	Recorded by TC3 prior to test	Video File: Boson_Capture_34.tiff Thermocouple File: 009
Format: 16-bit TIFF sequence (IR16) AGC Settings: Pre-AGC FFC: Manual, 16 frames integration, performed immediately before test Video Duration (after heating): 400s	TWI EchoTherm 2x 5000 J Flash Tubes	Flash Duration: 30 ms Flash Power Level: 100%	Recorded by TC3 prior to test	Video File: Boson_Capture_35.tiff Thermocouple File: 010 Didn't see all flaw, so I decided not to test G11-STD-4 or FGB parts
Format: 16-bit TIFF sequence (IR16) AGC Settings: Pre-AGC FFC: Manual, 16 frames integration, performed immediately before test Video Duration (after heating): 60s	TWI EchoTherm 2x 5000 J Flash Tubes	Flash Duration: 30 ms Flash Power Level: 100%	Recorded by TC3 prior to test	Video File: Boson_Capture_36.tiff Thermocouple File: 011
Format: 16-bit TIFF sequence (IR16) AGC Settings: Pre-AGC FFC: Manual, 16 frames integration, performed immediately before test Video Duration (after heating): 60s	TWI EchoTherm 2x 5000 J Flash Tubes	Flash Duration: 30 ms Flash Power Level: 100%	Recorded by TC3 prior to test	Video File: Boson_Capture_37.tiff Thermocouple File: 012 Moved camera up (zoomed out) but would still like to zoom out more, if possible
Format: 16-bit TIFF sequence (IR16) AGC Settings: Pre-AGC FFC: Manual, 16 frames integration, performed immediately before test Video Duration (after heating): 60s	TWI EchoTherm 2x 5000 J Flash Tubes	Flash Duration: 30 ms Flash Power Level: 100%	Recorded by TC3 prior to test	Video File: Boson_Capture_38.tiff Thermocouple File: 013 Rotated 90 degrees and inspected half of the specimen at a time
Format: 16-bit TIFF sequence (IR16) AGC Settings: Pre-AGC FFC: Manual, 16 frames integration, performed immediately before test Video Duration (after heating): 60s	TWI EchoTherm 2x 5000 J Flash Tubes	Flash Duration: 30 ms Flash Power Level: 100%	Recorded by TC3 prior to test	Video File: Boson_Capture_39.tiff Thermocouple File: 014 Moved to the other half and moved TCs (see pictures)
Format: 16-bit TIFF sequence (IR16) AGC Settings: Pre-AGC FFC: Manual, 16 frames integration, performed immediately before test Video Duration (after heating): 60s	TWI EchoTherm 2x 5000 J Flash Tubes	Flash Duration: 30 ms Flash Power Level: 100%	Recorded by TC3 prior to test	Video File: Boson_Capture_40.tiff Thermocouple File: 015 Didn't see any flaws, sliding up the camera and retesting
Format: 16-bit TIFF sequence (IR16) AGC Settings: Pre-AGC FFC: Manual, 16 frames integration, performed immediately before test Video Duration (after heating): 60s	TWI EchoTherm 2x 5000 J Flash Tubes	Flash Duration: 30 ms Flash Power Level: 100%	Recorded by TC3 prior to test	Video File: Boson_Capture_41.tiff Thermocouple File: 016
Format: 16-bit TIFF sequence (IR16) AGC Settings: Pre-AGC FFC: Manual, 16 frames integration, performed immediately before test Video Duration (after heating): 120s	TWI EchoTherm 2x 5000 J Flash Tubes	Flash Duration: 30 ms Flash Power Level: 100%	Recorded by TC3 prior to test	Video File: Boson_Capture_42.tiff Thermocouple File: 017
Format: 16-bit TIFF sequence (IR16) AGC Settings: Pre-AGC FFC: Manual, 16 frames integration, performed immediately before test Video Duration (after heating): 120s	TWI EchoTherm 2x 5000 J Flash Tubes	Flash Duration: 30 ms Flash Power Level: 100%	Recorded by TC3 prior to test	Video File: Boson_Capture_43.tiff Thermocouple File: 018
Format: 16-bit TIFF sequence (IR16) AGC Settings: Pre-AGC FFC: Manual, 16 frames integration, performed immediately before test Video Duration (after heating): 60s	TWI EchoTherm 2x 5000 J Flash Tubes	Flash Duration: 30 ms Flash Power Level: 100%	Recorded by TC3 prior to test	Video File: Boson_Capture_44.tiff Thermocouple File: 019

Figure C-22: Flash Tubes Heating Test Notes 1 (continued)

Date	Time (approx. time specimen is placed in the flash bulbs box, to the minute)	Location	Temp Data (Location of Thermocouples)	Test Specimen ID	Test #	IR Camera
6/5/2017	3:38pm	894/157	TC1 (K Type): Front, Top Left TC2 (K Type): Back, Top Left TC3 (K Type): Room Temp	GLF-S05-C6T2	2	FLIR Boson Resolution: 320x256 Frame Rate: 60 Hz S/N: 2338
6/5/2017	3:47pm	894/157	TC1 (K Type): Front, Top Left TC2 (K Type): Back, Top Left TC3 (K Type): Room Temp	GLF-S06-C4T2	1	FLIR Boson Resolution: 320x256 Frame Rate: 60 Hz S/N: 2338
6/5/2017	3:52pm	894/157	TC1 (K Type): Front, Top Left TC2 (K Type): Back, Top Left TC3 (K Type): Room Temp	GLF-S06-C4T2	2	FLIR Boson Resolution: 320x256 Frame Rate: 60 Hz S/N: 2338
6/5/2017	3:56pm	894/157	TC1 (K Type): Front, Top Left TC2 (K Type): Back, Top Left TC3 (K Type): Room Temp	GLF-S06-C4T2	3	FLIR Boson Resolution: 320x256 Frame Rate: 60 Hz S/N: 2338
6/5/2017	4:18pm	894/157	TC1 (K Type): Front, Top Left TC2 (K Type): Back, Top Left TC3 (K Type): Room Temp	REF-STD-1-050-TPI-1	1	FLIR Boson Resolution: 320x256 Frame Rate: 60 Hz S/N: 2338
6/5/2017	4:27pm	894/157	TC1 (K Type): Front, Top Left TC2 (K Type): Back, Top Left TC3 (K Type): Room Temp	REF-STD-1-050-TPI-1	2	FLIR Boson Resolution: 320x256 Frame Rate: 60 Hz S/N: 2338
6/5/2017	5:05pm	894/157	TC1 (K Type): Front, Top Left TC2 (K Type): Back, Top Left TC3 (K Type): Room Temp	REF-STD-1-050-TPI-1	3	FLIR Boson Resolution: 320x256 Frame Rate: 60 Hz S/N: 2338
6/5/2017	5:11pm	894/157	TC1 (K Type): Front, Top Left TC2 (K Type): Back, Top Left TC3 (K Type): Room Temp	REF-STD-1-050-TPI-1	4	FLIR Boson Resolution: 320x256 Frame Rate: 60 Hz S/N: 2338
6/5/2017	5:14pm	894/157	TC1 (K Type): Front, Top Left TC2 (K Type): Back, Top Left TC3 (K Type): Room Temp	REF-STD-1-050-TPI-1	5	FLIR Boson Resolution: 320x256 Frame Rate: 60 Hz S/N: 2338
6/5/2017	5:18pm	894/157	TC1 (K Type): Front, Top Left TC2 (K Type): Back, Top Left TC3 (K Type): Room Temp	REF-STD-1-050-TPI-1	6	FLIR Boson Resolution: 320x256 Frame Rate: 60 Hz S/N: 2338
6/5/2017	5:24pm	894/157	TC1 (K Type): Front, Top Left TC2 (K Type): Back, Top Left TC3 (K Type): Room Temp	REF-STD-1-050-TPI-1	7	FLIR Boson Resolution: 320x256 Frame Rate: 60 Hz S/N: 2338
6/5/2017	5:28pm	894/157	TC1 (K Type): Front, Top Left TC2 (K Type): Back, Top Left TC3 (K Type): Room Temp	REF-STD-1-050-TPI-1	8	FLIR Boson Resolution: 320x256 Frame Rate: 60 Hz S/N: 2338
6/5/2017	5:36pm	894/157	TC1 (K Type): Front, Top Left TC2 (K Type): Back, Top Left TC3 (K Type): Room Temp	REF-STD-1-050-TPI-1	9	FLIR Boson Resolution: 320x256 Frame Rate: 60 Hz S/N: 2338
6/5/2017	5:41pm	894/157	TC1 (K Type): Front, Top Left TC2 (K Type): Back, Top Left TC3 (K Type): Room Temp	REF-STD-1-050-TPI-1	10	FLIR Boson Resolution: 320x256 Frame Rate: 60 Hz S/N: 2338
6/5/2017	5:46pm	894/157	TC1 (K Type): Front, Top Left TC2 (K Type): Back, Top Left TC3 (K Type): Room Temp	REF-STD-1-050-TPI-1	11	FLIR Boson Resolution: 320x256 Frame Rate: 60 Hz S/N: 2338

Figure C-23: Flash Tubes Heating Test Notes 2

IR Camera Settings	Heat Source	Heat Source Settings	Air Temperature (°F)	Notes (see photos for part orientation)
Format: 16-bit TIFF sequence (IR16) AGC Settings: Pre-AGC FFC: Manual, 16 frames integration, performed immediately before test Video Duration (after heating): 60s	TWI EchoTherm 2x 5000 J Flash Tubes	Flash Duration: 30 ms Flash Power Level: 100%	Recorded by TC3 prior to test	Video File: Boson_Capture_45.tiff Thermocouple File: 020
Format: 16-bit TIFF sequence (IR16) AGC Settings: Pre-AGC FFC: Manual, 16 frames integration, performed immediately before test Video Duration (after heating): 60s	TWI EchoTherm 2x 5000 J Flash Tubes	Flash Duration: 30 ms Flash Power Level: 100%	Recorded by TC3 prior to test	Video File: Boson_Capture_46.tiff Thermocouple File: 021
Format: 16-bit TIFF sequence (IR16) AGC Settings: Pre-AGC FFC: Manual, 16 frames integration, performed immediately before test Video Duration (after heating): 60s	TWI EchoTherm 2x 5000 J Flash Tubes	Flash Duration: 30 ms Flash Power Level: 100%	Recorded by TC3 prior to test	Video File: Boson_Capture_47.tiff Thermocouple File: 022
Format: 16-bit TIFF sequence (IR16) AGC Settings: Pre-AGC FFC: Manual, 16 frames integration, performed immediately before test Video Duration (after heating): 60s	TWI EchoTherm 2x 5000 J Flash Tubes	Flash Duration: 30 ms Flash Power Level: 100%	Recorded by TC3 prior to test	Video File: Boson_Capture_48.tiff Thermocouple File: 023
Format: 16-bit TIFF sequence (IR16) AGC Settings: Pre-AGC FFC: Manual, 16 frames integration, performed immediately before test Video Duration (after heating): 60s	TWI EchoTherm 2x 5000 J Flash Tubes	Flash Duration: 30 ms Flash Power Level: 100%	Recorded by TC3 prior to test	Video File: Boson_Capture_50.tiff Thermocouple File: 025 Focused on upper 3 grease and pillow insert flaws
Format: 16-bit TIFF sequence (IR16) AGC Settings: Pre-AGC FFC: Manual, 16 frames integration, performed immediately before test Video Duration (after heating): 60s	TWI EchoTherm 2x 5000 J Flash Tubes	Flash Duration: 30 ms Flash Power Level: 100%	Recorded by TC3 prior to test	Video File: Boson_Capture_51.tiff Thermocouple File: 026 Focused on upper 3 pillow insert and microballoon flaws
Format: 16-bit TIFF sequence (IR16) AGC Settings: Pre-AGC FFC: Manual, 16 frames integration, performed immediately before test Video Duration (after heating): 60s	TWI EchoTherm 2x 5000 J Flash Tubes	Flash Duration: 30 ms Flash Power Level: 100%	Recorded by TC3 prior to test	Video File: Boson_Capture_52.tiff Thermocouple File: 027 Focused on middle 2 pillow insert and microballoon flaws
Format: 16-bit TIFF sequence (IR16) AGC Settings: Pre-AGC FFC: Manual, 16 frames integration, performed immediately before test Video Duration (after heating): 60s	TWI EchoTherm 2x 5000 J Flash Tubes	Flash Duration: 30 ms Flash Power Level: 100%	Recorded by TC3 prior to test	Video File: Boson_Capture_53.tiff Thermocouple File: 028 Focused on middle 2 grease and pillow insert flaws
Format: 16-bit TIFF sequence (IR16) AGC Settings: Pre-AGC FFC: Manual, 16 frames integration, performed immediately before test Video Duration (after heating): 60s	TWI EchoTherm 2x 5000 J Flash Tubes	Flash Duration: 30 ms Flash Power Level: 100%	Recorded by TC3 prior to test	Video File: Boson_Capture_54.tiff Thermocouple File: 029 Focused on lower 3 pillow insert and grease flaws
Format: 16-bit TIFF sequence (IR16) AGC Settings: Pre-AGC FFC: Manual, 16 frames integration, performed immediately before test Video Duration (after heating): 60s	TWI EchoTherm 2x 5000 J Flash Tubes	Flash Duration: 30 ms Flash Power Level: 100%	Recorded by TC3 prior to test	Video File: Boson_Capture_55.tiff Thermocouple File: 030 Focused on lower 2 pillow insert and grease flaws
Format: 16-bit TIFF sequence (IR16) AGC Settings: Pre-AGC FFC: Manual, 16 frames integration, performed immediately before test Video Duration (after heating): 60s	TWI EchoTherm 2x 5000 J Flash Tubes	Flash Duration: 30 ms Flash Power Level: 100%	Recorded by TC3 prior to test	Video File: Boson_Capture_56.tiff Thermocouple File: 031 Focused on lower 3 pillow insert and microballoon flaws
Format: 16-bit TIFF sequence (IR16) AGC Settings: Pre-AGC FFC: Manual, 16 frames integration, performed immediately before test Video Duration (after heating): 60s	TWI EchoTherm 2x 5000 J Flash Tubes	Flash Duration: 30 ms Flash Power Level: 100%	Recorded by TC3 prior to test	Video File: Boson_Capture_57.tiff Thermocouple File: 032 Focused on lower 3 pillow insert and microballoon flaws
Format: 16-bit TIFF sequence (IR16) AGC Settings: Pre-AGC FFC: Manual, 16 frames integration, performed immediately before test Video Duration (after heating): 60s	TWI EchoTherm 2x 5000 J Flash Tubes	Flash Duration: 30 ms Flash Power Level: 100%	Recorded by TC3 prior to test	Video File: Boson_Capture_58.tiff Thermocouple File: 033 Focused on lower 3 pull tab flaws
Format: 16-bit TIFF sequence (IR16) AGC Settings: Pre-AGC FFC: Manual, 16 frames integration, performed immediately before test Video Duration (after heating): 60s	TWI EchoTherm 2x 5000 J Flash Tubes	Flash Duration: 30 ms Flash Power Level: 100%	Recorded by TC3 prior to test	Video File: Boson_Capture_59.tiff Thermocouple File: 034 Focused on upper 3-5 pull tab flaws
Format: 16-bit TIFF sequence (IR16) AGC Settings: Pre-AGC FFC: Manual, 16 frames integration, performed immediately before test Video Duration (after heating): 60s	TWI EchoTherm 2x 5000 J Flash Tubes	Flash Duration: 30 ms Flash Power Level: 100%	Recorded by TC3 prior to test	Video File: Boson_Capture_60.tiff Thermocouple File: 035 Focused on upper 3 pull tab flaws Forgot to move TC1

Figure C-24: Flash Tubes Heating Test Notes 2 (continued)

Date	Time (approx. time specimen is placed in the flash bulbs box, to the minute)	Location	Temp Data (Location of Thermocouples)	Test Specimen ID	Test #	IR Camera
6/6/2017	9:28am	894/157	TC1 (K Type): Front, Top Left TC2 (K Type): Back, Top Left TC3 (K Type): Room Temp	WIND-1-029	1	FLIR Boson Resolution: 320x256 Frame Rate: 60 Hz S/N: 2338
6/6/2017	9:37am	894/157	TC1 (K Type): Front, Top Left TC2 (K Type): Back, Top Left TC3 (K Type): Room Temp	WIND-1-029	2	FLIR Boson Resolution: 320x256 Frame Rate: 60 Hz S/N: 2338
6/6/2017	9:43am	894/157	TC1 (K Type): Front, Top Left TC2 (K Type): Back, Top Left TC3 (K Type): Room Temp	WIND-1-029	3	FLIR Boson Resolution: 320x256 Frame Rate: 60 Hz S/N: 2338
6/6/2017	9:49am	894/157	TC1 (K Type): Front, Top Left TC2 (K Type): Back, Top Left TC3 (K Type): Room Temp	WIND-1-029	4	FLIR Boson Resolution: 320x256 Frame Rate: 60 Hz S/N: 2338
6/6/2017	9:56am	894/157	TC1 (K Type): Front, Top Left TC2 (K Type): Back, Top Left TC3 (K Type): Room Temp	WIND-1-029	5	FLIR Boson Resolution: 320x256 Frame Rate: 60 Hz S/N: 2338
6/6/2017	10:08am	894/157	TC1 (K Type): Front, Top Left TC2 (K Type): Back, Top Left TC3 (K Type): Room Temp	WIND-2-044-SPAR-085	1	FLIR Boson Resolution: 320x256 Frame Rate: 60 Hz S/N: 2338
6/6/2017	11:06am	894/157	TC1 (K Type): Front, Top Left TC2 (K Type): Back, Top Left TC3 (K Type): Room Temp	WIND-2-044-SPAR-085	2	FLIR Boson Resolution: 320x256 Frame Rate: 60 Hz S/N: 2338
6/6/2017	11:12am	894/157	TC1 (K Type): Front, Top Left TC2 (K Type): Back, Top Left TC3 (K Type): Room Temp	WIND-2-044-SPAR-085	3	FLIR Boson Resolution: 320x256 Frame Rate: 60 Hz S/N: 2338
6/6/2017	11:17am	894/157	TC1 (K Type): Front, Top Left TC2 (K Type): Back, Top Left TC3 (K Type): Room Temp	WIND-2-044-SPAR-085	4	FLIR Boson Resolution: 320x256 Frame Rate: 60 Hz S/N: 2338
6/6/2017	11:23am	894/157	TC1 (K Type): Front, Top Left TC2 (K Type): Back, Top Left TC3 (K Type): Room Temp	WIND-2-044-SPAR-085	5	FLIR Boson Resolution: 320x256 Frame Rate: 60 Hz S/N: 2338
6/6/2017	11:34am	894/157	TC1 (K Type): Front, Top Left TC2 (K Type): Back, Top Left TC3 (K Type): Room Temp	WIND-3-110-SPAR-150	1	FLIR Boson Resolution: 320x256 Frame Rate: 60 Hz S/N: 2338
6/6/2017	11:40am	894/157	TC1 (K Type): Front, Top Left TC2 (K Type): Back, Top Left TC3 (K Type): Room Temp	WIND-3-110-SPAR-150	2	FLIR Boson Resolution: 320x256 Frame Rate: 60 Hz S/N: 2338
6/6/2017	1:11pm	894/157	TC1 (K Type): Front, Top Left TC2 (K Type): Back, Top Left TC3 (K Type): Room Temp	WIND-4-161	1	FLIR Boson Resolution: 320x256 Frame Rate: 60 Hz S/N: 2338
6/6/2017	1:18pm	894/157	TC1 (K Type): Front, Top Left TC2 (K Type): Back, Top Left TC3 (K Type): Room Temp	WIND-4-161	2	FLIR Boson Resolution: 320x256 Frame Rate: 60 Hz S/N: 2338

Figure C-25: Flash Tubes Heating Test Notes 3

IR Camera Settings	Heat Source	Heat Source Settings	Air Temperature (°F)	Notes (see photos for part orientation)
Format: 8-bit .avi (UVC) AGC Settings: Pre-AGC FFC: Manual, 16 frames integration, performed immediately before test Video Duration (after heating): 60s	TWI EchoTherm 2x 5000 J Flash Tubes	Flash Duration: 30 ms Flash Power Level: 100%	Recorded by TC3 prior to test	Video File: Boson_Capture_6.avi Thermocouple File: 036 Incorrect file format (.avi) Focused on upper left 3 flat bottom holes
Format: 16-bit TIFF sequence (IR16) AGC Settings: Pre-AGC FFC: Manual, 16 frames integration, performed immediately before test Video Duration (after heating): 60s	TWI EchoTherm 2x 5000 J Flash Tubes	Flash Duration: 30 ms Flash Power Level: 100%	Recorded by TC3 prior to test	Video File: Boson_Capture_61.tiff Thermocouple File: 037 Focused on upper left 3 flat bottom holes (repeat of previous test with correct file format)
Format: 16-bit TIFF sequence (IR16) AGC Settings: Pre-AGC FFC: Manual, 16 frames integration, performed immediately before test Video Duration (after heating): 60s	TWI EchoTherm 2x 5000 J Flash Tubes	Flash Duration: 30 ms Flash Power Level: 100%	Recorded by TC3 prior to test	Video File: Boson_Capture_62.tiff Thermocouple File: 038 Focused on lower left 3 flat bottom holes
Format: 16-bit TIFF sequence (IR16) AGC Settings: Pre-AGC FFC: Manual, 16 frames integration, performed immediately before test Video Duration (after heating): 120s	TWI EchoTherm 2x 5000 J Flash Tubes	Flash Duration: 30 ms Flash Power Level: 100%	Recorded by TC3 prior to test	Video File: Boson_Capture_63.tiff Thermocouple File: 039 Focused on lower right 3 flat bottom holes
Format: 16-bit TIFF sequence (IR16) AGC Settings: Pre-AGC FFC: Manual, 16 frames integration, performed immediately before test Video Duration (after heating): 120s	TWI EchoTherm 2x 5000 J Flash Tubes	Flash Duration: 30 ms Flash Power Level: 100%	Recorded by TC3 prior to test	Video File: Boson_Capture_64.tiff Thermocouple File: 040 Focused on upper right 3 flat bottom holes
Format: 16-bit TIFF sequence (IR16) AGC Settings: Pre-AGC FFC: Manual, 16 frames integration, performed immediately before test Video Duration (after heating): 120s	TWI EchoTherm 2x 5000 J Flash Tubes	Flash Duration: 30 ms Flash Power Level: 100%	Recorded by TC3 prior to test	Video File: Boson_Capture_65.tiff Thermocouple File: 041 Focused on upper left 3 flat bottom holes
Format: 16-bit TIFF sequence (IR16) AGC Settings: Pre-AGC FFC: Manual, 16 frames integration, performed immediately before test Video Duration (after heating): 60s	TWI EchoTherm 2x 5000 J Flash Tubes	Flash Duration: 30 ms Flash Power Level: 100%	Recorded by TC3 prior to test	Video File: Boson_Capture_66.tiff Thermocouple File: 042 Focused on lower left 3 flat bottom holes
Format: 16-bit TIFF sequence (IR16) AGC Settings: Pre-AGC FFC: Manual, 16 frames integration, performed immediately before test Video Duration (after heating): 120s	TWI EchoTherm 2x 5000 J Flash Tubes	Flash Duration: 30 ms Flash Power Level: 100%	Recorded by TC3 prior to test	Video File: Boson_Capture_67.tiff Thermocouple File: 043 Focused on lower right 3 flat bottom holes Didn't see any flaws
Format: 16-bit TIFF sequence (IR16) AGC Settings: Pre-AGC FFC: Manual, 16 frames integration, performed immediately before test Video Duration (after heating): 120s	TWI EchoTherm 2x 5000 J Flash Tubes	Flash Duration: 30 ms Flash Power Level: 100%	Recorded by TC3 prior to test	Video File: Boson_Capture_68.tiff Thermocouple File: 044 Focused on lower right 3 flat bottom holes (repeat with camera shifted more towards the middle of specimen)
Format: 16-bit TIFF sequence (IR16) AGC Settings: Pre-AGC FFC: Manual, 16 frames integration, performed immediately before test Video Duration (after heating): 120s	TWI EchoTherm 2x 5000 J Flash Tubes	Flash Duration: 30 ms Flash Power Level: 100%	Recorded by TC3 prior to test	Video File: Boson_Capture_69.tiff Thermocouple File: 045 Focused on upper right 3 flat bottom holes
Format: 16-bit TIFF sequence (IR16) AGC Settings: Pre-AGC FFC: Manual, 16 frames integration, performed immediately before test Video Duration (after heating): 60s	TWI EchoTherm 2x 5000 J Flash Tubes	Flash Duration: 30 ms Flash Power Level: 100%	Recorded by TC3 prior to test	Video File: Boson_Capture_70.tiff Thermocouple File: 046 Focused on upper right 3 flat bottom holes
Format: 16-bit TIFF sequence (IR16) AGC Settings: Pre-AGC FFC: Manual, 16 frames integration, performed immediately before test Video Duration (after heating): 120s	TWI EchoTherm 2x 5000 J Flash Tubes	Flash Duration: 30 ms Flash Power Level: 100%	Recorded by TC3 prior to test	Video File: Boson_Capture_71.tiff Thermocouple File: 047 Focused on lower right 3 flat bottom holes Might barely see the flaws
Format: 16-bit TIFF sequence (IR16) AGC Settings: Pre-AGC FFC: Manual, 16 frames integration, performed immediately before test Video Duration (after heating): 60s	TWI EchoTherm 2x 5000 J Flash Tubes	Flash Duration: 30 ms Flash Power Level: 100%	Recorded by TC3 prior to test	Video File: Boson_Capture_72.tiff Thermocouple File: 048 Focused on upper right 3 flat bottom holes
Format: 16-bit TIFF sequence (IR16) AGC Settings: Pre-AGC FFC: Manual, 16 frames integration, performed immediately before test Video Duration (after heating): 120s	TWI EchoTherm 2x 5000 J Flash Tubes	Flash Duration: 30 ms Flash Power Level: 100%	Recorded by TC3 prior to test	Video File: Boson_Capture_73.tiff Thermocouple File: 049 Focused on lower right 3 flat bottom holes

Figure C-26: Flash Tubes Heating Test Notes 3 (continued)

C.2 Internal Forced Air (Heat Gun) Heating Test Notes

Date	Time (approx. time specimen is placed in the heat gun box, to the minute)	Location	Temp Data (Location of Thermocouples)	Test Specimen ID	Test #	IR Camera
5/31/2017	4:06pm	Heating: 894/157 Cooling: 894/157	TC1 (K Type): Front, Top Left TC2 (K Type): Back, Top Left TC3 (K Type): Box TC4 (K Type): Room	G11-STD-2	1	FLIR Boson Resolution: 320x256 Frame Rate: 60 Hz S/N: 2338
5/31/2017	4:18pm	Heating: 894/157 Cooling: 894/157	TC1 (K Type): Front, Top Left TC2 (K Type): Back, Top Left TC3 (K Type): Box TC4 (K Type): Room	G11-STD-2	2	FLIR Boson Resolution: 320x256 Frame Rate: 60 Hz S/N: 2338
5/31/2017	4:42pm	Heating: 894/157 Cooling: 894/157	TC1 (K Type): Front, Top Left TC2 (K Type): Back, Top Left TC3 (K Type): Box TC4 (K Type): Room	G11-STD-3	1	FLIR Boson Resolution: 320x256 Frame Rate: 60 Hz S/N: 2338
5/31/2017	5:00pm	Heating: 894/157 Cooling: 894/157	TC1 (K Type): Front, Top Left TC2 (K Type): Back, Top Left TC3 (K Type): Box TC4 (K Type): Room	G11-STD-3	2	FLIR Boson Resolution: 320x256 Frame Rate: 60 Hz S/N: 2338
5/31/2017	5:25pm	Heating: 894/157 Cooling: 894/157	TC1 (K Type): Front, Top Left TC2 (K Type): Back, Top Left TC3 (K Type): Box TC4 (K Type): Room	G11-STD-3	3	FLIR Boson Resolution: 320x256 Frame Rate: 60 Hz S/N: 2338
6/1/2017	4:24pm	Heating: 894/157 Cooling: 894/157	TC1 (K Type): Front, Top Left TC2 (K Type): Back, Top Left TC3 (K Type): Box TC4 (K Type): Room	G11-STD-4	1	FLIR Boson Resolution: 320x256 Frame Rate: 60 Hz S/N: 2338
6/1/2017	4:35pm	Heating: 894/157 Cooling: 894/157	TC1 (K Type): Front, Top Left TC2 (K Type): Back, Top Left TC3 (K Type): Box TC4 (K Type): Room	G11-STD-4	2	FLIR Boson Resolution: 320x256 Frame Rate: 60 Hz S/N: 2338
6/1/2017	5:15pm	Heating: 894/157 Cooling: 894/157	TC1 (K Type): Front, Top Left TC2 (K Type): Back, Top Left TC3 (K Type): Box TC4 (K Type): Room	G11-STD-1	1	FLIR Boson Resolution: 320x256 Frame Rate: 60 Hz S/N: 2338

Figure C-27: Internal Forced Air (Heat Gun) Heating Test Notes 1

IR Camera Settings	Heat Gun Settings	Heating Duration (s)	Heating Box Air Temperature (°F)	Inside Air Temperature (°F)	Notes (Peak Temperatures are approximate)
Format: 16-bit TIFF sequence (IR16) AGC Settings: Pre-AGC FFC: Manual, 16 frames integration, performed immediately before test Video Duration (after heating): 65	Hot	15	Recorded by TC3 peak temperature during heating	Recorded by average TC4 temp during heating and cooling/videoing	Video File: Boson_Capture_13.tiff Peak Temp: 108° F
Format: 16-bit TIFF sequence (IR16) AGC Settings: Pre-AGC FFC: Manual, 16 frames integration, performed immediately before test Video Duration (after heating): 65	Hot	30	Recorded by TC3 peak temperature during heating	Recorded by average TC4 temp during heating and cooling/videoing	Video File: Boson_Capture_14.tiff Peak Temp: 108° F Goal is for TC3 < 80° F and |TC1 - TC2| < 0.5° F
Format: 16-bit TIFF sequence (IR16) AGC Settings: Pre-AGC FFC: Manual, 16 frames integration, performed immediately before test Video Duration (after heating): 65	Hot	15	Recorded by TC3 peak temperature during heating	Recorded by average TC4 temp during heating and cooling/videoing	Video File: Boson_Capture_15.tiff Peak Temp: 116° F
Format: 16-bit TIFF sequence (IR16) AGC Settings: Pre-AGC FFC: Manual, 16 frames integration, performed immediately before test Video Duration (after heating): 65	Hot	30	Recorded by TC3 peak temperature during heating	Recorded by average TC4 temp during heating and cooling/videoing	Video File: Boson_Capture_16.tiff Peak Temp: 134° F
Format: 16-bit TIFF sequence (IR16) AGC Settings: Pre-AGC FFC: Manual, 16 frames integration, performed immediately before test Video Duration (after heating): 120	Hot	60	Recorded by TC3 peak temperature during heating	Recorded by average TC4 temp during heating and cooling/videoing	Video File: Boson_Capture_17.tiff Peak Temp: 167° F
Format: 16-bit TIFF sequence (IR16) AGC Settings: Pre-AGC FFC: Manual, 16 frames integration, performed immediately before test Video Duration (after heating): 240	Hot	60	Recorded by TC3 peak temperature during heating	Recorded by average TC4 temp during heating and cooling/videoing	Video File: Boson_Capture_18.tiff Peak Temp: 160° F
Format: 16-bit TIFF sequence (IR16) AGC Settings: Pre-AGC FFC: Manual, 16 frames integration, performed immediately before test Video Duration (after heating): 240	Hot	120	Recorded by TC3 peak temperature during heating	Recorded by average TC4 temp during heating and cooling/videoing	Video File: Boson_Capture_19.tiff Peak Temp: 200° F Started when TC3 = 86° F
Format: 16-bit TIFF sequence (IR16) AGC Settings: Pre-AGC FFC: Manual, 16 frames integration, performed immediately before test Video Duration (after heating): 65	Hot	15	Recorded by TC3 peak temperature during heating	Recorded by average TC4 temp during heating and cooling/videoing	Video File: Boson_Capture_20.tiff Peak Temp: 113° F Started when TC3 = 82° F after running heat gun in cold mode

Figure C-28: Internal Forced Air (Heat Gun) Heating Test Notes 1 (continued)

Date	Time (approx. time specimen is placed in the heat gun box, to the minute)	Location	Temp Data (Location of Thermocouples)	Test Specimen ID	Test #	IR Camera
6/2/2017	9:00am	Heating: 894/157 Cooling: 894/157	TC1 (K Type): Front, Top Left TC2 (K Type): Back, Top Left TC3 (K Type): Box TC4 (K Type): Room	G11-STD-3	4	FLIR Boson Resolution: 320x256 Frame Rate: 60 Hz S/N: 2338
6/2/2017	9:23am	Heating: 894/157 Cooling: 894/157	TC1 (K Type): Front, Top Left TC2 (K Type): Back, Top Left TC3 (K Type): Box TC4 (K Type): Room	G11-STD-3	5	FLIR Boson Resolution: 320x256 Frame Rate: 60 Hz S/N: 2338
6/2/2017	9:34am	Heating: 894/157 Cooling: 894/157	TC1 (K Type): Front, Top Left TC2 (K Type): Back, Top Left TC3 (K Type): Box TC4 (K Type): Room	G11-STD-3	6	FLIR Boson Resolution: 320x256 Frame Rate: 60 Hz S/N: 2338
6/2/2017	10:02am	Heating: 894/157 Cooling: 894/157	TC1 (K Type): Front, Top Left TC2 (K Type): Back, Top Left TC3 (K Type): Box TC4 (K Type): Room	G11-STD-3	7	FLIR Boson Resolution: 320x256 Frame Rate: 60 Hz S/N: 2338
6/2/2017	10:45am	Heating: 894/157 Cooling: 894/157	TC1 (K Type): Front, Top Left TC2 (K Type): Back, Top Left TC3 (K Type): Box TC4 (K Type): Room	G11-STD-3	8	FLIR Boson Resolution: 320x256 Frame Rate: 60 Hz S/N: 2338
6/2/2017	10:59am	Heating: 894/157 Cooling: 894/157	TC1 (K Type): Front, Top Left TC2 (K Type): Back, Top Left TC3 (K Type): Box TC4 (K Type): Room	G11-STD-2	3	FLIR Boson Resolution: 320x256 Frame Rate: 60 Hz S/N: 2338
6/2/2017	11:20am	Heating: 894/157 Cooling: 894/157	TC1 (K Type): Front, Top Left TC2 (K Type): Back, Top Left TC3 (K Type): Box TC4 (K Type): Room	G11-STD-2	4	FLIR Boson Resolution: 320x256 Frame Rate: 60 Hz S/N: 2338
6/2/2017	11:31am	Heating: 894/157 Cooling: 894/157	TC1 (K Type): Front, Top Left TC2 (K Type): Back, Top Left TC3 (K Type): Box TC4 (K Type): Room	G11-STD-1	2	FLIR Boson Resolution: 320x256 Frame Rate: 60 Hz S/N: 2338
6/2/2017	11:40am	Heating: 894/157 Cooling: 894/157	TC1 (K Type): Front, Top Left TC2 (K Type): Back, Top Left TC3 (K Type): Box TC4 (K Type): Room	G11-STD-4	3	FLIR Boson Resolution: 320x256 Frame Rate: 60 Hz S/N: 2338
6/2/2017	1:40pm	Heating: 894/157 Cooling: 894/157	TC1 (K Type): Front, Top Left TC2 (K Type): Back, Top Left TC3 (K Type): Box TC4 (K Type): Room	FGB-1	1	FLIR Boson Resolution: 320x256 Frame Rate: 60 Hz S/N: 2338
6/2/2017	Continuation of previous test	Heating: 894/157 Cooling: 894/157	TC1 (K Type): Front, Top Left TC2 (K Type): Back, Top Left TC3 (K Type): Box TC4 (K Type): Room	FGB-1	2	FLIR Boson Resolution: 320x256 Frame Rate: 60 Hz S/N: 2338
6/2/2017	Continuation of previous test	Heating: 894/157 Cooling: 894/157	TC1 (K Type): Front, Top Left TC2 (K Type): Back, Top Left TC3 (K Type): Box TC4 (K Type): Room	FGB-1	3	FLIR Boson Resolution: 320x256 Frame Rate: 60 Hz S/N: 2338

Figure C-29: Internal Forced Air (Heat Gun) Heating Test Notes 2

IR Camera Settings	Heat Gun Settings	Heating Duration (s)	Heating Box Air Temperature (°F)	Inside Air Temperature (°F)	Notes (Peak Temperatures are approximate) *Peak Temperature copied from TC data
Format: 16-bit TIFF sequence (IR16) AGC Settings: Pre-AGC FFC: Manual, 16 frames integration, performed immediately before test Video Duration (after heating): 120	Hot	60	Recorded by TC3 peak temperature during heating	Recorded by average TC4 temp during heating and cooling/videoing	Video File: Boson_Capture_21.tiff Peak Temp: 146° F Added aluminum tape to the backside of flat bottom holes, which made a significant difference
Format: 16-bit TIFF sequence (IR16) AGC Settings: Pre-AGC FFC: Manual, 16 frames integration, performed immediately before test Video Duration (after heating): 120	Hot	30	Recorded by TC3 peak temperature during heating	Recorded by average TC4 temp during heating and cooling/videoing	Video File: Boson_Capture_22.tiff Peak Temp: 125° F(?) Thermocouples cut out, peak temperature based on quick look at TC monitor
Format: 16-bit TIFF sequence (IR16) AGC Settings: Pre-AGC FFC: Manual, 16 frames integration, performed immediately before test Video Duration (after heating): 120	Hot	30	Recorded by TC3 peak temperature during heating	Recorded by average TC4 temp during heating and cooling/videoing	Video File: Boson_Capture_23.tiff Peak Temp: 139° F
Format: 16-bit TIFF sequence (IR16) AGC Settings: Pre-AGC FFC: Manual, 16 frames integration, performed immediately before test Video Duration (after heating): 65	Hot	15	Recorded by TC3 peak temperature during heating	Recorded by average TC4 temp during heating and cooling/videoing	Video File: Boson_Capture_25.tiff Peak Temp: (?) Thermocouples cut out, switching to recording on TC Datalogger and then transferring files later
Format: 16-bit TIFF sequence (IR16) AGC Settings: Pre-AGC FFC: Manual, 16 frames integration, performed immediately before test Video Duration (after heating): 65	Hot	15	Recorded by TC3 peak temperature during heating	Recorded by average TC4 temp during heating and cooling/videoing	Video File: Boson_Capture_26.tiff Thermocouple File: 001 Peak Temp: 107° F Maybe should have videoed longer
Format: 16-bit TIFF sequence (IR16) AGC Settings: Pre-AGC FFC: Manual, 16 frames integration, performed immediately before test Video Duration (after heating): 65	Hot	15	Recorded by TC3 peak temperature during heating	Recorded by average TC4 temp during heating and cooling/videoing	Video File: Boson_Capture_27.tiff Thermocouple File: 002 Peak Temp: 111° F Maybe should have videoed longer
Format: 16-bit TIFF sequence (IR16) AGC Settings: Pre-AGC FFC: Manual, 16 frames integration, performed immediately before test Video Duration (after heating): 120	Hot	30	Recorded by TC3 peak temperature during heating	Recorded by average TC4 temp during heating and cooling/videoing	Video File: Boson_Capture_28.tiff Thermocouple File: 003 Peak Temp: 133° F*
Format: 16-bit TIFF sequence (IR16) AGC Settings: Pre-AGC FFC: Manual, 16 frames integration, performed immediately before test Video Duration (after heating): 120	Hot	15	Recorded by TC3 peak temperature during heating	Recorded by average TC4 temp during heating and cooling/videoing	Video File: Boson_Capture_29.tiff Thermocouple File: 004 Peak Temp: 115° F*
Format: 16-bit TIFF sequence (IR16) AGC Settings: Pre-AGC FFC: Manual, 16 frames integration, performed immediately before test Video Duration (after heating): 240	Hot	120	Recorded by TC3 peak temperature during heating	Recorded by average TC4 temp during heating and cooling/videoing	Video File: Boson_Capture_30.tiff Thermocouple File: 005 Peak Temp: 198° F*
Format: 16-bit TIFF sequence (IR16) AGC Settings: Pre-AGC FFC: Manual, 16 frames integration, performed immediately before test Video Duration (after heating): 420	Hot	60	Recorded by TC3 peak temperature during heating	Recorded by average TC4 temp during heating and cooling/videoing	Video File: Boson_Capture_31.tiff Thermocouple File: 006 Peak Temp: 179° F* Kept thermocouple file running for next test
Format: 16-bit TIFF sequence (IR16) AGC Settings: Pre-AGC FFC: Manual, 16 frames integration, performed immediately before test Video Duration (after heating): N/A (special test)	Hot	60	Recorded by TC3 peak temperature during heating	Recorded by average TC4 temp during heating and cooling/videoing	Video File: Boson_Capture_32.tiff Thermocouple File: 006 Peak Temp: 194° F* Waited ~60s after previous test Started video 30s into heating, recorded for 240s Kept thermocouple file running for previous test
Format: 16-bit TIFF sequence (IR16) AGC Settings: Pre-AGC FFC: Manual, 16 frames integration, performed immediately before test Video Duration (after heating): N/A (special test)	Hot	900+	Recorded by TC3 peak temperature during heating	Recorded by average TC4 temp during heating and cooling/videoing	Video File: N/A Thermocouple File: N/A Peak Temp: N/A No video or thermocouple data Goal was to keep the temperature at ~200° F and watch live IR video feed No flaws were visible even after the top surface reached 80° F and the bottom surface reached 130° F+ Flaws became visible after cooling, when the top surface reached ~84° F

Figure C-30: Internal Forced Air (Heat Gun) Heating Test Notes 2 (continued)

C.3 Solar Radiation (Sun/Shade) Heating Test Notes

Date	Time (approx. time specimen is placed on outside table, to the minute)	Location	Temp Data (Location of Thermocouples)	Test Specimen ID	Test #	IR Camera
6/14/2017	2:35pm	Heating: Outside (West) of 894/157 Cooling: 894/157	TC1 (K Type): Front, Top Left TC2 (K Type): Back, Top Left TC3 (K Type): Air	G11-STD-2	1	FLIR Boson Resolution: 320x256 Frame Rate: 60 Hz S/N: 2338
6/14/2017	2:45pm	Heating: Outside (West) of 894/157 Cooling: 894/157	TC1 (K Type): Front, Top Left TC2 (K Type): Back, Top Left TC3 (K Type): Air	G11-STD-2	2	FLIR Boson Resolution: 320x256 Frame Rate: 60 Hz S/N: 2338
6/14/2017	3:12pm	Heating: Outside (West) of 894/157 Cooling: 894/157	TC1 (K Type): Front, Top Left TC2 (K Type): Back, Top Left TC3 (K Type): Air	G11-STD-3	1	FLIR Boson Resolution: 320x256 Frame Rate: 60 Hz S/N: 2338
6/14/2017	3:30pm	Heating: Outside (West) of 894/157 Cooling: 894/157	TC1 (K Type): Front, Top Left TC2 (K Type): Back, Top Left TC3 (K Type): Air	G11-STD-3	2	FLIR Boson Resolution: 320x256 Frame Rate: 60 Hz S/N: 2338
6/14/2017	3:45pm	Heating: Outside (West) of 894/157 Cooling: 894/157	TC1 (K Type): Front, Top Left TC2 (K Type): Back, Top Left TC3 (K Type): Air	G11-STD-4	1	FLIR Boson Resolution: 320x256 Frame Rate: 60 Hz S/N: 2338
6/14/2017	3:56pm	Heating: Outside (West) of 894/157 Cooling: 894/157	TC1 (K Type): Front, Top Left TC2 (K Type): Back, Top Left TC3 (K Type): Air	G11-STD-4	2	FLIR Boson Resolution: 320x256 Frame Rate: 60 Hz S/N: 2338

Figure C-31: Solar Radiation (Sun/Shade) Heating Test Notes 1

IR Camera Settings	Global Normal Solar Irradiance	Heating Duration (s)	Outside Air Temperature	Inside Air Temperature	Notes (Transition Time is the approx. time required to move the part into the shade)
Format: 16-bit TIFF sequence (IR16) AGC Settings: Pre-AGC FFC: Manual, 16 frames integration, performed immediately before test Video Duration (after heating): 30	Recorded by MATLAB PV_Website_Read function every 1 minute File: Solar Irradiance Data 6-14-17.xlsx	30	Recorded by TC3 peak temperature during heating Also recorded by MATLAB PV_Website_Read function every 1 minute	Recorded by TC3 after test	Video File: Boson_Capture_74.tiff Thermocouple File: 051 Transition Time: 9s Part placed on plastic rails to provide an airgap under the part After this test this rails were moved in slightly to prevent them from contacting TC2
Format: 16-bit TIFF sequence (IR16) AGC Settings: Pre-AGC FFC: Manual, 16 frames integration, performed immediately before test Video Duration (after heating): 60	Recorded by MATLAB PV_Website_Read function every 1 minute File: Solar Irradiance Data 6-14-17.xlsx	60	Recorded by TC3 peak temperature during heating Also recorded by MATLAB PV_Website_Read function every 1 minute	Recorded by TC3 after test	Video File: Boson_Capture_75.tiff Thermocouple File: 052 Transition Time: 6s + 6s Started video 6s too early
Format: 16-bit TIFF sequence (IR16) AGC Settings: Pre-AGC FFC: Manual, 16 frames integration, performed immediately before test Video Duration (after heating): 90	Recorded by MATLAB PV_Website_Read function every 1 minute File: Solar Irradiance Data 6-14-17.xlsx	60	Recorded by TC3 peak temperature during heating Also recorded by MATLAB PV_Website_Read function every 1 minute	Recorded by TC3 after test	Video File: Boson_Capture_76.tiff Thermocouple File: 053 Transition Time: 9s |TC1 - TC2| = 0.6° F
Format: 16-bit TIFF sequence (IR16) AGC Settings: Pre-AGC FFC: Manual, 16 frames integration, performed immediately before test Video Duration (after heating): 120	Recorded by MATLAB PV_Website_Read function every 1 minute File: Solar Irradiance Data 6-14-17.xlsx	120	Recorded by TC3 peak temperature during heating Also recorded by MATLAB PV_Website_Read function every 1 minute	Recorded by TC3 after test	Video File: Boson_Capture_77.tiff Thermocouple File: 054 Transition Time: 9s |TC1 - TC2| = 0.9° F
Format: 16-bit TIFF sequence (IR16) AGC Settings: Pre-AGC FFC: Manual, 16 frames integration, performed immediately before test Video Duration (after heating): 150	Recorded by MATLAB PV_Website_Read function every 1 minute File: Solar Irradiance Data 6-14-17.xlsx	120	Recorded by TC3 peak temperature during heating Also recorded by MATLAB PV_Website_Read function every 1 minute	Recorded by TC3 after test	Video File: Boson_Capture_78.tiff Thermocouple File: 055 Transition Time: 9s Didn't observe any flaws on the live IR feed
Format: 16-bit TIFF sequence (IR16) AGC Settings: Pre-AGC FFC: Manual, 16 frames integration, performed immediately before test Video Duration (after heating): 240	Recorded by MATLAB PV_Website_Read function every 1 minute File: Solar Irradiance Data 6-14-17.xlsx	240	Recorded by TC3 peak temperature during heating Also recorded by MATLAB PV_Website_Read function every 1 minute	Recorded by TC3 after test	Video File: Boson_Capture_79.tiff Thermocouple File: 056 Transition Time: 8s

Figure C-32: Solar Radiation (Sun/Shade) Heating Test Notes 1 (continued)

Date	Time (approx. time specimen is placed on outside table, to the minute)	Location	Temp Data (Location of Thermocouples)	Test Specimen ID	Test #	IR Camera
6/15/2017	2:37pm	Heating: Outside (West) of 894/157 Cooling: 894/157	TC1 (K Type): Front, Top Left TC2 (K Type): Back, Top Left TC3 (K Type): Air	G11-STD-4	3	FLIR Boson Resolution: 320x256 Frame Rate: 60 Hz S/N: 2338
6/15/2017	3:02pm	Heating: Outside (West) of 894/157 Cooling: 894/157	TC1 (K Type): Front, Top Left TC2 (K Type): Back, Top Left TC3 (K Type): Air	G11-STD-3	3	FLIR Boson Resolution: 320x256 Frame Rate: 60 Hz S/N: 2338
6/15/2017	3:18pm	Heating: Outside (West) of 894/157 Cooling: 894/157	TC1 (K Type): Front, Top Left TC2 (K Type): Back, Top Left TC3 (K Type): Air	FGB-1	1	FLIR Boson Resolution: 320x256 Frame Rate: 60 Hz S/N: 2338
6/15/2017	3:29pm	Heating: Outside (West) of 894/157 Cooling: 894/157	TC1 (K Type): Front, Top Left TC2 (K Type): Back, Top Left TC3 (K Type): Air	FBG-2	1	FLIR Boson Resolution: 320x256 Frame Rate: 60 Hz S/N: 2338
6/15/2017	3:56pm	Heating: Outside (West) of 894/157 Cooling: 894/157	TC1 (K Type): Front, Top Left TC2 (K Type): Back, Top Left TC3 (K Type): Air	FBG-2	N/A	FLIR Boson Resolution: 320x256 Frame Rate: 60 Hz S/N: 2338
6/15/2017	4:11pm	Heating: Outside (West) of 894/157 Cooling: 894/157	TC1 (K Type): Front, Top Left TC2 (K Type): Back, Top Left TC3 (K Type): Air	FGB-1	2	FLIR Boson Resolution: 320x256 Frame Rate: 60 Hz S/N: 2338

Figure C-33: Solar Radiation (Sun/Shade) Heating Test Notes 2

IR Camera Settings	Global Normal Solar Irradiance	Heating Duration (s)	Outside Air Temperature	Inside Air Temperature	Notes (Transition Time is the approx. time required to move the part into the shade)
Format: 16-bit TIFF sequence (IR16) AGC Settings: Pre-AGC FFC: Manual, 16 frames integration, performed immediately before test Video Duration (after heating): N/A	Recorded by MATLAB PV_Website_Read function every 1 minute File: Solar Irradiance Data 6-15-17.xlsx	600+	Recorded by TC3 peak temperature during heating Also recorded by MATLAB PV_Website_Read function every 1 minute	Recorded by TC3 after test	Video File: Boson_Capture_80.tiff Thermocouple File: 057 Videoed while heating Video crashed/corrupted due to file size Flaws were not visible until later when the part was removed from the sun
Format: 16-bit TIFF sequence (IR16) AGC Settings: Pre-AGC FFC: Manual, 16 frames integration, performed immediately before test Video Duration (after heating): 180	Recorded by MATLAB PV_Website_Read function every 1 minute File: Solar Irradiance Data 6-15-17.xlsx	186	Recorded by TC3 peak temperature during heating Also recorded by MATLAB PV_Website_Read function every 1 minute	Recorded by TC3 after test	Video File: Boson_Capture_81.tiff Thermocouple File: 059 Videoed during heating and cooling There was some shade covering the .450 thick flat bottom hole and TC1, so we shifted the part entirely in the sun ~100s into testing
Format: 16-bit TIFF sequence (IR16) AGC Settings: Pre-AGC FFC: Manual, 16 frames integration, performed immediately before test Video Duration (after heating): 180	Recorded by MATLAB PV_Website_Read function every 1 minute File: Solar Irradiance Data 6-15-17.xlsx	369	Recorded by TC3 peak temperature during heating Also recorded by MATLAB PV_Website_Read function every 1 minute	Recorded by TC3 after test	Video File: Boson_Capture_82.tiff Thermocouple File: 060 Videoed during heating and cooling Video crashed/corrupted due to file size
Format: 16-bit TIFF sequence (IR16) AGC Settings: Pre-AGC FFC: Manual, 16 frames integration, performed immediately before test Video Duration (after heating): 240	Recorded by MATLAB PV_Website_Read function every 1 minute File: Solar Irradiance Data 6-15-17.xlsx	420	Recorded by TC3 peak temperature during heating Also recorded by MATLAB PV_Website_Read function every 1 minute	Recorded by TC3 after test	Video File: Boson_Capture_83.tiff Thermocouple File: 061
Format: 16-bit TIFF sequence (IR16) AGC Settings: Pre-AGC FFC: Manual, 16 frames integration, performed immediately before test Video Duration (after heating): N/A	Recorded by MATLAB PV_Website_Read function every 1 minute File: Solar Irradiance Data 6-15-17.xlsx	N/A	Recorded by TC3 peak temperature during heating Also recorded by MATLAB PV_Website_Read function every 1 minute	Recorded by TC3 after test	Image File: Boson_Capture_3.tiff Thermocouple File: N/A Performed an image capture several minutes after previous test
Format: 16-bit TIFF sequence (IR16) AGC Settings: Pre-AGC FFC: Manual, 16 frames integration, performed immediately before test Video Duration (after heating): 180	Recorded by MATLAB PV_Website_Read function every 1 minute File: Solar Irradiance Data 6-15-17.xlsx	120	Recorded by TC3 peak temperature during heating Also recorded by MATLAB PV_Website_Read function every 1 minute	Recorded by TC3 after test	Video File: Boson_Capture_84.tiff Thermocouple File: 062

Figure C-34: Solar Radiation (Sun/Shade) Heating Test Notes 2 (continued)

Date	Time (approx. time specimen is placed on outside table, to the minute)	Location	Temp Data (Location of Thermocouples)	Test Specimen ID	Test #	IR Camera
6/16/2017	2:08pm	Heating: Outside (West) of 894/157 Cooling: 894/157	TC1 (K Type): Front, Top Left TC2 (K Type): Back, Top Left TC3 (K Type): Air	Dry Spots	1	FLIR Boson Resolution: 320x256 Frame Rate: 60 Hz S/N: 2338
6/16/2017	2:19pm	Heating: Outside (West) of 894/157 Cooling: 894/157	TC1 (K Type): Front, Top Left TC2 (K Type): Back, Top Left TC3 (K Type): Air	Dry Spots	2	FLIR Boson Resolution: 320x256 Frame Rate: 60 Hz S/N: 2338
6/16/2017	2:36pm	Heating: Outside (West) of 894/157 Cooling: 894/157	TC1 (K Type): Front, Top Left TC2 (K Type): Back, Top Left TC3 (K Type): Air	WIND-1-029	1	FLIR Boson Resolution: 320x256 Frame Rate: 60 Hz S/N: 2338
6/16/2017	2:54pm	Heating: Outside (West) of 894/157 Cooling: 894/157	TC1 (K Type): Front, Top Left TC2 (K Type): Back, Top Left TC3 (K Type): Air	WIND-1-029	2	FLIR Boson Resolution: 320x256 Frame Rate: 60 Hz S/N: 2338
6/16/2017	3:05pm	Heating: Outside (West) of 894/157 Cooling: 894/157	TC1 (K Type): Front, Top Left TC2 (K Type): Back, Top Left TC3 (K Type): Air	WIND-2-044-SPAR-085	1	FLIR Boson Resolution: 320x256 Frame Rate: 60 Hz S/N: 2338
6/16/2017	3:13pm	Heating: Outside (West) of 894/157 Cooling: 894/157	TC1 (K Type): Front, Top Left TC2 (K Type): Back, Top Left TC3 (K Type): Air	WIND-3-110-SPAR-140	1	FLIR Boson Resolution: 320x256 Frame Rate: 60 Hz S/N: 2338
6/16/2017	3:37pm	Heating: Outside (West) of 894/157 Cooling: 894/157	TC1 (K Type): Front, Top Left TC2 (K Type): Back, Top Left TC3 (K Type): Air	WIND-3-110-SPAR-140	2	FLIR Boson Resolution: 320x256 Frame Rate: 60 Hz S/N: 2338
6/16/2017	3:45pm	Heating: Outside (West) of 894/157 Cooling: 894/157	TC1 (K Type): Front, Top Left TC2 (K Type): Back, Top Left TC3 (K Type): Air	WIND-4-161	1	FLIR Boson Resolution: 320x256 Frame Rate: 60 Hz S/N: 2338

Figure C-35: Solar Radiation (Sun/Shade) Heating Test Notes 3

IR Camera Settings	Global Normal Solar Irradiance	Heating Duration (s)	Outside Air Temperature	Inside Air Temperature	Notes (Transition Time is the approx. time required to move the part into the shade)
Format: 16-bit TIFF sequence (IR16) AGC Settings: Pre-AGC FFC: Manual, 16 frames integration, performed immediately before test Video Duration (after heating): 180	Recorded by MATLAB PV_Website_Read function every 1 minute File: Solar Irradiance Data 6-16-17.xlsx	120	Recorded by TC3 peak temperature during heating Also recorded by MATLAB PV_Website_Read function every 1 minute	Recorded by TC3 after test	Video File: Boson_Capture_85.tiff Thermocouple File: 064
Format: 16-bit TIFF sequence (IR16) AGC Settings: Pre-AGC FFC: Manual, 16 frames integration, performed immediately before test Video Duration (after heating): 180	Recorded by MATLAB PV_Website_Read function every 1 minute File: Solar Irradiance Data 6-16-17.xlsx	180	Recorded by TC3 peak temperature during heating Also recorded by MATLAB PV_Website_Read function every 1 minute	Recorded by TC3 after test	Video File: Boson_Capture_86.tiff Thermocouple File: 065
Format: 16-bit TIFF sequence (IR16) AGC Settings: Pre-AGC FFC: Manual, 16 frames integration, performed immediately before test Video Duration (after heating): 180	Recorded by MATLAB PV_Website_Read function every 1 minute File: Solar Irradiance Data 6-16-17.xlsx	120	Recorded by TC3 peak temperature during heating Also recorded by MATLAB PV_Website_Read function every 1 minute	Recorded by TC3 after test	Video File: Boson_Capture_87.tiff Thermocouple File: 066 Shade from tripod affected part of image
Format: 16-bit TIFF sequence (IR16) AGC Settings: Pre-AGC FFC: Manual, 16 frames integration, performed immediately before test Video Duration (after heating): 180	Recorded by MATLAB PV_Website_Read function every 1 minute File: Solar Irradiance Data 6-16-17.xlsx	180	Recorded by TC3 peak temperature during heating Also recorded by MATLAB PV_Website_Read function every 1 minute	Recorded by TC3 after test	Video File: Boson_Capture_88.tiff Thermocouple File: 067
Format: 16-bit TIFF sequence (IR16) AGC Settings: Pre-AGC FFC: Manual, 16 frames integration, performed immediately before test Video Duration (after heating): 180	Recorded by MATLAB PV_Website_Read function every 1 minute File: Solar Irradiance Data 6-16-17.xlsx	120	Recorded by TC3 peak temperature during heating Also recorded by MATLAB PV_Website_Read function every 1 minute	Recorded by TC3 after test	Video File: Boson_Capture_89.tiff Thermocouple File: 068
Format: 16-bit TIFF sequence (IR16) AGC Settings: Pre-AGC FFC: Manual, 16 frames integration, performed immediately before test Video Duration (after heating): 180	Recorded by MATLAB PV_Website_Read function every 1 minute File: Solar Irradiance Data 6-16-17.xlsx	120	Recorded by TC3 peak temperature during heating Also recorded by MATLAB PV_Website_Read function every 1 minute	Recorded by TC3 after test	Video File: Boson_Capture_90.tiff Thermocouple File: 069 Some reflection issues
Format: 16-bit TIFF sequence (IR16) AGC Settings: Pre-AGC FFC: Manual, 16 frames integration, performed immediately before test Video Duration (after heating): 180	Recorded by MATLAB PV_Website_Read function every 1 minute File: Solar Irradiance Data 6-16-17.xlsx	120	Recorded by TC3 peak temperature during heating Also recorded by MATLAB PV_Website_Read function every 1 minute	Recorded by TC3 after test	Video File: Boson_Capture_91.tiff Thermocouple File: 070
Format: 16-bit TIFF sequence (IR16) AGC Settings: Pre-AGC FFC: Manual, 16 frames integration, performed immediately before test Video Duration (after heating): 180	Recorded by MATLAB PV_Website_Read function every 1 minute File: Solar Irradiance Data 6-16-17.xlsx	180	Recorded by TC3 peak temperature during heating Also recorded by MATLAB PV_Website_Read function every 1 minute	Recorded by TC3 after test	Video File: Boson_Capture_92.tiff Thermocouple File: 071

Figure C-36: Solar Radiation (Sun/Shade) Heating Test Notes 3 (continued)

Date	Time (approx. time specimen is placed on outside table, to the minute)	Location	Temp Data (Location of Thermocouples)	Test Specimen ID	Test #	IR Camera
6/16/2017	3:57pm	Heating: Outside (West) of 894/157 Cooling: 894/157	TC1 (K Type): Front, Top Left TC2 (K Type): Back, Top Left TC3 (K Type): Air	REF-STD-1-050-TPI-1 (top half)	1	FLIR Boson Resolution: 320x256 Frame Rate: 60 Hz S/N: 2338
6/16/2017	4:05pm	Heating: Outside (West) of 894/157 Cooling: 894/157	TC1 (K Type): Front, Top Left TC2 (K Type): Back, Top Left TC3 (K Type): Air	REF-STD-1-050-TPI-1 (bottom half)	2	FLIR Boson Resolution: 320x256 Frame Rate: 60 Hz S/N: 2338
6/19/2017	1:14pm	Heating: Outside (West) of 894/157 Cooling: 894/157	TC1 (K Type): Front, Top Left TC2 (K Type): Back, Top Left TC3 (K Type): Air	GLF-S06-C4T2	1	FLIR Boson Resolution: 320x256 Frame Rate: 60 Hz S/N: 2338
6/19/2017	1:37pm	Heating: Outside (West) of 894/157 Cooling: 894/157	TC1 (K Type): Front, Top Left TC2 (K Type): Back, Top Left TC3 (K Type): Air	GLF-S06-C4T2	2	FLIR Boson Resolution: 320x256 Frame Rate: 60 Hz S/N: 2338
6/19/2017	1:46pm	Heating: Outside (West) of 894/157 Cooling: 894/157	TC1 (K Type): Front, Top Left TC2 (K Type): Back, Top Left TC3 (K Type): Air	GLF-S05-C6T2	1	FLIR Boson Resolution: 320x256 Frame Rate: 60 Hz S/N: 2338
6/19/2017	1:54pm	Heating: Outside (West) of 894/157 Cooling: 894/157	TC1 (K Type): Front, Top Left TC2 (K Type): Back, Top Left TC3 (K Type): Air	GLF-S04-C4T2	1	FLIR Boson Resolution: 320x256 Frame Rate: 60 Hz S/N: 2338
6/19/2017	2:06pm	Heating: Outside (West) of 894/157 Cooling: 894/157	TC1 (K Type): Front, Top Left TC2 (K Type): Back, Top Left TC3 (K Type): Air	GLF-S05-C4T2-P5-02	1	FLIR Boson Resolution: 320x256 Frame Rate: 60 Hz S/N: 2338
6/19/2017	2:14pm	Heating: Outside (West) of 894/157 Cooling: 894/157	TC1 (K Type): Front, Top Left TC2 (K Type): Back, Top Left TC3 (K Type): Air	GLF-S05-C4T2	1	FLIR Boson Resolution: 320x256 Frame Rate: 60 Hz S/N: 2338

Figure C-37: Solar Radiation (Sun/Shade) Heating Test Notes 4

IR Camera Settings	Global Normal Solar Irradiance	Heating Duration (s)	Outside Air Temperature	Inside Air Temperature	Notes (Transition Time is the approx. time required to move the part into the shade)
Format: 16-bit TIFF sequence (IR16) AGC Settings: Pre-AGC FFC: Manual, 16 frames integration, performed immediately before test Video Duration (after heating): 120	Recorded by MATLAB PV_Website_Read function every 1 minute File: Solar Irradiance Data 6-16-17.xlsx	60	Recorded by TC3 peak temperature during heating Also recorded by MATLAB PV_Website_Read function every 1 minute	Recorded by TC3 after test	Video File: Boson_Capture_93.tiff Thermocouple File: 072
Format: 16-bit TIFF sequence (IR16) AGC Settings: Pre-AGC FFC: Manual, 16 frames integration, performed immediately before test Video Duration (after heating): 120	Recorded by MATLAB PV_Website_Read function every 1 minute File: Solar Irradiance Data 6-16-17.xlsx	60	Recorded by TC3 peak temperature during heating Also recorded by MATLAB PV_Website_Read function every 1 minute	Recorded by TC3 after test	Video File: Boson_Capture_94.tiff Thermocouple File: 073
Format: 8-bit .avi video (UVC) AGC Settings: Pre-AGC FFC: Manual, 16 frames integration, performed immediately before test Video Duration (after heating): 60	Recorded by MATLAB PV_Website_Read function every 1 minute File: Solar Irradiance Data 6-19-17.xlsx	60	Recorded by TC3 peak temperature during heating Also recorded by MATLAB PV_Website_Read function every 1 minute	Recorded by TC3 after test	Video File: Boson_Capture_8.avi Thermocouple File: 075 Accidientally used UVC output Added a sheet metal ramp to make it easier to roll cart inside
Format: 16-bit TIFF sequence (IR16) AGC Settings: Pre-AGC FFC: Manual, 16 frames integration, performed immediately before test Video Duration (after heating): 120	Recorded by MATLAB PV_Website_Read function every 1 minute File: Solar Irradiance Data 6-19-17.xlsx	60	Recorded by TC3 peak temperature during heating Also recorded by MATLAB PV_Website_Read function every 1 minute	Recorded by TC3 after test	Video File: Boson_Capture_95.tiff Thermocouple File: 076 Started using a cardboard shade
Format: 16-bit TIFF sequence (IR16) AGC Settings: Pre-AGC FFC: Manual, 16 frames integration, performed immediately before test Video Duration (after heating): 120	Recorded by MATLAB PV_Website_Read function every 1 minute File: Solar Irradiance Data 6-19-17.xlsx	60	Recorded by TC3 peak temperature during heating Also recorded by MATLAB PV_Website_Read function every 1 minute	Recorded by TC3 after test	Video File: Boson_Capture_96.tiff Thermocouple File: 077 Temporarily lost shade a couple times during cooling
Format: 16-bit TIFF sequence (IR16) AGC Settings: Pre-AGC FFC: Manual, 16 frames integration, performed immediately before test Video Duration (after heating): 120	Recorded by MATLAB PV_Website_Read function every 1 minute File: Solar Irradiance Data 6-19-17.xlsx	60	Recorded by TC3 peak temperature during heating Also recorded by MATLAB PV_Website_Read function every 1 minute	Recorded by TC3 after test	Video File: Boson_Capture_97.tiff Thermocouple File: 078
Format: 16-bit TIFF sequence (IR16) AGC Settings: Pre-AGC FFC: Manual, 16 frames integration, performed immediately before test Video Duration (after heating): 120	Recorded by MATLAB PV_Website_Read function every 1 minute File: Solar Irradiance Data 6-19-17.xlsx	60	Recorded by TC3 peak temperature during heating Also recorded by MATLAB PV_Website_Read function every 1 minute	Recorded by TC3 after test	Video File: Boson_Capture_98.tiff Thermocouple File: 079
Format: 16-bit TIFF sequence (IR16) AGC Settings: Pre-AGC FFC: Manual, 16 frames integration, performed immediately before test Video Duration (after heating): 120	Recorded by MATLAB PV_Website_Read function every 1 minute File: Solar Irradiance Data 6-19-17.xlsx	60	Recorded by TC3 peak temperature during heating Also recorded by MATLAB PV_Website_Read function every 1 minute	Recorded by TC3 after test	Video File: Boson_Capture_99.tiff Thermocouple File: 080

Figure C-38: Solar Radiation (Sun/Shade) Heating Test Notes 4 (continued)

APPENDIX D. SOLAR IRRADIANCE TEST DATA

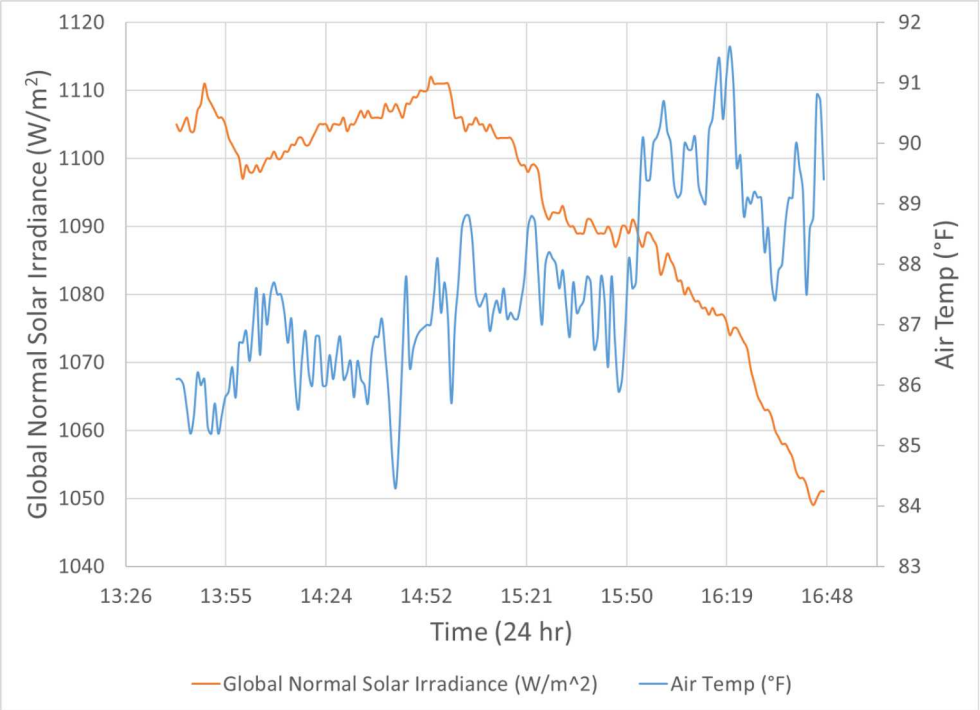

Figure D-39: Solar Irradiance and Air Temperature Data vs. Time Plot for September 14, 2017 Solar Radiation Benchtop Testing

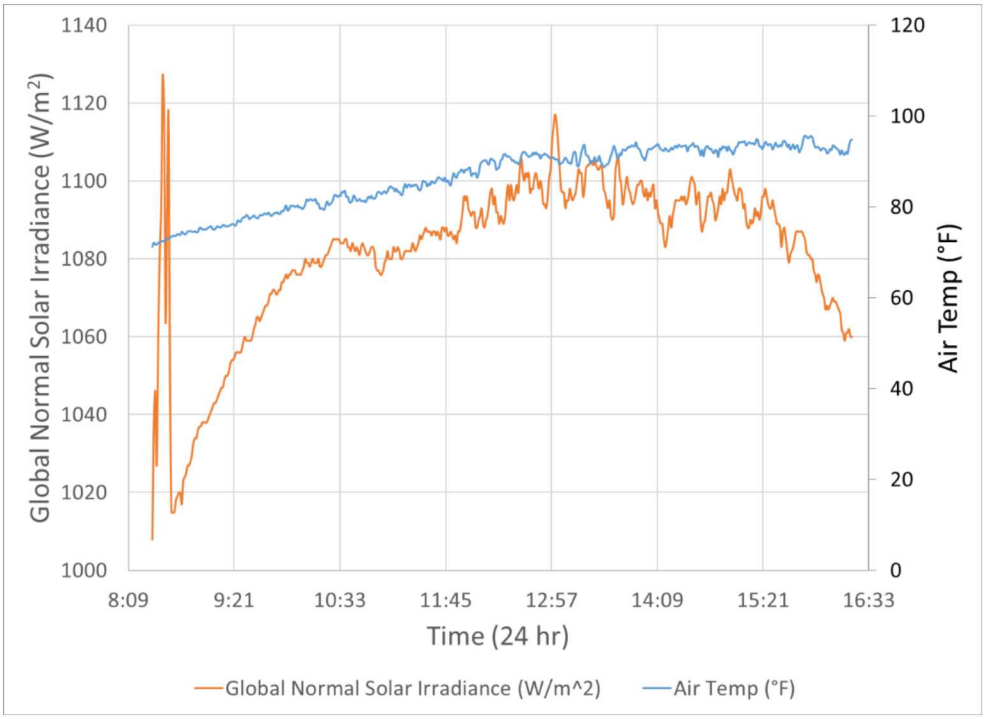

Figure D-40: Solar Irradiance and Air Temperature Data vs. Time Plot for September 15, 2017 Solar Radiation Benchtop Testing

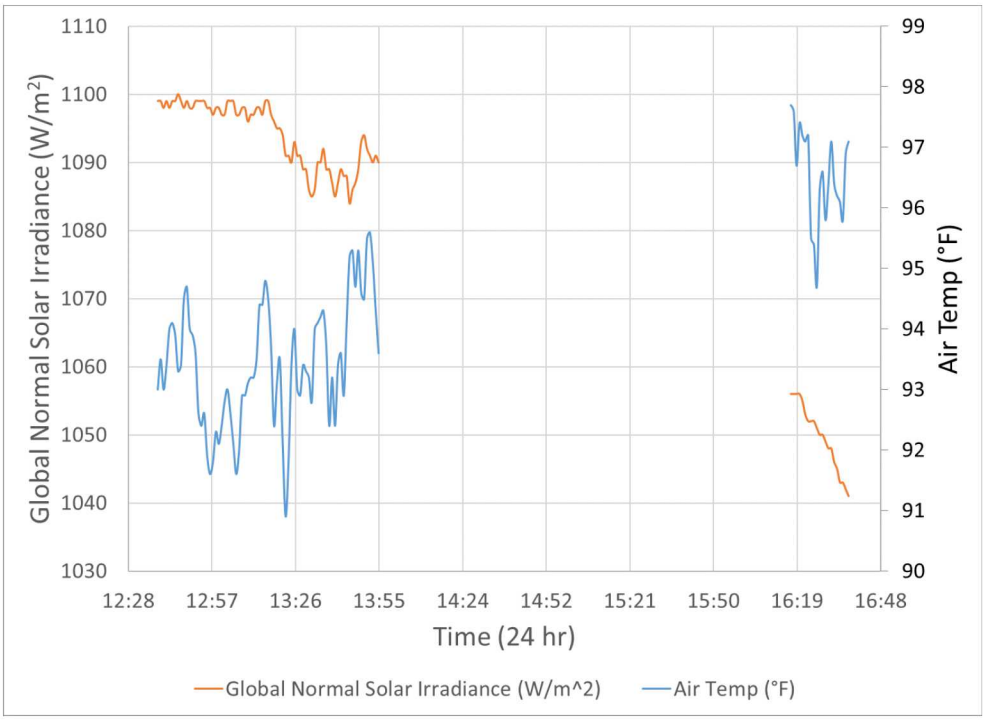

Figure D-41: Solar Irradiance and Air Temperature Data vs. Time Plot for September 16, 2017 Solar Radiation Benchtop Testing

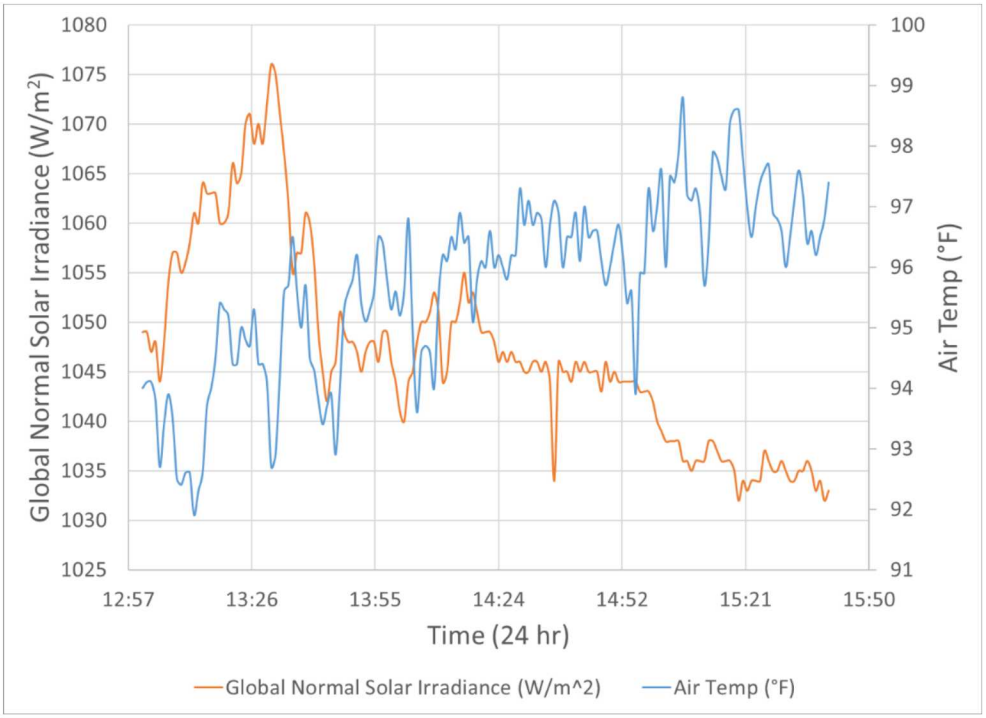

Figure D-42: Solar Irradiance and Air Temperature Data vs. Time Plot for September 19, 2017 Solar Radiation Benchtop Testing

THIS PAGE INTENTIONALLY LEFT BLANK

Distribution List

Vineesh Agrawal
Clipper Windpower, LLC
Carpinteria, CA

Jim Ahlgrimm
U.S. Dept of Energy
Washington, D.C.

Tasdiq Ahmed
TWI
Ferndale, MI

Kevin Alewine
Shermco Industries Inc.
Irving, CA

Daryoush Allaei
SheerWind
Chaska, MN

Matt Allen
University of Wisconsin - Madison
Madison, WI

Nick Althoff
Pointis Engineering
LaCrosse, WI

Shreyas Ananthan
U.S. Dept of Energy
Washington, DC

Jan Vig Andersen
Force Technology
Aalborg, Denmark

Clemens Asmussen
Repower Systems SE
Osterrönfeld, SH Germany

Greg Atchley
General Dynamics Satcom Technologies
Richardson, TX

Mohammad Attia
GE Global Research
Niskayuna, NY

Jared Baker
University of Wyoming
Laramie, WY

Jonathan Baker
Frontier Wind
Rocklin, CA

Pramod Bangalore
Chalmers University of Technology
SE 412 96 Gothenburg, Sweden

Dan Barnard
Iowa State University
Ames, IA

Dev Barpanda
The Dow Chemical Company
Midland, MI

Petr Bartusek
TGM Wind Services
Abilene, TX

Natalie Barrett
Purdue Center for Systems Integrity
Lafayette, IN

Rashi Bates
Shell WindEnergy Inc.
Houston, TX

Christina Beller
Technical University of Denmark
Roskilde, Denmark

Federico Belloni
Technical Univ of Denmark
Roskilde, Denmark

Matt Benoist
ITW Polymer Technologies
Montgomeryville, PA

Chad Benton
Mesalands Community College
Tucumcari, NM

William Berger
Duke Energy
Charlotte, NC

Rob Bergman
GE Energy
Schenectady, NY

Phil Berling
MTS Systems Corporation
Eden Prairie, MN

Derek Berry
NREL/NWTC
Golden, CO

Jay Bhatia
BASF Corporation
Florham Park, NJ

Gunjit Bir
Clipper Windpower
Carpinteria, CA

Keith Blackwell
Milliken & Company
Spartanburg, SC

Chris Bley
Rope Partner
Santa Cruz, CA

Chris Bley
InspecTools
Santa Cruz, CA

Eric Book
Shell WindEnergy Inc.
Houston, TX

John Borgmann
Ocean Power Technologies
Pennington, NJ

Maaik Borst
Knowledge Centre Wind Turbine
Wieringerwerf, The Netherlands

Theo Botha
Blade Dynamics
New Orlenas, LA

Carlo Bottasso
Politecnico di Milano
Milano, Italy

Francis Boudreault-Leclerc
Olympus NDT
Montreal, Canada

Cyril Boussion
Techical Univ Delft
Delft, The Netherlands

Tony Brandon
Milliken and Company
Spartanburg, SC

Wesley Bratton
Vista Engineering Technologies
Richland, WA

Ralph Brillhart
ATA Engineering
San Diego, CA

Ethan Brown
TPI Composites
Warren, MI

Bruce Burton
Huntsman Corporation
The Woodlands, TX

Gregor Cadman
Google Inc.
San Carlos, CA

Doug Cairns
Montana State University
Bozeman, MT

Scott Campbell
Milliken and Company
Dayton, OH

Nannan Cao
Frontier Wind
Rocklin, CA

Mark Capellaro
University Stuttgart
Stuttgart, Germany

Pepe Carnevale
Blade Dynamics
HampshireUK

Mike Carr
Office of the Assistant Secretary - EERE
Washington, DC

Christopher Caruso
GE Energy
Greenville, SC

Luciano Castillo
Texas Tech University
Lubbock, TX

Luis Cerezo
Electrical Power Research Institute
Charlotte, NC

Karun Chakravarthy
Dassault Systemes
Waltham, MA

Santhosh Chandrabalan
3M Company
Maplewood, MN

David Chang
Raycon
San Jose, CA

Xiao Chen
University of Houston NWEC
Houston, TX

Phillip Chiu
UCLA
Los Angeles, CA

John Christiansen
MTS Systems Corporation
Eden Prairie, MN

Thomas Christiansen
Strategic Power Systems, Inc.
Charlotte, NC

David Clark
Bachmann Electronic Corp.
Grayslake, IL

David Coffey
AWS Truepower
Chicago, IL

Jonathan Colby
Verdant Power
New York, NY

Bill Cole
University of Houston NWEC
Houston, TX

Taylor Coleman
Poseidon Systems, LLC
Rochester, NY

Craig Collier
Collier Research Corporation
Newport News, VA

Daniel Contreras
Robotic Technology Solutions
Alamogordo, NM

Matthew Conwell
Invenergy
Chicago, IL

Dean Corren
Verdant Power
New York, NY

Stéphan Couture
Olympus
Quebec, CANADA

Joshua Crayton
Rope Partner
Santa Cruz, CA

Matt Crompton
Dantec Dynamics
Del Rey Oaks, CA

Marty Crotty
Up Wind Solutions
San Diego, CA

Subbareddy Daggumati
GE Global Research,
Bangalore, Karnataka -India

Rick Damiani
RRD Engineering
Arvada, CO

Rory Davis
ATA Engineering
San Diego, CA

Salvatore Della Villa
Strategic Power Systems, Inc.
Charlotte, NC

Tom DeMint
Owens Corning
Seattle, WA

Mike Derby
U.S. Dept of Energy
Washington, DC

Mike Desmond
National Renewable Energy Laboratory
Golden, CO

Sharon Donohoe
Clipper Windpower
Carpinteria, CA

PJ Dougherty
SMI Inc.
Washington, DC

Timothy Downey
Department of Transportation
Washington, DC

Vuk Dragovic
Wing d.o.o.
Belgrade, Serbia

Rodrigo Duarte
SSE Renewables Portugal
Lisbon, Portugal

Marc Dubios
iPhoton Solutions LLC
Ft. Worth, TX

Paul Dvorak
WTWH Media LLC
Cleveland, OH

Katherine Dykes
National Renewable Energy Laboratory
Golden, CO

Chris Edwards
Fulcrum Composites Inc.
Midland, MI

Kate Edwards
Ocean Power Technologies
Pennington, NJ

Dave Eisenberg
Siemens Energy Inc.
Boulder, CO

Andrew Elliott
MSC Software
Mesa, AZ

Danny Ellis
SkySpecs
Ann Arbor, MI

Kevin Elsken
Bayer Material Science
Pittsburgh, PA

Enno Eyb
Senvion SE
Osterronfeld, Germany

Tim Fallon
TPI Composites
Warren, RI

Bob Farris
Momentive Specialty Chemicals
Stafford, TX

Stefan Faulstich
Fraunhofer IWES
Bremerhaven, Germany

Brian Feeny
Michigan State University
East Lansing, MI

Albert Fisas-Camanes
ALSTOM Power Inc.
Richmond, VA

Cash Fitzpatrick
U.S. Dept of Energy
Washington, DC

Alex Fleming
Ecomerit
Santa Barbara, CA

Vince Foody
Milliken and Company
Spartanburg, SC

Matthew Frank
Iowa State University
Ames, IA

Stefan Frazen
Aachen University
Aachen, Germany

Xu Fu
GE Global Research
Shanghai, China

Bernie Fu
BASF
Florham Park, NJ

Bill Fuller
Exxon Mobil Corp.
Irving, TX

Robert Gallaher
NextEra Energy Resources
Juno Beach, FL

Enrique Garcia
Gamesa Wind Power
Sarriguren, Spain

Benjamin Gaskill
Shell WindEnergy Inc.
Houston, TX

Anis Gawandi
Siemens Wind Power
Boulder, CO

Lillie Ghobrial
Dept of Energy
Washington, DC

Steve Gibbs
Clipper Windpower
Cedar Rapids, IA

Peter Gilchrist
Vestas
Portland, OR

Adrian Gill
Vestas
Boulder, CO

Ben Givens
AEP
Trent, TX

Chad Glinsky
Romax Technology Inc.
Nottingham, United Kingdom

Alon Goldis
LM Windpower
Grad Forks, ND

Clint Goolsbay
Hexcel Composites
Arlington, TX

Mitch Graff
Blade Dynamics
New Orleans, LA

Carol Graham
Creative Foam Corporation
Fenton, MI

Francesco Grasso
ECN
Petten, Netherlands

Anne Marie Graves
GL Garrad Hassan
Houston, TX

Karl Gregory
Vestas
Boulder, CO

Martin Greiff
Exova
Linkoping, Sweden

Ronald Grife
EDPR
Houston, TX

Ernesto Grossmann
CU Boulder
Boulder, CO

Joel Gruhn
NEPTCO Inc.
Pawtucket, RI

Qiang Guo
Iowa State University
Ames, IA

Todd Haber
Micron Optics Inc.
Atlanta, GA

Jason Habermehl
Olympus NDT
Montreal, Canada

Berthold Hahn
Fraunhofer IWES
Kassel, Germany

Mohsan Haider
Clipper Windpower LLC
Carpinteria, CA

Kurt Hallamasek
Google, Inc.
San Carlos, CA

Jeffrey Hammit
NextEra Energy Resources
Boca Raton, FL

Scott Hearon
ITW WindGroup
Neptune, NJ

Thies Hecker
Senvion
Osterronfeld, Germany

Jeremey Heinks
LM Wind Power
Grand Forks, ND

Troy Hetherington
Stran Technologies
Naugatuck, CT

Mark Higgins
U.S. Department of Energy
Washington, DC

Satyanarayana Himakuntla
Enercon India Ltd.,
Daman – India

Karasawa Hirokazu
Toshiba Power System Inspection Services
Yokohama, Japan

Juan Hodelin
Physical Optics Corp.
Torrance, CA

Bianka Hoffman
Siemens
Aalborg, Denmark

Wataru Horimoto
Kurabo Industries
Osaka, Japan

D.M. Hoyt
NSE Composites
Seattle, WA

Irfan Huda
BASF
Tarrytown, NY

Cliff Hudson
Emerging Technology Ventures Inc.
Alamogordo, NM

Gary Huff
ER Systems
Rockford, MN

Scott Hughes
National Renewable Energy Laboratory
Golden, CO

Byungsun Hwang
Korea Inst. Of Materials Science
Changwon, Korea

Eric Jacobsen
GE Global Research
Greenville, SC

Torben Jacobsen
LM Windpower
Lunderskov, Denmark

Salim Jaffer
General Electric - Bently Nevada
Phoenix, AZ

Anant Jain
Texas Tech University
Lubbock, TX

Johnny Jakobsen
Aalborg Univ
Aalborg, Denmark

Chuck Jenkins
General Electric - Bently Nevada
Hamilton, OH

John Jeno
LM Windpower
Grand Forks, ND

Find Mølholt Jensen
Bladena Aps
Ringsted, Denmark

Erik Jensen
Blaest
Aalborg, Denmark

Jae-ho Jeong
Samsung Heavy Indus/Wind Turbine Div.
Geoje-si, Korea

Joyce Jin
Worldwide Aeros Corp.
Montebello, CA

Kevin Joesel
Fusion UV Systems, Inc.
Gaithersburg, MD

Wade Johanns
Iowa State University
Ames, IA

Justin Johnson
EDP Renewables North America LLC
Houston, TX

Perry Johnson
UCLA, Wirz Research Group
Los Angeles, CA

Desiree Johnson
Iberdrola Renewables
Portland, OR

Nick Johnson
NREL
Golden, CO

James Jones
Composites Consulting Group
DeSoto, TX

Yellavenkatasunil Jonnalagadda
Siemens energy, Inc. - Wind Power
Boulder, CO

Wandan Joo
Doosan
Daejeon, Republic of Korea

Peter Joosse
CTC Engineering
Hengelo, Netherlands

Rob Kamisky
WINDprove, Inc.
Davis, CA

Gary Kanaby
Molded Fiber Glass Companies
Sherman, CA

Aaron Kaplan
Luna Technologies
Blacksburg, VA

Hirokazu Karasawa
Toshiba Power System Inspection Services
Tokyo, Japan

Donald Kasperski
GE Energy
Greenville, SV

Stefan Kern
GE Global Research
Garcging n. Munich

Ole Kils
Clipper Windpower
Carpinteria, CA

Seong-Hun Kim
Samsung Heavy Industries/Wind Turbine
Geoje-si, Gyeongsangnam-do, South Korea

Mac Klingler
M.G. Klingler, Ltd.
Galena, IL

Dave Klozik
Comau Inc.
Southfield, MI

Justin Klure
Northwest Energy Innovations
Portland, OR

Sandie Klute
Luna Innovations
Blacksburg, VA

Keith Konieczka
Owens Corning
Wauseon, OH

Steven Kopf
Northwest Energy Innovations
Portland, OR

Brett Kreiser
Iberdola Renewables
Tiskilwa, IL

Sriram Krishnamurthy
GE Global Research,
Bangalore, India

David Kroeker
Texas Tech University
Lubbock, TX

Annie Kyriakides
GE Energy
Schenectady, NY

Richard LaFountain
Molded Fiber Glass Companies
Gainesville, TX

Carl LaFrance
Molded Fiber Glass Companies
Ashtabula, OH

Brian LaMay
Infigen Energy
Dallas, TX

Gary Lamberton
GE Oil & Gas
Skaneateles, NY

Kevin Lambrych
Ashland Performance Materials
Dublin, OH

Brenda Langley
NW Nat'l Marine Renewable Energy Center
Corvallis, OR

Francesco Lanza di Scalea
UC San Diego
LaJolla, CA

Scott Larwood
University of the Pacific
Stockton, CA

Bernard Laskowski
Analatom Inc
Sunnyvale, CA

Bob Lasser
Imperium Inc.
Beltsville, MD

John Leahey
Vestas
Boulder, CO

Jihyun Lee
Samwon Millennia
Seongnam, South Korea

Ken Lee
Wetzel Engineering, Inc.
Lawrence, KS

Sanghonn Lee
Doosan
Daejeon, Republic of Korea

Yeon-Seung Lee
Korea Adv Inst. of Science & Technology
Yuseong-gu, Daejeon, Republic of Korea

Hak Gu Lee
Wind Turbine Tech Research Center
Daejeon, Republic of Korea

Paul Legac
J. P. Morgan
Chicago, IL

Thierry Lemaigre
Dow Corning Corporation
Seneffe, Belgium

Nick Lennings
Knowledge Center WMC
Wieringerwerf, The Netherlands

Martin Leong
Siemens
Aalborg, Denmark

Obdulia Ley
Mistras
Princeton Junction, NJ

Jianfu Li
Chinese Wind Energy Association
Beijing, China

Bob Liekar
Fluitec Wind
Jersey City, NJ

Wendy Lin
GE Global Research
Niskayuna, NY

Lindberg Lindberg
Electric Power Research Institute
Charlotte, NC

Jack Little
Evisive Inc
Baton Rouge, LA

Marcus Lihua Liu
Owens Corning
Shanghai, China

K.H. Lo
University of Houston NWEC
Houston, TX

Kevin Long
JRL Ventures
Cape Coral , FL

Guillermo Lozano
E.On
Malmo, Sweden

Peter Lucon
Resodyn Corporation
Butte, MT

Matthew Lueker
University of Minnesota
Minneapolis, MN

Doug Lutz
GE Sensing &Inspection Technologies
Lewistown, PA

Liangkai Ma
The Dow Chemical Company
Midland, MI

Del Mackey
System Technology Solutions
Alamogordo, NM

Helge Madsen
Risøe National Laboratory
Roskilde, Denmark

Sam Maggio
ICM
Ithaca, NY

Andrew Magstadt
University of Wyoming
Laramie, WY

Mark Main
BASF Corporation
Canton, MI

Ninochska Maldonado
eDF-RE
Palm Beach Gardens, FL

Matt Malkin
DNV
Seattle , WA

John Mandell
Montana State University
Bozeman, MT

Imanol San Martin
Enel Green Power
Andover, MA

James Martin
Blade Dynamics
New Orleans, LA

Alex Martinez
System Technology Solutions
Alamogordo, NM

Christophe Mattei
Exova
Jonkoping, Sweden

Timothy McCarthy
Materia Inc.
Pasadena, CA

Megan McCluer
Dept of Energy
Washington, DC

Bill McCroskey
Intl Health Monitoring Systems
Dayton, OH

Jarlath McEntee
Ocean Power Renewable Company
Portland, ME

Ken McGraw
Wind Energy Services
Gainesville, TX

Thomas McKay
BASF Corporation
South Lyon, MI

Rock McNeil
BASF Corporation
Southfield, MI

Suchit Meshram
Enercon India Ltd.,
Daman – India

Hendrik Mester
Repower Systems SE
Osterrönfeld, SH Germany

Angie Miller
Huntsman
The Woodlands, TX

William Miller
Huntsman Advanced Materials
The Woodlands, TX

Akira Miyase
University of Houston NWEC
Houston, TX

David Model
Triton
Chelmsford, MA

Dave Modos
IMCORP
Manchester, CT

Jiwon Mok
GE Global Research
Niskayuna, NY

Carsten Moller
R&D A/S
Hinnerup, Denmark

Henrik Møller
DNV-GL
Fredericia, Denmark

Robert Monroe
Fulcrum Composites Inc.
Midland, MI

Iain Montghomery
AGY
Aiken, SC

Jin Bum Moon
Wind Turbine Tech Research Center
Daejeon, Republic of Korea

Ernesto More
Ernesto More
Navarra, Spain

Pat Moriarty
NREL/NWTC
Golden, CO

Willard Morris
Imperium Inc.
Beltsville, MD

Justin Morse
ALSTOM Power Inc.
Richmond, VA

Patrick Muglia
AmTech Composites
Wapato , WA

Eduardo Munoz
Applus RTD
Houston, TX

Pedro Munoz de Filipe
AeroBlade
Minano, Spain

Noah Myrent
Purdue Center for Systems Integrity
Lafayette, IN

Jacques Nader
Siemens
Boulder, CO

Mala Nagarajan
Owens Corning
Granville, OH

Kamesh Narasimhan
NEPTCO Inc.
Granite Falls, NC

Jonathan Naughton
University of Wyoming
Laramie, WY

Ryan Neahr
General Dynamics Satcom Technologies
Richardson, TX

Jeff Nelson
Transalta
Calgary, Canada

John Newman
Laser Technology Inc.
Norristown, PA

Per Nielsen
Siemens
Aalborg, Denmark

Steen Arnfred Nielsen
Force Technology
Brøndby, Denmark

Khanh Nguyen
National Wind Technology Center/NREL
Louisville, CO

Daniel Nies
Nordex
Hamburg, Germany

Chris Niezrecki
UMass Lowell
Lowell, MA

Rogier Jijssen
Knowledge Centre Wind Turbine
Wieringerwerf, The Netherlands

Pourya Nikoueeyan
University of Wyoming
Laramie, WY

Simeon Andrew Ning
NREL/NWTC
Golden, CO

Maya Nissim
EDP Renewables
Houston, TX

Steve Nolet
TPI Composites
Warren, RI

Mark Noordanus
Global Blade Technology
Wieringerwerf, The Netherlands

Germán Moreno Notario
Applus+ LGAI
Barcelona, Spain

John Obrecht
Siemens
Boulder, CO

Frank O'Connor
ServusNet Informatics
Cork, Ireland

Ryan O'Connor
EDF-RE
Denver, CO

Ganzalo Palacio
Gamesa Wind Power
Vizcaya, Spain

Sharon Papke
Bayer MaterialScience
Pittsburgh, PA

James Parle
Muir Data Systems
Pasadena, CA

James Payant
Janicki Industries
Sedro-Woolley, WA

Raymond Pearson
Lehigh University
Bethlehem, PA

Eduardo Perez
Power Equipment Maintenance, Inc.
Piedmont, SC

Will Perry
GEIT
Lewistown, PA

Frank Peters
Iowa State University
Ames, IA

Soren Horn Petersen
Bladena Aps
Ringsted, Denmark

Stanton Peterson
BP Wind Energy
Houston, TX

Lars Pettersson
Vattenfall AB
Stockholm, Sweden

Tyler Phillips
Energetx
Holland , MI

Sascha Plath
Automated Precision
Heidelberg, Germany

Yuri Plotnikov
GE Global Research
Niskayuna, NY

Alejandro Ponce
Tecsis dba WindCom Services
Houston, TX

Nathan Post
NREL
Golden, CO

David Potter
National Instruments
Austin, TX

Eric Powell
Ashland, Inc.
Dublin, OH

Amar Pradhan
Fluitec Wind
Jersey City, NJ

Larry Preston
Heartland Energy Solutions
Mt Ayr, IA

Charles Previte
DIAB Sales, Inc.
DeSoto, TX

Padmakumar Puthillath
Milliken and Company
Spartanburg, SC

Jaime Rabell
Dow Corning
Mexico City, Mexico

Venkat Ramakrishnan
Michigan State University
East Lansing, MI

Amar Reddy
International Wind Inc
Long Beach, CA

Joan Ascanius Reffs
Force Technology
Brondby, Denmark

John Register
R-Conn NDT Inc
Menomonie, WI

Katelyn Reynolds
Invenergy, LLC
Chicago, IL

Pat Rezza
Resolute Marine Energy
Boston, MA

Ken Rhinefrank
Columbia Power Technologies
Corvallis, OR

Amir Riahi
GE Wind
Greenville, SC

William Riddle
Montana State University
Livingston, MT

Bradley Ring
Dept of Energy
Washington, DC

Garth Ripton
Iberdrola Renewables
Portland, OR

Richard Roberts
Hexcel
Dublin, CA

James Rodgers
Airgia LCC
Mesa, AZ

Daniel Rodriguez
AOC LLC
Collierville, TN

Jacob Roosma
We4Ce
Almelo, The Netherlands

Bjoern Roscher
EWEM
Delft

Stan Rosinski
Electrical Power Research Institute (EPRI)
Charlotte, NC

Ralph Rotolante
MovieTherm
Boxborough, MA

James Sadlo
3M-Industrial & Transporation Business
Round Rock, TX

Jon Salmon
enXco Corporation
Forest City, IA

Angelica Sanchez
Cabot Corporation
Billerica, MA

Daniel Sanchez
U.S. Department of Energy
Albuquerque, NM

Chris Sauer
Ocean Power Renewable Company
Portland, ME

Hely Ricardo Savio
Jade Systems S.I.
Zizur Mayor Navarra, Spain

Philip Schell
Zoltek Corporation
St. Louis, MO

Thomas Schmack
InspecTools
Santa Cruz, CA

John Schroeder
Texas Tech University
Lubbock, TX

Roel Schuring
LM Windpower
Lunderskov, Denmark

Juan Serrano
PPG Industries
Shelby, NC

Roland Sesselmann
Siemens Energy
Boulder, CO

Eric Shain
GE Renewable Energy
Grand Forks, ND

Shawn Sheng
NREL/NWTC
Golden, CO

Chris Shennan
HEXCEL
Duxford, United Kingdom

Steve Shepard
Thermal Wave Imaging
Ferndale, MI

Mark Shepler
Creative Foam Corporation
Fenton, MI

Robert Sherwin
EAPC Wind Energy
Norwich, VT

Rick Shumaker
Heron Wind
Traverse City, MI

Ryan Sievers
Siemens Wind Power
Boulder, CO

Matt Sigala
EDF Renewable Services
Adrian, TX

Elizabeth Sims
Cabot Corporation
Billerica, MA

Susan Skemp
SE Nat'l Marine Renewable Energy Center
Boca Raton, FL

Eskil Skoglund
DolphiTech
Raufoss, Norway

Matt Skinner
GE Oil & Gas
Skaneatele, NY

Jeff Smith
Gamesa
Trevose, PA

Ron Smith
Verdant Power
New York, NY

James Snelson
Infigen Energy
Sweetwater , TX

Dave Snowberg
NREL/NWTC
Golden, CO

Seyed Soltani
Wichita State University
Wichita, KS

Felipe Soriano
DIAB Sales, Inc.
DeSoto, TX

Sritharan Sri
Iowa State University
Ames, IA

Bill Staby
Resolute Marine Energy
Boston, MA

Bob Stakenborghs
Evisive
Baton Rouge, LA

Kevin Standish
Envision Energy
San Francisco, CA

Markus Stieglbauer
BASF Coatings
Oldenburg, Germany

Fred Stoll
Milliken and Company
West Chester, OH

Jan Sumfleth
Repower Systems SE
Schleswig-Holstein, Germany

Ryan Suncheefore
U.S. Dept of Energy
Washington, D.C.

Henry Swales
Clipper Windpower
Santa Barbara, CA

Paul Sweat
National Instruments
Thornton, CO

Todd Tagatz
MTS Systems Corporation
Eden Prairie, MN

Jason Testa
General Electric
Greenville, SC

Jim Thomas
Strategic Power Systems, Inc.
Charlotte, NC

Nick Tiedje
TPI Composites
Newton, IA

Henrik Stensgaard Toft
Aalborg University/EMD International A/S
Aalborg, Denmark

Ville Turkia
VTT Tehnical Research Centre of Finland
P.O. Box 1000, Fl-02044 VTT, Finland

Alan Turner
Micron Optics Inc.
Atlanta, GA

Paul Ubrich
Momentive Specialty Chemicals
Stafford, TX

Mary Uchida
University of Colorado
Boulder, CO

Hans Urich Thornberg
Bach Composites
Ft. Lupton, CO

C.P. (Case) Van Dam
University of California - Davis
Davis, CA

Ehren Van Schmus
Clipper Windpower
Santa Barbara, CA

Paul Veers
National Renewable Energy Laboratory
Golden, CO

Luis Vega
Hawaii Nat'l Renewable Energy Center
Honolulu, HI

Dayal Vinay
Iowa State University
Ames, IA

Alexander Vossler
General Electric
Greenville, SC

Tomas Vronsky
Vestas
Boulder, CO

Chris Walford
Wind Energy
Seattle, WA

Aaron Wahlstrom
Broadwind
Abilene, TX

Su Su Wang
University of Houston NWEC
Houston, TX

Siyong Wang
Chinese Wind Energy Association
Beijing, China

Sheryl Weinstein
Rope Partners
Santa Cruz, CA

Carsten Westergaard
NextraTEC, Inc.
Houston, TX

Kyle Wetzel
Wetzel Engineering
Austin, TX

Cecilia Wilson
Structural Integrity Assoc
San Jose, CA

Martin Winther-Jensen
Siemens
Brande, Denmark

John Wirt
VEC Technology, LLC
Greenville, PA

Hoon ill Won
Texas Tech University
Lubbock, TX

Geoff Wood
Profile Composites
Sidney BC, Canada

David Woodcock
Huntsman Corporation
The Woodlands, TX

Sean Xun
U.S. Dept of Energy
Washington, DC

Ke Yang
Institute of Engineering Thermohphysics
Beijing, China

Aaron Yarbrough
General Electric
Greenville, SC

Chandra Yerramalli
GE Electric-GRC
Schenectady, NY

Dong-Jin Yoon
Korea Research Inst of Stds & Science
Daejeon, Korea

Mostafa Yossef
Arab Academy for Science and Technology
Cairo Egypt

Usama Younes
Bayer Material Science LLC
Pittsburgh, PA

Robert Youssi
G.E.
Fallbrook, CA

Tung Pei Yu
University of Houston NWEC
Houston, TX

Wenbin Yu
Utah State University/AnalySwift LLC
Logan, UT

Paul Zakian
Bruel and Kjaer
San Diego, CA

Dave Zanier
Bladena
Roskilde, Denmark

Jose Zayas
U.S. Department of Energy
Washington, DCChina

Mingming Zhang
Institute of Engineering Thermohphysics
Beijing, China

Huiyi Zhang
Iowa State University
Ames, IA

Qi (Joyee) Zhu
GE Energy
Greenville, SC

Siqi Zhu
Iowa State University
Ames, IA

Sandia National Labs:

163 Erik Ridley
1515 Matthew Barone
1521 Garrett Nelson
1521 Paul Titus
1529 Carl Jacques
1531 Rich Jepsen
1541 Stefan Domino
1815 Bernadette Hernandez-Sanchez
1833 David Calkins
1833 Ernest Gonzales
3651 Stephanie Holinka
6000 Doug Bruder
6600 Justine Johannes
6620 Roberto Mata
6620 Dennis Roach
6621 Mark Retter
6621 Ray Ely
6621 Clay Newton
6621 Tom Rice
6622 Jason Bradbury
6623 Mark Soo Hoo
6624 Robert Baca
6625 Barry Boughton
6626 Charlie Richardson
6626 Genaro Montoya
6626 Stephen Neidigk
6630 Brad Parks
6640 Steve Heffelfinger
8800 Carol Adkins
8820 Amy Randolph Halloran
8821 Jonathan Berg
8821 Joshua Bryant
8821 Brandon Davis
8821 Brandon Ennis
8821 Thomas Herges
8821 Wesley Johnson
8821 Benjamin Karlson
8821 Chris Kelley
8821 David Maniaci
8821 David Mitchell
8821 Brian Naughton
8821 Josh Paquette
8821 Jonathan White
8822 Peter Kobos
8822 Budi Gunawan
9532 Recorded Information Management
10756 Technical Library

THIS PAGE INTENTIONALLY LEFT BLANK

Sandia National Laboratories